INSTABILITIES AND RADIATION OF THIN, BAROCLINIC JETS

Lynne D. Talley

B.A., Oberlin College (1976)
B.M., Oberlin College Conservatory (1976)

Submitted in Partial Fulfillment of the
Requirements for the Degree of
DOCTOR OF PHILOSOPHY

at the

Massachusetts Institute of Technology

and the

Woods Hole Oceanographic Institution

June, 1982

Signature of Author _____
Joint Program in Oceanography, Massachusetts
Institute of Technology - Woods Hole Oceano-
graphic Institution, April, 1982.

Certified by _____
Thesis Supervisor

Accepted by _____
Chairman, Joint Committee for Physical
Oceanography, Massachusetts Institute of
Technology - Woods Hole Oceanographic
Institution.

INSTABILITIES AND RADIATION OF THIN, BAROCLINIC JETS

by

Lynne D. Talley

ABSTRACT

Oceanic fluctuations are dependent on geographical location. Near
intense currents, the eddy field is highly energetic and has broad meri-
dional extent. It is likely that the energy arises from instabilities of
the intense current. However, the meridional extent of the linearly most
unstable modes of such intense jets is much narrower than the observed
region of energetic fluctuations. It is proposed here that weaker insta-
bilities, in the linear sense, which are very weakly trapped to the cur-
rent, may be the dominant waves in the far field.

As a preliminary problem, the (barotropic) instability of parallel
shear flow on the beta plane is discussed. An infinite zonal flow with
a continuous cross-stream velocity gradient is approximated with segments
of uniform flow, joined together by segments of uniform potential vortic-
ity. This simplification allows an exact dispersion relation to be found.
There are two classes of linearly unstable solutions. One type is trap-
ped to the source of energy and has large growth rates. The second type
are weaker instabilities of the shear flow which excite Rossby waves in

the far field: the influence of these weaker instabilities extends far beyond that of the most unstable waves.

The central focus of the thesis is the linear stability of thin, two-layer, zonal jets on the beta plane, with both horizontal and vertical shear. The method used for the parallel shear flow is extended to the two-layer flow. Each layer of the jet has uniform velocity in the center, bordered by shear zones with zero potential vorticity gradient. The velocity in each layer outside the jet is constant in latitude. Separate linearly unstable modes arise from horizontal and vertical shear. The energy source for the vertical shear modes is nearly all potential while the source for the horizontal shear modes is both kinetic and potential. The most unstable waves are tightly trapped to the jet, within two or three deformation radii for small but nonzero beta. Rossby waves and baroclinically unstable waves (in the presence of vertical shear) exist outside the jet because of a nonzero potential vorticity gradient there. Weakly growing jet instabilities can force these waves when their phase speeds and wavelengths match. In particular, westward jets and any jets with vertical shear exterior to the jet can radiate in this sense. The radiating modes influence a large region, their decay scales inversely proportional to the growth rate. Two types of radiating instability are found: (1) a subset of the main unstable modes near marginal stability and (2) modes which appear to be destabilized neutral modes. Westward jets have more vigorously unstable radiating modes.

Applications of the model are made to the eddy field south of the Gulf Stream, using data from the POLYMODE settings along 55°W and farther into

the gyre at MODE. The energy decay scale and the variation of vertical structure with latitude in different frequency bands can be roughly explained by the model. The lower frequency disturbances decay more slowly and become more surface intensified in the far field. These disturbances are identified with the weak, radiating instabilities of the model. The higher frequency disturbances are more trapped and retain their vertical structure as they decay, and are identified with the trapped, strongly unstable modes of the jet.

Thesis Supervisor: Joseph Pedlosky, Senior Scientist
Department of Physical Oceanography
Woods Hole Oceanographic Institution

ACKNOWLEDGEMENTS

My greatest thanks go to my thesis advisor, Joseph Pedlosky, for suggesting the problem and providing patient guidance and an example of clear, insightful thinking. I appreciated the helpful discussions with my thesis committee members, Bill Schmitz, Glenn Flierl and Dale Haidvogel. I particularly enjoyed Bill Schmitz's aid with the material for Chapter 4. Nelson Hogg was also very helpful in that regard.

I am especially grateful to Mike McCartney for supporting me for the first two and a half years of graduate school. Mary Raymer has been a wonderful help throughout and drafted a large number of the Figures. Anne-Marie Michael did the typing.

This work was supported by a grant from the National Science Foundation, Office of Atmospheric Science.

Table of Contents

List of Figures

3.1.2   Velocity profile and potential vorticity gradient, modified by the contribution of the profile breaks to the term $(-U_{yy})$. Four different configurations for the velocity in the shear zone are shown, along with the resulting effective potential vorticity gradient. It is arbitrarily assumed here that $\partial \hat{\pi}/\partial y$ is positive in Region III and negative in Region I.

3.2.1   Neutral stability curves for the two-layer model of baroclinic instability, where the layers have equal depths and the channel has half-width W (cf, Pedlosky, 1979). F is assumed to be 5 and $(U_1-U_2) = 1.0$. β and k are varied. Two half-widths are used: W = 1 (dashed) and W = 1.7 (solid).

3.2.2   (a) U(y) as given by (3.2.2) and (b) $\partial \hat{\pi}/\partial y$, the effective potential vorticity gradient (3.1.8).

3.2.3   Neutral stability curves in the β-k plane for the profile (3.2.2). Here F = 5 and D = 1.7. The plane extends to negative β: an eastward jet has positive β and a westward jet has negative β. The solid curves are $c_i = 0$, the dashed curves $\ell_i = \ell_r$. The dot-dash curves are also $c_i=0$, but based on only a few points. S = stable; ut = trapped instability; ur = radiating instability. There are three modes at $\beta > 0$ shown in two diagrams: (a) longwave, vertical shear mode (2) and (b) upper layer, horizontal shear mode (1) and shortwave, vertical shear mode (3). For $\beta < 0$, Modes 1 and 3 become the upper layer horizontal shear mode.

3.2.4   For the flow in Figure 3.2.2 at $\beta = 1$: (a) $c_r(k)$ and (b) $c_i(k)$. Modes are labelled as in Figure 3.2.3.

3.2.5   For the flow in Figure 3.2.2 at $\beta = 1$: (a) kinetic energy transfer in the upper (U) and lower (L) layers and (b) potential energy transfer to the perturbations. The total energy transfer is proportional to the growth rate, kc_i.

3.2.6   Eigenfunctions for each mode of Figure 3.2.3. The wavenumber k, c_r and c_i are listed at the left. (a) Horizontal shear mode, (b) longwave vertical

shear mode, (c) shortwave vertical shear mode, and
(d) radiating longwave mode.

3.2.7 (e)   Barotropic (BT) and baroclinic (BC Rossby wave dis-
            persion relations $\beta = 1$ for $\ell = 0$ and $\ell \to \infty$. The
            dashed curves are c_r from (a), rescaled with $U = -1$.

3.2.8   For the flow of Figure 3.2.2 at $\beta = -1$: (a) $\ell_1(k)$ and
            (b) $\ell_2(k)$. The solid curves are the real and the dashed
            curves the imaginary parts of .

3.2.9   For the flow in Figure 3.2.2 at $\beta = -1$: (a) kinetic
            energy transfer and (b) potential energy transfer to
            the perturbations.

3.2.10   (a) $U(y)$ as given by (3.2.3) and (b) $\partial\hat{\pi}/\partial y$, the effec-
            tive potential vorticity gradient (3.1.8).

3.2.11   Neutral stability curves in the β-k plane for the pro-
            file (3.2.3). The plane extends to negative β, as in
            Figure 3.2.3. Notation is as in Figure 3.2.3. There
            are two modes shown separately: (a)longwave, vertical
            shear mode (2) and (b) combination of the shortwave,
            vertical shear mode and the upper layer, horizontal
            shear mode (3).

3.2.12   For the flow in Figure 3.2.10 at $\beta = 1$: (a) $c_r(k)$ and
            (b) $c_i(k)$.

3.2.13   For the flow in Figure 3.2.10 at $\beta = 1$: (a) kinetic
            energy transfer and (b) potential energy transfer
            to the perturbations. The lower layer kinetic energy
            transfers are negligible.

3.2.14   For the flow in Figure 3.2.10 at $\beta = -1$: (a) $c_r(k)$ and
            (b) $c_i(k)$.

3.2.15   For the flow in Figure 3.2.10 at $\beta = -1$: (a) kinetic
         energy transfer and (b) potential energy transfer
         to the perturbations.

3.2.16   (a) $U(y)$ as given by (3.2.4) and (b) $\partial\hat{\pi}/\partial y$, the effec-
         tive potential vorticity gradient (3.1.8).

3.2.17   Neutral stability curves in the β-k plane for the
         profile (3.2.4). There are two basic modes labelled
         (2) and (3), as in Figure (3.2.11). Notation is as
         in Figure 3.2.3. The long-dashed boundaries are where
         c_i drops to .01.

3.2.18   For the flow in Figure 3.2.16 at $\beta = 5$: (a) $c_r(k)$ and
         (b) $c_i(k)$.

3.2.19   For the flow in Figure 3.2.16 at $\beta = 5$: (a) kinetic
         energy transfer and (b) potential energy transfer
         to the perturbations. The upper layer kinetic en-
         ergy transfer is negative and the lower layer trans-
         fer is negligible.

3.2.20   For the flow in Figure 3.2.16 at $\beta = 1$: (a) $c_r(k)$ and
         (b) $c_i(k)$.

3.2.21   For the flow in Figure 3.2.16 at $\beta = 1$: (a) kinetic
         energy transfer and (b) potential energy transfer
         to the perturbations.

3.2.22   The eigenfunction for a radiating, horizontal shear
         mode for the flow in Figure 3.2.16: the trapped
         modes are very similar to the modes shown in
         Figure 3.2.6 and are not pictured here.

3.2.23   Rossby wave dispersion relation for a fluid with
         two layers of equal depth and vertical shear
         $(U_1-U_2) = 0.0$ at $\ell = 0$ and $\ell = 100$. The baro-
         tropic wave is marked BT and the baroclinic
         is marked BC. The dashed curves are the phase
         speeds of the unstable waves at $\beta = -5$, rescaled
         with $U = -1$.

3.2.24   Rossby wave dispersion relation for a fluid with two layers of equal depth and vertical shear (U_1-U_2) = .15. The phase speed is shown as a function of k at ℓ = 0 for (a) β = .1 and (b) β = 1. Notice that the phase speed is complex for β = .1. The solid curves are the real part and the dashed curves the imaginary part of c.

3.2.25   (a) U(y) as given by (3.2.7) and (b) $\partial\hat{\pi}/\partial y$, the effective potential vorticity gradient (3.1.8).

3.2.26   Neutral stability curves in the β-k plane for the profile (3.2.7). The notation is as in Figure 3.2.17. The radiating shortwaves become stable at 5 < k < 6. The high β cutoffs of modes 1 and 4 were not determined.

3.2.27   For the flow of Figure 3.2.25 at β = 4: (a) $c_r(k)$, (b) $c_i(k)$.

3.2.28   For the flow of Figure 3.2.25 at β = 4: (a) $\ell_1(k)$ and (b) $\ell_2(k)$. The solid curves are the real part and the dashed curves the imaginary part of .

3.2.29   A radiating eigenfunction for the profile (3.2.7): the trapped modes are very similar to the modes shown in Figure 3.2.6 and are not pictured here.

3.2.30   Rossby wave dispersion relations for a fluid with two layers of equal depth and vertical shear (U_1-U_2) = -.15. The phase speed is shown as a function of k for ℓ = 0 for (a) β = .1 and (b) β = 1. The solid curves are the real part and the dashed curves the imaginary part of c.

3.2.31   (a) U(y) as given by (3.2.8) and (b) $\partial\hat{\pi}/\partial y$, the effective potential vorticity gradient (3.1.8).

3.2.32   Neutral stability curves in the β-k plane for the profile (3.2.8). The boundaries are as in Figure 3.2.17. (a) Longwave, vertical shear mode (2), (b) combined shortwave vertical shear mode and hor-

izontal shear mode (3), and (c) horizontal shear
mode (4). Notation is as in Figure 3.2.17. The
dotted curve in (b) and (c) indicates that Modes
3 and 4 are connected there.

3.2.33   For the flow of Figure 3.2.31 at $\beta = 1$: (a) $c_r(k)$,
(b) $c_i(k)$.

3.2.34   For the flow of Figure 3.2.31 at $\beta = 1$: (a) $\ell_1(k)$
and (b) $\ell_2(k)$.

3.2.35   A radiating eigenfunction at $\beta = 1$ for the flow of
Figure 3.2.31.

3.3.1   Neutral stability diagram in the β-k plane for the
profile (3.3.1). (a) Both vertical shear modes (2)
and (3) and (b) upper layer horizontal shear modes
(1). Because of the reduced shear zone width, there
is more than one horizontal shear mode (see Chapter 2).

3.3.2   Neutral stability diagram in the β-k plane for the
profile (3.3.2). The horizontal shear modes of
Figure 3.3.1b are coalesced with the vertical
shear modes.

3.3.3   Neutral stability diagram in the F-k plane for the
profile (3.2.3), at $\beta = 0$. There are two unstable
modes (see Figure 3.2.9 for the complementary dia-
gram in the β-k plane).

3.3.4   The effect of channel walls which are distant from
the jet relative to the internal deformation radius:
the imaginary phase speed c_i of the long wave, radi-
ating part of the mode shown in Figure 3.2.19b, at
$\beta = 2$, for (a) a channel without walls and (b) a
channel with walls at $H = \pm100$.

4.3.1   Mean eastward flow, $\overline{U}$, along 55°W at 600 m and
4000 m using all three settings of the POLYMODE
array. See Schmitz (1978, 1980).

4.3.2   Approximate mean potential vorticity gradient at 55°W, using the mean flows of Figure 4.3.1, assuming an eastward flow of 50 cm/sec at 600 m at 40°N.

4.3.3   Mean momentum flux, $\overline{u'v'}$, along 55°W at 600 m and 4000 m using all three settings of the POLYMODE array. See Schmitz and Holland (1981).

4.3.4   Mean heat flux, $\overline{v'T'}$, along 55°W at 600 m and 4000 m using all three settings of the POLYMODE array.

4.3.5   (a) Transfer of kinetic energy at 600 m from the mean to the eddies, $-(\overline{u'v'})\partial\overline{U}/\partial y$; kinetic energy at 600 m from the eddies to the mean, $-\overline{U}(\partial\overline{u'v'}/\partial y)$; potential energy at 800 m from the mean to the eddies, $-(f/\overline{T}_z)\overline{v'T'}(\partial\overline{U}/\partial z)$. (b) Transfer of kinetic energy at 4000 m from the mean to the eddies, $-(\overline{u'v'})\partial U/\partial y$; kinetic energy at 4000 m from the eddies to the mean, $-\overline{U}(\partial\overline{u'v'}/\partial y)$.

4.4.1   (Dimensional) frequency vs. wavenumber of the unstable modes for four jets: (a) eastward jet with a westward undercurrent and no vertical shear in the ocean interior; (b) eastward jet in the upper layer with small eastward vertical shear in the ocean interior; (c) eastward jet in the upper layer with small, westward vertical shear in the ocean interior; (d) westward jet in the upper layer, no vertical shear in the interior. All jets have non-dimensional values of .1 for β. [The scales for (d) show the wavelength in kilometers and period in days.]

4.4.2   (Dimensional) growth rate, kc_i, vs. wavenumber for the same cases as Figure 4.4.1. Wavelength and period scales are shown in (d).

4.4.3   (Dimensional) frequency vs. meridional decay scale for the same cases as Figure 4.4.1. A period scale is also shown in (d).

CHAPTER I: INTRODUCTION

The central subject of this thesis is the linear stability of certain geophysical flows: thin, baroclinic jets with large horizontal and vertical shear. A major focus of the theory and applications is the existence of "radiating" instabilities, which have very large meridional decay scales. While the high eddy energy which occurs directly in strong currents is undoubtedly due to the most unstable waves of the currents, the meridional decay of the energy is much too slow to be explained by the most unstable waves. Radiating instabilities are explored as a possible source of this slowly decaying, highly energetic eddy field. The primary application explored here is to intense, separated subtropical jets, such as the Gulf Stream east of Cape Hatteras. The theory could just as easily be applied to the Antarctic Circumpolar Current or to westward flows like the North Equatorial Current. More detailed observational and theoretical background are given below, followed by short summaries of the three chapters which are the bulk of the thesis.

1.   Observational background

The large-scale, low-frequency, eddy energy distribution in mid-latitude oceans is highly inhomogeneous. Maps of any measure of the eddy energy show very energetic fluctuations in the area of the strongest currents, weaker fluctuations near and in weaker currents and the weakest fluctuations where the currents are very gentle. The relation between the current strength and the eddy energy is quite clear: it is evident

in horizontal maps of the thermocline potential energy (Dantzler, 1977) and surface kinetic energy (Richardson, 1981; Wyrtki, Magaard and Hager, 1976) in the North Atlantic. The inhomogeneity is evident in zonal XBT sections in the North Pacific (Bernstein and White, 1977) where much higher fluctuation energy occurred in the west. It is evident in the results of long-term current meter arrays in the western North Atlantic (Schmitz, 1978) and the North Pacific (Schmitz, Niiler, Bernstein and Holland, 1982).

Various sources for the eddy energy in the oceans have been explored. These fall in the categories of direct atmospheric forcing, topographic forcing, local instability and radiation from localized disturbances. These mechanisms are reviewed by Philander (1978). Atmospheric forcing (Frankignoul and Muller, 1979 and Muller and Frankignoul, 1981) seems to be a satisfactory explanation for the low-level, background eddy energy found even in the quietest parts of the ocean, such as the Northeast Atlantic. Atmospheric forcing has neither the strength nor the spatial inhomogeneity to account for the higher eddy energy encountered elsewhere in the ocean. Topographic forcing may be quite important: topography can change the structure of fluctuations, can cause a flow to be unstable that would otherwise be stable (Pedlosky, 1980) and can be the source of perturbations to an unstable flow. Although intensification of eddy energy can be seen where the topography is rough (such as over the New England Seamounts), topography alone does not account for the general eddy field of the western subtropical oceans. Local flow instability is the suggested source of eddies directly in currents such as the Gulf

Stream and the North Equatorial Current (Gill, Green and Simmons, 1974) and in these currents' counterparts in numerical models (Haidvogel and Holland, 1978). Local instability of the westward return flow in the subtropical gyre may also account for the variability observed there (Holland and Lin, 1975).

None of these mechanisms can really account for the spatial distribution of the eddy energy in the western North Atlantic and North Pacific. Specifically, while the energy levels directly in the Gulf Stream and Kuroshio are high and clearly are due to local processes, the slow decay of this energy to the south of these currents cannot be entirely explained by local processes. (Chapter IV discusses these scales in more detail for the North Atlantic.) That is, the eddy field in the subtropical gyres may be more related to the presence of the intense currents (Gulf Stream and Kuroshio) than to local instability processes. The energy from the instabilities of these intense currents finds its way into the gyre interiors: one mechanism which is being explored is the propagation and decay of Gulf Stream rings (Flierl, 1975, 1977; Flierl, Larichev, McWilliams and Reznik, 1980). It is the purpose of this thesis to explore a simpler, but related possibility: namely, that the structure of the eddy field south of the Gulf Stream can be understood through a consideration of the unstable modes of the Gulf Stream itself. While the linear stability problem cannot tell us exactly what the fully-developed eddy field will look like, it can tell us what the possibilities are. Then a comparison of linear stability results with observations may predict which linearly unstable waves are most important at finite amplitude. Con-

versely, knowledge of the possible instabilities can predict aspects of
the actual eddy field. Since Gulf Stream rings are the ultimate product
of the Gulf Stream's finite amplitude instability, perhaps their struc-
ture and preferred size can be deduced, or at least reconciled with, the
instabilities of the Gulf Stream.

2. Theoretical background

This thesis is concerned with the stability of vertically-sheared
thin jets in which both horizontal and vertical shear by themselves can
produce instability. Jets with various geometries are explored to find
as many of their unstable modes as possible. The unstable modes are clas-
sed according to their vertical and meridional structure. While the waves
with the largest linear growth rates are explored here and are clearly
important in the finite amplitude state, attention is focused on waves
with lower growth rates and very large meridional decay scales. It is
hypothesized that the fully-developed flow contains more than just the
initial basic flow and the most unstable waves: it is suggested that
waves with lower growth rates survive and grow and that these waves,
which have much larger meridional decay scales than the more unstable
waves, dominate the far field of the jet while the most unstable waves
are the most important waves right in the jet.

Instabilities of baroclinic jets arise from both the horizontal and
vertical shear. One result of the following study is that each unstable
mode can be classified as a horizontal or vertical shear mode in that it

exists when either the vertical or horizontal shear, respectively, is removed. However, the exact source of energy for the unstable mode may be a strong mixture of both kinetic and potential energy, independent of whether the mode is identified as a horizontal or a vertical shear mode. Empirically, it is found that no additional modes arise when both shears are present. Thus it is sensible to consider barotropic and baroclinic instabilities separately before combining them together in a mixed flow.

The study of barotropic instability began in the nineteenth century with Helmholtz's (1868) and Rayleigh's (1879, 1880) considerations of the stability of parallel shear flow. (The problem of the stability of homogeneous, horizontally-sheared flows on the f-plane is identical with the problem for non-rotating, parallel shear flow.) Piecing flow profiles from straight lines, Rayleigh (1879, 1880) obtained analytic solutions for a variety of cases, including shear layers and jets, with and without boundaries. He also derived a necessary condition for instability based on the occurrence of an inflection point in the velocity (Rayleigh, 1887). A second necessary condition for instability of parallel shear flow was derived by Fjørtoft (1950).

The stability of parallel shear flows in the presence of β was first studied by Kuo (1949). He showed that logarithmic singularities in solutions at points where the phase speed of neutral solutions matches the flow speed requires that the potential vorticity gradient vanish there. Thus the number of neutral solutions with phase speeds in the range of the flow speed is less than or equal to the number of zeros of the potential vorticity gradient. Drazin and Howard (1962) and Howard (1964) showed

that, when $\beta = 0$, such neutral solutions have contiguous unstable solutions. Since the number of neutral solutions is equal to the number of inflection points, and all of these neutral solutions have contiguous unstable solutions, the number of unstable modes can be predicted (equal to the number of inflection points). This criterion has not been extended to the β plane.

The stability of specific parallel shear flows on the β plane was investigated by Howard and Drazin (1964). They found analytical solutions for simple flows and a neutral stability curve for the shear flow, $U(y) = \tanh y$. Most importantly for the present investigation, they predicted an additional long-wave mode for the hyperbolic-tangent flow with non-zero β: this long-wave mode is not tied to the neutral solutions associated with the zeroes of the potential vorticity gradient, $(\beta - U_{yy})$.

Dickinson and Clare (1973) took up the search for the unstable modes of the hyperbolic-tangent profile on the β plane. They confirmed Howard and Drazin's suspicions, finding that there is indeed an additional long-wave mode when β is non-zero. Moreover, they paid close attention to the horizontal structure of the instabilities and found that the unstable waves identified with the hyperbolic-tangent instability at $\beta = 0$ are strongly trapped to the shear zone, while the unstable long-waves resemble Rossby waves in the westerly part of the flow. These "Rossby" waves have large meridional decay scales. They suggested that the new mode can be interpreted as over-reflection of Rossby waves from the shear zone.

The existence of the Rossby-wave-like solutions (radiating solutions) found by Dickinson and Clare (1973) requires an ambient potential

vorticity gradient (e.g., β) in the outer field. It also depends crucially on the overlapping of the unstable wave phase speeds and zonal wavenumbers with possible Rossby-wave phase speeds and zonal wavenumbers. McIntyre and Weissman (1978) discussed this phase speed condition; they also discussed the definition and existence of radiating waves, perhaps a little too adamantly defining a radiating wave as one with a zero growth rate (since only non-growing waves can be purely wavelike in all horizontal directions). The definition of radiation is extended here to include instabilities which are similar to Rossby waves in the flow external to the energy source.

Since strict limits can be placed on the instability phase speeds (Howard, 1961; Pedlosky, 1964) and since the Rossby wave dispersion relation gives the phase speeds of the Rossby waves in the far field, it is easy to predict when an unstable flow will not radiate. (Proving the existence of radiating solutions, of course, requires solving the specific problem.) Instability phase speeds must be within the range of the mean flow speed (with a small correction due to β) and Rossby wave phase speeds must be westward with respect to the mean flow. Thus a monotonic shear layer or a westward jet may radiate, while an eastward, barotropic jet cannot radiate. A basically eastward jet might radiate if, for instance, vertical shear (in the form of a westward undercurrent or weak vertical shear in the far field) or westward jets on either side of the eastward jet are included.

A relevant investigation of how neutral (Rossby) waves in a flow with vertical shear can be forced by a moving boundary was made by Ped-

losky (1976). The vertically-sheared flow is stable because of large, non-zero β. The disturbances forced by the boundary are either strongly trapped or purely radiating (semi-infinite Rossby waves), depending on whether the phase speed condition, matching the phase speed and zonal wavenumbers of the moving boundary and the Rossby waves, is satisfied. The present study extends this theory to the situation which motivated it, namely whether periodic instabilities of a zonal current can excite the ambient waves of the far field and carry the instabilities' energy far away into the ocean interior.

Baroclinic instability results from the horizontal density gradient of rotating flow. Phillips (1954) introduced the layer model of baroclinic instability, which tremendously simplified the mathematics of the general, continuously-stratified problem. Of course, the two-layer model resolves only the first two vertical modes of the flow. Phillips showed how baroclinic instability depends on the size of the horizontal density gradient and how β stabilizes the flow. Pedlosky (1964a, b) further extended the results for the two-layer model. He also derived two necessary conditions for instability for flow with both horizontal and vertical shear which are the β-plane analogs of Rayleigh's and Fjørtoft's theorems, for both continuously stratified and two-layer flow.

The stability of flows with both vertical and horizontal shear has been considered by a number of authors. Most relevant to the present investigation are those involving the stability of quasi-geostrophic flows with strong horizontal shear in at least one of the layers. Orlanski (1969) considered the effects of topography and varying stratification

on the instability of a baroclinic jet. Hart (1974) showed how the relative importance of barotropic and baroclinic instability depends on the relative layer depths and Froude number. Gent (1974, 1975) discussed the effect of variable jet widths and β on the unstable modes, showing that the meridional scale of the most unstable wave is set by the jet width rather than the Rossby deformation radius. Haidvogel and Holland (1978) showed that a linear stability analysis of instantaneous and time-averaged flow profiles taken from two-layer, eddy-resolving general circulation models yields meaningful results for the lowest order properties (wavenumber, phase speed and growth rate) of the dominant waves in the complete model. Holland and Haidvogel (1980) investigated the effect of selected parameter changes (amount of horizontal shear in the lower layer, Froude number, relative layer depths, ratio of β to the relative vorticity) on the relative importance of barotropic and baroclinic instability.

One important difference between the present study and these mixed instability studies is their concentration on the most unstable waves. The usual assumption in linear stability analyses is that the most unstable wave is the most likely to succeed in growing to the greatest amplitude and is the most likely to be observed. (Indeed, comparison of the most unstable waves of Eady's (1949) and Charney's (1947) models with atmospheric observations shows that this is approximately true, while Haidvogel and Holland (1978) showed that the linearly most unstable waves explain much about the fully-nonlinear eddy field in general circulation models.) However, more weakly unstable waves may also be important,

especially if their meridional structure is very different from that of the most unstable waves, e.g. if their meridional decay is much slower than the decay of the most unstable waves.

Studies of weakly non-linear, finite-amplitude instability (e.g., Pedlosky, 1970) show how the most unstable waves develop. Pedlosky (1981) also showed, however, that the most unstable wave is not necessarily the one which dominates the final solution. As the most unstable wave grows, it alters the mean flow in such a way as to make it more hospitable for longer, less unstable waves to grow. The final, finite-amplitude solution is dominated by a longer wave with smaller linear growth rates than the most unstable wave. In other studies (Loesch, 1974; Pedlosky, 1975), it was shown that nonlinear interactions between unstable and stable waves can feed energy to stable waves. These results are important for this thesis because it is assumed here that waves other than the most unstable wave can survive and grow to finite amplitude so that the final field is composed of several different waves with radically different linear growth rates and meridional decay scales.

3.   Thesis outline

The stability of homogeneous, parallel shear flow on the β-plane is discussed in Chapter II. Flow profiles are simplified using Rayleigh's method (1879, 1880), extended to flow on the β-plane. Necessary conditions are derived and a definition of radiating instabilities is given. Unstable solutions of a monotonically sheared flow and a thin jet are

found. When β is non-zero, so that there is a potential vorticity gradient throughout the fluid, the monotonically-sheared flow and a westward jet have radiating instabilities. (An eastward jet cannot radiate outside the jet because its instabilities do not meet the phase speed condition.) The radiating modes are mainly <u>destabilized</u> Rossby waves rather than modes which were trapped when circumstances did not permit radiation (e.g., when $\beta = 0$).

Chapter III is the heart of the thesis, containing results for thin baroclinic jets. The jets all have two layers and strong horizontal shear. First the results for non-radiating jets are carefully explored. The geometry is then changed slightly to allow these jets to radiate: a jet with a westward undercurrent, jets with small vertical shear in the ocean interior and westward-flowing jets are studied. There are two types of radiating instability: (1) trapped instabilities of the non-radiating jet which are now enabled, by virtue of the change in geometry, to radiate and (2) destabilized Rossby waves of the interior ocean.

Chapter IV is a comparison of the model results of Chapter III with observations in the western North Atlantic. The radiating solutions of Chapter III have distinctive vertical structures depending on their characteristic phase speeds and their ability to propagate in each of the two layers in the ocean interior. There is rough agreement between the model and observations if a basic state is chosen which has an eastward Gulf Stream, westward sidelobes and eastward vertical shear in the ocean interior. The observed eddy field can then be made up of highly unstable, trapped waves in the Gulf Stream and more slowly growing, radiating waves in the ocean interior.

CHAPTER II: BAROTROPIC INSTABILITY

The main subject of the thesis is the stability of thin baroclinic jets, which have both horizontal and vertical shear. It is helpful to first break the mixed baroclinic-barotropic problem into its constituents, barotropic and baroclinic instability, so that the role of each is better understood. The approximations used to model the mean velocity profiles, necessary conditions for instability as applied to such models and the definition of and conditions for radiation are more easily discussed in the context of barotropic instability. This chapter is a discussion of the linear stability of parallel shear flow on the β-plane, using a method similar to Rayleigh's (1879) to approximate the mean flow. Several specific flows are then examined for their stability to infinitesimal perturbations.

2.1 Formulation of the Linear Stability Problem for Homogeneous, Parallel Shear Flow.

The fluid whose flow is examined for stability is assumed to be homogeneous and inviscid. The flow is assumed to be quasi-geostrophic in that the velocities can be written in terms of a stream function ψ. The non-dimensionalized potential vorticity equation is derived and discussed by Pedlosky (1979). It is:

$$\left(\frac{\partial}{\partial t} - \psi_y \frac{\partial}{\partial x} + \psi_x \frac{\partial}{\partial y}\right) (\nabla^2 \psi + \beta y) = 0$$

(2.1.1)

This is already non-dimensionalized, with

$$[x,y] = L, \quad [u,v] = U_0, \quad [t] = L/U_0, \quad [\psi] = LU_0$$

and $\beta = \beta_0 L^2/U_0$. (The square brackets here mean "the scale of".) It is further assumed that the velocity and stream-function are composed of two well-separated parts: a mean, steady flow and infinitesimal perturbations on the flow. The basic flow is assumed to be zonal and to vary only with latitude. Thus

$$\psi = \Psi(y) + \phi(x,y,t)$$

$$u = U(y) + u'(x,y,t) = -\Psi_y - \phi'_y$$

$$v = v'(x,y,t) = \phi_x$$

where $\phi \ll \Psi$. Linearizing the potential vorticity equation (2.1.1) to include only terms of order ϕ, we obtain

$$\left(\frac{\partial}{\partial t} + U(y)\frac{\partial}{\partial x}\right) \nabla^2\phi + \phi_x (\beta-U_{yy}) = 0$$

The domain of the flow is infinite in the x-direction and may be bounded by walls at $y = \pm H$. The boundary condition at $y = \pm H$ is that $v = \phi_x = 0$ there. If $H \to \infty$, the boundary condition is that the solution be bounded at infinity, or equally that the energy flux be outward at infinity.

Seeking normal mode solutions

$$\phi(x,y,t) = A(y) e^{ik(x-ct)},$$

where k is real and $A(y)$ and c are complex, the potential vorticity equation becomes the familiar

$$[U(y) - c]\left(\frac{d^2A}{dy^2} - k^2A\right) + (\beta - U_{yy}) A = 0 \qquad (2.1.2)$$

Solutions to this equation are sought, with particular interest focused on solutions with complex c, which therefore have exponential growth.

There are four useful theorems which yield some information about the stability of a particular flow U(y) before the detailed stability analysis is undertaken. They are all well-known, so only a brief statement of each will be given here. The first two are necessary (but not sufficient) conditions for instability. In their non-β-plane forms, they are Rayleigh's inflection point theorem (Rayleigh, 1880) and the Fjørtoft extension of this theorem (Fjørtoft, 1950). The β-plane extension of the Rayleigh theorem was made by Kuo (1949) for homogeneous flow, by Charney and Stern (1962) for stratified flow and by Pedlosky (1964) to include upper and lower boundary conditions. An extension of Fjørtoft's theorem to the β-plane, including stratification, was made by Pedlosky (1964). Using the notation of Pedlosky (1979), these two theorems in their normal mode, β-plane form, for unstratified flow, are:

$$c_i \int_{-H}^{H} dy \ \frac{|A|^2}{|U-c|^2} \ \frac{\partial \pi}{\partial y} = 0 \qquad (2.1.3)$$

and

$$\int_{-H}^{H} dy \ \frac{|A|^2}{|U-c|^2} \ U \ \frac{\partial \pi}{\partial y} > 0 \qquad (2.1.4)$$

where $\partial \pi / \partial y = (\beta - U_{yy})$. Here the integrals are taken over the domain of the flow (-H,H), H can be extended to infinity and a is any constant. The first theorem says that, if the growth rate of the perturbation is to be non-zero, the potential vorticity gradient $(\beta - U_{yy})$ must change sign somewhere in the flow. The second theorem says that the product $U(\beta - U_{yy})$

must be positive somewhere in the flow. [Taking the two theorems together, $(U-a)(\beta-U_{yy})$ must be positive somewhere for instability to be possible, where a is any constant.]

A third useful theorem, which places bounds on the phase speed and growth rate of the perturbations, is the semi-circle theorem, derived in its non-β-plane form by Howard (1961) and extended to the β-plane by Pedlosky (1964). Again using notation from Pedlosky (1979), this theorem says that if the phase speed is complex ($c = c_r + ic_i$), so that the perturbation ϕ is growing exponentially, then its phase speed has limits:

$$U_{min} - \frac{\beta}{2(\pi^2/4 + k^2)} < c_r < U_{max} \qquad (2.1.5a)$$

$$c_i^2 \leq \left(\frac{U_{max} - U_{min}}{2}\right)^2 + \frac{\beta}{k^2 + \pi^2/4} \frac{U_{max} - U_{min}}{2} \qquad (2.1.5b)$$

In the absence of β, the complex phase speed must lie within the semi-circle of radius $(U_{max}-U_{min})/2$, centered at

$$(c_r, c_i) = \left(\frac{U_{max} + U_{min}}{2}, 0\right)$$

A fourth useful theorem, only applicable to flows where β is zero, is Howard's inflection point theorem (1961). This theorem predicts the number of neutral modes that exist in a parallel shear flow. For each inflection point ($U_{yy} = 0$) there is one neutral mode with contiguous unstable solutions. This theorem has not been extended to the β-plane: it is clear from the work of Howard and Drazin (1964) and Dickinson and Clare (1973) that additional modes appear as soon as β is non-zero. The added

modes appear, from the present work, to arise when the latitudinal structure of the eigenfunctions can be wavelike.

2.2   Choice of Flow Profiles

The solution of (2.1.2) is made difficult by the possible presence of critical layers, where $c = U(y_c)$, within the flow. If the disturbance is growing, so that $c_i \neq 0$, the problem is non-singular on the real line and has a well-behaved solution. If the flow velocity, U, changes continuously with y, the only allowed neutral modes must have phase speeds either outside the range of the flow speed or equal to the flow speed where the potential vorticity gradient vanishes (Kuo, 1949).

In order to avoid problems associated with critical layers, Rayleigh (1879) introduced a way of approximating flow profiles (with $\beta = 0$) which significantly simplified the finding of solutions. Rather than allow the flow to change continuously in y, with isolated zeroes of the vorticity gradient, he required that U_{yy} vanish everywhere <u>except</u> at isolated points. Flows were approximated with straight lines

$$U = a$$

or

$$U = a + by$$

where a and b are constants. This effectively compresses non-zero U_{yy} into delta functions at points where straight lines are joined together.

Rayleigh's method is extended here to the β-plane. On the β-plane, the flow is pieced together out of regions where the potential vorticity gradient either vanishes <u>or</u> is independent of y. The problem (2.1.2) is

simplified by approximating the flow $U(y)$ by

$$U = a$$

or

$$\beta - U_{yy} = 0$$

This is slightly different from Rayleigh's formulation in that the potential vorticity gradient does not vanish <u>everywhere</u>, but is equal to β, the planetary vorticity gradient, where U is independent of y. Solutions to (2.1.2) are then found in each separate region of the flow profile. Boundary conditions at the northern and southern walls, or at $y = \pm \infty$, are applied. Then, in order to determine the rest of the structure of $A(y)$ and to find $c(k)$, matching conditions on the pressure and normal velocity are applied at each profile break.

The matching conditions, originally due to Rayleigh (1880), are that the displacement of the material (zonal) interface between the two regions of the flow be the same in both regions on either side of the interface. Thus, if the streamfunction is

$$\phi = A(y) e^{ik(x - ct)} \quad ,$$

the meridional velocity is

$$v = ik A(y) e^{ik(x - ct)}$$

and the interface displacement is

$$\eta = F(y) e^{ik(x - ct)} \quad ,$$

then the velocity and displacement are related by

$$v = \frac{D\eta}{Dt} = ik (U-c) F(y) e^{ik(x-ct)} \quad .$$

The function $F(y)$ must be the same each side of the interface; thus

$$F(y) = \frac{A(y)}{U-c}$$

must be continuous across the interface. If the profile break occurs at $y = 0$ for instance, this condition is written as

$$\left[\frac{A(y)}{U-c} \right]_0 = 0 \tag{2.2.2}$$

where the square brackets indicate the jump in the quantity from $y = 0 + \epsilon$ to $y = 0 - \epsilon$.

The second jump condition is that the tangential pressure gradient at the interface be given equally on both sides of the interface. This condition is

$$\left[(U-c) \frac{dA}{dy} - A \frac{dU}{dy} \right]_0 = 0 \tag{2.2.3}$$

Both of the matching conditions are unaffected by non-zero β. Application of these matching conditions and the appropriate boundary conditions to the solutions in each flow region gives the full solution and the complex phase speed $c(k)$.

2.3   Necessary Conditions for Instability for "Broken Line" Profiles

When the flow $U(y)$ or its derivative dU/dy are discontinuous, there are slight changes in the necessary conditions (2.1.3) and (2.1.4). The potential vorticity equation (2.1.2) is multiplied by $A*/(U-c)$. The equation is then integrated over the entire y domain and the real and imaginary parts are separated to give the two necessary conditions for instabil-

ity. For example, if there is a simple discontinuity in $U(y)$ or its derivative at $y = y_0$, the integrated equation is

$$-[A^*A_y]_{y_0} + \int_{-H}^{y_{0-}} dy \left\{ - |A_y|^2 - k^2|A|^2 + \frac{|A|^2}{U-c} \frac{\partial \pi}{\partial y} \right\}$$

$$+ \int_{y_0+}^{H} dy \left\{ - |A_y|^2 - k^2|A|^2 + \frac{|A|^2}{U-c} \frac{\partial \pi}{\partial y} \right\} = 0 \qquad (2.3.1)$$

where $\frac{\partial \pi}{\partial y} = \beta - U_{yy}$ and where the square brackets denote the jump in the bracketed quantity across y_0. Evaluation of this jump using the matching conditions (2.2.2) and (2.2.3) at y_0 yields

$$-[A^*A_y]_{y_0} = A_-^*A_{-y} \frac{U_+-c^*}{U_--c^*} \left\{ \frac{U_--c^*}{U_+-c^*} - \frac{U_--c}{U_+-c} \right\} + |A_-|^2 \frac{U_+-c}{U_--c} \left\{ \frac{U_{-y}}{U_+-c} - \frac{U_{+y}}{U_--c} \right\} \qquad (2.3.2)$$

where the subscripts (-) and (+) indicate evaluation of the function on the southern and northern sides of the profile breaks respectively. If, as in most of the cases of interest here, we have $U_+ = U_-$ with a discontinuity in dU/dy across the break, this expression becomes

$$- [A^*A_y]_{y_0} = \frac{|A|^2}{U-c} (U_{-y} - U_{+y}) \quad , \qquad (2.3.3)$$

where U is the velocity at the break. Note that according to matching condition (2.2.2), the function $A(y)$ is continuous at the break, but dA/dy is not. Equation (2.3.3) can be rewritten in delta function form:

$$-[A^*A_y]_{y_0} = \int_{-H}^{+H} \frac{|A|^2}{U-c} (U_{-y} - U_{+y}) \delta (y - y_0) dy \qquad (2.3.4)$$

The potential vorticity gradient can be rewritten in a generalized way:

$$\frac{\partial \hat{\pi}}{\partial y} = \frac{\partial \pi}{\partial y} + \left(U_{y_{0-}} - U_{y_{0+}} \right) \delta (y - y_0) \qquad (2.3.5)$$

where $\frac{\partial \pi}{\partial y}$ is the well-behaved part of the potential vorticity gradient in the regions between profile breaks and $(U_{y_{0-}} - U_{y_{0+}})\delta(y - y_0)$ is a delta function contribution to the potential vorticity gradient due to the profile breaks. (It does not have any real meaning unless included in an integral over y.) The integrated potential vorticity equation (2.3.1) can be written:

$$-\int_{-H}^{y_{0-}} dy \left\{ |A_y|^2 + k^2|A|^2 \right\} dy - \int_{y_{0+}}^{H} dy \left\{ |A_y|^2 + k^2 |A|^2 \right\} \qquad (2.3.6)$$

$$+ \int_{-H}^{+H} \frac{|A|^2}{U-c} \frac{\partial \hat{\pi}}{\partial y} dy = 0 \quad .$$

The imaginary part of this equation is

$$c_i \int_{-H}^{+H} \frac{|A|^2}{|U-c|^2} \frac{\partial \hat{\pi}}{\partial y} = 0 \qquad (2.3.7)$$

This is the analog (normal mode form) of the necessary condition (2.1.3) when there is a discontinuity in dU/dy at y_0. If c_i is different from zero, there must be a change of sign in the effective potential vorticity gradient, which is now

$$\beta - U_{yy} + (U_{-y} - U_{+y}) \delta (y - y_0)$$

The necessary condition can be satisfied if, for instance, $\frac{\partial \pi}{\partial y} = \beta - U_{yy}$, were everywhere positive or zero and $(U_{-y} - U_{+y})$ were negative.

The second necessary condition is obtained from the real part of (2.3.6). It is

$$\int_{-H}^{+H} \frac{|A|^2}{|U-c|^2} (U-c_r) \frac{\partial \hat{\pi}}{\partial y} \, dy = \int_{-H}^{y_0-} |A_y|^2 \, dy + \int_{y_0+}^{H} |A_y|^2 \, dy$$

$$\text{(2.3.8)}$$

$$+ \int_{-H}^{H} k^2 |A|^2 \, dy > 0$$

This is the normal mode analog of (2.1.4) when there is a discontinuity in dU/dy. Thus, if $(U - c_r)\left\{\frac{\partial \hat{\pi}}{\partial y} + (U_{-y} - U_{+y})\delta(y-y_0)\right\}$ is everywhere negative, the flow must be stable.

Both of these necessary conditions are very useful in seeing whether a given flow might be unstable. Using delta functions to represent the potential vorticity gradient at profile breaks, it is easy to see if a flow is definitely stable. Application of these conditions will be made for some of the specific flows considered below.

When the flow $U(y)$ is itself discontinuous, the first derivative, dU/dy, at profile breaks can be represented by a delta function. The potential vorticity gradient at the profile breaks is dominated by $(\beta-U_{yy})$, which looks like a delta function derivative. I have not been able to find a simple statement of the necessary conditions for this case.

2.4 Radiation Conditions

One of the purposes of this thesis is to explore the occurrence of "radiating" modes of instability. In a heuristic sense, this means to seek solutions which have their primary energy source in some well-defined region and which can propagate this energy to large distances (compared with the internal deformation radius, say) from the source. The word "radia-

ting" usually describes a pure wave, say of the form $e^{\ell y} e^{ikx}$, where k is real and ℓ is imaginary. When ℓ is purely real, the solution is "trapped". When the phase speed c is complex so that the wave is growing, the y-wave-number is also complex. The solution is then wavelike with an evanescent envelope in y, because the _source_ of energy for the wave is localized in space (at the region of horizontal shear for these barotropic instabilities). Since the disturbance is growing in time, at any time after the onset of instability, there will be a spatially decaying disturbance outside the jet, because it takes a finite time for the (initially small) disturbance to reach a point far from the jet. Therefore, any growing wave will not look like a purely "radiating" disturbance away from the source of energy. Neutral solutions, on the other hand, will enjoy the distinction of being either purely wavelike or purely evanescent in the y direction. The growing waves can be identified as radiating or trapped by the structure of the contiguous neutral mode, which will be either wavelike or evanescent away from the energy source. We identify "radiating" waves as unstable waves which neighbor neutral Rossby waves. These unstable, radiating waves look _nearly_ like Rossby waves except that they have slowly decaying envelopes imposed on the wavelike structure in y.

There are quantitative means for determining if waves are radiating. If the disturbance is of the form

$$e^{i(kx + \ell_i y - kc_r t)} \quad e^{-\ell_r y + kc_i t}$$

north of the energy source, the envelope of the disturbance moves out at the rate kc_i/ℓ_r. As an example, look at a single unstable wave which satisfies the barotropic Rossby wave dispersion relation in the far field,

but which has complex phase speed and y-wavenumber. Its dispersion rela-
tion is

$$c_r + i \, c_i = U - \frac{\beta \, (\ell_i^2 - \ell_r^2 + k^2)}{|k^2 + \ell^2|^2} + i \, \frac{2\beta \, \ell_i \ell_r}{|k^2 + \ell^2|^2} \qquad (2.4.1)$$

Thus

$$\frac{c_i}{\ell_r} = \frac{2\beta \, \ell_i}{|k^2 + \ell^2|^2} \qquad (2.4.2)$$

The ratio kc_i/ℓ_r is the meridional group velocity. The group velocity
approaches a non-zero constant as $c_i \to 0$ if the outside field is really a
Rossby wave unless the solution for given c and k happens to have $\ell_i \to 0$
as $c_i \to 0$,. If however the group velocity approaches zero as $c_i \to 0$, the
decay scale $(\ell_r)^{-1}$ remains non-zero and the disturbance is trapped. (Some
"radiating" solutions are actually found which have $\ell_i \to 0$ as $c_i \to 0$, but
contiguous, slightly unstable waves clearly have large decay scales and
wavelike behavior in y.)

One is tempted to define a radiating instability as one which looks
wavy in y. In fact, this is an acceptable criterion. Again, consider-
ing a barotropic Rossby wave, the y wavenumber can be written as

$$\ell_i + i \, \ell_r = \sqrt{\frac{\beta}{U - c_r - ic_i} - k^2}$$

If, as $c_i \to 0$, $(U - c_r)$ is positive and k^2 is small, the radicand is posi-
tive and ℓ_r tends to zero. The resulting disturbance is a Rossby wave
with y-wavenumber ℓ_i. If, as $c_i \to 0$, either $(U - c_r)$ is negative or
$(U - c_r)$ is positive and k^2 is large, the radicand is negative so that

ℓ_i tends to zero and the disturbance is trapped. Thus, if as $c_i \rightarrow 0$,

$$\frac{\ell_i}{\ell_r} \rightarrow 0 \qquad \text{trapped disturbance}$$

(2.4.3)

$$\frac{\ell_i}{\ell_r} \rightarrow \infty \qquad \text{radiating disturbance}$$

Visually, this is a measure of how "wiggly" the eigenfunction appears as $c_i \rightarrow 0$. If, as $c_i \rightarrow 0$, there are more and more oscillations before the disturbance decays away in y, the mode is radiating. Also, when $\ell_r = \ell_i$, we have

$$\frac{\beta(U - c_r)}{|U - c|^2} - k^2 = 0$$

If the wave is not growing, if $c_i = 0$, waves with

$$k^2 < \frac{\beta(U - c_r)}{|U - c|^2}$$

are purely wavelike in y, while waves with

$$k^2 > \frac{\beta(U - c_r)}{|U - c_r|^2}$$

are evanescent in y. The transition from waviness to evanescence as a function of k persists when c_i is non-zero. The criterion, $\ell_r = \ell_i$, will be used to distinguish between unstable modes which are more wavelike (and less trapped) and those which are more evanescent.

Under what circumstances will a mode be radiating away from the energy source? The first obvious requirement for radiating disturbances is that the flow in the irradiated region be capable of supporting waves.

This means that there must be a potential vorticity gradient there. In this chapter, where the flows have no vertical shear and the horizontal shear is confined to a small region, β must be non-zero in order to allow the possibility of radiated waves. In the next chapter, some of the flows have vertical shear everywhere outside the horizontal shear region. For these flows, the potential vorticity gradient is non-zero and waves can be supported even when β is zero.

As seen above, an unstable wave will not radiate if its eastward phase speed is greater than the flow velocity in the exterior region, since Rossby waves propagate westward with respect to the flow they are embedded in. This is known as the phase speed condition (McIntyre and Weissman, 1972): if a forced disturbance is to radiate, the phase speed and x-wavenumber of the forcing (in this case, the unstable wave) must match the phase speed and x-wavenumber of a free wave (essentially a Rossby wave in this case). From the semicircle theorem, we can put limits on the allowed phase speed of an unstable wave. From the Rossby wave dispersion relation in the outer field, we can determine the range of Rossby wave phase speeds. For the phase speed condition to be met, the instability phase speed must be westward with respect to the flow speed in the radiation region since Rossby waves have only westward phase speeds. This means that either a shear flow with $U_\infty \neq U_{-\infty}$ or a westward jet might radiate easily while the possibilities for radiation from an eastward jet are much more restricted.

2.5 Shear Layer Instability

In this and the next section, specific results will be obtained for several velocity profiles. "Shear" layers, defined as flows with different velocities at $+ \infty$ and $- \infty$ or at the northern and southern walls (Howard and Drazin, 1964), are discussed in this section. "Jet" profiles, where the flow is the same at the outer boundaries, are discussed in section 2.6.

(a) Shear Layer with a Discontinuity in U(y)

The simplest shear flow is the vortex sheet, which has a single discontinuity in U(y), at say $y = 0$. The non-rotating (or equally, f-plane) case was discussed by Rayleigh (1879). The case with non-zero β was discussed by Howard and Drazin (1964). It is instructive to look carefully at the results for this profile, adding details about exactly where the flow is unstable in β and k and what the eigenfunction structures are. The velocity profile is shown in Figure 2.5.1 along with a sketch of its potential vorticity gradient, modified by the double delta function arising from U_{yy} at $y = 0$. The necessary conditions for instability are satisfied because the potential vorticity gradient has both signs, albeit in a rather strange way concentrated at the origin. The potential vorticity equation on the β-plane is

$$(U - c) \left(\frac{d^2A}{dy^2} - k^2 A \right) + \beta A = 0 \qquad (2.5.1)$$

The solution, subject to the boundedness boundary condition at $y = \pm \infty$, is

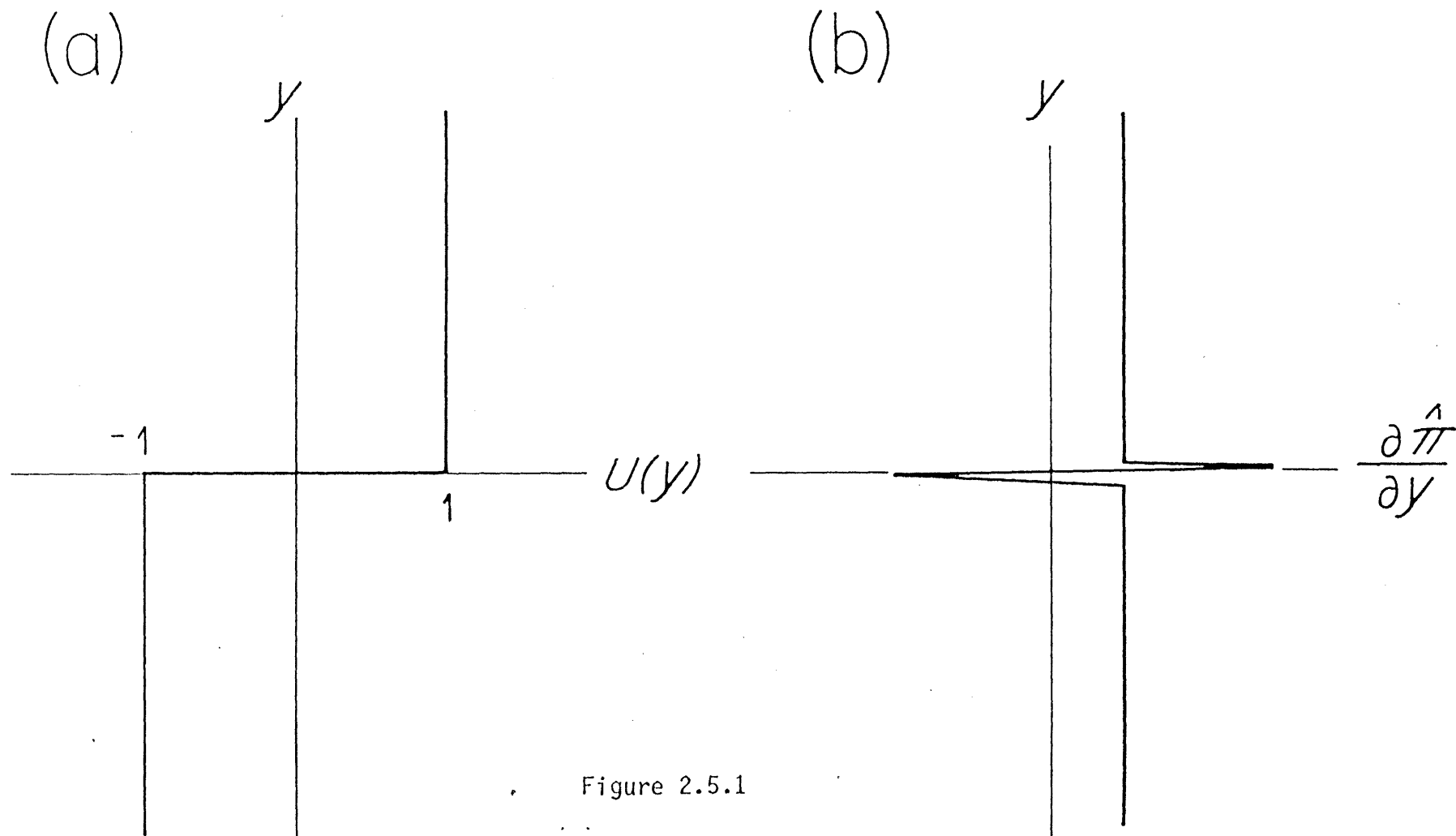$$A = e^{-\ell_I y} \qquad y > 0 \qquad (2.5.2)$$

$$A = e^{-\ell_{II} y} \qquad y < 0$$

Figure 2.5.1

Vortex sheet: (a) $U(y)$ and (b) the potential vorticity gradient,
$\partial\hat{\pi}/\partial y = \beta - U_{yy}$ including a double delta function contribution arising
from U_{yy} at the profile break at $y = 0$.

where

$$\ell_I = \sqrt{k^2 + \frac{\beta}{c-1}} \qquad , \qquad \ell_{II} = \sqrt{k^2 + \frac{\beta}{c+1}} \quad .$$

When c is complex, ℓ_I and ℓ_{II} are chosen to have positive real parts, to satisfy the boundedness condition on the eigenfunctions at infinity. When c is real, the ℓ's are purely real or purely imaginary. If real, they must be positive. If imaginary, the branch of ℓ is chosen which has outward group velocity, $dc/d\ell$.

Applying the matching conditions (2.2.2) and (2.2.3) at $y = 0$, we find that

$$a = - \frac{1 - c}{c}$$

and   (2.5.3)

$$(c-1)^2 = \sqrt{k^2 + \frac{\beta}{c-1}} \quad , \qquad (c+1)^2 = \sqrt{k^2 + \frac{\beta}{c+1}} = 0$$

This was the solution found by Howard and Drazin (1964). When β is zero, ℓ_I and ℓ_{II} reduce to k and the dispersion relation is

$$c = \pm i$$ (2.5.4)

$$A = e^{-ky} \qquad y > 0$$

and the solution is

$$A = e^{ky} \qquad y < 0 \quad .$$

All waves are unstable when $\beta = 0$ and they are nondispersive. Their phase speed is 0, the average speed of the flow. The imaginary part of the phase speed is .5, so the growth rate is $k/2$, increasing without bound with k.

When β is non-zero, (2.5.3) can be written, after squaring, as

$$c (c^2 + 1) + \frac{\beta}{4 k^2} (3 c^2 + 1) = 0 \quad .$$

Howard and Drazin (1964) found the solutions $c(k)$. There are three roots, one of them real (neutral) and the other two complex conjugates. The real root is only a solution if $c = \pm U_0$ and $\beta/k^2 = \mp 2U_0$, corresponding to Rossby waves. The complex roots are the unstable (growing and decaying) modes. The imaginary part of the phase speed is non-zero for all k, so all of these waves are unstable, just as when $\beta = 0$. This arises because (1) no β is large enough to cause the potential vorticity gradient, $\beta - U_{yy}$, to be of a single sign and (2) even the shortest waves have non-zero decay scales in y at the profile break and can sense the change in sign of $\beta - U_{yy}$, since U_{yy} takes on both signs right at the profile break. These waves are, however, dispersive in contrast to the vortex sheet modes at $\beta = 0$. As $\beta/k^2 \to 0$, $c \to \pm iU_0$, which is the result in (2.5.4). As $\beta/k^2 \to \infty$, $c \to \pm iU_0/\sqrt{3}$. The way that the complex phase speeds fit into the c_r-c_i semicircle is shown in Figure 2.5.2a and the complex phase speed (c_r, c_i) is shown as a function of k in Figure 2.5.2b. The phase speed depends only on the ratio β/k^2, so the roots for all β's follow the same curve in the c_r-c_i plane. The retarding effect of β on the phase speed c_r is clearly seen at intermediate wavelengths.

What is the structure of the eigenfunctions? From (2.5.2), with $b \equiv \beta/k^2$

$$\frac{\ell_I^2}{k^2} = 1 + \frac{b}{\left|c-1\right|^2}(-1 + c_r - i c_i), \quad \frac{\ell_{II}^2}{k^2} = 1 + \frac{b}{\left|c+1\right|^2}(1 + c_r - i c_i) \quad .$$

As β becomes very important and $b \to \infty$, so that $c \to \pm iU_0/\sqrt{3}$,

$$\frac{\ell_I^2}{k^2} \to \frac{2b}{\sqrt{3}\left|c-1\right|^2} e^{-i5\pi/6} \quad , \quad \frac{\ell_{II}^2}{k^2} \to \frac{2b}{\sqrt{3}\left|c+1\right|^2} e^{-i\pi/6}$$

and ℓ_1/k is proportional to $e^{-i5\pi/12} = (.26 - .97i)$ while ℓ_{II}/k is proportional to $e^{-i\pi/12} = (.97 - .26i)$. In the northern half of the profile where the flow is more eastward, the eigenfunction is _more_ oscillatory and decays more slowly than in the southern half. (To the north, the instability phase speeds are always less than the flow speed so the long waves satisfy the phase speed condition and look like Rossby waves with complex phase speed and complex y-wavenumber.) However, because the growth rate of the disturbance is non-zero for all choices of β and k, the disturbance always has a pronounced decaying envelope.

(b) Shear Profile with Discontinuities in dU/dy.

The vortex sheet results of the previous section explain some of the behavior of the unstable modes of a shear profile, but since any realistic shear zone has a non-zero width, the results strictly apply only to the behavior of long waves, which see a shear zone as a discontinuity in U(y). In a realistic flow where the shear zone has non-zero width, we expect the short waves to be stabilized and that there should be a wave with intermediate wavelength with maximum growth rate. (Maximum growth rate for the vortex sheet occurs as $k \rightarrow \infty$.) A realistic, smoothly varying flow will also be stable if β is large enough to make the potential vorticity gradient positive everywhere.

We choose a simple flow using the method of Section 2.2 in which the potential vorticity gradient is zero or uniform in discrete regions of the flow. The velocity profile and a schematic of its potential vorticity gradient are shown in Figure 2.5.3. The flow is uniform for $|y| > 1$ and has zero potential vorticity gradient ($\beta - U_{yy}$) for $|y| < 1$. The potential
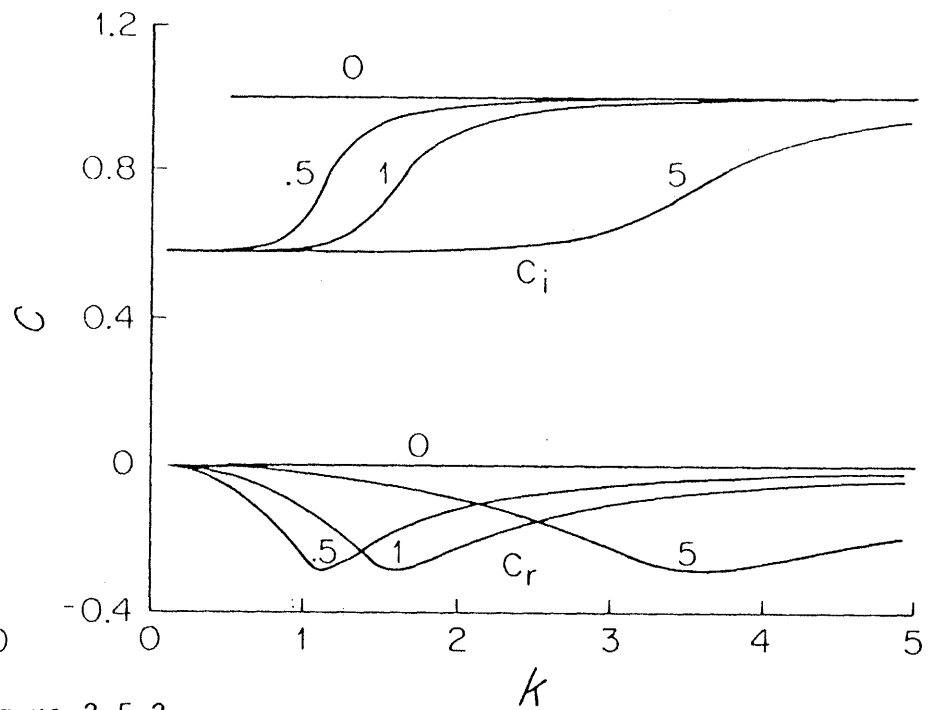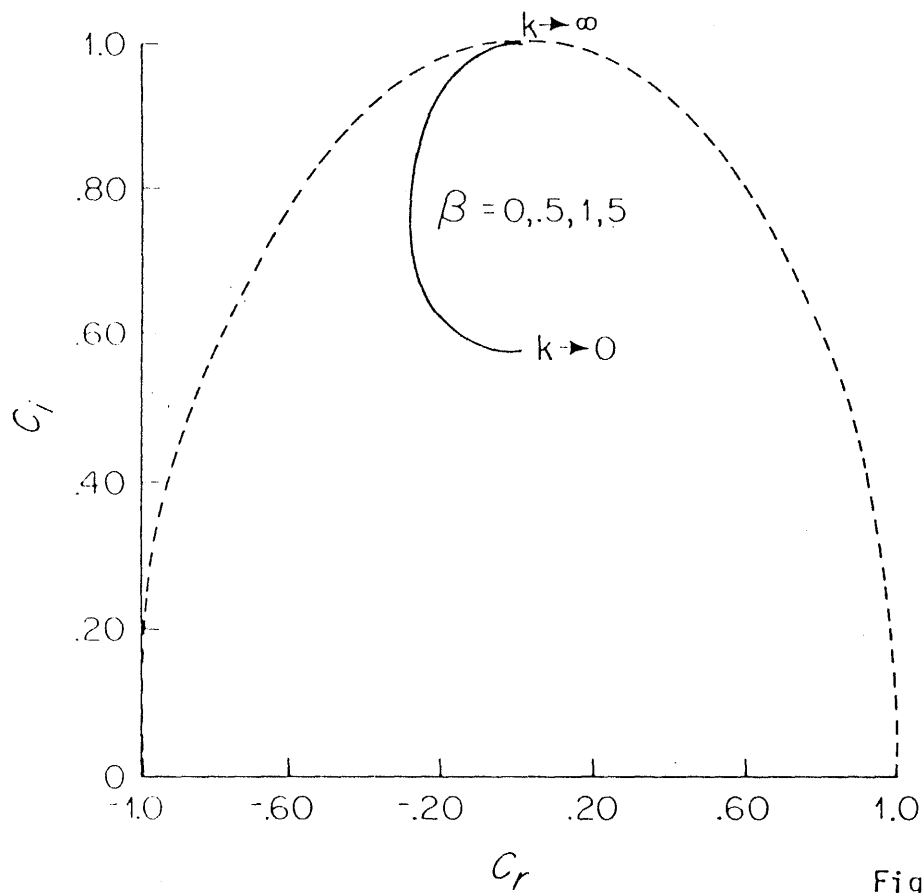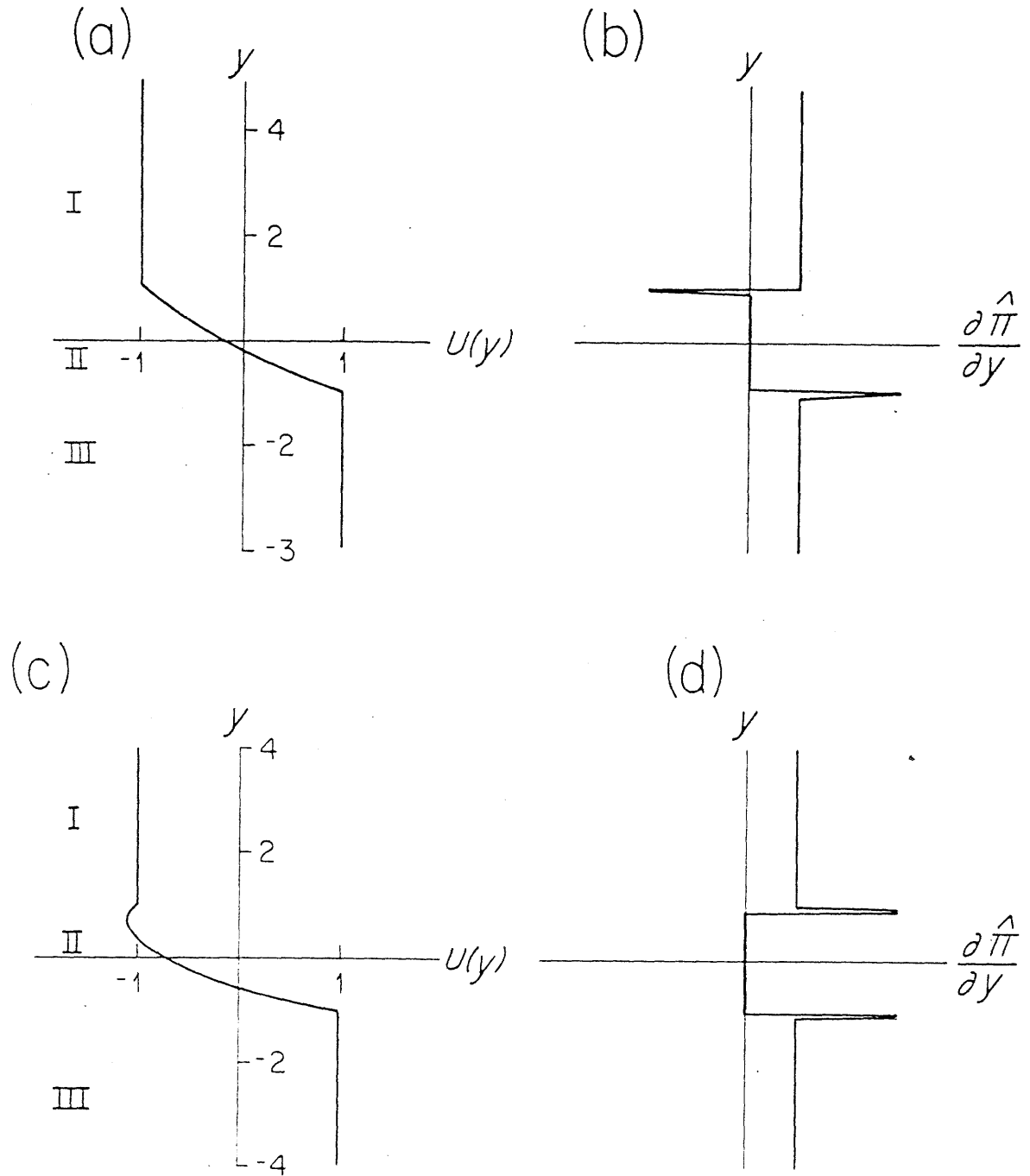
Figure 2.5.2

Vortex sheet dispersion relation: (a) c_i vs. c_r and (b) c_r and c_i vs. k. At $\beta = 0$, c_r and c_i must fall below the dashed curves according to the semicircle theorem.

Figure 2.5.3

Shear layer: U(y) and $\partial \hat{\pi}/\partial y$ for two choices of β. (a) and (b):
β = .5 (supercritical). (c) and (d): β = 1.5 (subcritical).

vorticity equation (2.1.2) is nondimensionalized using the half-width of the shear zone as a length-scale and the absolute value of U at $\pm \infty$ as a velocity scale. The potential vorticity equation is then

$$(U(y) - c) \left(\frac{d^2 A}{dy^2} - k^2 A \right) + (\beta - U_{yy}) A = 0$$

where

$$y = y*/L \; , \quad \beta = \frac{\beta_0 L^2}{U_\infty} \; , \quad U(y) = \frac{U*(y)}{U_\infty} \; , \quad c = \frac{c*}{U_\infty} \; , \quad k = k* L.$$

The velocities are

$$U_I = -1$$

$$U_{II} = -\frac{\beta}{2} - y + \frac{\beta}{2} y^2 \tag{2.5.5}$$

$$U_{III} = 1 \; .$$

β and k are the only two parameters. The potential vorticity gradient is β in Regions I and III, so waves can be supported there when β is non-zero. At $y = \pm 1$, the potential vorticity gradient is the delta function in $(\beta - U_{yy})$, as in Section 2.3. Change in sign of the potential vorticity gradient occurs only because of these contributions at $y = \pm 1$, since it is positive or zero everywhere in Regions I, II and III. As β increases, the velocity profile changes in Region II until both contributions to $(\beta - U_{yy})$ are positive. At this β ($= \beta_c$), the flow must be stable, and hence this patched profiles mimics the β-stabilization that occurs in smoothly varying flows. This can be seen in Figure 2.5.3 where $U(y)$ and $\partial\hat{\pi}/\partial y$ are shown for a supercritical and a subcritical β. The maximum β for which instability is possible is $\beta = 1$. (At this β, dU_{II}/dy at $y = 1$ is zero and the potential vorticity gradient is positive or zero everywhere.)

The potential vorticity equation in each region is

$$\text{I.} \quad \left(\frac{d^2}{dy^2} - k^2\right) A_I - \frac{\beta}{1+c} A_I = 0$$

$$\text{II.} \quad \left(\frac{d^2}{dy^2} - k^2\right) A_{II} = 0$$

$$\text{III.} \quad \left(\frac{d^2}{dy^2} - k^2\right) A_{III} - \frac{\beta}{1-c} A_{III} = 0$$

The solutions, subject to boundedness conditions at infinity, are

$$A_I = e^{-\ell_I y}$$

$$A_{II} = a_1 e^{ky} + a_2 e^{-ky} \qquad (2.5.6)$$

$$A_{III} = d\, e^{\ell_{III} y}$$

where $\ell_I^2 = k^2 + \frac{\beta}{1+c}$ and $\ell_{III}^2 = k^2 - \frac{\beta}{1-c}$, just as in the previous example. The constants and phase speed are determined from the matching conditions (2.2.2) and (2.2.3) at $y = \pm 1$. The dispersion relation so obtained is

$$e^{-4k}\left\{\left(1 - \sqrt{1 + \frac{b}{1+c}}\right)(1+c) + \frac{1}{k}(1-\beta)\right\}\left\{\left(1 - \sqrt{1 + \frac{b}{c-1}}\right)(1-c) + \frac{1}{k}(1+\beta)\right\}$$

$$\qquad\qquad (2.5.7)$$

$$-\left\{-\left(1 + \sqrt{1 + \frac{b}{1+c}}\right)(1+c) + \frac{1}{k}(1-\beta)\right\}\left\{-\left(1 + \sqrt{1 + \frac{b}{c-1}}\right)(1-c) + \frac{1}{k}(1+\beta)\right\} = 0$$

where $b \equiv \beta/k^2$.

The parameters which can be varied are β and k. Let us look at various limits of this relation before solving it numerically. There are four basic limits:

(1) $k \to 0$, β fixed: the dispersion relation is

$$2 \sqrt{\beta} \left\{ \beta + c + \beta \sqrt{c^2-1} + \sqrt{\beta(1+c)} + \sqrt{\beta(c-1)} \right\} + (1+c)^{3/2} + (c-1)^{3/2} = 0$$

As $\beta \to 0$, $c \to \pm i/\sqrt{3}$, which is the longwave limit of the vortex sheet instability.

As $\beta \to \infty$, $c \to - (\beta/k^2)$ [from (2.5.7) with $k = 0(1/\beta)$].

(2) $k \to \infty$, β fixed: $c = \pm 1$ for all β.

(3) $\beta \to 0$, k fixed:

$$c = \pm \sqrt{1 - \frac{1}{k} + \frac{1}{(2k)^2} (1 - e^{-4k})}$$

As $k \to 0$, $c = \pm i$, which is the shortwave limit of the vortex sheet problem.

As $k \to \infty$, $c = \pm 1$.

(4) $\beta \to \infty$, k fixed: $c = \beta(1-2k)$.

Additional informative limits are obtained by letting the length scale L approach zero and infinity, with $\beta = \beta_* L^2/U$ and $k = k* L$.

(5) $L \to 0$: $(\ell_I/k)(1+c)^2 + (\ell_{III}/k)(1-c)^2 = 0$, the vortex sheet dispersion relation.

(6) $L \to \infty$: $c \to -\beta/2k$.

One other limit which reveals the retarding effect of β is

(7) $k \to \infty$, $\beta = 0(k)$: $c = \pm 1 - \beta/2k$.

The longwave limits are identical to the vortex sheet results: when β approaches zero faster than k, the limit $c = \pm i$ is obtained, while when β approaches zero slower than k, the limit is $c = \pm i/\sqrt{3}$. The shortwave limit in all cases is a stable solution, with $c = \pm 1$. For the limit

where L increases to ∞, β increases faster than k, which also increases. The flow looks more and more like an infinitely wide Couette flow to the shorter and shorter waves, which are thus stable.

These limits delineate the results to be expected from the dispersion relation. The dispersion relation was solved numerically using the secant method with complex arithmetic to find the roots c(k) for given β and k. Figure 2.5.4 is the neutral stability diagram in the β - k plane for this profile. The dashed curve is the locus $Re(\ell_{III}) = Im(\ell_{III})$. The short waves are more trapped and less wavelike in region III than the long waves. The stability cutoffs were found up to $\beta = .95$: extrapolating the growth rates of the long waves to the β where $c_i = 0$, the long waves all appear to be unstable up to $\beta = 1.0$ and the short waves are probably also unstable up to 1.0, with a cusp in the stability diagram there. At high β, there are two separate ranges of unstable wavenumbers. These are two separate modes which coalesce as β decreases, and are similar to the two separate modes found by Dickinson and Clare (1973). (A thorough comparison with Dickinson and Clare's results will be found at the end of this section.) The flow is stable for all β's greater than 1, the cutoff required by the necesssary condition for instability: the necessary condition is sufficient for this profile.

Figure 2.5.5a shows c_i as a function of c_r for several choices of β. At $\beta = 0$, the well-known result for a Rayleigh broken line profile with a non-zero width shear zone is obtained. In addition to the unstable waves (complex c), there is a continuum of neutral modes with phase speeds $c_r < 1$. While the unstable solutions are representative of the

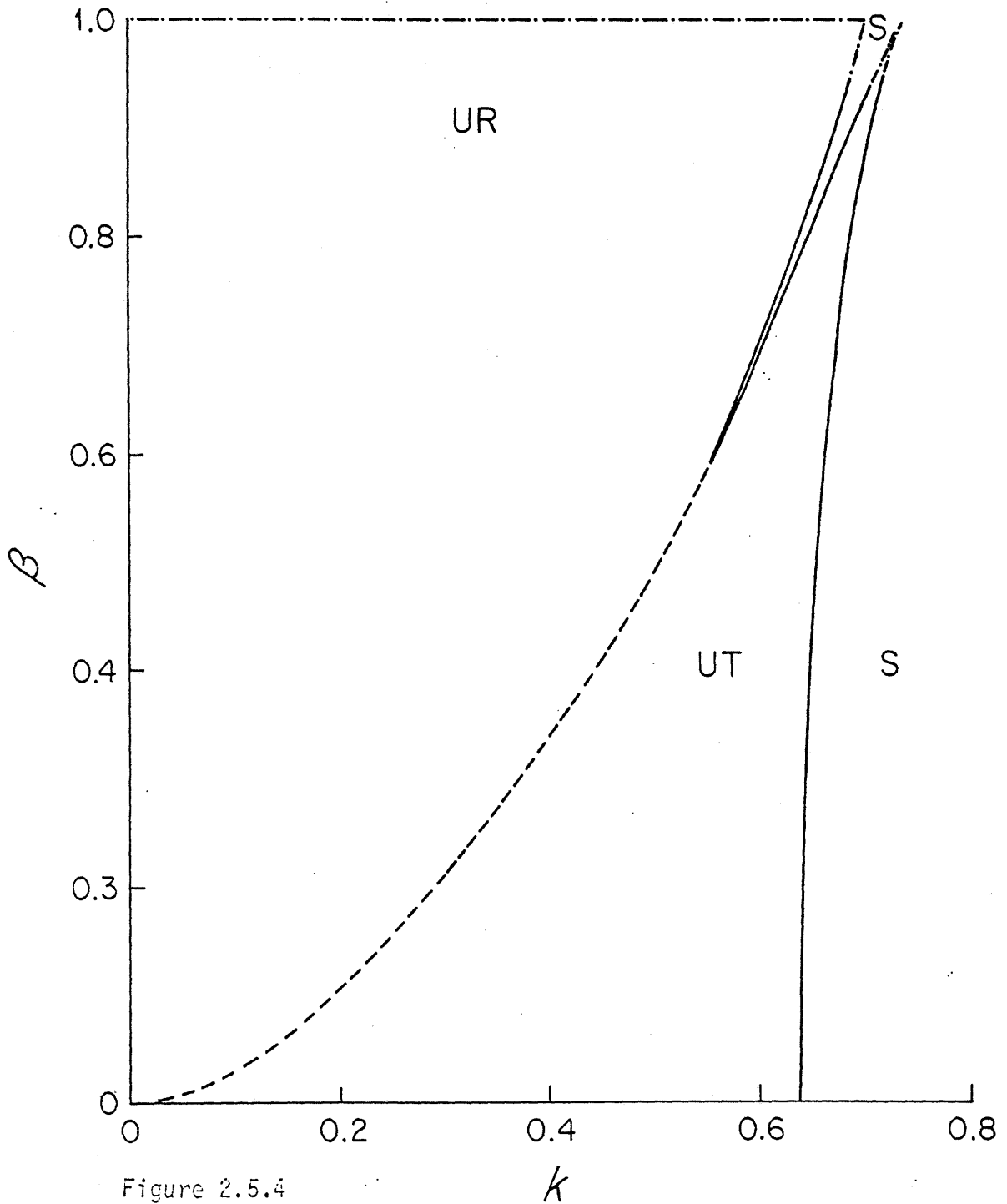Figure 2.5.4

Shear layer stability diagram. The solid curves indicate $c_i = 0$. The dotted curve is where $\mathcal{R}e(k_{II}) = \mathcal{I}m(k_{II})$, and corresponds to the transition from radiating long-waves to trapped short-waves. The dot-dash curves are extrapolated stability boundaries, $c_i = 0$.
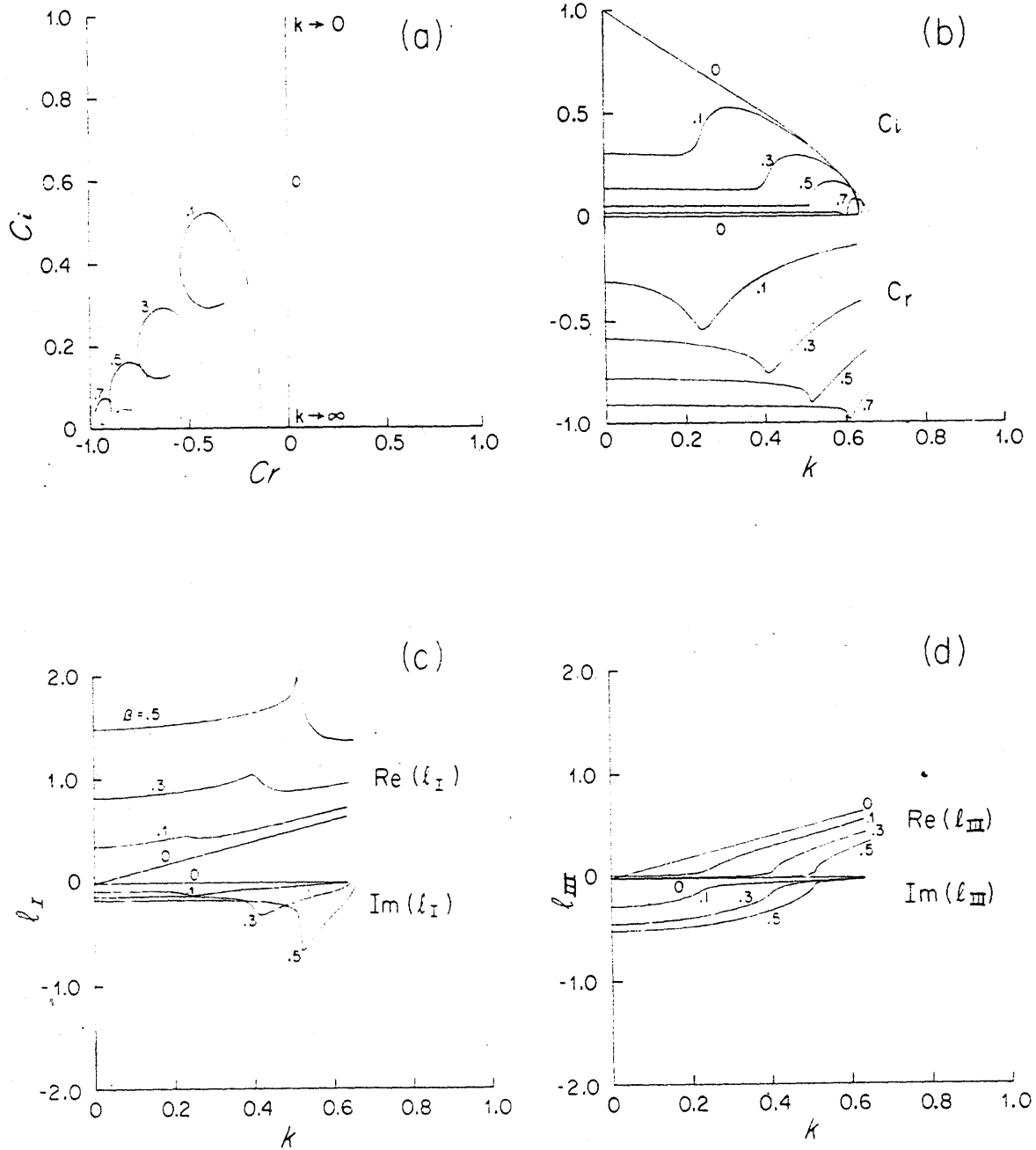
Figure 2.5.5

Shear layer dispersion relation [for s = 0, .1, .3, .5, .7]
(a) c_i vs. c_r (b) c_r and c_i vs. k, (c) ℓ_I and ℓ_{II} vs. k, and (d) ℓ_{II}
vs. k. $(\ell_I)^{-1}$ and $(\ell_{II})^{-1}$ are the northern and southern decay
scales, respectively.

unstable modes of a continuous, rather than broken line, profile, only the neutral mode with $c_r = 0$ survives when the profile is made continuous (Betchov and Kriminale, 1967). There is a dramatic change in the long wave behavior when even a small amount of β is introduced. The growth rate drops dramatically, but does not vanish and the phase speed of all unstable waves is retarded (made more westward). At high β, a tiny intermediate range of wavenumbers is stabilized. As β nears the cutoff of 1, the phase speed of all unstable waves approaches -1 and the growth rate approaches 0.

The dispersion relation $c(k)$ for different values of β is shown in Figure 2.5.5b. The drop in growth rate of the long waves and retardation of all real phase speeds due to β are clearly seen. The long- and short-wave dispersion relations look quite different from each other when β is non-zero: as the wavenumber is decreased, the real phase speed has a cusp and then becomes nearly constant while the imaginary phase speed drops off suddenly to a nearly constant value. At higher β, the long- and short-waves separate into two distinct modes with an intermediate range of stable waves. There was no evidence of two separate, overlapping modes at lower β (as was seen in Dickinson and Clare's results for the tanh y profile), so it seems that these two modes coalesced as soon as their wave-number ranges overlapped. The structure of the long and shortwave modes are quite different. Figures 2.5.5c and d show the real and imaginary parts of ℓ_I and ℓ_{III} for several β's. The decay scales are given by $[Re(\ell_I)]^{-1}$ and $[Re(\ell_{III})]^{-1}$ and the y-wavenumbers by $Im(\ell_I)$ and $Im(\ell_{III})$. We note that on the northern side of the profile where $\ell = \ell_I$, the disturb-

ances are trapped. On the southern side (where $\ell = \ell_{III}$), the long waves are like Rossby waves with a clear transition to trapped waves as k increases. The two separate modes at large β are simply the separated radiating (long-wave) and trapped (short-wave) modes.

Examples of eigenfunctions at β = .5 are shown in Figure 2.5.6, showing the difference in trapping scales of the radiating and trapped modes. The short wave mode is clearly trapped on both sides of the shear layer. In contrast, eigenfunctions on the long wave side of the dotted boundary in Figure 2.5.4 look oscillatory on the southern (more eastward) side of the flow. Only at high β is there a neutral stability curve adjacent to the modes, so only at high β can the radiation criterion of Section 2.4 be strictly applied (and it shows that the long waves are radiating). However, the long wave eigenfunctions at lower β so strongly resemble those which are clearly radiating at higher β, that one may call them radiating also. (Because of the coalescence of the long and short wave modes, the neutral curve has been lost at low β).

Both radiating and trapped solutions are evanescent on the northern side where the flow is easterly and the phase speed condition cannot be satisfied. On the southern side of the shear layer, the short wavelength modes are trapped and the long waves are radiating, even though the phase speeds of both modes are westward with respect to the flow speed. The difference in behavior is due to satisfaction (or lack thereof) of the phase speed condition. The Rossby wave dispersion relation for β = .5 is plotted in Figure 2.5.7 for two extreme y-wavenumbers. Also shown in Figure 2.5.7 is the phase speed of the unstable mode at β = .5. The

(a)

Shear layer eigenfunction amplitude, $\Lambda(y)$, at $\beta = .5$ for (a) $k = .5$ (radiating mode) and (b) $k = .6$ (trapped mode).

(b)

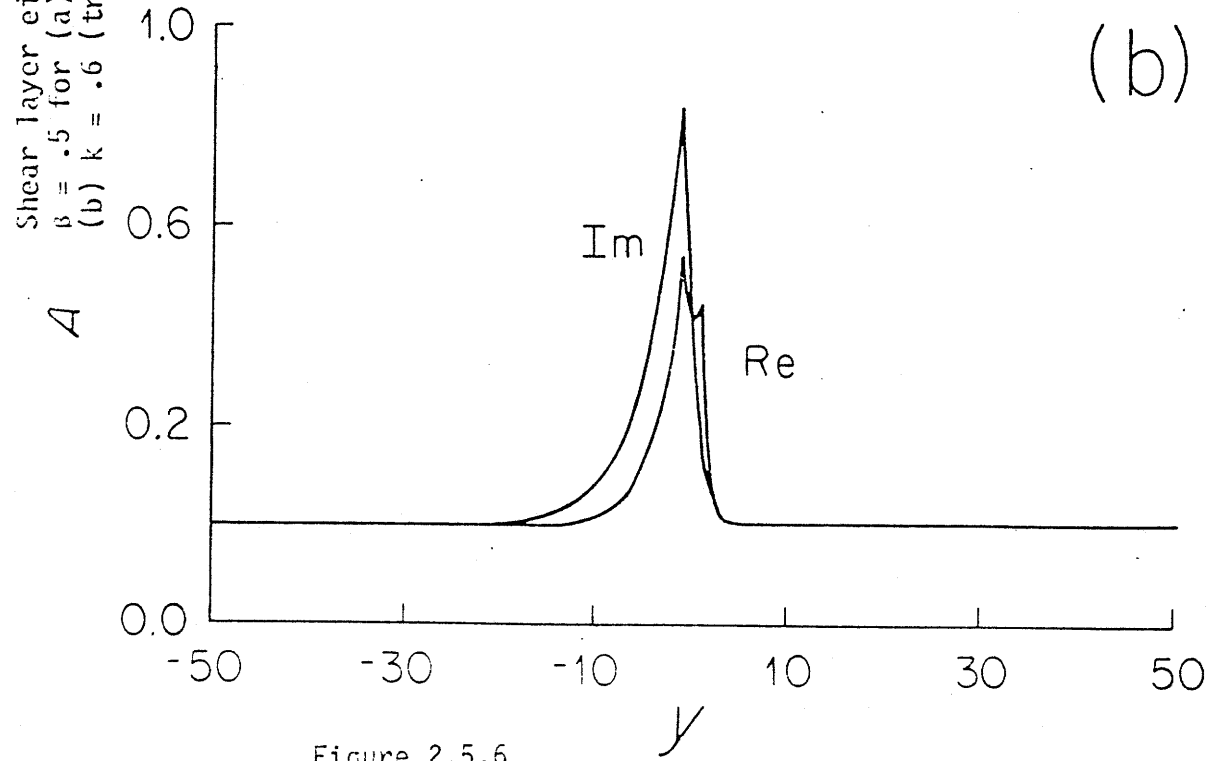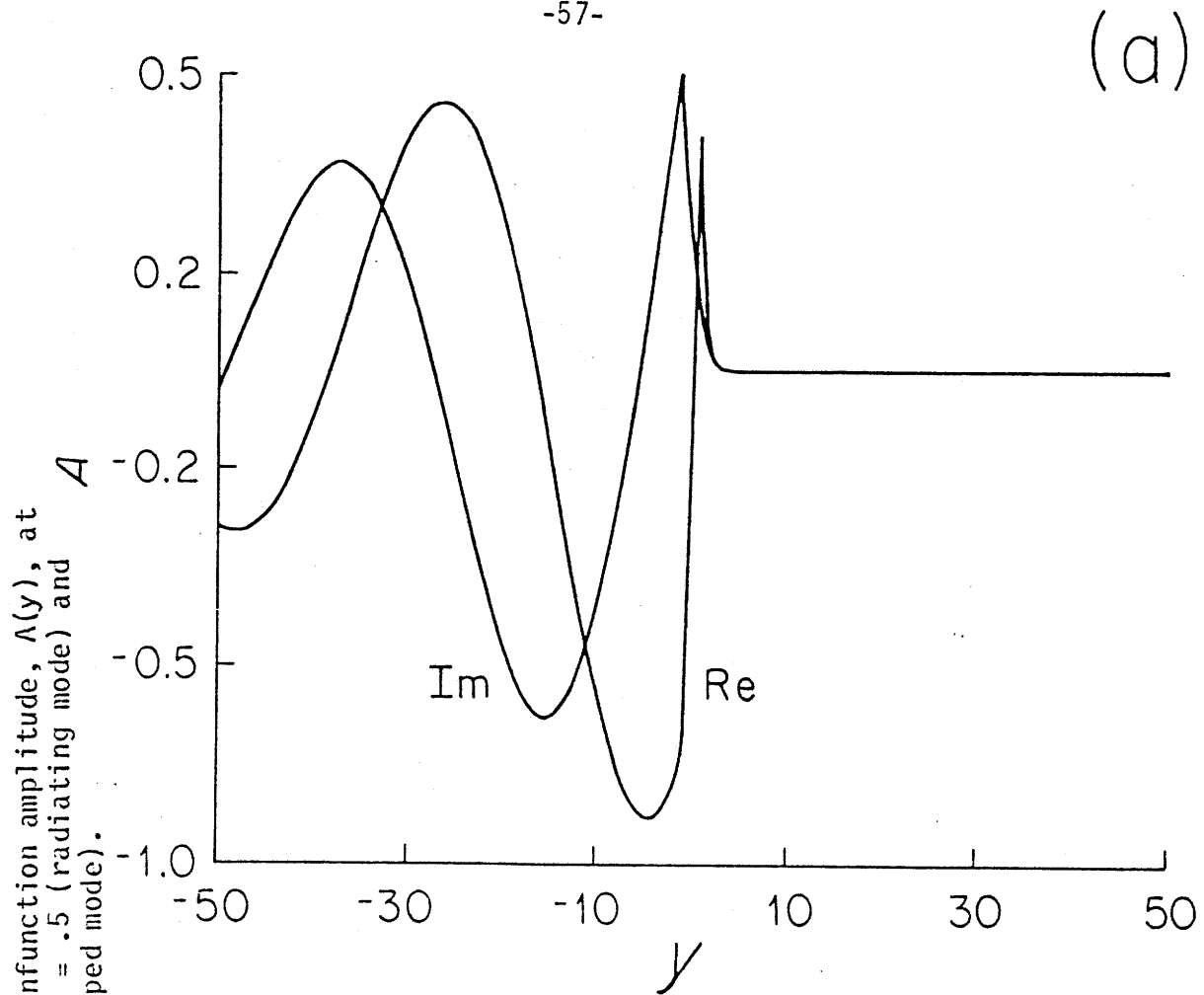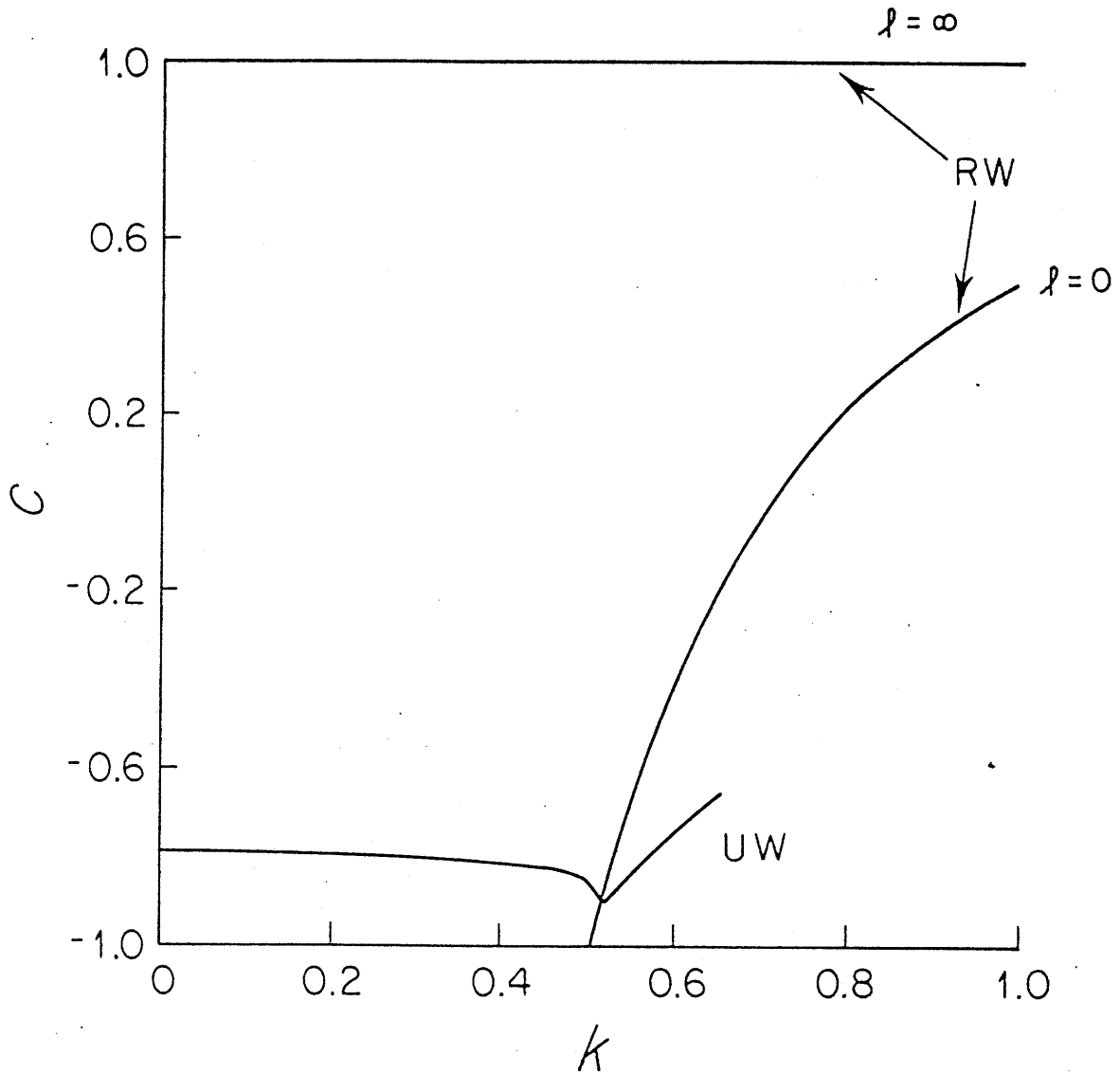Figure 2.5.6

Figure 2.5.7

Dispersion relations for barotropic Rossby waves and shear layer instabilities at β = .5. The real phase speeds of the shear layer instabilities are labelled "UW". The barotropic Rossby wave phase speed in a mean flow U = 1 is labelled "RW", for y-wavenumbers of 0 and 1000. There are no Rossby waves on the high k side of the ℓ = 0 curve.

phase speed for the Rossby wave with $\ell = 0$ crosses the unstable mode's phase speed. The phase speed condition for matching instabilities to Rossby waves is thus satisfied on the long-wave side of this crossover. At higher k, there are no Rossby waves to match to: the y-wavenumber is imaginary and the disturbance must be evanescent in y.

Thus for a simple shear profile, it has been seen that whenever the phase speed condition can be satisfied, there are radiating modes. These can be thought of as destabilized Rossby waves, rather than as inherent instabilities of the shear layer. The puzzle is that, for each k from 0 to ∞, there are an infinite number of neutral Rossby waves, with y-wavenumbers from 0 to ∞. A single phase speed, a single Rossby wave, is selected for destabilization at each k. For this profile, the radiating modes all have growth rates which are a substantial fraction of the growth rates of the trapped modes.

Comparison of the results from this profile and the results of Howard and Drazin (1964) and Dickinson and Clare (1973) for the shear profile, $U(y) = \tanh y$, are fruitful, partly because it indicates how well the broken profile represents a smoothly-varying flow. Howard and Drazin (1964) made the first theoretical study of the hyperbolic tangent profile on the β-plane. They found a neutral curve in the β-k plane with contiguous unstable solutions. At $\beta=0$, there is a single neutral mode at high k, corresponding to the single change in sign of $-U_{yy}$. At slightly non-zero β, there are two neutral modes, one with k near 0 and one at high k, corresponding to the two changes in sign of $\frac{\partial \hat{\pi}}{\partial y}$. The longwaves associated with this neutral curve are stabilized by β. The maximum value of β for which

instability occurs is given correctly by the necessary condition for instability. They also predicted an additional set of unstable, long wave low β modes which were not predicted by Howard's inflection point theorem (1964).

Kuo (1973) filled in Howard and Drazin's stability diagram, showing the phase speeds and growth rates of the unstable modes. He apparently did not find separate neutral stability curves for the two modes at small β and small wavenumber, although behavior due to both modes was apparent.

Dickinson and Clare (1973) made a complete numerical study of the solutions for the hyperbolic tangent profile, but because of its complexity, did not attempt to complete the stability diagram in the crucial low wavenumber region where the second mode of Howard and Drazin appears. In this range of β and k, Dickinson and Clare found two distinct modes of instability, overlapping in wavenumber. The main mode was contiguous to the neutral curve found by Howard and Drazin and was stable at the longest wavelengths. The second mode was unstable for long waves and had a shortwave cutoff. The first mode was strongly trapped to the region of maximum horizontal shear while the second mode was "radiating" and had much slower decay.

The unstable modes of the shear layer found in the beginning of this section are very similar to the unstable modes of the hyperbolic-tangent flow. The similarities are: (1) the trapped instabilities occur inside a neutral curve with both a long and a shortwave stability cutoff at non-zero β. All of these waves are trapped to the shear layers since their wavenumbers are too large to force Rossby waves on the westerly side

of the flow (the neutral curve was given analytically by Howard and Drazin for the tanh y profile and there is an <u>apparent</u> neutral curve for the broken profile); (2) the long waves at non-zero β are unstable and radiating, forming a second unstable mode which is most distinct at larger β. All radiating waves are in the range of β and k where Rossby waves in the westerly flow are possible. The main differences are that (1) at low β where the (tanh y) flow has two separate modes, overlapping in wavenumber, the shear layer has a single mode which is a combination of the two (tanh y) modes without the lower growth rate parts of the overlapping modes and (2) where the oscillatory mode for the hyperbolic tangent profile is limited to a small range of β and k, the oscillatory mode for the shear layer occurs for all values of β up to the cutoff dictated by the necessary condition for instability. The first difference suggests that the mode coalescence which occurs so readily for broken line profiles (this is true of the jets examined in Chapter 3 also) does not occur when the profile is continuous.

2.6   Barotropic Jets

A jet is defined as a flow which has the same velocity at $+\infty$ and $-\infty$ (Howard and Drazin, 1964). Only symmetric jets with no more than two inflection points in U are considered here. When there are two inflection points (where $U_{yy} = 0$), Howard's inflection point theorem predicts two neutral modes with contiguous unstable modes at $\beta = 0$. The theorem, of course, predicts nothing about the number of modes when β is non-zero and, in fact, we saw in the previous section that a new mode, associated with Rossby waves outside the shear layer, was introduced when β was non-zero.

A search for unstable modes of a jet can, however, be begun at $\beta = 0$ where there will be two unstable modes. If the jet is symmetric, the two modes will be the sinuous mode (symmetric) and the varicose mode (antisymmetric).

The jets that will be considered are: (1) top-hat, eastward jet, (2) eastward jet with shear layers, and (3) westward jet with shear layers. ("Westward" jets were explored by allowing β to be negative: β is negative when the scale velocity is negative.) Eastward and westward jets are considered separately because their potential for radiation of energy far from the jet differs so greatly. (The energy from the horizontal shear of an eastward jet essentially "radiates" to the inside of the jet.) While the phase speeds of the eastward jet instabilities will be generally too large to match to Rossby waves outside the jet, there will be no such difficulty for the westward jets. In fact, the results for westward jets look very much like the shear layer results of the previous section.

Figure 2.6.1 shows the eastward jets and a schematic of their potential vorticity gradients. The potential vorticity gradient for the top-hat jet is always β inside and outside the jet and a double delta function (because of U_{yy}) at the profile breaks. Because the top-hat shape is independent of β, there is no range of β for which this flow is absolutely stable by the necessary condition (2.3.6) since the potential vorticity gradient changes sign for any choice of β. The shear layer jet is different in this respect. Its shape in the shear zones (Region II in the figure) depends on β. When β becomes large enough, dU/dy at $y = D-\epsilon$ and $-D+\epsilon$ becomes negative. When this happens, the delta function
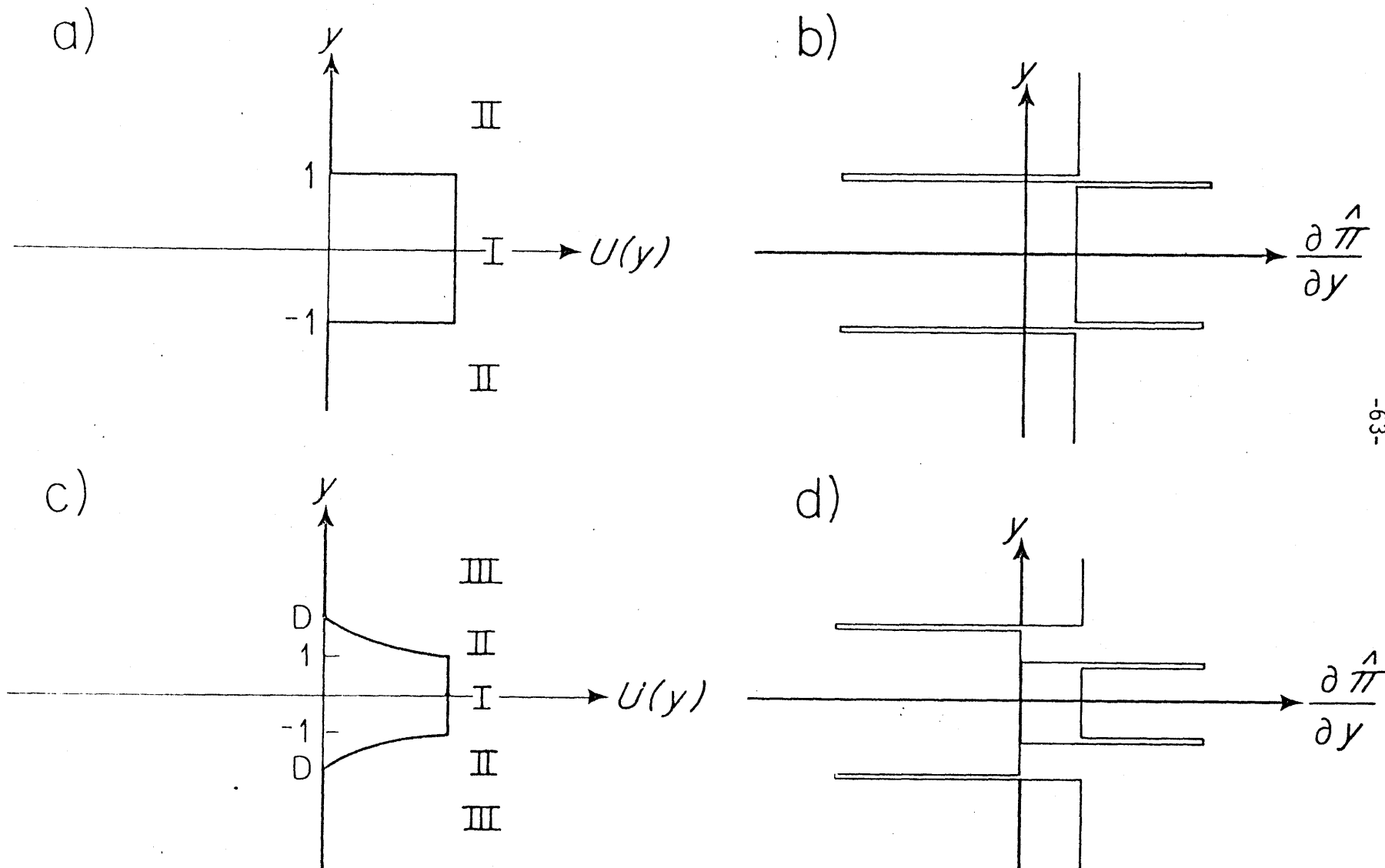
a)

b)

c)

d)

Figure 2.6.1   Barotropic jets: (a) U(y) and (b) $\partial \hat{\pi}/\partial y$ for the top-hat jet (c) U(y) and (d) $\partial \hat{\pi}/\partial y$ for the barotropic jet.

for U_{yy} changes sign and the potential vorticity gradient is positive everywhere (for eastward flow). The flow then must be stable for all β larger than a critical value, called β_c. β_c depends on the width D of the shear layer.

(a) Eastward Top-Hat Jet

The unstable modes of the top-hat jet are well known, although aspects of their behavior as β increases are explored here for the first time. A symmetric flow has symmetric and antisymmetric perturbation eigenfunctions. They are known as the sinuous and varicose modes, respectively. Only the sinuous (symmetric) mode is treated extensively in this thesis. The varicose mode is explored for the barotropic, top-hat jet only.

Rayleigh (1879) first posed the problem of the top-hat jet, for the case $\beta = 0$. Howard and Drazin (1964) extended it to the β-plane, giving analytical results for the phase speed and growth rate for various limits of wavenumber and β. Flierl (1975) discussed the full behavior for varying values of β/k^2, although he did not completely explore the β and k parameter ranges.

When $\beta = 0$, the well-known dispersion relations for the two jet modes obtained from the solutions (2.1.1) in regions I and II and the matching conditions (2.2.2) and (2.2.3) are

$$c_1^2 + (1 - c_1)^2 \ \tanh \ k = 0$$

$$c_2^2 \ \tanh \ k + (1 - c_2)^2 = 0$$

The sinuous (symmetric) mode has phase speed c_1 and the varicose (asymmet-

ric) mode has phase speed c_2. Both modes have precisely the same growth rates at the same wavenumbers. The eigenfunctions for these modes are strictly evanescent in y, with a decay scale of $(1/k)$.

When β is non-zero, the two dispersion relations are (Howard and Drazin, 1964)

$$c_1^2 \, \ell_I \; + \; \ell_{II} \, (1 - c_1)^2 \; \tanh \, \ell_{II} = 0$$

$$c_2^2 \, \ell_I \, \tanh \, \ell_{II} \; + \; \ell_{II} \, (1 - c_2)^2 \; = 0$$

(2.6.1)

where

$$\ell_I^2 \; = \; k^2 + \beta/c$$

$$\ell_{II}^2 \; = \; k^2 + \frac{\beta}{1-c}$$

(2.6.2)

Again, c_1 corresponds to the symmetric mode and c_2 to the antisymmetric mode. The eigenfunction is

$$A_I = e^{-\ell_I y}$$

$$A_{II} = d \, (e^{\ell_{II} y} \pm e^{-\ell_{II} y})$$

(2.6.3)

where the $\oplus$ sign is for the sinuous mode and the $\ominus$ sign for the varicose mode and $d \equiv \dfrac{c-1}{c} \dfrac{e^{-\ell_I}}{e^{\ell_{II}} \pm e^{-\ell_{II}}}$.

The limits of the dispersion relation as β/k^2 and k take extreme values have been explored by Howard and Drazin (1964), so the results will not be repeated here. It is sufficient to say that both the varicose and sinuous modes are unstable at very large k [where $c \to 1/2(1 \pm i)$] and very large β [where $c \to 1/2(1 \pm i/\sqrt{3})$].

Figure 2.6.2

Top-hat jet (sinuous mode) stability diagram. The stable region (marked "S") becomes vanishingly thin as β increases.
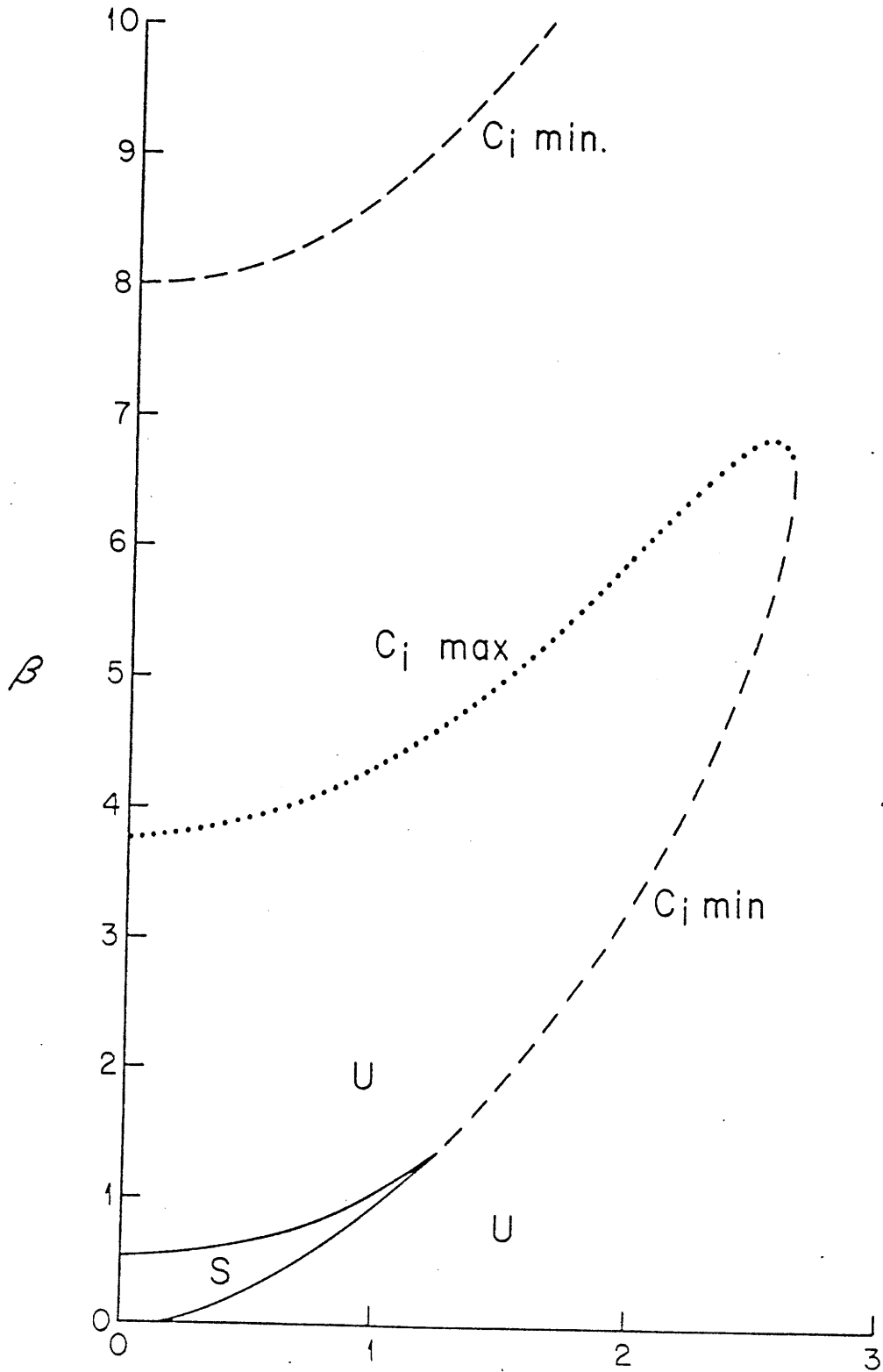
The sinuous modes of the eastward top-hat jet are unstable for ranges of β and k shown in the stability diagram of Figure 2.6.2. Notice that the long waves are stabilized by low β's, but that higher β actually destabilizes the modes again. These modes will be called "β-destabilized" modes. Because of the top-hat profile, the short waves and modes with high β are all unstable (they are stable when the shear zone has some width). A sample dispersion relation is shown in Figure 2.6.3 for $\beta = .55$. In Figure 2.6.4 are plotted the real and imaginary parts of ℓ_I and ℓ_{II}. Both the main mode and the β-destabilized mode are trapped to the jet. Their behavior is different inside the jet however: from ℓ_{II}, we see that the β-destabilized mode is wavelike and the main mode is evanescent inside the jet. The β-destabilized mode is the lowest cross-channel mode, with a y-wavenumber of roughly $\pi/2$ at small k.

The varicose mode of the top-hat jet has a stability diagram (Figure 2.6.4) which looks similar to the sinuous mode diagram (Figure 2.6.2). Again there is a small region where the varicose mode is stable, but it is now centered at higher β. All waves are trapped to the jet. The details of the stability diagram depend on the structure of the eigenfunctions within the jet: eigenfunctions from the long-wave, high-β side of the stable region and dashed curve are more wavelike inside the jet than those from the short-wave, low-β side. Dispersion relations as a function of k for several β's are shown in Figure 2.6.5. The shift in phase speed across the stable part of the stability diagram is very apparent for $\beta \geq 3$. The y-dependence outside the jet clearly indicates that the disturbances are trapped. The y-dependence inside the jet shows the wavy

Figure 2.6.3
Top-hat jet: sinouous mode at $\hat{a}$ = .55. (a) c_i vs. c_r, (b) c_r and c_i vs. k, (c) ℓ_I vs. k, and (d) ℓ_{II} vs. k.
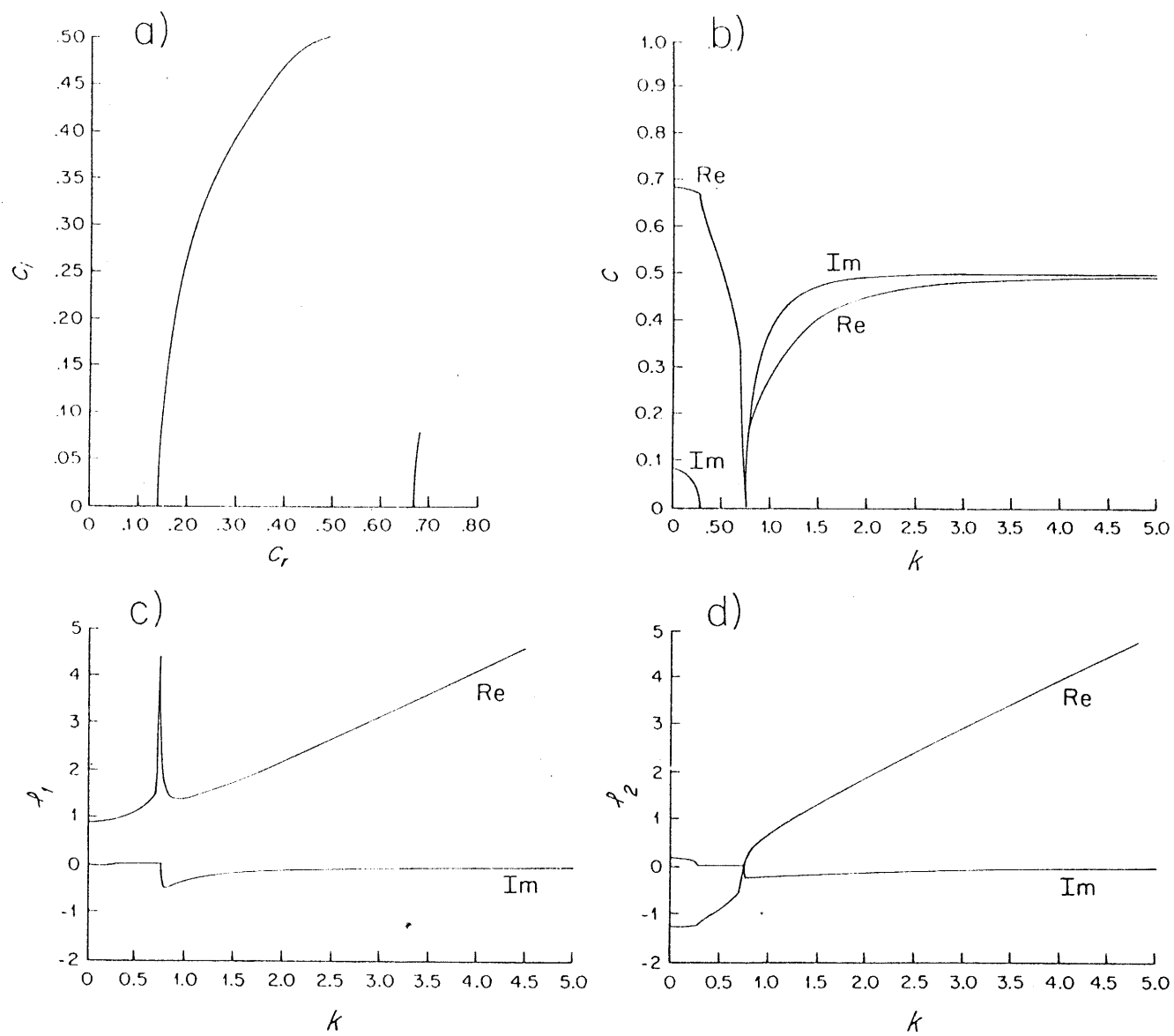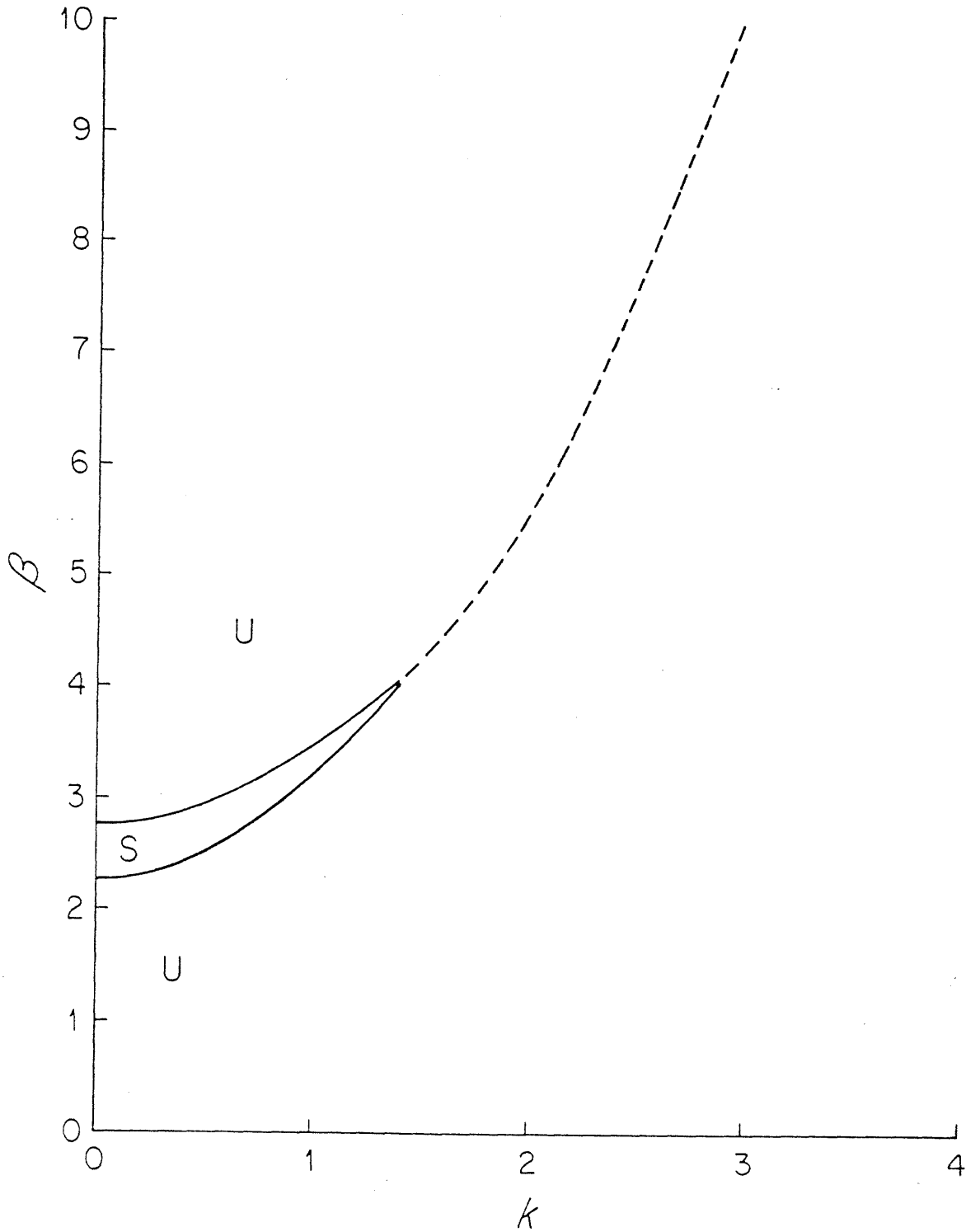
Figure 2.6.4

Top-hat jet (varicose mode) stability diagram. The dashed curve is
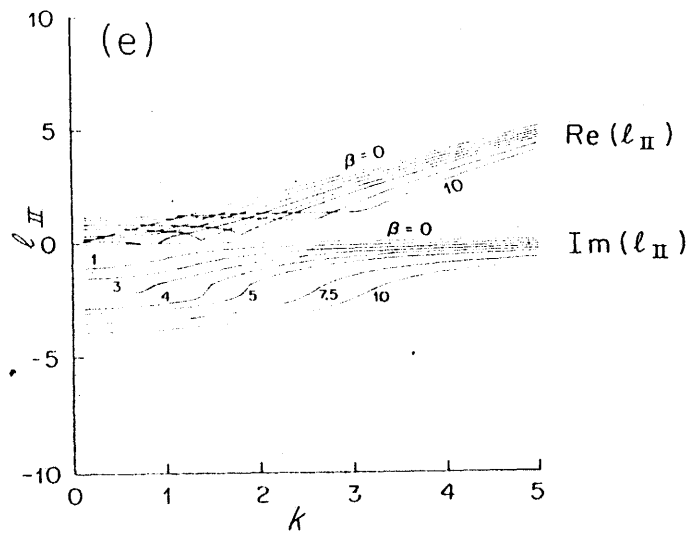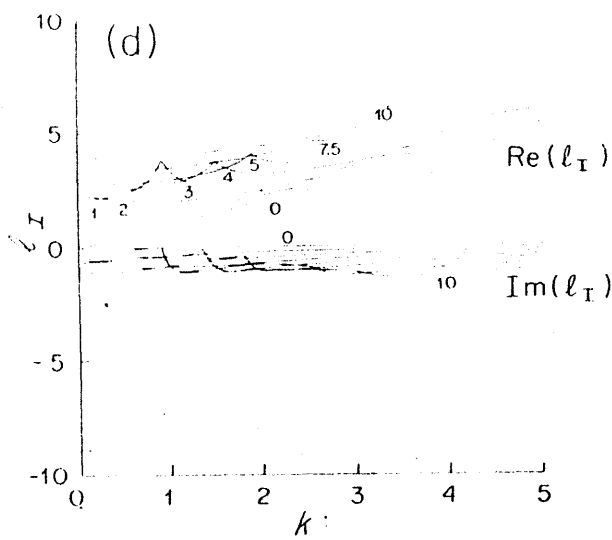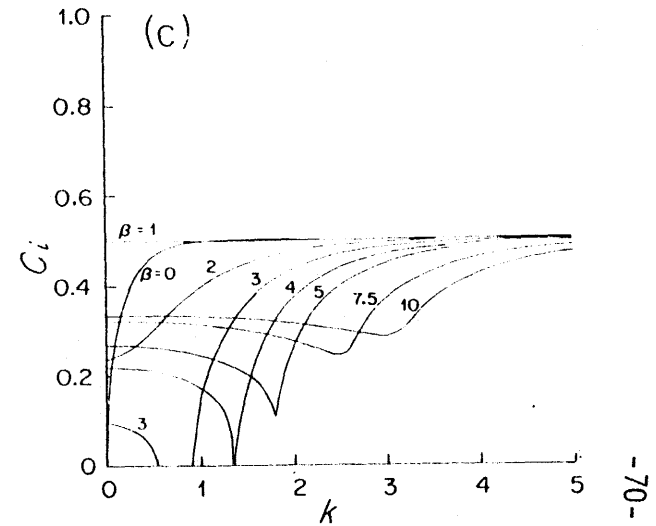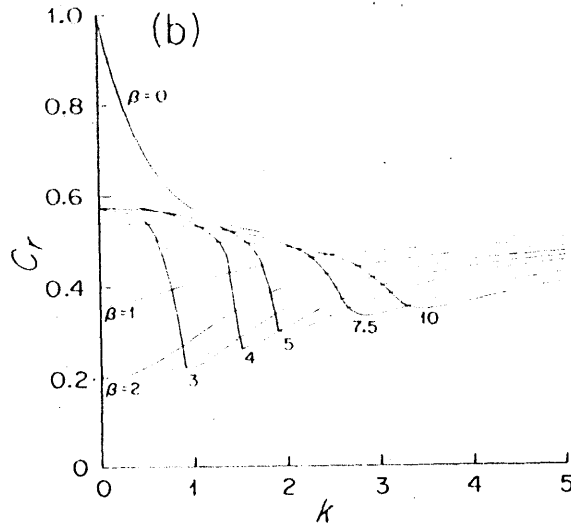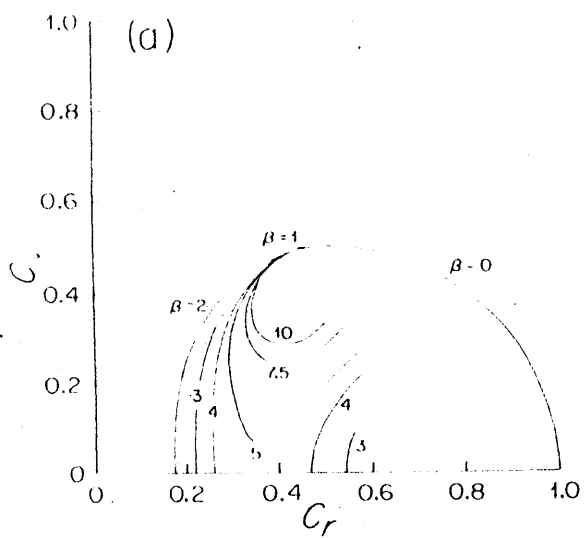the locus of minimum c_i.

Figure 2.6.5

Top-hat jet: varicose mode. (a) c_i vs. c_r, (b) c_r vs. k, (c) c_i vs. k, and (d) ℓ_I vs. k, and (e) ℓ_{II} vs. k for β's marked on the curves.

nature of the eigenfunction at low k and high β. The y-wavelength inside the jet for these eigenfunctions is roughly π, corresponding with the lowest cross-channel antisymmetric mode.

Both the sinuous and the varicose modes are stable in a small region of the β-k plane, with a locus of minimum c_i extending off to infinite β from the stable region. The stable region and curve of minimum c_i mark a transition from evanescent to radiating behavior <u>inside</u> the jet. That is, since

$$\ell^2 = k^2 - \frac{\beta}{1-c}$$

inside the jet, ℓ^2 is positive or negative depending on how large k and β are if c is real. When k is large or β small, the disturbance is evanescent inside the jet. As β increases relative to k, ℓ becomes imaginary and the disturbance is wavelike inside the jet. When c is complex, this distinction is blurred. However, the waves with high k and low β in Figures 2.6.2 and 2.6.4 are more evanescent inside the jet than the low-k, high-β waves. I do not have an explanation for the stability of the profile in the narrow wedge in the β-k plane.

(b) Barotropic Jet

The logical extension of the top-hat jet is a jet with horizontal shear occurring over a zone of non-zero width, just as in the shear layer examples of Section 2.5. The eastward barotropic jet was shown in Figure 2.6.1 with its potential vorticity gradient. This profile is similar to the the shear layer profile, so it can be predicted that any Rossby-wave-like behavior will be confined to the more westerly part of the flow, which is the central jet in this case. Thus the eastward jet will probably not radiate energy outside the jet. In contrast to the top-hat jet,

the barotropic jet is stabilized when β is large enough to make the potential vorticity gradient single-signed, just as for the shear layer. The barotropic jet is also stable to short wavelength perturbations, like the shear layer, since the short waves are less able to sample the full width of the shear zone (which they must do if they are to "see" the change in sign of the potential vorticity gradient.)

The profile has uniform velocity in Regions I and III and

$$U = 1 - \left(\frac{1-y}{1-D}\right) + \frac{\beta}{2} [D(1-y) -y + y^2]$$

in Region II. The potential vorticity is β in Regions I and III and zero in Region II. The length scale L^* is the half-width of the central jet, Region III. The width of the shear zone, Region II, is (D^*-L^*) and its non-dimensional width is $(D-1)$. The flow is stable when β is large enough to make dU/dy at $y = \pm D$ negative. This occurs when

$$\beta = \beta_c = \frac{2}{(D-1)^2} \tag{2.6.4}$$

The dispersion relation derived from the matching conditions for the symmetric mode is

$$e^{-kS} \left[c(1-\sqrt{1 + \frac{a}{c}})+\frac{1}{k} (\frac{1}{S}+\frac{\beta}{2} S) \right] \left[(1-c)(1-\sqrt{1 - \frac{a}{1-c}} \ \tanh k \ \sqrt{1-\frac{a}{1-c}})+\frac{1}{k} (\frac{1}{S}+\frac{\beta}{2} S) \right]$$

$$\tag{2.6.5}$$

$$+e^{kS} \left[c(1+ \sqrt{1 + \frac{a}{c}})-\frac{1}{k} (\frac{1}{S}+\frac{\beta}{2} S) \right] \left[-(1-c)(1+\sqrt{1 - \frac{a}{1-c}} \ \tanh k \ \sqrt{1-\frac{a}{1-c}})+\frac{1}{k} (\frac{1}{S}+\frac{\beta}{2} S) \right] = 0$$

where $\qquad S = (D - 1)$ and $a = \frac{\beta}{k^2}$.

Limits of the phase speed $(c_r + ic_i)$ as β and k take on extreme values are as follows:

(1) $S = (D-1) \rightarrow 0$: this gives the top-hat dispersion relation (2.6.1)

(2) $k \rightarrow \infty$, β fixed: $c = 0, 1$

(3) $k \rightarrow \infty$, $\beta = O(k)$: $c = -\beta S/2k$, $1 - \beta S/2k$

(4) $k \rightarrow 0$, β fixed:

$$\beta \left\{ c\left(-1 - \frac{S}{2} \sqrt{\frac{\beta}{c}}\right) + \frac{1}{2} + \frac{S^2}{4} \right\} + (1-c) \sqrt{\frac{\beta}{c-1}} \tanh \sqrt{\frac{\beta}{c-1}} \left\{ c \sqrt{\beta \left(\frac{1}{c} - \frac{S}{2}\right) + \frac{1}{S}} \right\} = 0$$

(5) $\beta = 0$, k fixed:

$$e^{-kS} \left(\frac{1}{S}\right) \left[(1-c) k (1 - \tanh k) + \frac{1}{S} \right]$$

$$+ e^{kS} \left(2 ck - \frac{1}{S}\right) \left[-(1-c) k (1 + \tanh k) + \frac{1}{S} \right] = 0$$

The limits tell us that the dispersion relation is correct, since the top-hat and the correct dispersion relation at $\beta = 0$ can be derived from it. The limits also show that the profile is stable at large wavenumber, but give no information when β is large for fixed wavenumber (in this limit, the flow must be stable because of the necessary condition for instability).

The stability diagram for this jet is shown in Figure 2.6.6 in the β-k plane with various choices of shear zone width. (There are three independent parameters in the problem: β, k and D.) The β_c's for several shear zone widths are listed in Table II.1.

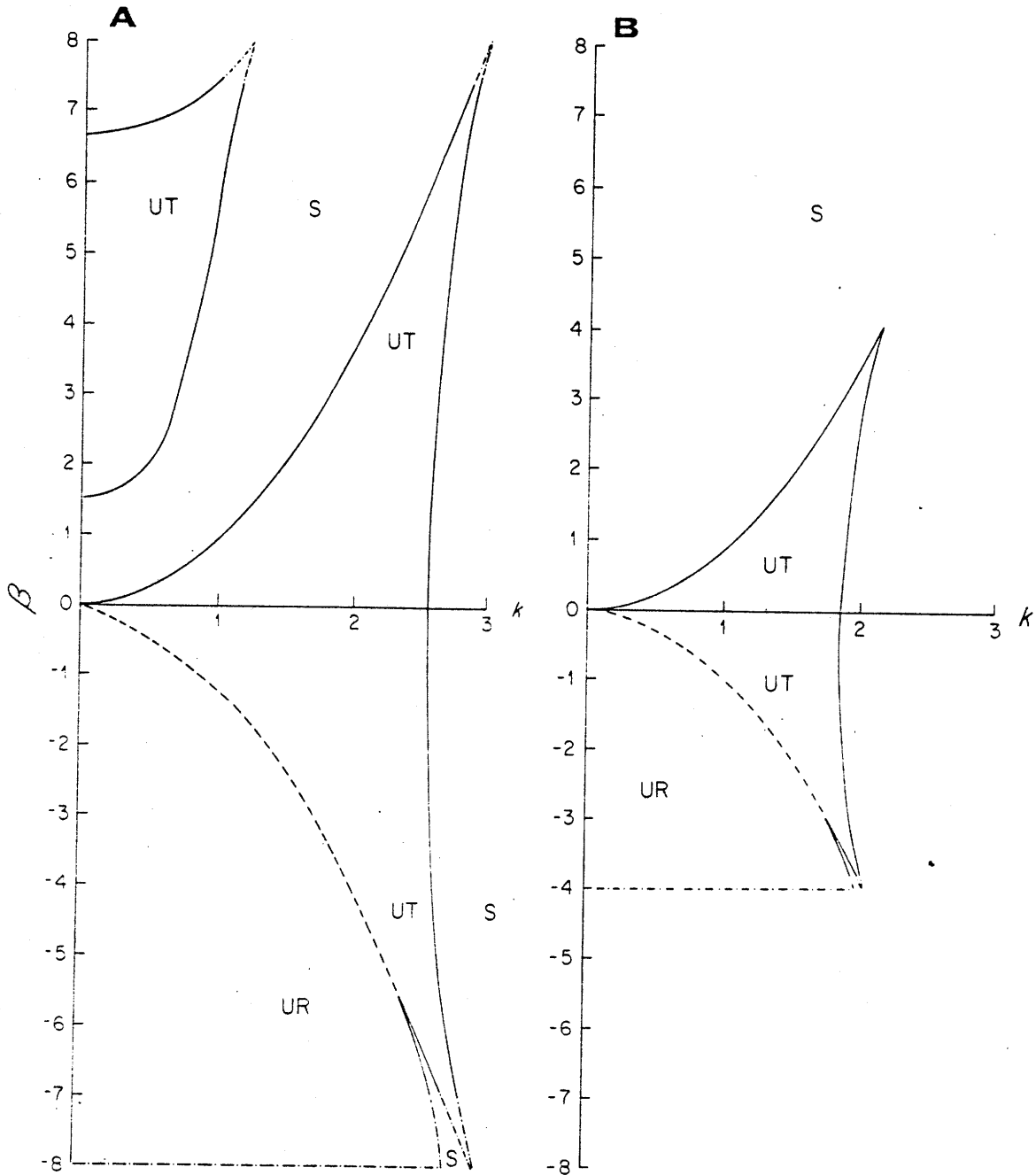| $(D - 1)$	β_c
0.0	∞
0.05	800.00
0.5	8.00
0.7	4.08
1.0	2.00
9.0	.02

Figure 2.6.6

Barotropic jet, sinuous mode: stability diagram in the β-k plane for shear zone widths (D-1) = .5 and .7. "S" = stable, "UT" = unstable, trapped, "UR" = unstable, radiating. The solid curves are stability boundaries and the dot-dash curves are extrapolated stability boundaries. The dashed curves are the loci $Re(c_I) = Im(c_I)$.

Three effects of increasing the shear zone width (D-1) are seen: (1) the shortwave cutoff occurs at lower values of k; (2) as the shear zone widens, β_c decreases, from ∞ for a top-hat jet to 2 for a jet with shear zone widths equal to the central jet half-width; (3) the β-destabilized modes occur at higher β as D increases. The last two tendencies are opposing: as the shear zone gets wider, the β-destabilitzed modes disappear since β_c is decreasing while the modes occur at higher and higher β. When (D-1) > .6, the β-destabilized modes vanish. On the other hand, as the shear zone gets narrower, there are more and more β-destabilized modes. For the narrowest shear zone considered here, the behavior at high β is difficult to work out since it appears that there are many, many β-destabilized modes separated by stable regions. When D is small and β is increased to β_c at k = 0, there are many alternations between unstable and stable waves. As the shear zone is widened, fewer and fewer of these unstable modes appear until there is only one unstable mode when D is between 1.55 and 1.6. This single mode persists for all D's beyond 1.6.

The unstable regions on the stability diagram (2.6.6) all terminate in a cusp at β_c. This cusp may be an artifact of the specific choice of profile with breaks in U or dU/dy.

Dispersion relations and c_r vs. c_i for different values of β at D = 1.5 and 1.7 are shown in Figure 2.6.7. Both of these shear zone widths are used in the two-layer jet cases of the next chapter. There are two barotropically unstable modes when D = 1.5 and only one when D = 1.7. Note that β tends to decrease the eastward phase speed of these sinuous modes, while it decreases the growth rates. The complex y-wavenumbers,
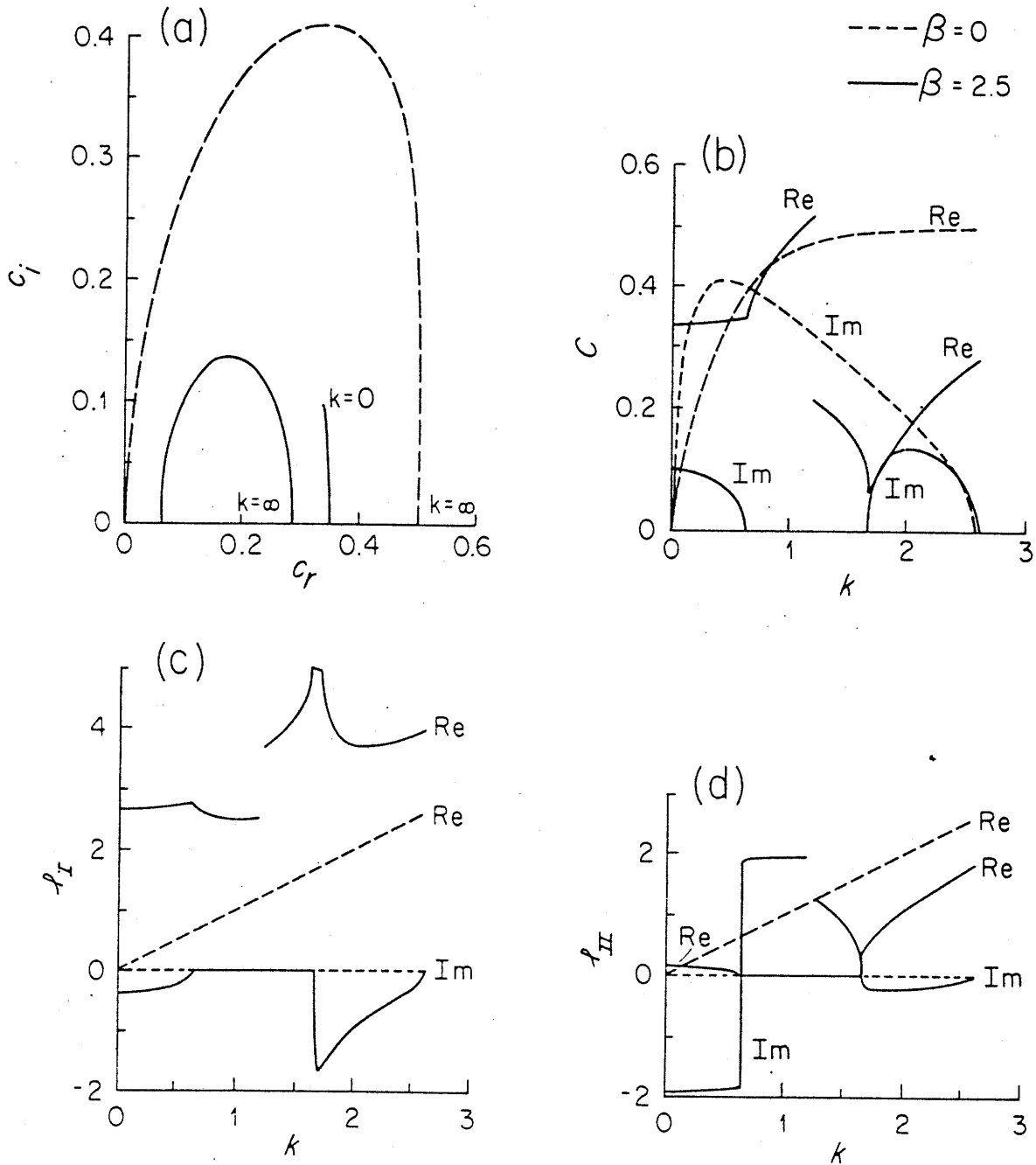
Figure 2.6.7

Barotropic jet, sinuous mode: dispersion relations for D = 1.5: (a) c_i vs. c_r, (b) c_r (Re) and c_i (Im) vs. k, (c) λ_I vs. k and (d) λ_{II} vs. k for β = 0, 2.5.
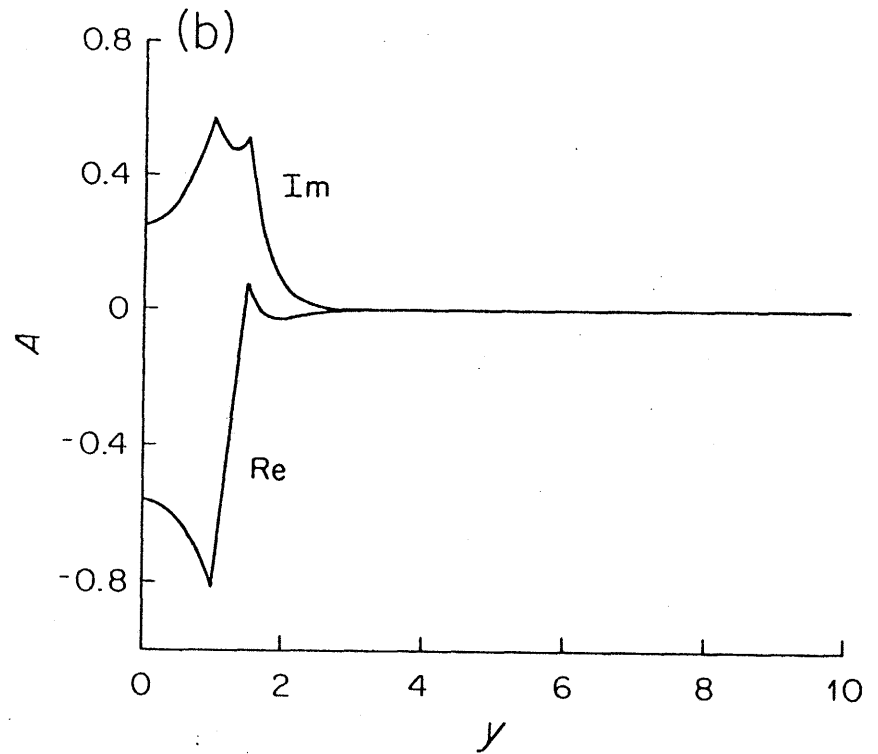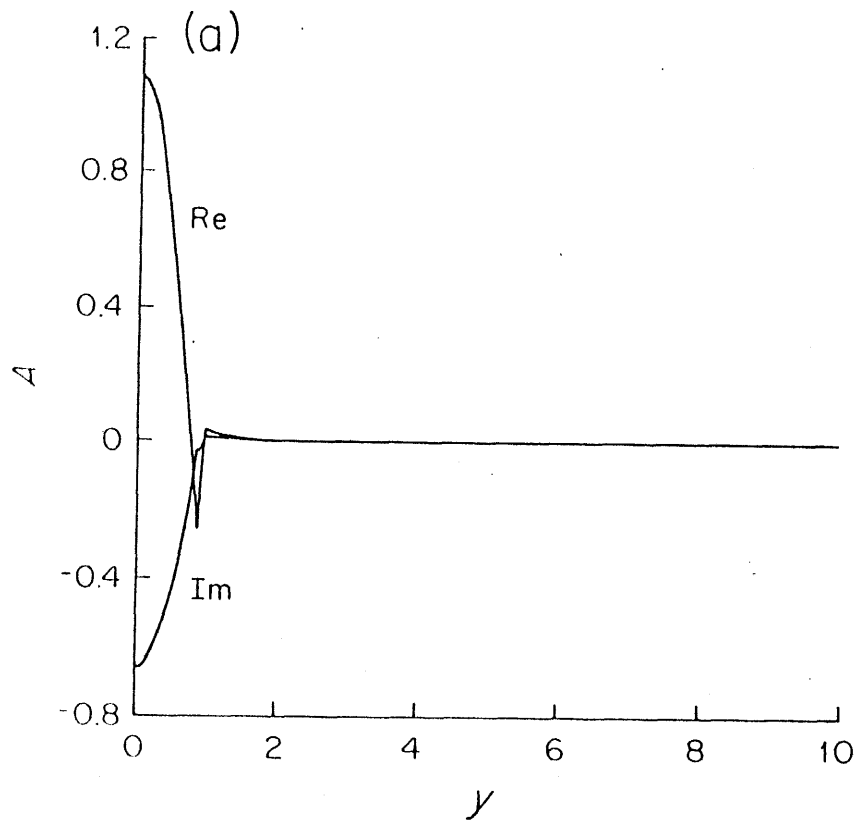
Figure 2.6.8

Barotropic jet, sinuous mode: eigenfunctions at $D = 1.5$ and $\beta = 2.5$:
(a) $k = .1$ and (b) $k = 2.0$.

ℓ_{II} and ℓ_I, are also shown in Figure 2.6.7. Eigenfunctions for the two modes when $D = 1.5$ are shown in Figure 2.6.8.

None of the unstable modes of the barotropic eastward jet are radiating since their phase speeds are always more eastward than the flow speed outside the jet. Note that this could not be predicted by the semi-circle theorem, since the semi-circle theorem is modified when β is non-zero to include the possibility of unstable waves with phase speeds less than the minimum phase speed. However, Tung (1981) showed that the neutral mode contiguous to unstable modes with phase speeds outside the range of $U(y)$ must have its phase speed within the range of $U(y)$. Using Tung's result, then, the lack of radiating modes for the eastward barotropic jet could have been predicted.

A westward barotropic jet could, however, radiate easily: all of its instability phase speeds are in the range of Rossby wave phase speeds. Moreover, the barotropic jet resembles the barotropic shear layer, folded over onto itself, which had radiating solutions in the more westerly part of the flow. To look at westward jets, we simply allow $\beta = \beta_0 L^2/U$ to be negative. The stability diagram (Figure 2.6.6) extends to negative β. The stability diagram is very similar to the shear layer stability diagram (Figure 2.5.4). The dotted curve effectively separates radiating solutions, on the long wave side, from trapped solutions, on the short wave side. At large β, there is actually a range of stable waves between the radiating and trapped instabilities. The stability boundary at large β is at $\beta = \beta_c$ for both the radiating and trapped solutions. While the unstable region for the trapped solutions terminates in a cusp at $\beta =$

β_c, the radiating solutions are unstable for all wavenumbers between 0 and the transition to trapped solutions (at small $|\beta|$ and their shortwave cutoffs at large $|\beta|$. The shortwave cutoff for the radiating modes is solely determined by the phase speed condition: for $k > k_s$, there is no y wavenumber ℓ_I for which the instability phase speed can match a Rossby wave phase speed ($\ell = 0$ at $k = k_s$ and $\ell \sim i\ell_I$ for $k < k_s$).

The dispersion relations and eigenfunctions for the westward jets are also very similar to those of the barotropic shear layer. In Figures 2.6.9 and 2.6.10, dispersion relations, y dependencies [$\ell_I(k)$, $\ell_{II}(k)$] and eigenfunctions are shown. The similarity to those of the shear layer (Figures 2.5.6 and 2.5.7) is obvious.

2.7 Summary of Barotropic Instability Results

In this chapter a method for simplifying a barotropic flow profile when the ambient potential vorticity gradient is non-zero was introduced. The results for a simple shear layer agreed well with the numerically-obtained linear stability results for a continuous shear layer, calculated by Dickinson and Clare (1973). Results for eastward and westward jets were also explored, assuming that these results also resemble the results for a continuous flow profile. Necessary conditions for instability were restated to include the effects of discontinuities in the first derivative of the basic velocity, dU/dy.

Because of the way the profiles with shear layers are constructed, they simulate the behavior of continuous flows, which can be stabilized by β. It was found that the necessary conditions for instability are
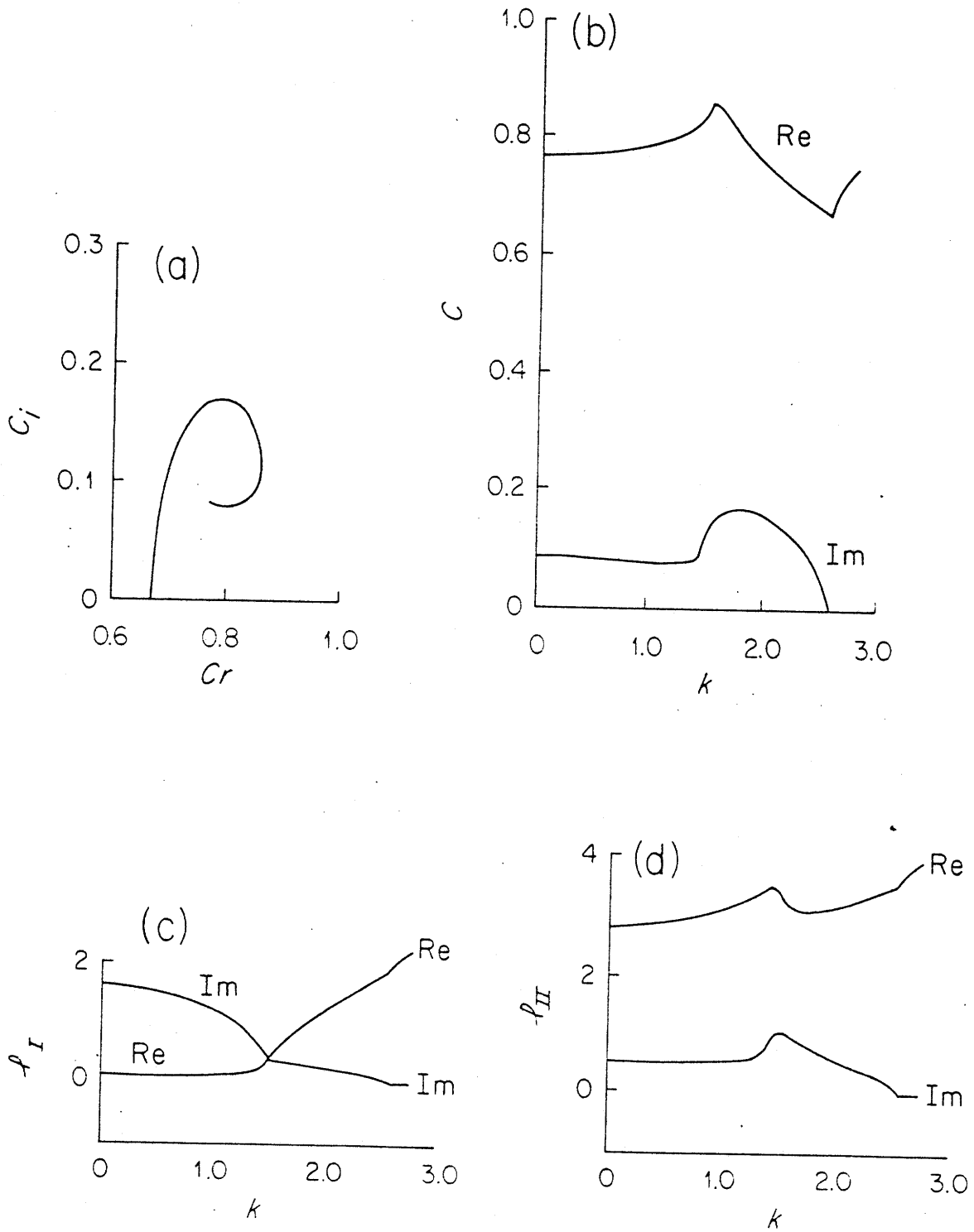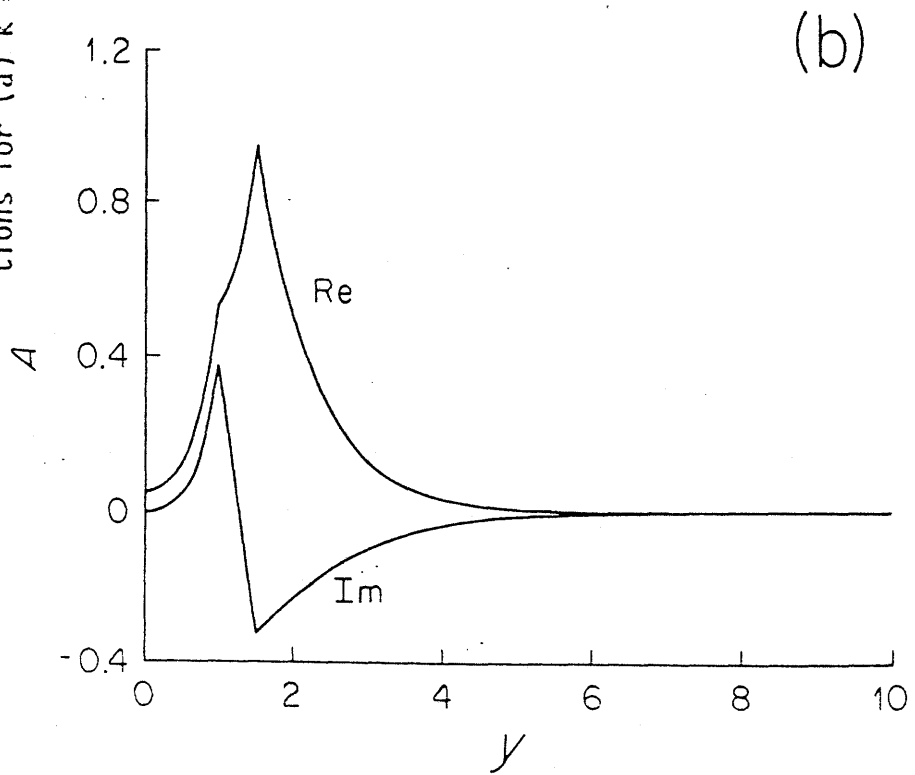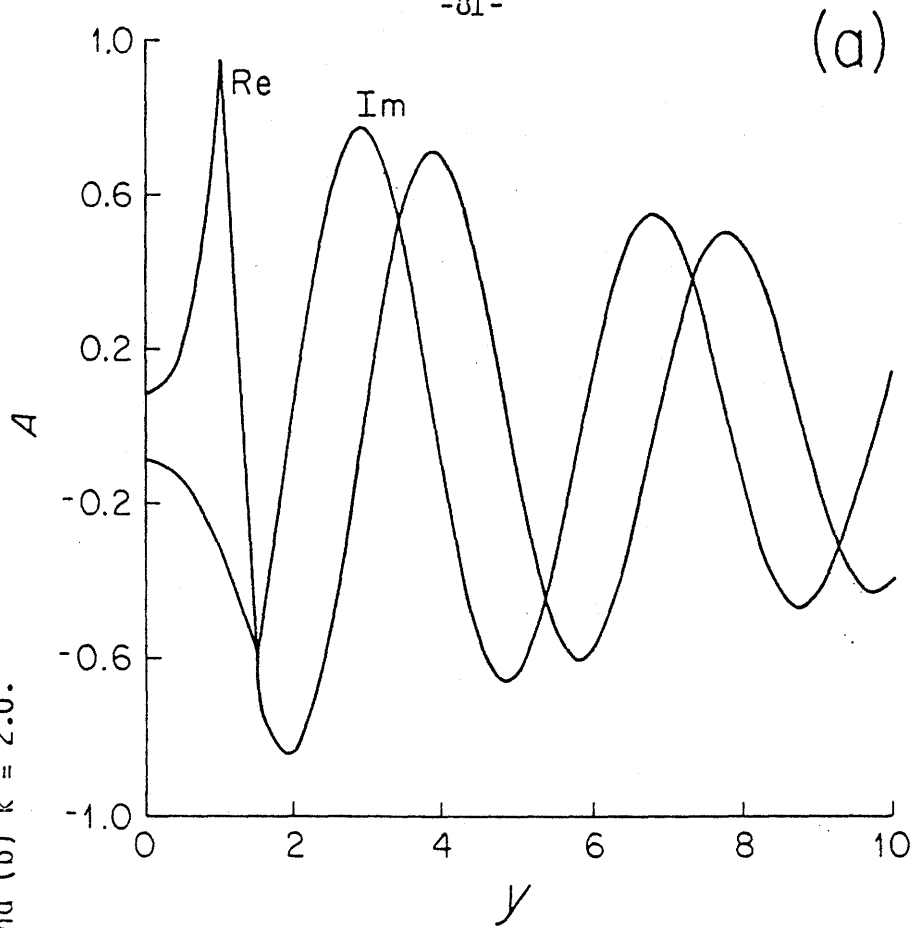
Figure 2.6.9

Barotropic jet, sinuous mode, at $D = 1.5$ and $\beta = -2.0$: (a) c_r vs. c_i, (b) c_r and c_i vs. k, (c) λ_I vs. k and (d) λ_{II} vs. k.

Figure 2.6.10

Barotropic jet, sinuous mode, at D = 1.5 and ß = -2.0: eigenfunc-
tions for (a) k = .1 and (b) k = 2.0.

sufficient for these profiles. Special attention was given to the existence of radiating modes. A definition of radiation in terms of the structure of the neutral mode contiguous to the instabilities was made. It was found that there are radiating instabilities whenever the Rossby wave phase speed range overlaps the flow speed range. These instabilities are additions to the trapped instabilities of the flow. These radiating modes are really destabilized Rossby waves.

An interesting peculiarity was found - for the eastward, non-radiating jet, small values of β stabilize the profile but larger values destabilize it again. The β-destabilized modes, for positive β, seem to be related to the eigenfunction structure inside the jet. Each separate mode which enters as β increases can be identified as the next higher cross-channel mode. When D is small (small shear zones), β_c is large and many of these modes can be seen. As D increases, β_c decreases and the higher cross-channel modes are eliminated. There is a symmetry between the results for the eastward and westward jets. The β-destabilized modes occur in the region of the β-k plane where wavelike solutions (in y) are possible inside the jet. The radiating modes of the westward jet occur where wavelike solutions are possible outside the jet. Whereas there are unstable radiating modes for all negative β's with $|\beta| < \beta_c$, there are stable regions in the positive β range separating the β-destabilized modes. The stability is probably related to the quantization of cross-channel modes in the jet: although the channel width is not well-defined because the jet sides are not rigid walls, the waves are still travelling in the waveguide due to the jet. When the wave is an "exact" cross-channel mode, its

amplitude is negligible where the potential vorticity gradient is a delta function, and the wave may well be stable. The existence of additional modes when β is non-zero which are not predicted by Howard's inflection point theorem is thus related strongly to the existence of wavelike solutions in y.

CHAPTER III: THIN TWO-LAYER JETS

In many parts of the ocean, the circulation is concentrated in narrow currents. These currents are nearly zonal and may be modelled as quasi-geostrophic jets. The jets are usually baroclinic as well as having large horizontal shear. Thus they may have the capacity for both baroclinic and barotropic instability. Ocean observations show that variability in velocity and density is very large in and near such currents: the variability is undoubtedly due to instability.

It is the purpose of this chapter to determine the linearly unstable modes of symmetric, quasi-geostrophic jets which have both horizontal and vertical shear. All unstable jets have instabilities which are firmly tied to the jet, penetrating only a short distance into the stable (or less unstable) bordering regions. Another type of instability is "radiating", as defined in Chapter 2. These instabilities penetrate large distances into the bordering regions. A major focus of this chapter is the existence and structure of these radiating instabilities. The "radiation" takes the form of modified Rossby waves in the ocean interior. A condition for the existence of radiating instabilities is that the phase speed and x-wavenumbers of the jet instabilities and the modified Rossby waves correspond. In the previous chapter, it was seen that this condition predisposes westward, barotropic jets to radiate while eastward, barotropic jets do not radiate. In this chapter, basically eastward jets are changed slightly to allow some of their instabilities to radiate. The stability of westward, baroclinic jets is also considered: both trapped and radiating instabilities are found.

The chief importance in these results, in addition to being yet another discussion of the linearly most unstable modes of currents like the Gulf Stream, is that they suggest that at least part of the "mid"-ocean eddy field can be generated some distance away by more intense currents. The results only suggest this possibility since we cannot predict from linear stability analysis alone which instabilities will survive to dominate the fully nonlinear flow.

3.1   Formulation for Two-Layer Jets

(1) Potential Vorticity Equation

The stability of narrow, intense baroclinic jets is examined here using two simplifications for the flow profiles: the baroclinicity is represented by a two-layer model in which the two layers have equal depth, thus retaining only two vertical modes; the horizontal shear is restricted to specific zones, using flow profiles similar to Rayleigh's (1879) "broken line" profiles. It is assumed that the basic flow whose stability is examined is zonal and steady and that the perturbation stream function has much smaller amplitude than the mean flow stream function. The linearized, inviscid non-dimensional potential vorticity equations for the perturbations in the two layers are (c.f., Pedlosky, 1979):

$$(\frac{\partial}{\partial t} + U_1 \frac{\partial}{\partial x})[\nabla_H^2 \phi_1 + F(\phi_2 - \phi_1)] + [\beta - U_{1yy} + F(U_1 - U_2)]\frac{\partial \phi_1}{\partial x} = 0$$

$$(3.1.1)$$

$$(\frac{\partial}{\partial t} + U_2 \frac{\partial}{\partial x})[\nabla_H^2 \phi_2 - F(\phi_2 - \phi_1)] + [\beta - U_{2yy} - F(U_1 - U_2)]\frac{\partial \phi_2}{\partial x} = 0$$

Here, $(\nabla_H{}^2)$ is the two-dimensional Laplacian $(\partial^2/\partial x^2 + \partial^2/\partial y^2)$. ϕ_1 and ϕ_2 are the perturbation streamfunctions for the top and bottom layers, respectively. The equations were scaled using L, U and $\mathcal{H}$ (horizontal length, flow velocity and layer depth). The non-dimensional parameters are $\beta = \beta_0 L^2/U$ and $F = (L/L_R)^2$ where L_R is the internal deformation radius, $L_R = \sqrt{g'\mathcal{H}}/f$. The mean flow, U_1 and U_2, depends only on latitude, y. The potential vorticity gradient for the mean flow in each layer also depends on y and is

$$\frac{\partial \pi_1}{\partial y} = \beta - U_{1yy} + F(U_1 - U_2)$$

$$\frac{\partial \pi_2}{\partial y} = \beta - U_{2yy} - F(U_1 - U_2)$$

(3.1.2)

The boundary conditions are that the disturbances ϕ_1 and ϕ_2 be bounded at $y = \pm \infty$ (if the ocean is unbounded), or that $\phi_1 = \phi_2 = 0$ at $y = \pm H$ (if there are northern and southern boundaries at $\pm H$). If the wave is not growing and is oscillatory in y, the boundary condition at $y = \pm \infty$ is that the meridional group velocity be outward.

Normal mode solutions to (3.1.1) are sought, with $\phi_1 = \Phi_1(y)e^{ik(x-ct)}$ and $\phi_2 = \Phi_2(y)e^{ik(x-ct)}$. Both c and Φ_n are allowed to be complex while k is strictly real. Equation (3.1.1) becomes

$$(U_1 - c) \frac{d^2\Phi_1}{dy^2} - k^2 \Phi_1 + F(\Phi_2 - \Phi_1) + \frac{\partial \pi_1}{\partial y} \Phi_1 = 0$$

(3.1.3)

$$(U_2 - c) \frac{d^2\Phi_2}{dy^2} - k^2 \Phi_2 - F(\Phi_2 - \Phi_1) + \frac{\partial \pi_2}{\partial y} \Phi_2 = 0$$

(2) Profile Simplification

Specific flows are modelled in a similar way to the barotropic flows of Chapter 2. It is assumed that either

$$U_1 = \text{constant} \quad \text{and} \quad U_2 = \text{constant} \tag{3.1.4a}$$

or

$$\frac{\partial \pi_1}{\partial y} = \frac{\partial \pi_2}{\partial y} = 0 \tag{3.1.4b}$$

so that, in a given region, either the flow speeds are constant or that the potential vorticity gradient vanishes. Note that where the flow speeds are independent of y, the potential vorticity gradient is non-zero and independent of y.

The flow configuration is illustrated in Figure 3.1.1. The length scale used in non-dimensionalization is L^*, the half width of the central jet, Region I. The shear zone region (II) is $1 < |y| < D$. Boundaries are at $|y| = H$ where $H \gg L$ (in most models considered here, $H = \infty$). The velocity is specified in the upper and lower layers in the central jet (Region I) and outside the jet (Region III). The velocities are all scaled by U_{I1}^*. Thus, $U_{I2} = U_{I2}^*/U_{I1}^*$, $U_{01} = U_{01}^*/U_{I1}^*$ and $U_{02} = U_{02}^*/U_{I1}^*$. Also, $U_{02} = 0$ in all models.

The number of parameters which describe this geometry is large - the jet width, the shear zone width, the channel width, the velocities in the central jet and outside the jet, the wavelength of the disturbance, and non-dimensional β and F.

The requirement that $\partial \pi_1/\partial y = \partial \pi_2/\partial y = 0$ in the shear zone, Region II, specifies the velocities $U_1(y)$ and $U_2(y)$. Solving (3.1.4b) for U_1 and U_2, requiring that the velocities be continuous at $y = 1$ and D, results in
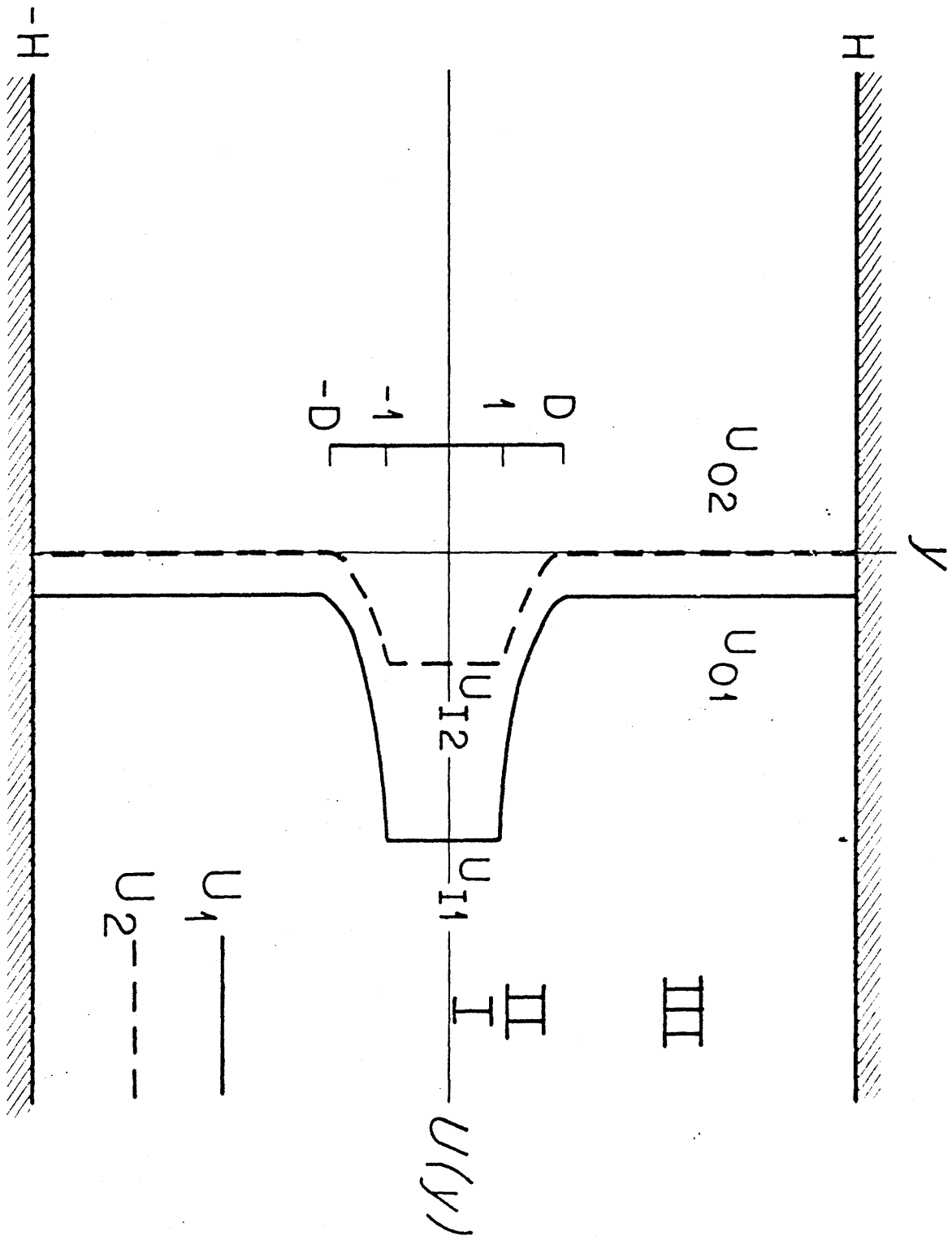
Figure 3.1.1

Baroclinic jet modelled with two layers and meridional regions of
uniform velocity or uniform potential vorticity.

$$U_1(y) = \frac{\beta^2}{2} + c_1 + c_2 y + c_3 \cosh \sqrt{2F}\, y + c_4 \sinh \sqrt{2F}\, y$$

$$(3.1.5)$$

$$U_2(y) = \frac{\beta^2}{2} + c_1 + c_2 y - c_3 \cosh \sqrt{2F}\, y - c_4 \sinh \sqrt{2F}\, y$$

where
$$c_1 = \frac{(U_{I1} + U_{I2})\, D - (U_{01} + U_{02})}{2\,(D-1)} + \frac{\beta D}{2}$$

$$c_2 = \frac{(U_{01} + U_{02})\, D - (U_{I1} + U_{I2})}{2\,(D-1)} - \frac{\beta(D-1)}{2}$$

$$c_3 = \frac{-(U_{01} - U_{02}) \sinh \sqrt{2F} + (U_{I1} - U_{I2}) \sinh \sqrt{2F}\, D}{2 \sinh \sqrt{2F}\,(D-1)}$$

$$c_4 = \frac{(U_{01} - U_{02}) \cosh \sqrt{2F} - (U_{I1} - U_{I2}) \cosh \sqrt{2F}\, D}{2 \sinh \sqrt{2F}\,(D-1)}$$

Note that if the upper and lower layer velocities are equal, this reduces to the same parabolic flow profile in both layers, as found in Chapter 2. Also, if the velocity in say, the lower layer, is the same in Regions I and III ($U_{In} = U_{on}$), there is still horizontal shear in Region II since the potential vorticity gradient is required to vanish there. Thus, the familiar two-layer baroclinic instabiity problem is only an exact limit of this problem if $D \gg 1$, eliminating Region II.

The problem to be solved then is

$$(U_n - c) \left(\frac{d^2 \phi_n}{dy^2} - k^2 \phi_n - (-1)^n F(\phi_2 - \phi_1) \right) + \frac{\partial \pi_n}{\partial y} \phi_n = 0; \quad n = 1, 2$$

in Regions I and III,

$$(3.1.6a)$$

and

$$(U_n-c)\left(\frac{d^2\phi_n}{dy^2} - k^2\phi_n - (-1)^n F(\phi_2 - \phi_1)\right) = 0; \quad n = 1, 2$$

in Region II. (3.1.6b)

The matching conditions on interface displacement and normal velocity at each profile break were given in Equations (2.2.2) and (2.2.3) for barotropic flows. These matching conditions are unaffected by baroclinicity and β: (3.1.3) can be written in displacement form:

$$\frac{d}{dy}\left\{(U_n-c)\frac{dG_n}{dy}\right\} + G_n\left\{(U_n-c)^2(-k^2-F) + \beta - (-1)^n F(U_1 - U_2)\right\}$$

(3.1.7)

$$+ G_n F(U_1-c)(U_2-c) = 0 .$$

Here G_n is the horizontal displacement of the interface between two regions of the flow, e.g.,

$$G_n = \frac{\phi_n}{U_n-c} .$$

If U_n has at most a simple discontinuity, then G_n and $(U_n-c)^2(dG_n/dy)$ must be continuous for (3.1.7) to make sense. Thus the matching conditions for the layer flows are identical with the matching conditions (2.2.2) and 2.2.3). They are applied at each profile break and in each layer, separately.

(3) Useful Theorems

The necessary conditions for instability are given by Pedlosky (1979) for two-layer flow on the β-plane. They are his equations (7.10.5) and (7.10.6):

$$c_i \sum_{n=1}^{2} \int_{-H}^{H} dy \; \frac{|\phi_n|^2}{|U_n-c|^2} \; \frac{\partial \pi_n}{\partial y} \;\; = \;\; 0$$

$$\sum_{n=1}^{2} \int_{-H}^{H} dy \left\{ U_n \; \frac{\partial \pi_n}{\partial y} \; \frac{|\phi_n|^2}{|U_n-c|^2} \right\} > \;\; 0$$

An effective potential vorticity gradient which includes contributions from the discontinuities in U and dU/dy was useful in showing if a barotropic flow was absolutely stable in Chapter 2. In barotropic flows in Chapter 2, the flow is stabilized by large β, because the flow in the shear zones is altered as β increases until the effective potential vorticity gradient is single-signed. This mimics the β-stabilization that occurs in continuous flow. The necessary conditions for two-layer flow with horizontal discontinuities in U(y) and/or dU/dy can be written in terms of this effective potential vorticity gradient, just as in chapter 2. The effective potential vorticity gradient is defined for each layer just as in equation (2.3.5):

$$\frac{\partial \hat{\pi}_n}{\partial y} \;\; = \;\; \frac{\partial \pi_n}{\partial y} \; - \; \left[\frac{dU_n}{dy} \right] \delta \; (y-y_0) \qquad (3.1.8a)$$

where [ ] indicates the jump in the bracketed quantity at $y = y_0$. The two-layer counterparts to (2.3.6) and (2.3.7), assuming that U is continuous but dU/dy is not, are

$$c_i \sum_{n=1}^{2} \int_{-H}^{H} dy \; \frac{|\phi_n|^2}{|U_n-c|^2} \; \frac{\partial \hat{\pi}_n}{\partial y} \;\;\; = \;\; 0$$

$$\qquad\qquad\qquad\qquad\qquad\qquad (3.1.8b)$$

$$\sum_{n=1}^{2} \int_{-H}^{H} dy \; \frac{|\phi_n|^2}{|U_n-c|^2} \; (U_n - c_r) \; \frac{\partial \hat{\pi}_n}{\partial y} \;\; > \;\; 0$$

In barotropic flow, stability depends only on the sign of the delta function contribution to the potential vorticity gradient. In two-layer flows, there are many different ways to satisfy the necessary conditions (3.1.8). The flow can be baroclinically unstable in Regions I or III if the vertical shear is large enough. The flow can be barotropically unstable in each layer if the potential vorticity gradient changes sign in that layer. A change in sign of the potential voticity gradient in a single layer can actually be due to the flow's baroclinicity since $\beta \pm F(U_1 - U_2)$ can change sign from Region I to Region III.

Figure 3.1.2 shows different possibilities for the potential vorticity gradient in each layer. This type of figure facilitates examination of the first necessary condition (3.1.8a). In the figures, it is arbitrarily assumed that the potential vorticity gradient, $\partial \pi / \partial y = \beta \pm F(U_1 - U_2)$, is positive in Region III and negative in Region I. Of course, for specific models considered in the chapter, these signs depend entirely on the relative sizes of β and $F(U_1 - U_2)$. The second necessary condition for instability should also be evaluated for each profile.

The semi-circle theorem, which limits the complex phase speed, is still given by (2.1.5). Howard's inflection point theorem, which predicts one neutral mode with neighboring unstable modes for each inflection point in a barotropic flow with $\beta = 0$, has not been extended to two-layer flow on the β-plane, although it seems safe to assume that the theorem holds for the barotropic instability of each layer taken by itself.

The focus here will be on the existence of radiating modes, just as in the previous chapter. The definition of radiating modes given in 2.4
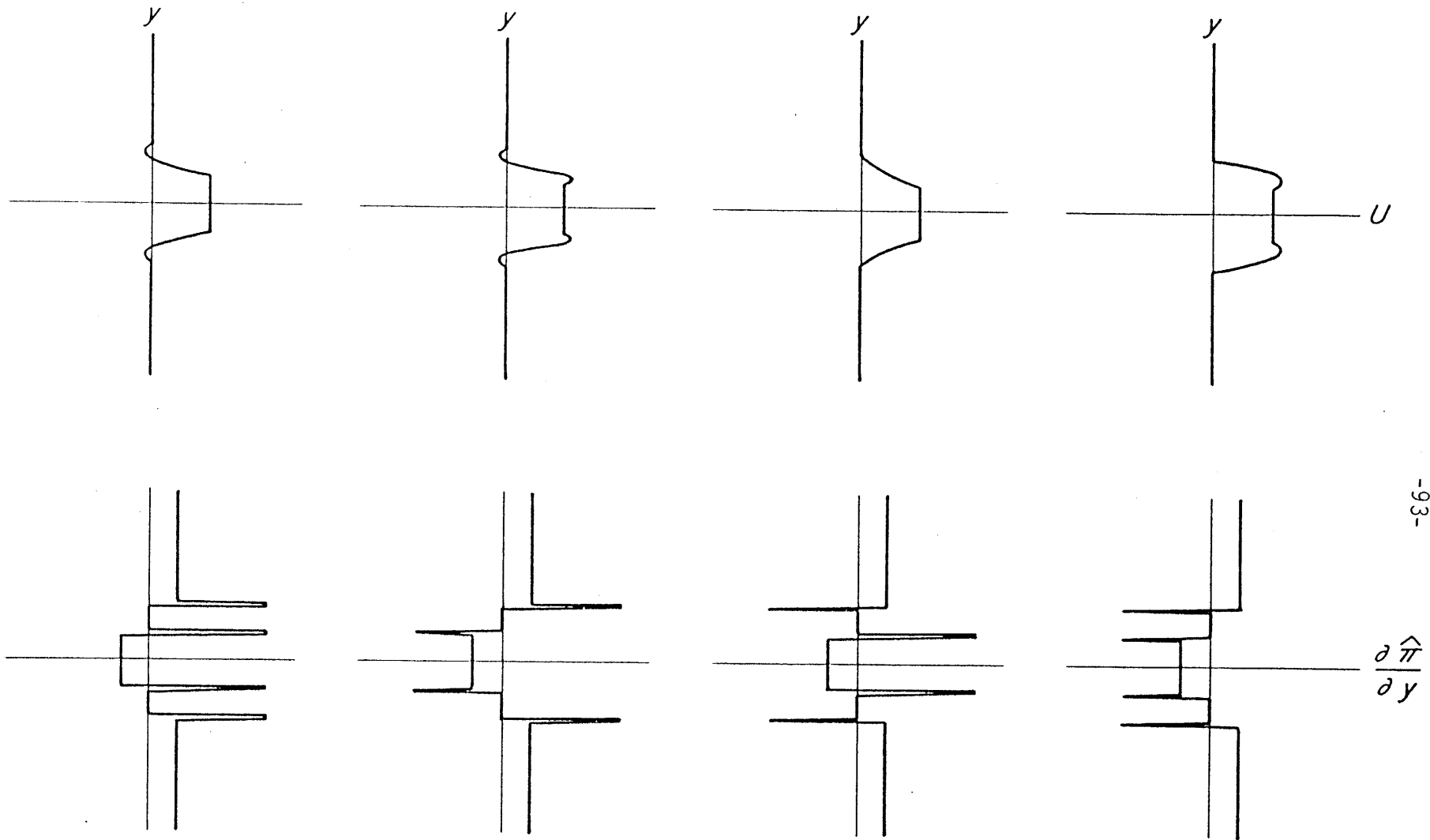
Figure 3.1.2   Velocity profile and potential vorticity gradient, modified by the contribution of the profile breaks to the term $(-U_{yy})$. Four different configurations for the velocity in the shear zone are shown, along with the resulting effective potential vorticity gradient. It is arbitrarily assumed here that $\partial\pi/\partial y$ is positive in Region III and negative in Region I.

is operative in this chapter also. The conditions for radiation are exactly the same: if the phase speed and wavenumber k of an instability match those of a free wave outside the jet, then the wave can be forced and the model is radiating.

(4) Energy Transfer

A point of interest in mixed barotropic-baroclinic flows is the source of energy for instabilities. Perturbation energy can come from either the horizontal shear or the horizontal temperature gradient (interface displacement between layers). The perturbation can feed on both the potential and kinetic energy, or it can feed on, as another example, just the mean flow potential energy and pass energy back to the mean flow kinetic energy (or vice versa). Evaluating the magnitudes and signs of the energy transfer and their dependence on the flow parameters may be useful in understanding the balances in real ocean currents.

The transfer of energy from the mean flow to the growing perturbations is accomplished by means of convergent, horizontal Reynolds stresses (which reduce the kinetic energy of the mean flow) and eddy heat fluxes (which reduce the horizontal temperature gradient). The presence of discontinuities in the mean flow and its horizontal shear may give rise to additional terms in the energy equation. A derivation of the perturbation energy equation for a flow with discontinuities in horizontal shear is given here. It is seen that there are no additional contributions to the eddy energy transfer due to the profile breaks, if the energy transfer is written in terms of the Reynolds stress and the horizontal shear of the mean flow.

The perturbation energy equation is obtained by multiplying the potential vorticity equation for each layer (3.1.1) by ϕ_n and the depth of the layer, adding the two layers' equations (to integrate in z) and then integrating over x and y. The summed and x-averaged energy equation is

$$\frac{\partial E(\phi)}{\partial t} - \frac{\partial}{\partial y}\left\{\overline{\phi_1 \left(\frac{\partial}{\partial t} + U_1 \frac{\partial}{\partial t}\right)\phi_{1y} + \phi_2 \left(\frac{\partial}{\partial t} + U_2 \frac{\partial}{\partial x}\right)\phi_{2y}}\right\} \qquad (3.1.9)$$

$$= \frac{dU_1}{dy} \overline{\phi_{1x}\phi_{1y}} + \frac{dU_2}{dy} \overline{\phi_{2x}\phi_{2y}} + F(U_1 - U_2) \overline{\phi_1\phi_{2x}}$$

where the overbar denotes the x-average. The averaged perturbation energy is

$$\overline{E(\phi)} = \frac{F}{2} \overline{(\phi_1 - \phi_2)^2} + \frac{1}{2} \sum_{n=1}^{2} \left\{\overline{(\phi_{nx})^2} + \overline{(\phi_{ny})^2}\right\}$$

For a continuous profile with boundary conditions of $\phi_{nx} = 0$ at $y = \pm H$ (the channel walls), integration of this equation in y eliminates the second bracketed term. With the introduction of discontinuities in U_n and U_{ny}, however, there may be contributions to this term at the discontinuities. Suppose there are discontinuities in U and dU/dy at $y = y_0$. Integrating the bracketed terms in (3.1.9) from one channel wall to the other yields

$$\left[\overline{\phi_1 \left(\frac{\partial}{\partial t} + U_1 \frac{\partial}{\partial x}\right)\phi_{1y} + \phi_2 \left(\frac{\partial}{\partial t} + U_2 \frac{\partial}{\partial x}\right)\phi_{2y}}\right]_{y = y_0} \qquad (3.1.10)$$

i.e., the jump in the bracketed quantity at $y = y_0$. The streamfunctions are expressed as normal mode solutions:

$$\phi_1 = \frac{\Phi_1(y) e^{ik(x-ct)} + *}{2}$$

$$\phi_2 = \frac{\Phi_2(y)\, e^{ik(x-ct)} + *}{2}$$

where "*" denotes complex conjugation. Then this jump is evaluated, using the pressure and velocity jump conditions for ϕ_1 and ϕ_2 at $y = y_0$ [equations (2.2.2) and (2.2.3)]. Denote the velocities north of the jump as U_n^+ and those south of it by U_n^-. Then (3.1.10) becomes, after integration in x and application of the matching conditions (2.2.2) and (2.2.3),

$$e^{2kc_i t} \frac{ik}{4} \sum_{n=1}^{2} |\Phi_n^+|^2 \; U_{ny}^+ \frac{(c-c^*)(U_1 - U_2)}{|U_1 - c|^2} + \Phi_n^{+*} \Phi_{ny}^+ \frac{(U_n^+ - c)}{U_n^+ - c^*} (U_n^+ - U_n^-) - *$$

(3.1.11)

This can be rewritten in delta function form:

$$e^{2kc_i t} \frac{ik}{4} \sum_{n=1}^{2} \int_{-H}^{H} dy \left\{ |\Phi_n^+|^2 \; U_{ny}^+ \frac{ic_i}{|U_1 - c|^2} + \Phi_n^{+*} \Phi_{ny}^+ \frac{(U_n^+ - c)}{U_n^+ - c^*} - * \right\} \cdot$$

$$(U_n^+ - U_n^-) \, \delta \, (y - y_0)$$

Thus (3.1.10) is like a delta function addition to the energy transfer term $(-\overline{u'v'})dU/dy$ in the perturbation energy equation. If $U_n^+ = U_n^-$, this term disappears because dU/dy no longer has "delta function" behavior at $y = y_0$. The integrated perturbation energy equation, when $U_n^+ = U_n^-$, is

$$\int_{-H}^{H} dy \, \frac{\overline{\partial E(\phi)}}{\partial t} = \int_{-H}^{H} dy \left\{ U_{1y} \overline{\phi_{1x}\phi_{1y}} + U_{2y} \overline{\phi_{2x}\phi_{2y}} + F(U_1 - U_2) \overline{\phi_1 \phi_{2x}} \right\} \quad (3.1.12)$$

This equation relates changes in perturbation energy to energy transfers

from the mean flow kinetic and potential energy. There are no additional transfers due to discontinuities in dU/dy, only due to discontinuities in U.

If, however, the first two terms on the right-hand side are integrated by parts in y and rewritten in terms of convergent Reynolds stresses, there will be contributions from the profile breaks. Thus, assuming that only dU/dy is discontinuous:

$$\int_{-H}^{H} dy \int_{-H}^{H} dy \left\{ \overline{U_{ny} \, \phi_{nx} \phi_{ny}} \right\} = -[\overline{U_n \, \phi_{nx} \phi_{ny}}]_{y=y_0} - \int_{-H}^{H} dy \; U_n \frac{\partial}{\partial y} (\overline{\phi_{nx} \phi_{ny}})$$

Rewriting ϕ in normal mode form, $\phi_n = {}_n(y)e^{ik(x-ct)}$ and applying the matching conditions (2.2.2) and (2.2.3) results in

$$\int_{-H}^{H} dy \; \frac{\partial E(\phi)}{\partial t} = \sum_{n=1}^{2} e^{2kc_i t} \; \frac{ikc_i}{4} \int_{-H}^{H} dy \left\{ \frac{U_n \, |\phi_n|^2}{|U_n - c|^2} (U_{ny}^- - U_{ny}^+) \, \delta(y-y_0) \right.$$

(3.1.13)

$$\left. - U_n \frac{\partial}{\partial y} (\phi_n \, \phi_{ny}^* - \phi_n^* \, \phi_{ny}) \right\} + e^{2kc_i t} \; \frac{ik}{4} \int_{-H}^{H} dy \; F(U_1 - U_2)(\phi_1 \, \phi_2^* + \phi_1^* \, \phi_2)$$

where the unsuperscripted U_n and ϕ_n are the continuous values of U_n and ϕ_n. This has been rewritten in delta function form. There is clearly a contribution to the convergent Reynolds stresses from the profile break because, even though U_n is continuous, $\overline{u'v'}$ is not continuous across the profile break. This effectively means that $U_n \frac{\partial}{\partial y} (\overline{u'v'})$ has a delta function contibution.

To measure the relative importance of baroclinic and barotropic transfers in specific models, the terms from the right-hand side of (3.1.12) will be plotted. The barotropic transfer terms will be non-zero only in Region II, where dU/dy is non-zero.

(5) The Problem

Now that the basic equation, the necessary conditions for instability, the semi-circle theorem, the radiation condition and the energy equations have been discussed, we can move on to actually solving the problem.

The potential vorticity equations for Regions I, II and III of Figure 3.1.1 are given in (3.1.6). <u>Only</u> symmetric solutions are sought. In Chapter 2, both symmetric and antisymmetric solutions for one-layer jets were obtained. While the varicose solutions were seen to be highly unstable, their growth rates were generally less than those of the sinuous mode. In the jet itself, the most unstable wave will probably dominate, so it is justified to omit the varicose mode for the near field. However, the notion that the most unstable waves will dominate in the finite amplitude field has been discarded in order to argue that the weakly growing, radiating modes may also be important, so it may not be altogether justified to discard the varicose modes.

In Regions I and III where the velocity is constant but different in the upper and lower layers, the solutions must satisfy (3.1.6a). Seeking solutions for the form $\phi_n = A_n e^{ry}$, the y dependence is:

$$r^2 = k^2 - \frac{\beta(U_1 + U_2 - 2c)}{2(U_1-c)(U_2-c)} + F + \frac{F(U_1 - U_2)^2}{2(U_1-c)(U_2-c)}$$

$$\pm \frac{1}{2(U_1-c)(U_2-c)} \left\{ \beta^2 (U_1 - U_2)^2 - 2\beta F (U_1 + U_2 - 2c)(U_1 - U_2)^2 \right.$$

$$\left. + F^2 [(U_1 - U_2)^2 + 2(U_1-c)(U_2-c)]^2 \right\}^{1/2}$$

(3.1.14)

The corresponding ratio of amplitudes in the upper and lower layers is

$$\frac{A_2}{A_1} = -\frac{(U_1-c)(r^2 - k^2 - F) + \beta + F(U_1 - U_2)}{F(U_1-c)}$$

Substituting for r^2

$$\frac{A_2}{A_1} = \frac{1}{2 R S F} \left\{ \beta U_S - F U_S (U_S + 2S) \right.$$

$$\left. \mp \sqrt{\beta^2 U_S^2 - 2\beta F (R + S) U_S^2 + F^2 (U_S^2 + 2 R S)^2} \right\} \tag{3.1.15}$$

where $R = U_1-c$, $S = U_2-c$ and $U_S = U_1-U_2$.

When the flow has no vertical shear ($U_1 = U_2$), the usual barotropic and baroclinic Rossby waves exist in the far field. The y e-folding scale, r^2, becomes

$$r^2 = \begin{cases} k^2 + 2 F - \dfrac{\beta}{U-c} \\ k^2 - \dfrac{\beta}{U-c} \end{cases}$$

and the amplitude ratio becomes

$$\frac{A_2}{A_1} = \begin{cases} -1 \\ 1 \end{cases}$$

When $\beta = 0$, r^2 reduces to

$$r^2 = \begin{cases} k^2 + F \dfrac{(U_1-c)^2 + (U_2-c)^2}{(U_1-c)(U_2-c)} \\ k^2 \end{cases} \tag{3.1.16}$$

and the corresponding amplitude ratio to

$$\frac{A_2}{A_1} = \begin{cases} \dfrac{U_1-c}{U_2-c} \\ -\dfrac{U_2-c}{U_1-c} \end{cases}$$

These are the solutions of the usual f-plane baroclinic instability problem. However, the second root, with $r = k$, does not usually appear when the flow has no horizontal shear since that part of the solution has zero amplitude when the flow has no horizontal shear. This root, however, must be included if the basic flow is y-dependent.

If, in addition to letting $\beta = 0$, we let the top and bottom layer velocities be equal so that, although the basic flow has no vertical structure, the disturbance has two vertical modes, we obtain

$$r^2 = \begin{cases} k^2 + 2F \\ k^2 \end{cases} \quad \text{with} \quad \frac{A_2}{A_1} = \begin{cases} 1 \\ -1 \end{cases} \tag{3.1.17}$$

The first solution is the baroclinic mode and the second the barotropic mode. These are the solutions when the basic potential vorticity gradient is zero and are therefore the solutions to the equation in the shear zone (Region II) where the governing equations are (3.1.6b).

The total solution is then, for Regions I, II and III

$$\Phi_1 = a_1 e^{m_1 y} + a_2 e^{-m_1 y} + a_3 e^{m_2 y} + a_4 e^{-m_2 y}$$

I. $\tag{3.1.18a}$

$$\Phi_2 = d_1 (a_1 e^{m_1 y} + a_2 e^{-m_1 y}) + d_2 (a_3 e^{m_2 y} + a_4 e^{-m_2 y})$$

where m_1 and m_2 are given by Equation (3.1.14) and d_1 and d_2 are the corresponding ratios, $\frac{A_2}{A_1}$, from Equation (3.1.15), both for $U_n = U_{In}$;

$$\Phi_1 = b_1 e^{ky} + b_2 e^{-ky} + b_3 e^{\ell y} + b_4 e^{-\ell y}$$

II. (3.1.18b)

$$\Phi_2 = b_1 e^{ky} + b_2 e^{-ky} - b_3 e^{\ell y} - b_4 e^{-\ell y}$$

where $\ell = \sqrt{k^2 + 2F}$, as given by (3.1.16);

$$\Phi_1 = c_1 e^{\ell_1 y} + c_2 e^{-\ell_1 y} + c_3 e^{\ell_2 y} + c_4 e^{-\ell_2 y}$$

III. (3.1.18c)

$$\Phi_2 = f_1 (c_1 e^{\ell_1 y} + c_2 e^{-\ell_1 y}) + f_2 (c_3 e^{\ell_2 y} + c_4 e^{-\ell_2 y})$$

where ℓ_1 and ℓ_2 and f_1 and f_2 are given by Equations (3.1.14) and (3.1.15), both for $U_n = U_{on}$. Application of the boundary conditions and matching conditions then allows evaluation of all but one of the coefficients a_n, b_n and c_n and yields the dispersion relation, $c(k)$. The dispersion relation is quite long and is written in full in the Appendix.

3.2 Solutions

This section describes the behavior of the solutions (3.1.18) for specific flows. For background, the solutions for a one-layer jet where the only energy source is the horizontal shear were described in Chapter II. In this chapter, instability of two-layer flow in a channel with no horizontal shear is reviewed, since it is anticipated that two-layer jet solutions will include modes due to both horizontal and vertical shear. Instability due to vertical shear in the jet will be similar to baro-

clinic instability of meridionally uniform flow in a channel. Solutions

for various jets follow: (1) eastward and westward jets with vertical

shear in the jet only (Regions I and II); (2) eastward jet in the upper

layer and westward jet in the lower layer, and no vertical shear in

Region III; (3) eastward jet in the upper layer, quiescent lower layer

and positive vertical shear in Region III; (4) eastward jet in the upper

layer, quiescent lower layer and negative vertical shear in Region III.

A discussion of all results follows, summarizing the types of unstable

modes, the conditions under which the instabilities radiate and the

vertical and meridional decay scales of the instabilties.

    (a) Two-Layer Baroclinic Instability in a Channel with No Horizon-
           tal Shear (a review).

The problem of the linear stability of a two-layer flow with ver-

tical shear and no horizontal shear was formulated by Phillips (1954) and

further discussed by Pedlosky (1964). A treatment is found in Pedlosky

(1979). The channel used in these models is roughly simulated by the jet

of the models discussed in this chapter: the jet acts as a waveguide with

evanescent solutions outside for all trapped instabilities. The disper-

sion relation for two-layer, baroclinic instability is [c.f. Pedlosky's

(1979) equation (7.11.13)]:

$$c = \frac{U_1 + U_2}{2} - \frac{\beta(K^2 + F)}{K^2(K^2 + 2F)} \pm \frac{\sqrt{4\beta^2 F^2 - K^4 U_3^2 (4F^2 - K^4)}}{2K^2(K^2 + 2F)} \qquad (3.2.1)$$

where it has been assumed that the layer depths are equal and K^2 is the

total wavenumber, $K^2 = k^2 + \ell^2$, and $\ell_j = (j+1/2)\pi/W$, where W is the half-

width of the channel. The stability diagram in the β-k plane for different choices of W is shown in Figure 3.2.1. The vertical shear is fixed at $U_S = 1$ (i.e., scaling the velocities by the total shear), and the stratification parameter F is fixed at 5 while β and k are allowed to vary. According to the necessary conditions for instability, the flow can only be unstable if β is less than the critical value $\beta_c = F U_S$. For this choice of parameters, $\beta_c = 5$. Only the first two cross-channel modes are unstable for the choices of W used here. The first mode is unstable whenever β is less than β_c. The phase speed of the instabilities are all 1/2 at $\beta = 0$. As $\beta > \beta_c$, the phase speeds decrease and may become more negative than the minimum flow speed.

(b) Eastward and Westward Jets With Vertical Shear in the Jet and
        No Vertical Shear Outside the Jet.

Within this category of jets, there are many variations to explore, although only a few relevant examples will be given. Looking at Figure 3.1.1 and Equations (3.1.6), we see that there are a large number of parameters which can be varied. These parameters are H (channel half-width), D [where (D-1) is the shear zone width], F, U_{I2}, U_{01}, U_{02}, β and k. The channel width was set at ∞ for all jets treated in this section. In Section 3.4, the inclusion of boundaries is seen to have a marked effect on radiating modes which are able to sense the boundary, setting up standing waves. The shear zone width was not varied a great deal: widening the shear zone stabilizes the flow with respect to barotropic instability. The measure of stratification, F, was also not varied much: increasing F (i.e, decreasing the Rossby radius with respect to the jet width) has the
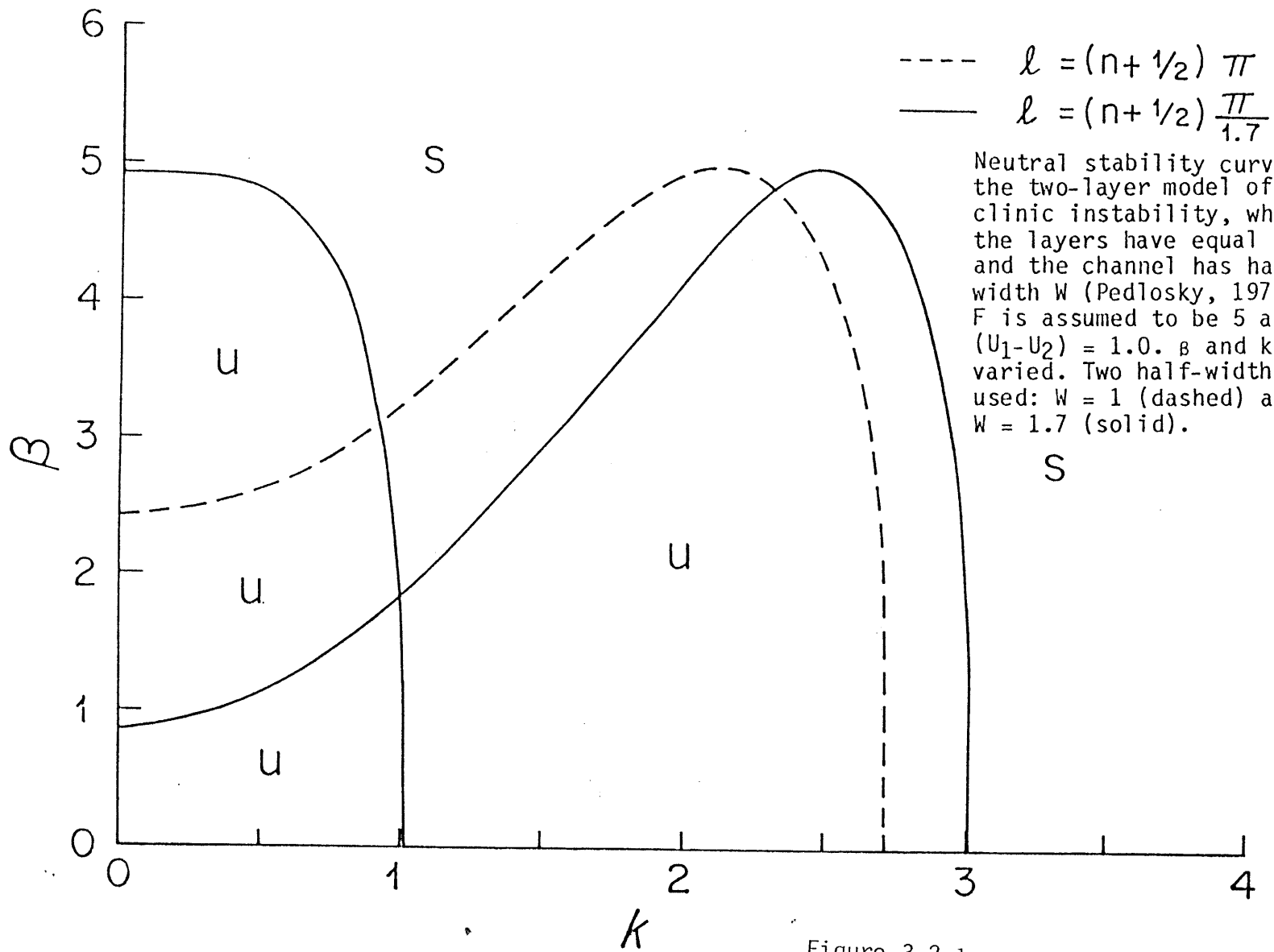
S

u

u

u

u

S

$\ell = (n + \frac{1}{2})\,\pi$

$\ell = (n + \frac{1}{2})\,\dfrac{\pi}{1.7}$

Neutral stability curves for the two-layer model of baro-clinic instability, where the layers have equal depths and the channel has half-width W (Pedlosky, 1979). F is assumed to be 5 and $(U_1 - U_2) = 1.0$. β and k are varied. Two half-widths are used: W = 1 (dashed) and W = 1.7 (solid).

β

k

Figure 3.2.1

obvious effects of increasing β_c [see (3.2.1)] and increasing the number of cross-jet, baroclinically unstable modes. There is a discussion of the effects of changing H, D and F at the end of this chapter.

The relative velocities in the profile can be shifted around and this section of the chapter is organized according to such changes. Once the profile is set, β and k are varied freely. Both positive and negative values of β are explored. Because $\beta = \beta^*L^2/U$, negative β is equivalent to westward flow.

The first example is the profile

$$U_{I1} = 1$$
$$U_{I2} = .5$$
$$U_{01} = 0$$
$$U_{02} = 0$$

$$D = 1.7$$
$$F = 5$$
$$H \rightarrow \infty$$

$$(3.2.2)$$

The profile is shown in Figure 3.2.2a with $\beta = 1$. [The flow in the shear zones is given by (3.1.5)]. The potential vorticity gradient is shown in Figure 3.2.2b. The first step is to find the values of β for which the necessary conditions for instability (3.1.8) are satisfied. The first necessary condition is broken down as follows: (1) for what β's does $\partial\hat{\pi}_1/\partial y$ change sign; (2) for what β's does $\partial\hat{\pi}_2/\partial y$ change sign; (3) for what β's are $\partial\pi_1/\partial y$ and $\partial\pi_2/\partial y$ in Region I of opposite sign; (4) for what β's are $\partial\pi_1/\partial y$ and $\partial\pi_2/\partial y$ in Region III of opposite sign; and (5) for what β's does $\partial\pi_n/\partial y$ change sign laterally because of the baroclinic term $F(U_1-U_2)$. We will call instabilities due to (1) and (2) <u>horizontal shear</u> instabil-
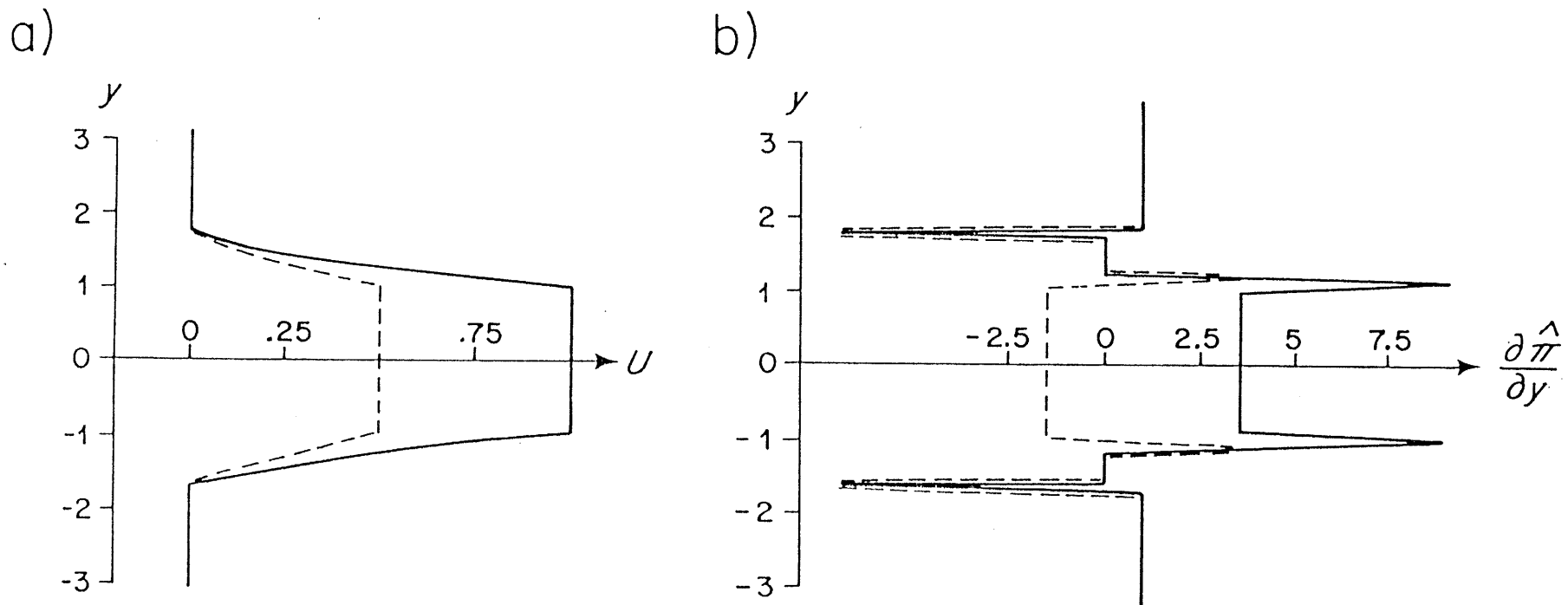
a) and b) figure axes

Figure 3.2.2

(a) U(y) as given by (3.2.2) and (b) $\partial\hat{\pi}/\partial y$, the effective potential vorticity gradient (3.1.8).

ities of the upper and lower layers, respectively; instabilities due to (3) and (4) will be called <u>vertical shear</u> instabilities of Regions I and III; instabilities due to (5) will be called <u>mixed</u> instabilities since the change in sign of $\partial \pi / \partial y$ with latitude is due to the change in vertical shear with latitude.

Note that the distinction between modes is not made on the basis of the dominant energy transfer, but rather on the basis of the parameter range in which they occur. Modes which are classified together also have similar-looking dispersion relations and characteristic eigenfunction structures. The dominant energy source for, say, the horizontal shear mode may in fact be the potential energy. This classification of modes is different from that of other authors (e.g., Hart, 1974; Holland and Haidvogel, 1980).

The types of instability which might occur for profile (3.2.2) at $F = 5$ are (1) horizontal shear instability in the upper layer for $-5.35 < \beta < 3.55$; (2) horizontal shear instability in the lower layer for $- .75 < \beta < 2.57$; (3) vertical shear instability in the central jet for $- 2.5 < \beta < 2.5$; (4) no vertical shear instability outside the jet since there is no vertical shear there; and (5) mixed instability in the lower layer when $0 < \beta < 2.5$ and mixed instability in the upper layer when $-2.5 < \beta < 0$.

Radiation will probably be very difficult when $\beta > 0$ since the phase speeds of the instabilities will generally be more eastward than the free wave phase speeds in Region III. It could, however, still be <u>possible</u> because of the effect of β on the semicircle theorem (2.1.5a) and because there is slight westward flow in the shear zone of the lower layer for

positive β because of the way the profile was constructed there. While barotropic instabilities cannot have contiguous neutral solutions with negative phase speeds according to Tung (1981) and therefore cannot radiate, baroclinic instabilities demonstrably have contiguous solutions with negative phase speeds (Pedlosky, 1964; Garcia and Norscini, 1970). On the other hand, radiation may occur readily for westward ($\beta>0$) jets since the phase speeds of all unstable modes will be westward with respect to the far field.

The stability diagram for both the eastward and the westward jet (i.e., positive and negative β) is shown in Figure 3.2.3. There are two overlaying diagrams shown to reduce confusion. At positive β, there are three obvious modes, labelled 1, 2 and 3. Using the necessary conditions for instability as a guide, these can be identified as the upper layer horizontal shear mode (β_c = 3.55), and two vertical shear modes of the central jet (β_c = 2.5). The similarity between the shape of the stability diagram for Mode 1 and the stability diagram for the barotropic jet (Figure 2.6.7) is striking. The stability curves for Modes 2 and 3 are very similar to the stability curves for the two cross-channel baroclinic instability modes of Figure 3.2.1: Mode 3 is identified as the gravest mode and Mode 2 as the next lowest mode of a "channel" whose apparent width is about the full width of the jet, including the shear zones. Dispersion relations $c_r(k)$ and $c_i(k)$ are shown in Figure 3.2.4 for β = 1. They are separated into the diagrams just as Figure 3.2.3 is. Again, identification of Mode 2 as a horizontal shear mode and Modes 2 and 3 as vertical shear modes is made: the phase speeds of the vertical

Neutral stability curves in the β-k plane for the profile (3.2.2).
Here F = 5 and D = 1.7. The plane extends to negative β: an east-
ward jet has positive β and a westward jet has negative β. The solid
curves are c_i = 0, the dashed curves ℓ_i = ℓ_r. The dot-dash curves
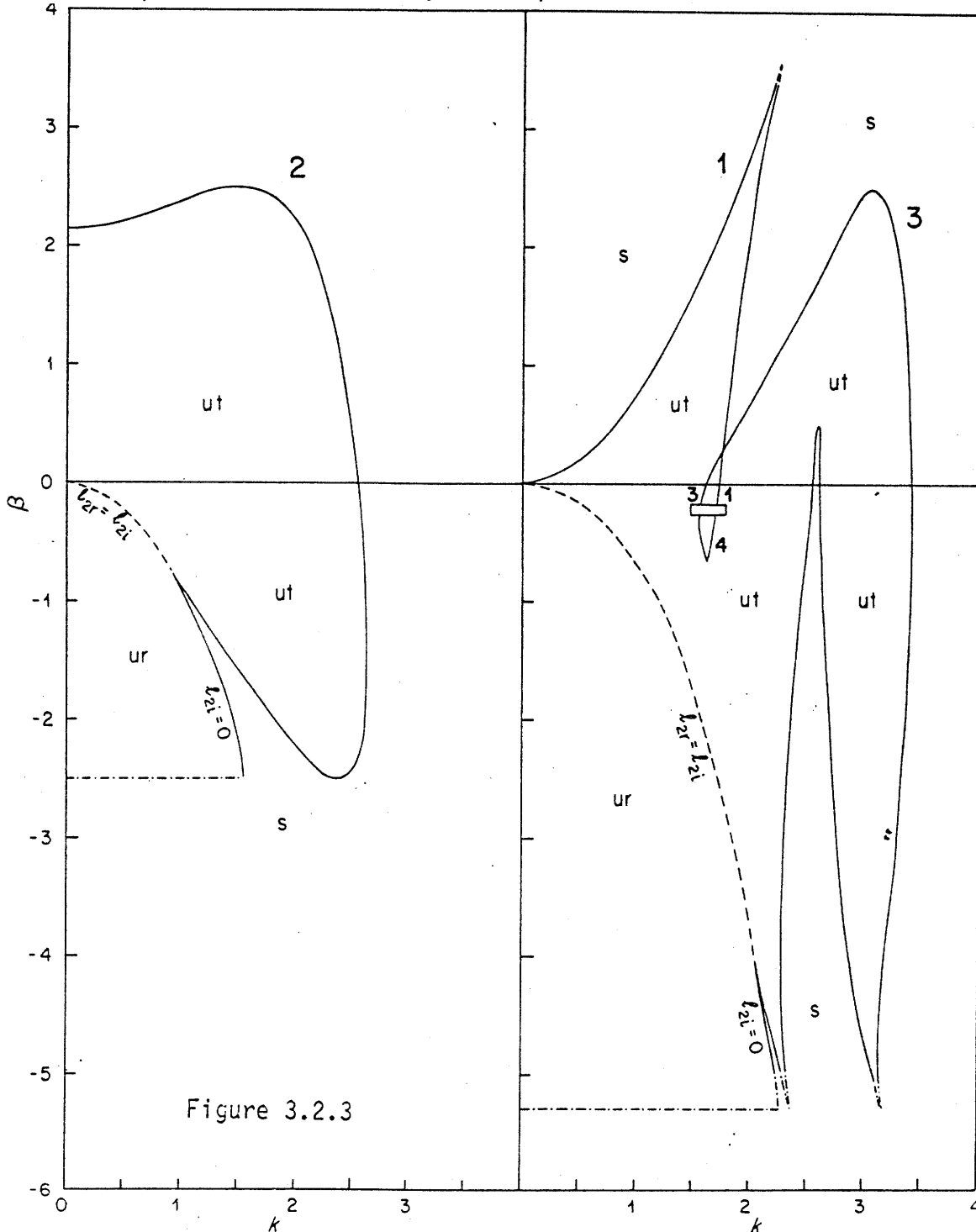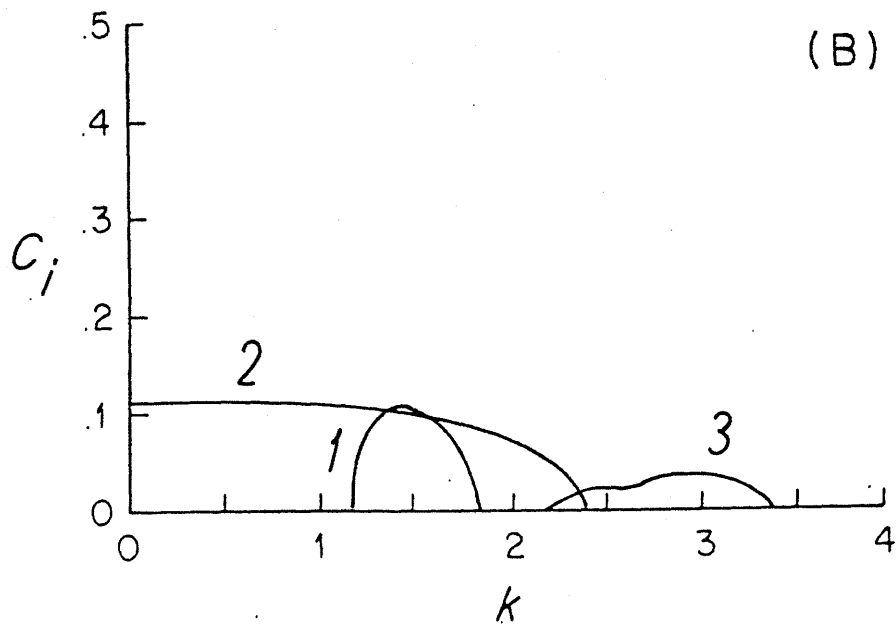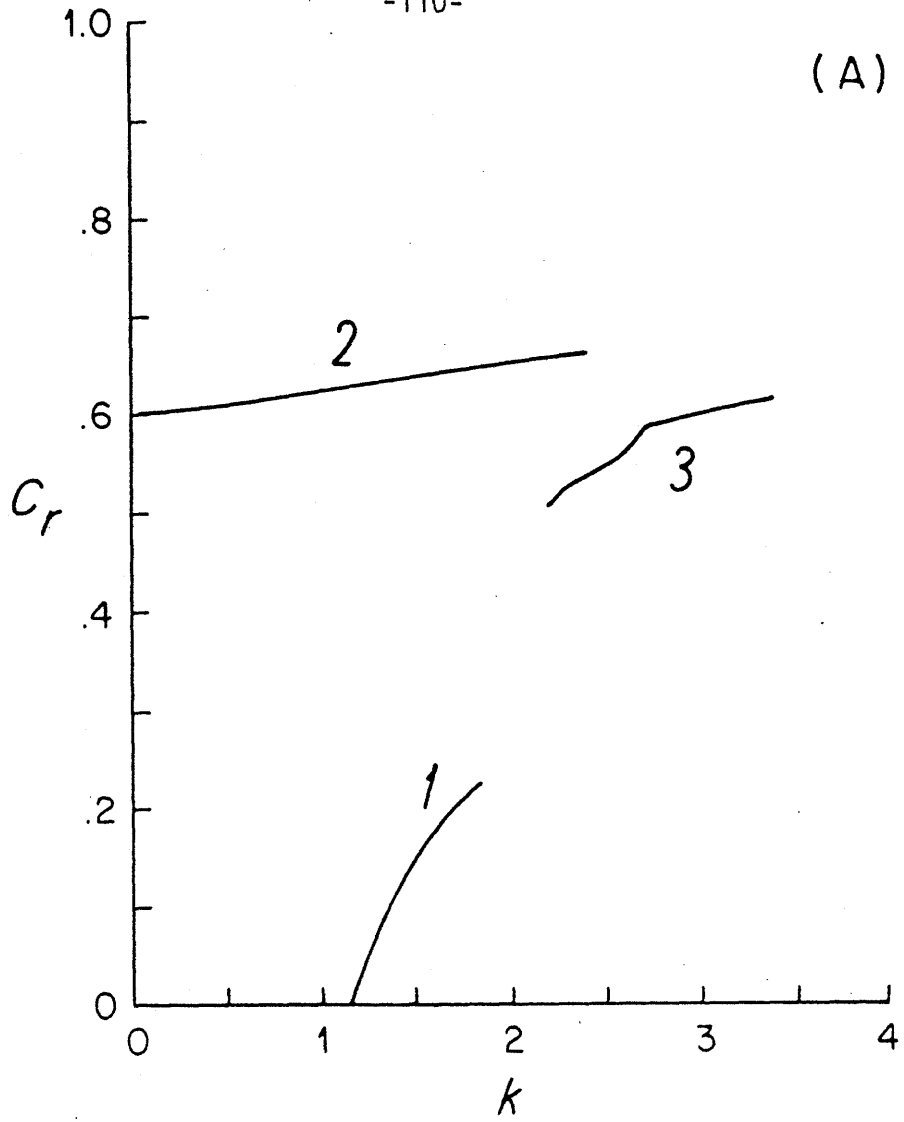are also c_i=0, but based on only a few points.

Figure 3.2.3

S = stable; ut = trapped instability; ur = radiating instability.
There are three modes at β·0 shown in two diagrams: (a) longwave,
vertical shear mode (2) and (b) upper layer, horizontal shear mode
(1) and shortwave, vertical shear mode (3). For β<0, Modes 1 and
3 become the upper layer horizontal shear mode.

(A)

(B)

Figure 3.2.4

For the flow in Figure 3.2.2 at $B = 1$: (a) $c_r(k)$ and (b) $c_i(k)$. Modes are labelled as in Figure 3.2.3.

shear modes are large, nearly equal to the vertically-averaged velocity in the jet center, while the phase speed for the horizontal shear mode is much lower and closely resembles the dispersion relation for the barotropic jet (Figure 2.6.7). All phase speeds and growth rates decrease to zero as β increases. The kinetic and potential energy transfers are shown in Figure 3.2.5, also for $\beta = 1$. Mode 1 is the only mode in which barotropic instability plays a significant role, with input of kinetic energy in both layers. Baroclinic instability also accounts for a fraction of Mode 1's energy. On the other hand, Modes 2 and 3 rely almost entirely on baroclinic instability for energy. Thus, the dominant instability in each mode is in keeping with its identification as a horizontal or vertical shear mode.

All disturbances for $\beta > 0$ are trapped to the jet: their phase speeds are always eastward with respect to the flow in the far field (Region III) and they cannot satisfy the phase speed condition. An example of an eigenfunction for each mode is shown in Figure 3.2.6.

When β is negative, the unstable modes can again be identified as horizontal and vertical shear modes, based on the necessary conditions for instability. In addition, because the phase speed condition can now be satisifed since the jet is westward with respect to the far field, both trapped and radiating modes are obtained.

Mode 2 is the simplest mode to describe so we begin with it: there are two distinct regions of instability in the β-k plane for $\beta < 0$, one marked "ur", meaning that the unstable waves are radiating and the other marked "ut", for trapped instabilities. Both parts of the mode are iden-

(A)

$K.E.$

1U

1L

2

3U

3L

k

(B)

$P.E.$

2

3

1

k

For the flow in Figure 3.2.2 at $\beta = 1$:
(a) kinetic energy transfer in the upper (U)
and lower (L) layers and (b) potential energy
transfer to the perturbations. The total energy
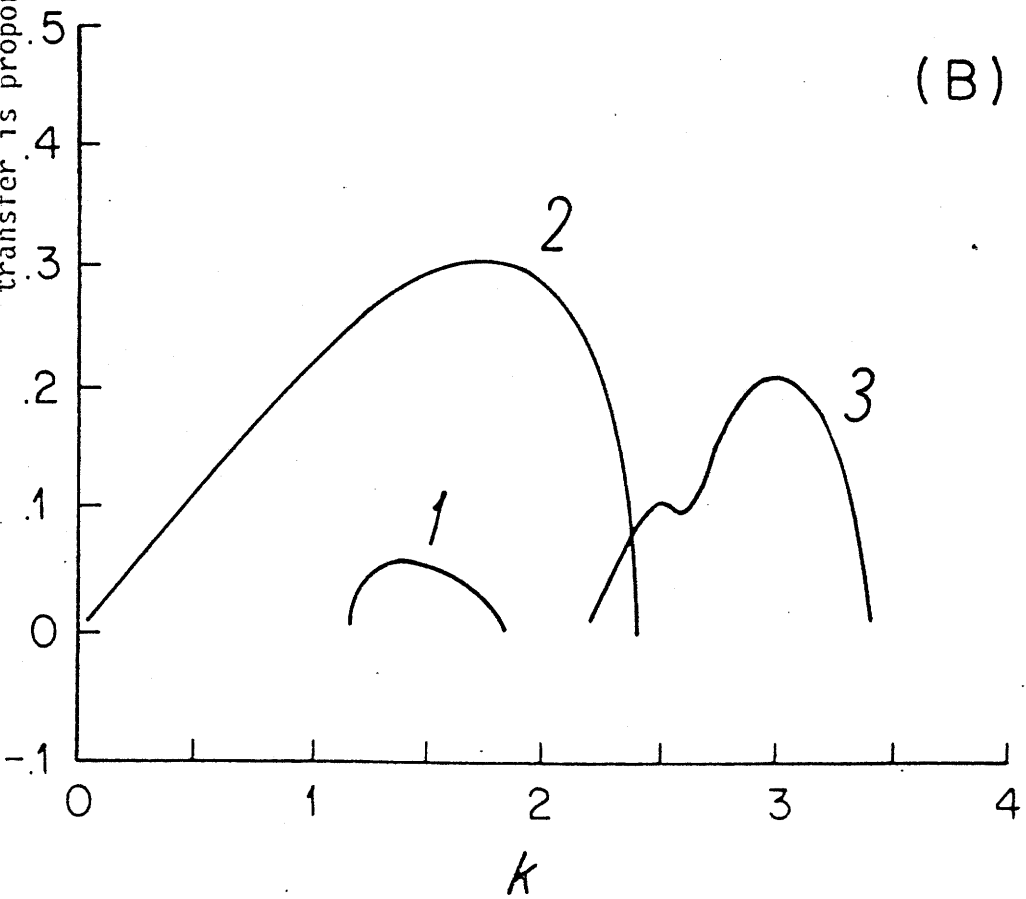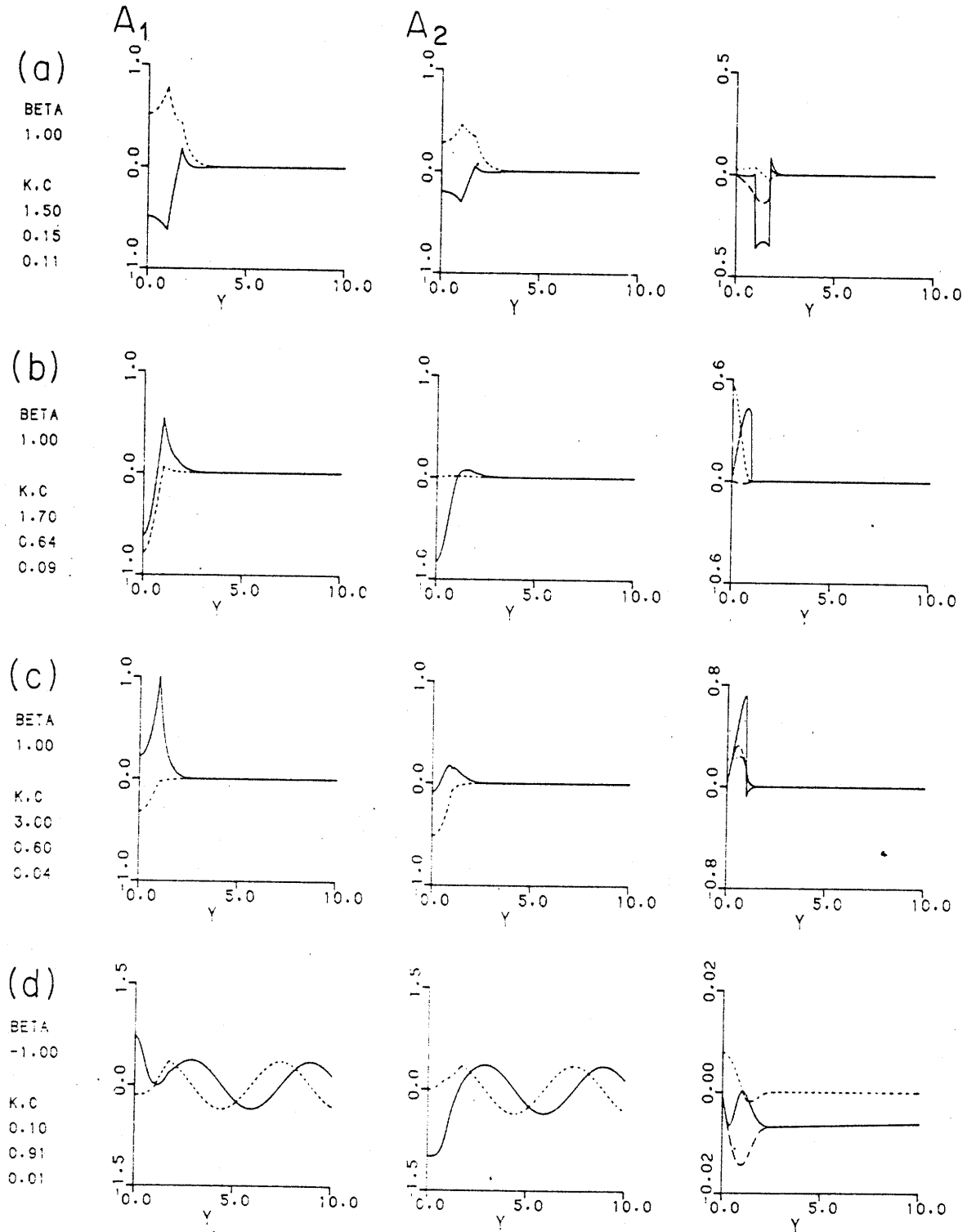transfer is proportional to the growth rate, kc_i.
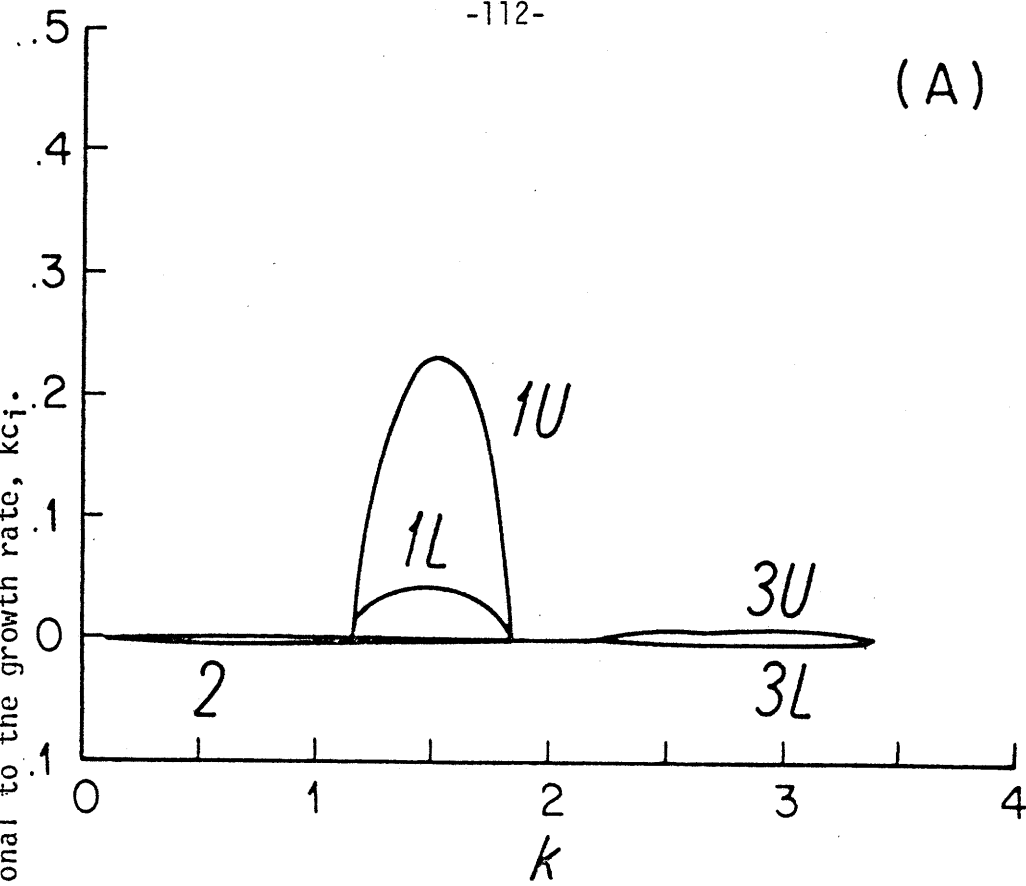
Figure 3.2.5

Figure 3.2.6

Eigenfunctions for each mode of Figure 3.2.3. The wavenumber k, c_r and c_i are listed at the left. (a) Horizontal shear mode, (b) longwave vertical shear mode, (c) shortwave vertical shear mode, and (d) radiating longwave mode.

tified as vertical shear modes because their β_c = -2.5. For -.8 < β < 0,
the two regions are separated from one another by the curve ℓ_{2i} = ℓ_{2r}.
To the left of this curve, ℓ_{2i} > ℓ_{2r} and the disturbances have wavelike
behavior in the meridional direction. For β < -.8, the radiating modes are
separated from the trapped modes by a set of stable waves. The curve of neu-
tral stability (c_i = 0) for the radiating modes is also the curve ℓ_{2i} = 0.
These points are illustrated in Figure 3.2.7 where c(k) for β = -1 is plot-
ted and in Figure 3.2.8 where ℓ_1(k) and ℓ_2(k) for β = -1 are plotted. The
radiating modes clearly have lower growth rates than the trapped modes.
While ℓ_1 is almost completely real (so this part of the solution in the
far field is trapped), ℓ_2 is mainly imaginary for the radiating modes
and mainly real for the trapped modes. The radiating modes thus have very
large decay scales compared with the trapped modes. The y-wavenumber of
the radiating modes is Im (ℓ_2): this is maximum at k = 0 and decreases
to 0 at the neutral curve for the radiating modes. We see in the stabil-
ity diagram, Figure 3.2.3, that the entire region of the β-k plane to the
left of the ℓ_{2i} = 0 curve is filled with unstable radiating modes, which
are stabilized only when β = -2.5. The conclusion is that radiating modes
exist everywhere in the β-k plane where Rossby waves exist: rather than
being fundamental unstable modes of the jet itself which just happed to
satisfy the phase speed condition, these modes are really destabilized
Rossby waves.

The Rossby wave dispersion relation at β = -1 for the far field
when there is no vertical shear there is pictured in Figure 3.2.7c where
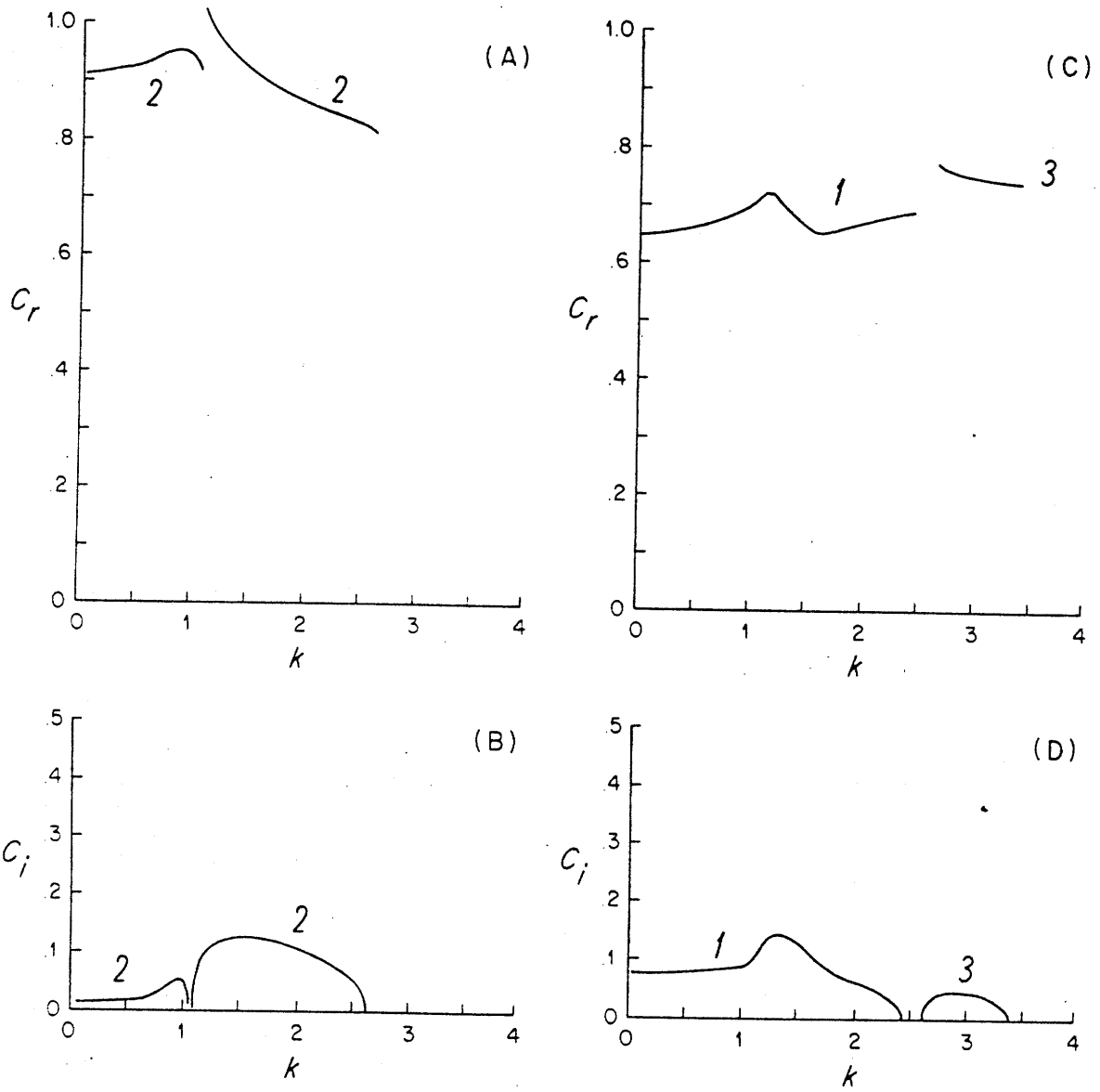c(k) for ℓ = 0 and $\ell \to \infty$ of both the baroclinic and barotropic modes is

Figure 3.2.7

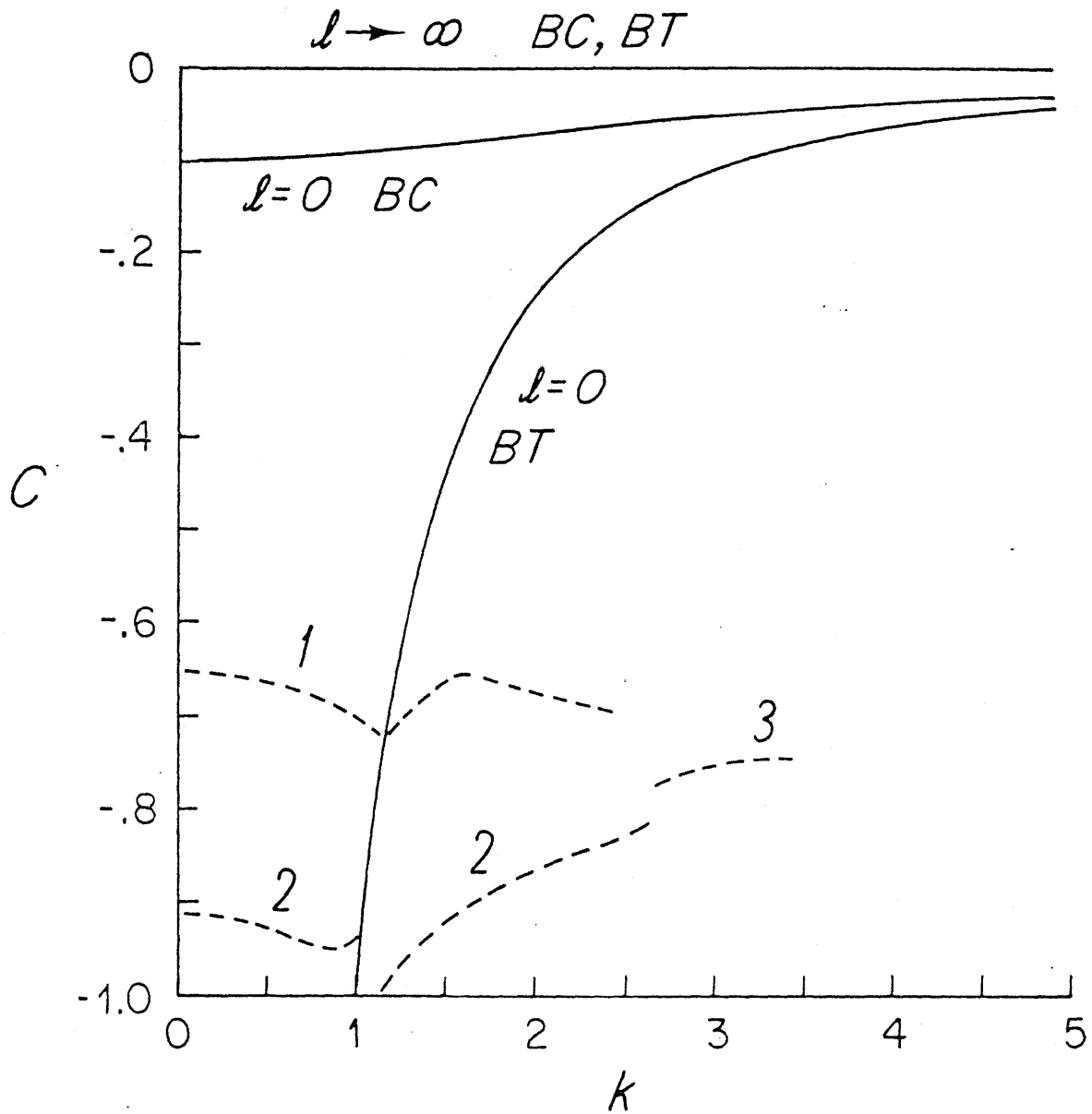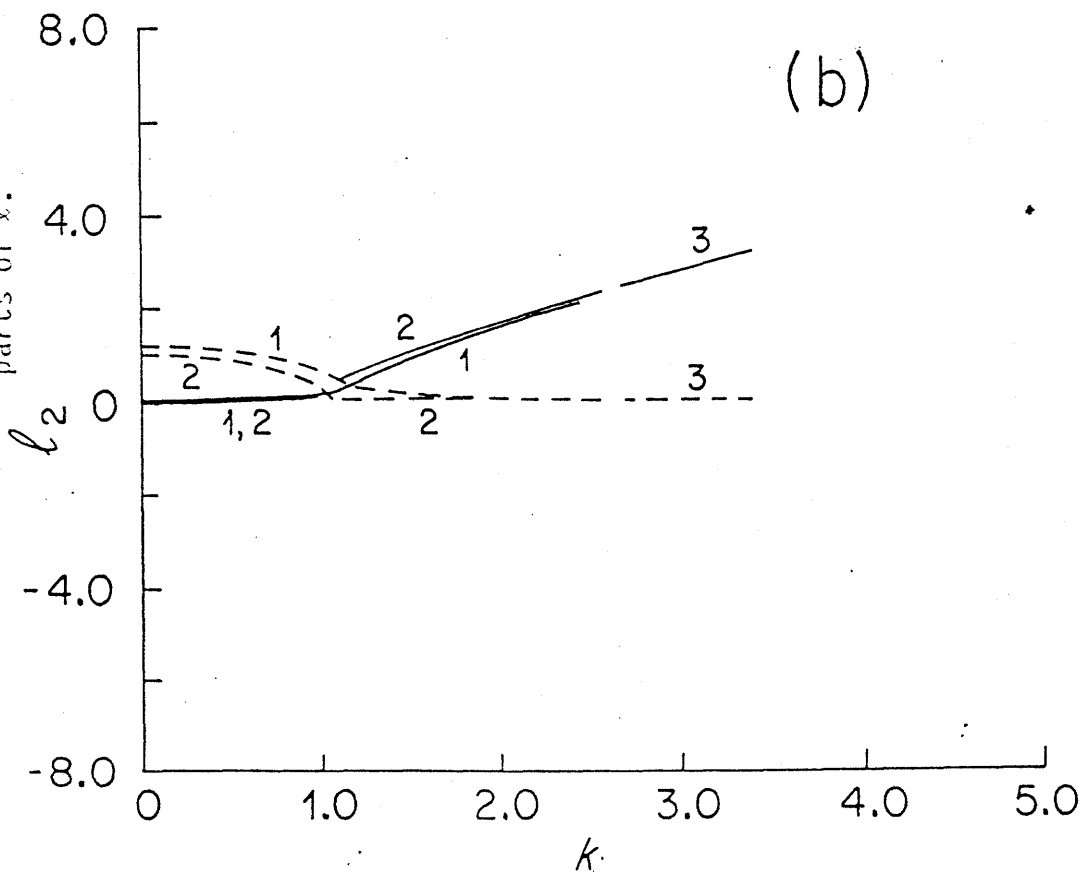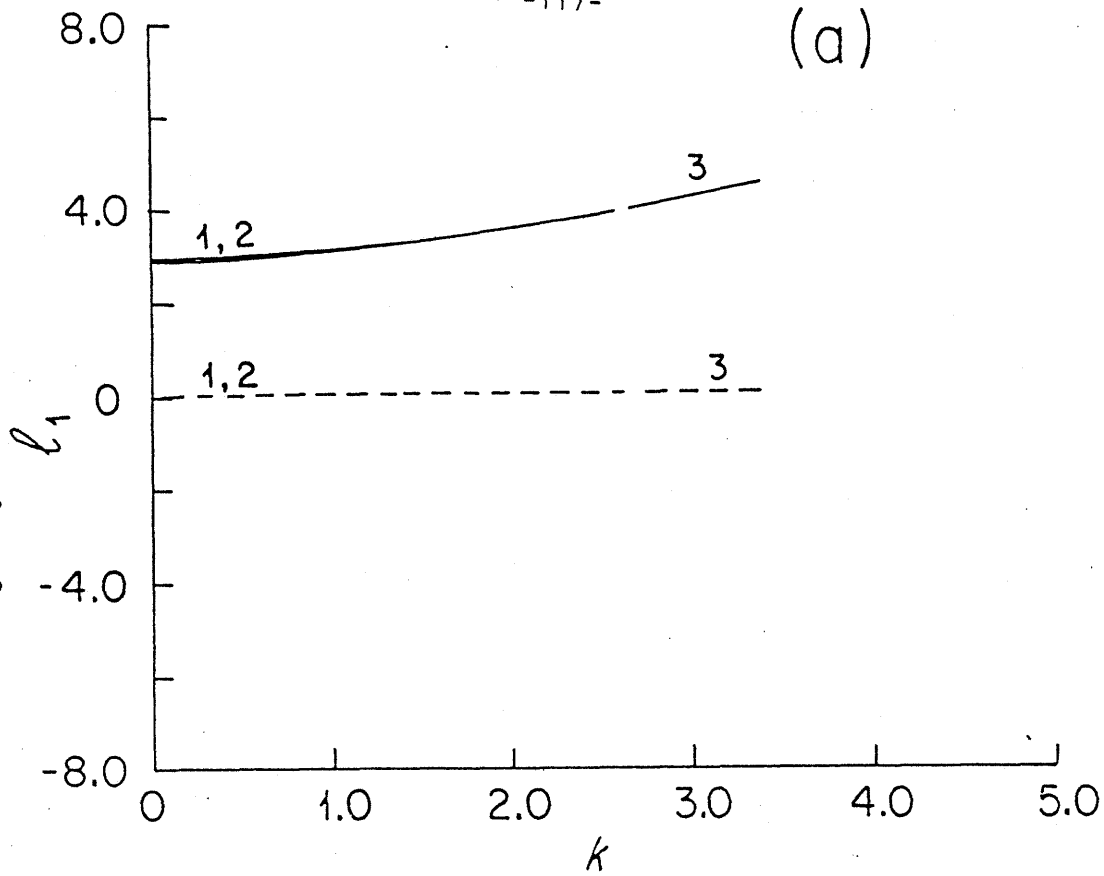For the flow of Figure 3.2.2 at ß = -1: (a), (c) $c_r(k)$ and (b), (d) $c_i(k)$.

Figure 3.2.7 (e)

Barotropic (BT) and baroclinic (BC Rossby wave dispersion relations
ε=1 for l = 0 and l → ∞. The dashed curves are c_r from (a),
rescaled with U = -1.

(a)

(b)

For the flow of Figure 3.2.2 at $\beta = -1$: (a) $\nu_1(k)$ and (b) $\nu_2(k)$. The solid curves are the real and the dashed curves the imaginary parts of ν.

Figure 3.2.8

plotted. No Rossby waves exist to the right of the $\ell = 0$ curve for the barotropic mode. In order for there to be radiation, c and k must fall within the $\ell = 0$ curve. This approach to finding the ranges of c and k where radiating instabilites can occur was used by Pedlosky (1976).

The radiating modes for the westward jet have phase speeds and zonal wavenumbers which fall in the right range for radiation on this diagram. Superimposed on the Rossby wave dispersion relations are the dispersion relations of the unstable modes at $\beta = -1$. Stability for the radiating modes occurs precisely where $\ell = 0$: beyond this point, no Rossby waves exist. Only the barotropic Rossby wave is excited by this jet.

Modes 1 and 3 have much more complicated behavior at negative β than Mode 2. First of all, it appears that Mode 3 loses its identity as a vertical shear mode: all instabilities associated with Modes 1 and 3 cutoff at the β_c of the upper layer horizontal shear mode when β is negative. At negative β, there are radiating and trapped instabilities just as for Mode 2. The same explanations apply: the entire region to the left of the dashed curve, $\ell_{2i} = \ell_{2r}$, and the solid curve $\ell_{2i} = c_i = 0$ is filled with destabilized Rossby waves, now associated with the horizontal shear of the upper layer. Notice that for many wavenumbers there are <u>two</u> destabilized Rossby waves (with different C and ℓ_2), one associated with the central jet vertical shear and the other with the upper layer horizontal shear. The energetics of all modes at $\beta = -1$ are shown in Figure 3.2.9. All modes except Mode 1 are dominated by baroclinic instability: note that this is also true of Mode 3, whose stability diagram identifies it as a "horizontal shear" mode.

(A)

K.E.

1U

2U 1L 2U

3U

2L 2L

3L

(B)

P.E.

2

3

2

1

Figure 3.2.9 For the flow in Figure 3.2.2 at β = -1: (a) kinetic energy transfer and (b) potential energy transfer to the perturbations.
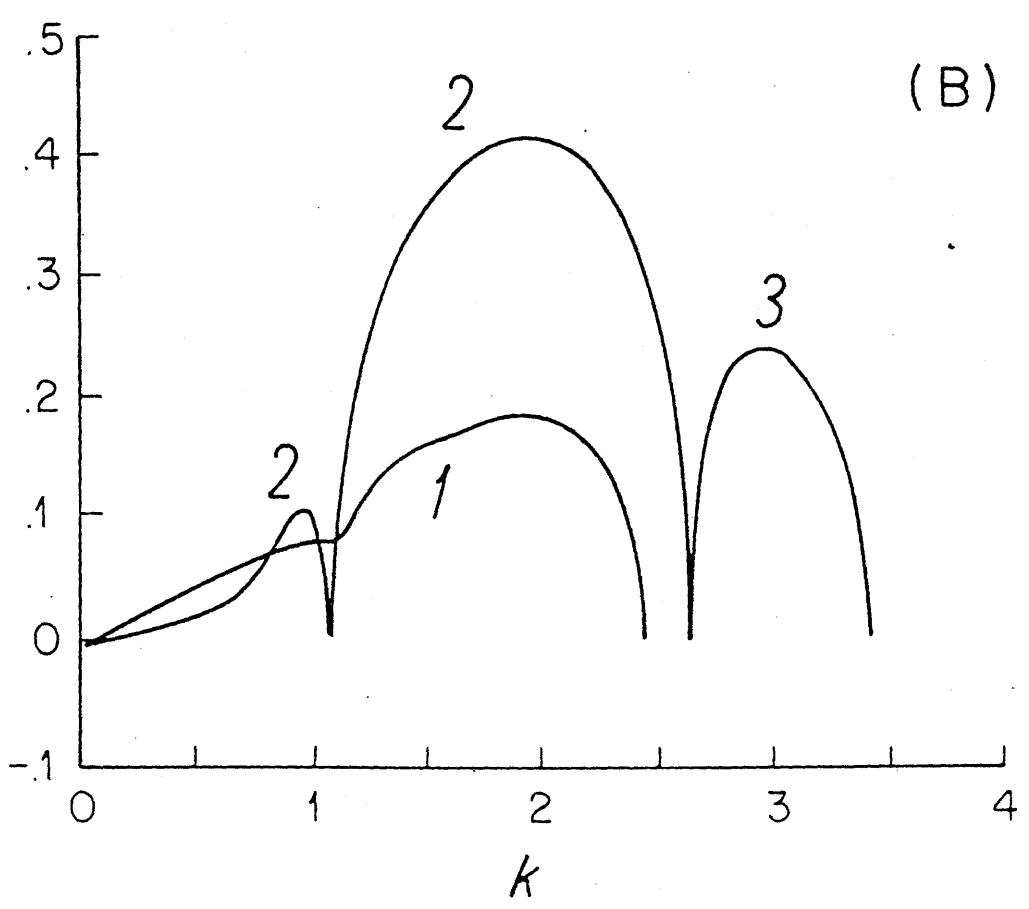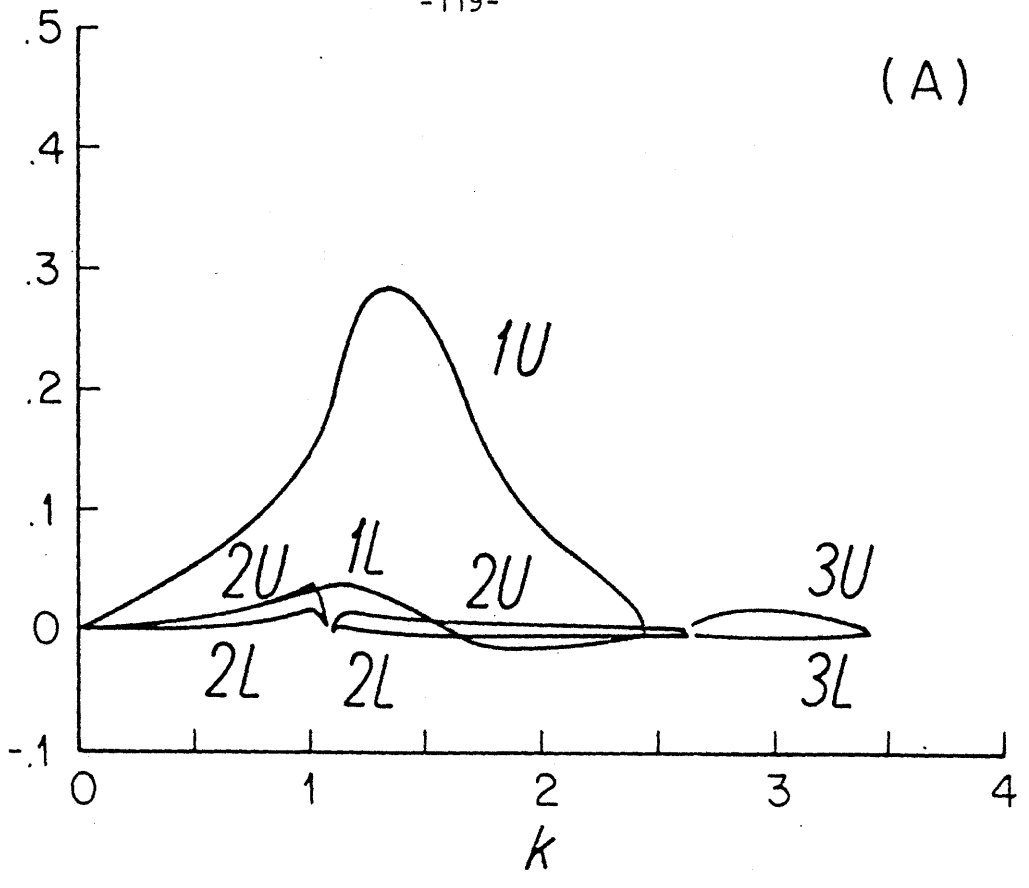
There is a complication in the stability diagram for Modes 1 and 3 for $-1 < \beta < 0$. The modes coalesce and produce an additional mode somewhere in the little box marked on the diagram. This separate mode is labelled 4 and exists for $-1 < \beta < -.3$. It is a radiating mode. The coalescence and mode production is best illustrated in the following schematic pictures of $c_i(k)$ at $\beta > -.2$ and $\beta < -.4$:
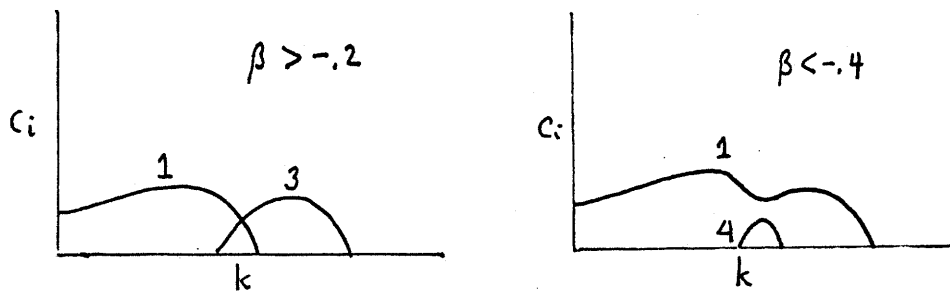
The new of Mode 1 at $\beta < -.4$ is combined from the higher growth rate parts of Modes 1 and 3 while Mode 4 is the remaining lower growth rate part. Such coalescences of modes mean that stability diagrams such as this one can be difficult to understand.

To summarize briefly the results for this profile: the eastward jet ($\beta > 0$) has only trapped solutions, which are easily identified as horizontal and vertical shear modes; the westward jet ($\beta < 0$) also has horizontal and vertical shear modes, both of which have radiating longwaves and trapped shortwaves. The maximum β for each mode is equal to one of the β's given by the necessary condition: in other words, the necessary conditions appear to be sufficient, at least for the central jet vertical shear mode and the upper layer horizontal shear mode. The radiating modes for $\beta < 0$ are identified as destabilized Rossby waves of the far field.

The second example of a jet with vertical shear in the central region and no vertical shear outside the jet is the profile

$$U_{I1} = 1 \qquad F = 5$$

$$U_{I2} = 0 \qquad D = 1.7 \qquad (3.2.3)$$

$$U_{01} = 0 \qquad H \to \infty$$

$$U_{02} = 0$$

This is similar to the previous profile but with no flow, and hence no horizontal shear, in the lower layer (there actually is a little flow in the shear zones, Region II, because of the potential vorticity constraint on the profile there). We might expect the importance of the horizontal shear to be diminished relative to the vertical shear compared with the previous profile. The profile shape and its potential vorticity gradient for $\beta = 1$ are shown in Figure 3.2.10. The necessary conditions for instability for this profile imply that there is possible (1) horizontal shear instability in the upper layer when $-6.67 < \beta < 3.05$, (2) no lower layer horizontal shear instability, (3) vertical shear instability in the central jet when $-5 < \beta < 5$, (4) no vertical shear instability outside the central jet and (5) no mixed instability in the lower layer because of the second necessary condition which requires that $U \frac{\partial \hat{\pi}}{\partial y} > 0$ somewhere for instability.

Again, radiation should be difficult for the eastward jet ($\beta > 0$) and easy for the westward jet. The stability diagram in the β-k plane is shown in Figure 3.2.11. The diagram is shown in two parts again. Although the stability diagram appears to be simpler, the types of un-
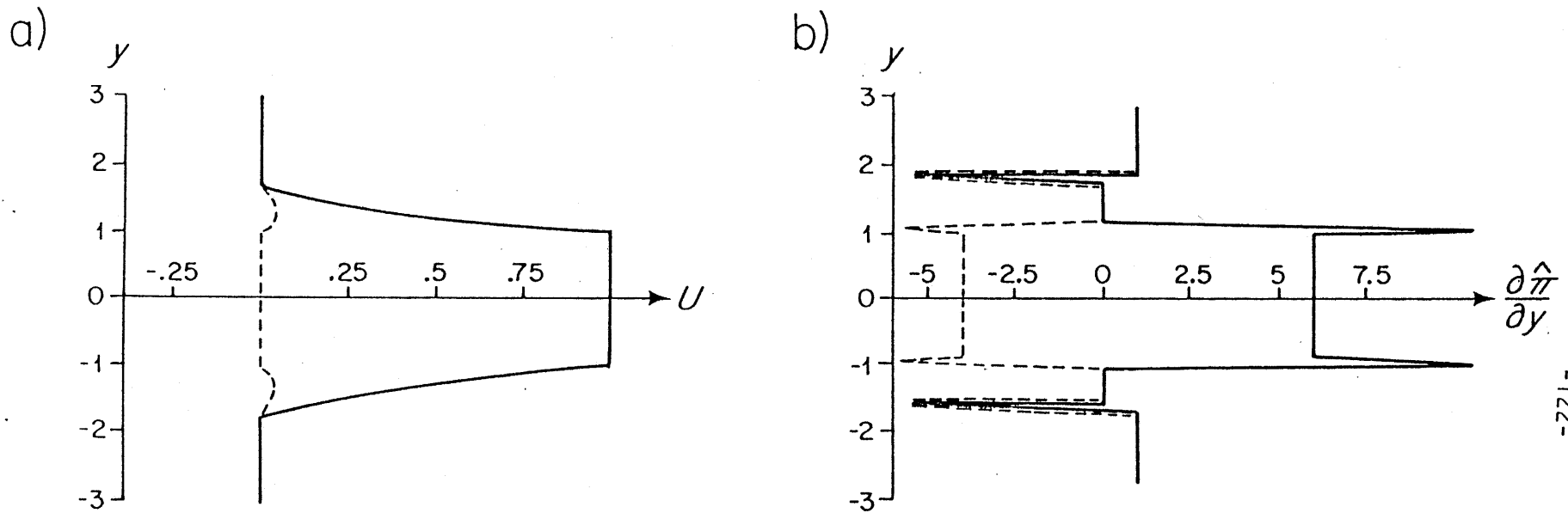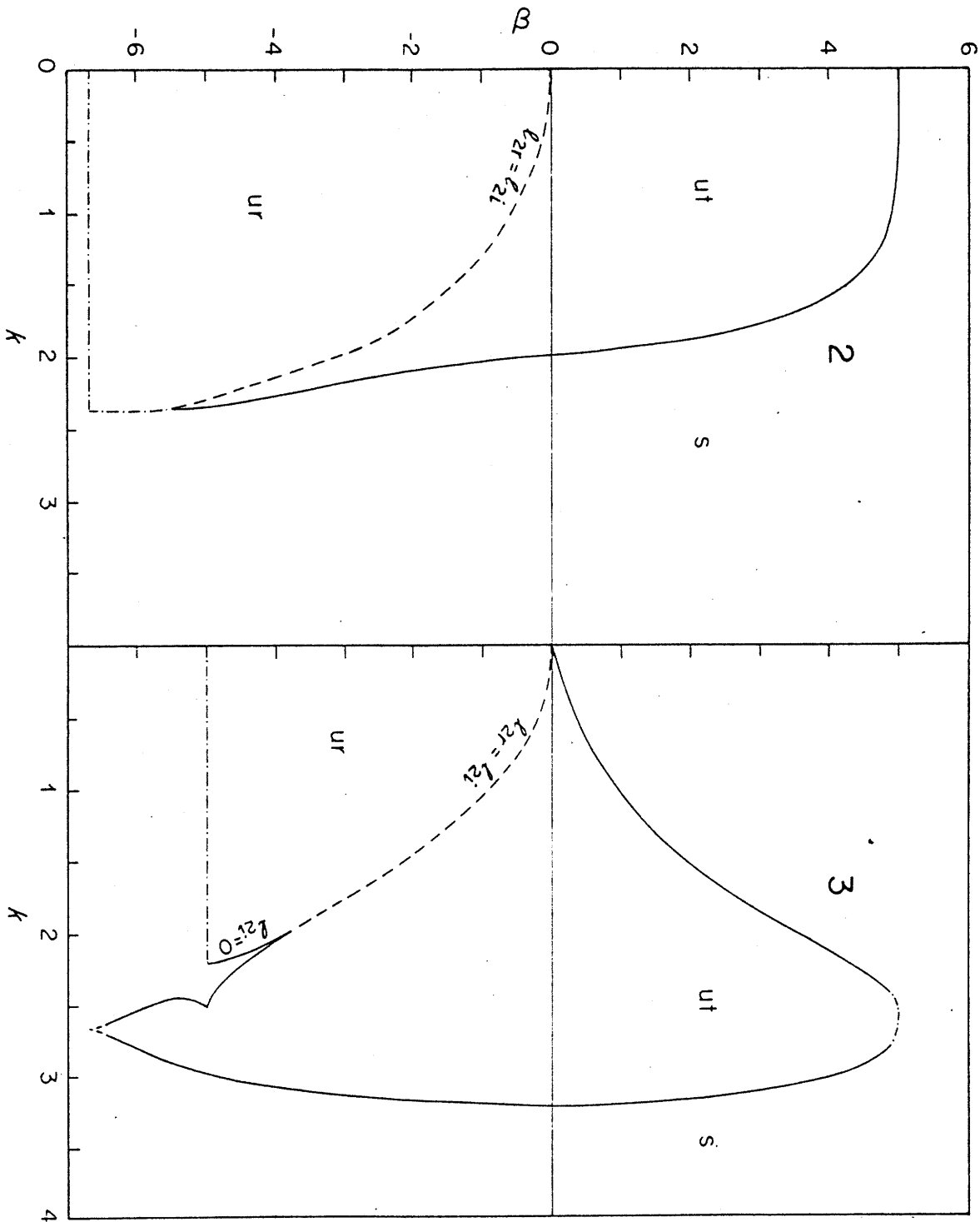
a) Graph with vertical axis y (labeled 3, 2, 1, 0, -1, -2, -3) and horizontal axis U (labeled -.25, .25, .5, .75).

b) Graph with vertical axis y (labeled 3, 2, 1, 0, -1, -2, -3) and horizontal axis $\frac{\partial \hat{\pi}}{\partial y}$ (labeled -5, -2.5, 0, 2.5, 5, 7.5).

Figure 3.2.10

(a) U(y) as given by (3.2.3) and (b) $\partial \pi/\partial y$, the effective potential vorticity gradient (3.1.8).

Figure 3.2.11

Neutral stability curves in the β-k plane for the profile (3.2.3).
The plane extends to negative β, as in Figure 3.2.3. Notation is as
in Figure 3.2.3. There are two modes shown separately: (a)longwave,
vertical shear mode (2) and (b) combination of the shortwave,
vertical shear mode and the upper layer, horizontal shear mode (3).

stable modes seen here are not as clear-cut as in the previous profile. For $\beta > 0$, there are two separate modes, rather than the three of the previous profile. Mode 2, which is a vertical shear mode of the central jet, is essentially unchanged by the increase in vertical shear. It is now unstable up to $\beta_c = 5.0$ because of the increase in shear. Its phase speed and growth rate at $\beta = 1$ are shown in Figure 3.2.12: the phase speed is now closer to .5 (the phase speed of a pure baroclinic instability at $\beta = 0$ where the vertical shear is 1.0). Mode 3 on the other hand is now a combination of Modes 1 and 3 from the previous profile (Figure 3.2.3). The combination of the two modes into one is clear when U_{12} is gradually reduced from .5 to 0. Apparently the loss of horizontal shear in the lower layer means that the overall flow is less barotropically unstable. Such a result was reported by Holland and Haidvogel (1980). Comparing the dispersion relations for Mode 3 (Figure 3.2.12) with the dispersion relation for Modes 1 and 3 when $U_{12} = .5$ (Figure 3.2.4), it is easy to see that both modes are really still present, although combined together. The energy source for Mode 3 is highly baroclinic (Figure 3.2.13) but there is still a barotropic source of energy associated with Mode 1. Mode 3 is thus some sort of mixed barotropic-baroclinic mode, since it is combined from a horizontal and a vertical phase mode. The flow is strongly dominated by baroclinic instability.

When $\beta < 0$, there is a rather odd trade in behavior: as can be seen in the stability diagram, Figure 3.2.11, Mode 2 essentially becomes a horizontal shear mode (because of its β_c) while Mode 3 retains its mixed character. Note that there are still just two sets of destabilized Rossby
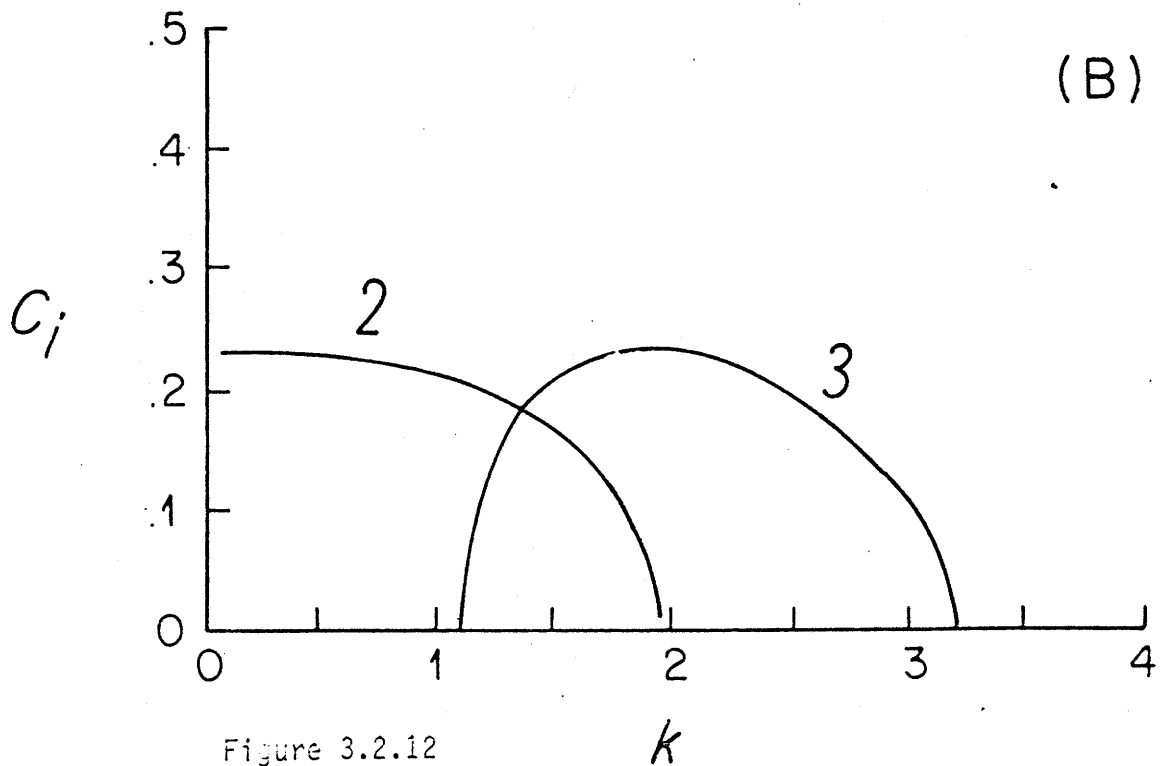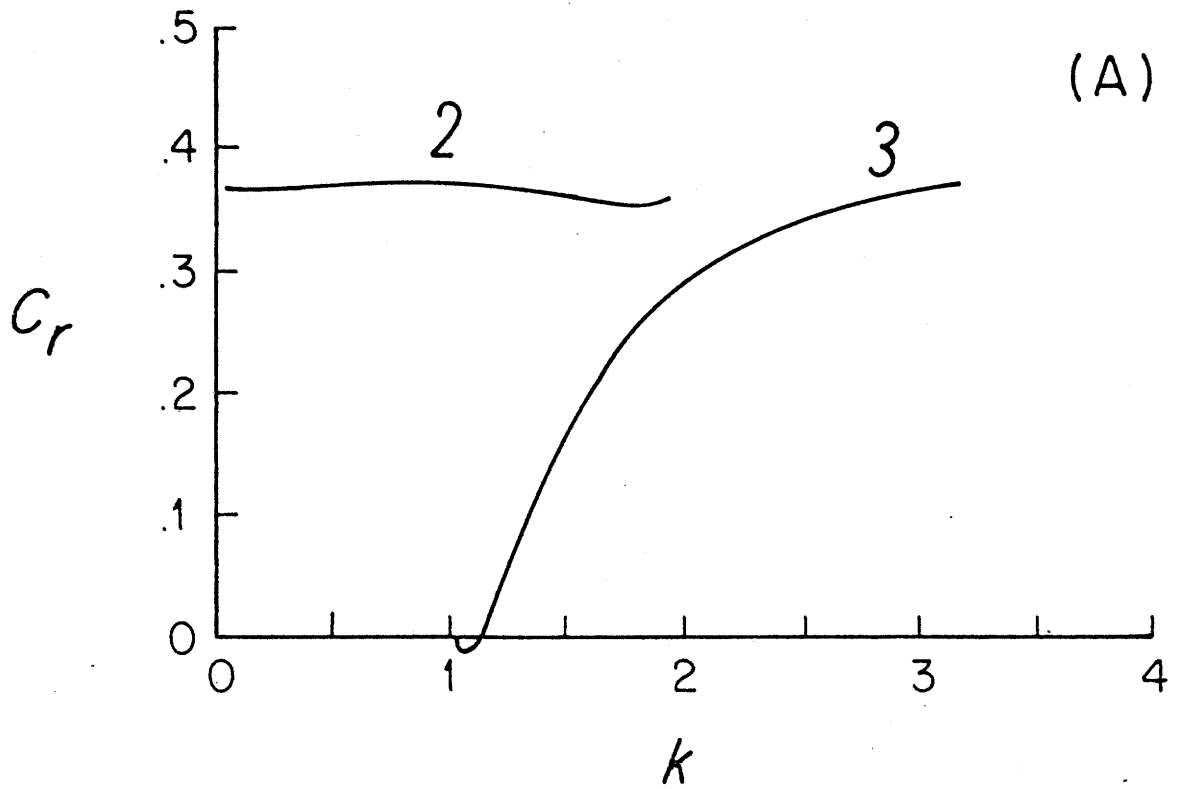
Figure 3.2.12

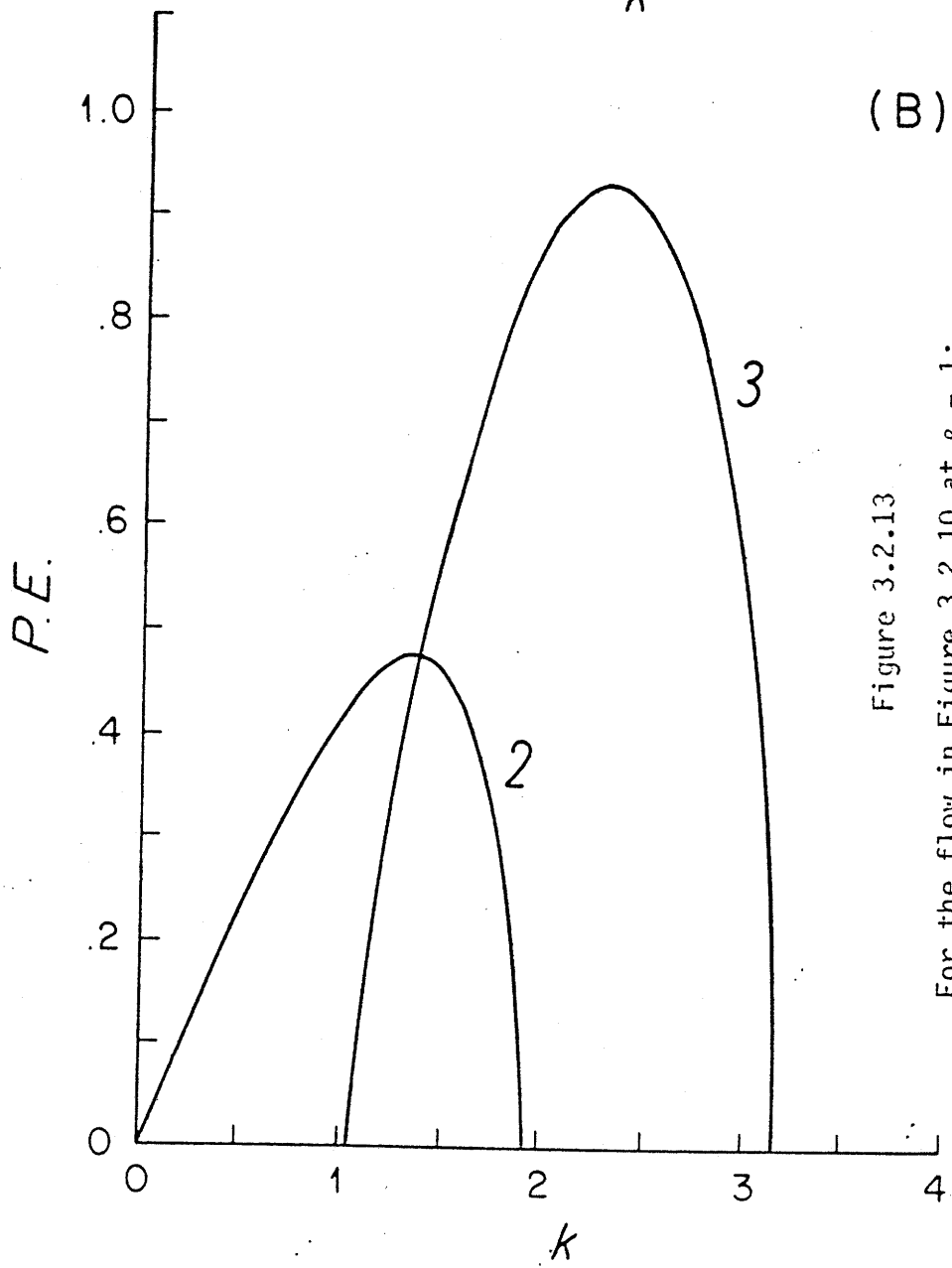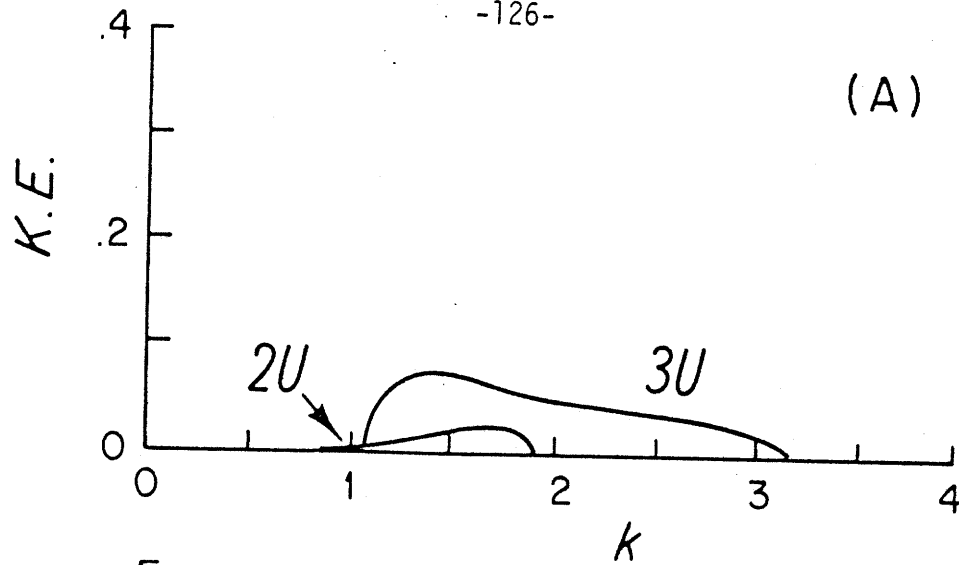For the flow in Figure 3.2.10 at $\varepsilon = 1$: (a) $c_r(k)$ and (b) $c_i(k)$.

Figure 3.2.13

For the flow in Figure 3.2.10 at β = 1:
(a) kinetic energy transfer and (b) potential
energy transfer to the perturbations. The
lower layer kinetic energy transfers are
negligible.

waves: one is associated with the horizontal shear (Mode 2) and the other with the vertical shear (Mode 3). The stability diagram for Mode 3 is peculiar at large negative β: the portion which is associated with the central jet vertical shear becomes stable at $\beta = -5$ while the portion associated with the horizontal shear is stable at $\beta = -6.67$.

Dispersion relations at $\beta = -1$ are shown in Figure 3.2.14. Again, it looks as though Modes 2 and 3 have switched places compared with the previous profile. The growth rate of the radiating waves is lower than that of the trapped waves, but not by much. The energy transfers for the two modes are shown in Figure 3.2.15 at $\beta = -1$. Mode 2 has nearly equal baroclinic and barotropic energy sources, again identifying it as a horizontal shear mode for $\beta < 0$. Mode 3 is very much dominated by baroclinic instability.

The confusing switch of behavior from horizontal to vertical shear modes and the coalescence of modes is not important, and should not be stressed. The important points are that there are instabilities which can be identified with different instability mechanisms (using the necessary conditions for instability and the energy transfers) and that, when the conditions are right (when this particular jet is westward), there are two radiating modes, one associated with the vertical and one with the horizontal shear.

(c) Eastward Jet with a Westward Undercurrent

The eastward jets discussed above were unable to successfully force Rossby waves in the outer region because of the mismatch of Rossby wave and instability phase speeds. The westward jets, on the other hand, were quite successful in radiating energy. A predominantly eastward jet might,

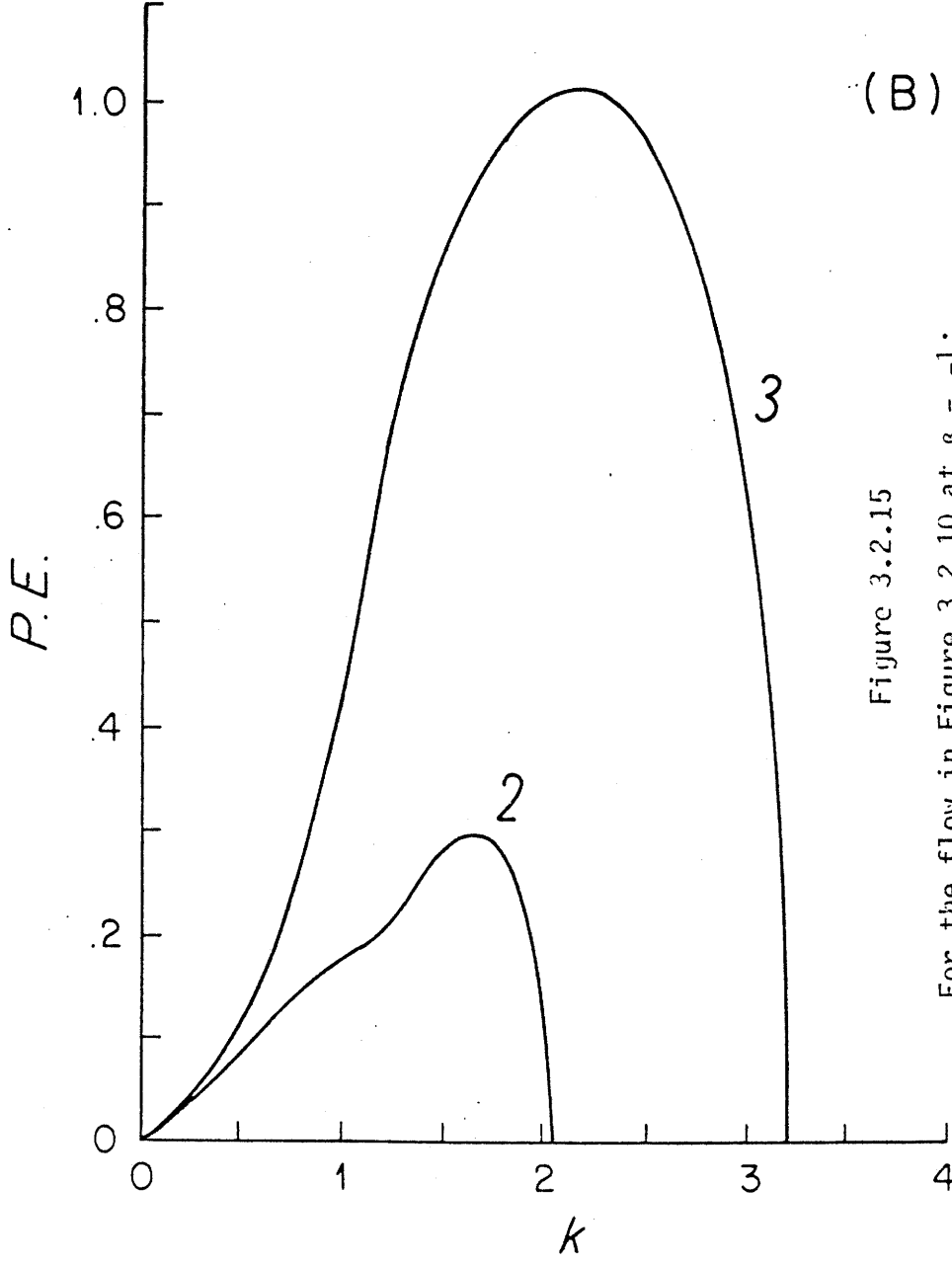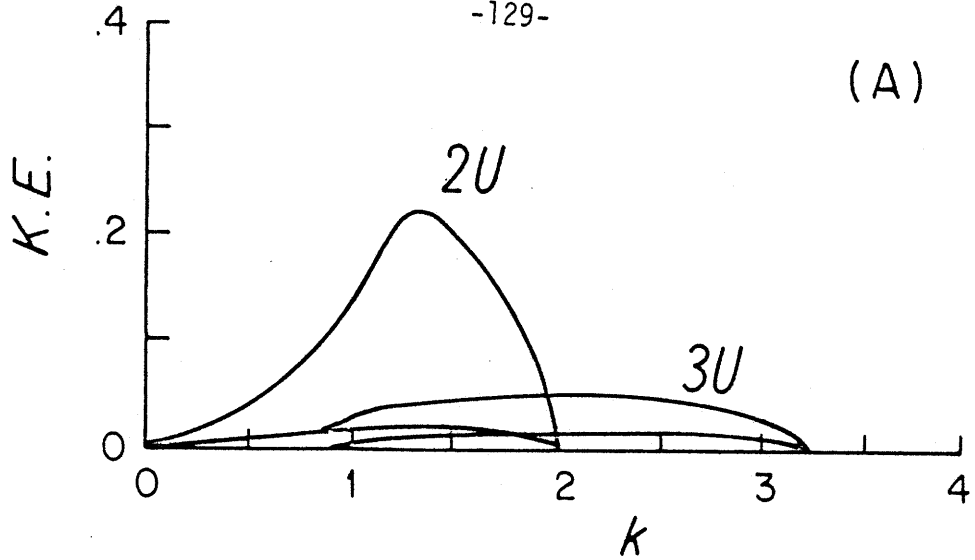Figure 3.2.14 For the flow in Figure 3.2.10 at $\beta = -1$: (a) $c_r(k)$ and (b) $c_i(k)$.
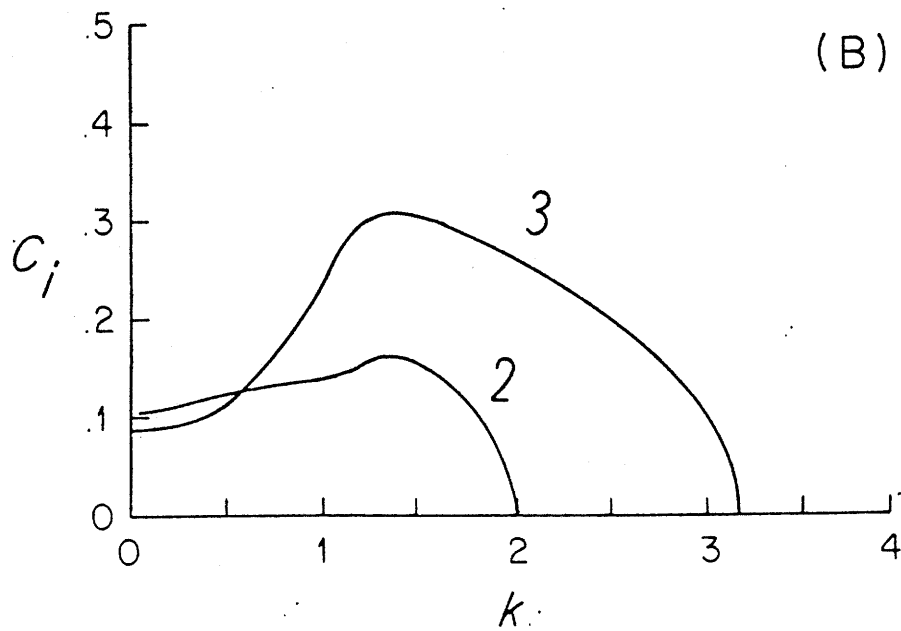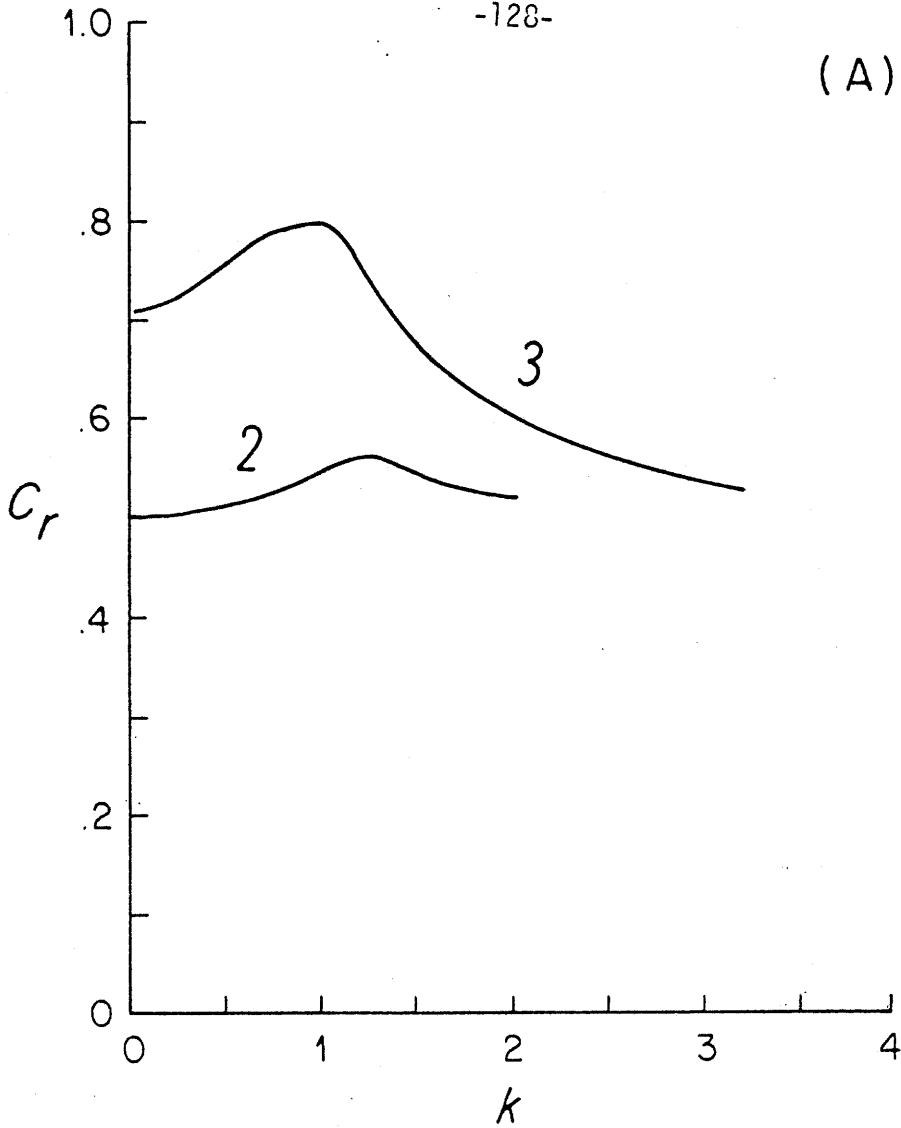
Figure 3.2.15

For the flow in Figure 3.2.10 at β = -1: (a) kinetic energy transfer and (b) potential energy transfer to the perturbations.

however, radiate if, for instance, it had (1) a westward jet underneath (like the westward undercurrent beneath the Gulf Stream), (2) vertical shear in Region III or (3) westward sidelobes to the south (and/or north) of the eastward jet. This subsection discusses the first possibility. The following two subsections give results for jets with positive and negative vertical shear exterior to the jet. The effect of westward side lobes was not investigated because of the increase in complexity of the dispersion relation. However, such a geometry may actually be the most realistic for the Gulf Stream (see Chapter 4) and would be extremely useful to investigate.

The flow configuration for the eastward jet with a weak westward undercurrent is shown in Figure 3.2.16, with its potential vorticity gradient, for $\beta = 1$.

The profile is

$$U_{I1} = 1 \qquad F = 5$$

$$U_{I2} = -.1 \qquad \qquad (3.2.4)$$

$$D = 1.7$$

$$U_{01} = 0$$

$$H \rightarrow \infty$$

$$U_{02} = 0$$

The necessary conditions are nearly unaltered from those of profile (3.2.3). There is possible (1) horizontal shear instability in the upper layer when $\beta < 2.94$, (2) horizontal shear instability in the lower layer when $\beta < 3.26$, (3) vertical shear instability in Region I when $\beta < 5.5$, (4) no vertical shear instability in Region III, and (5) mixed instability in the lower layer when $3.26 < \beta < 5.5$.
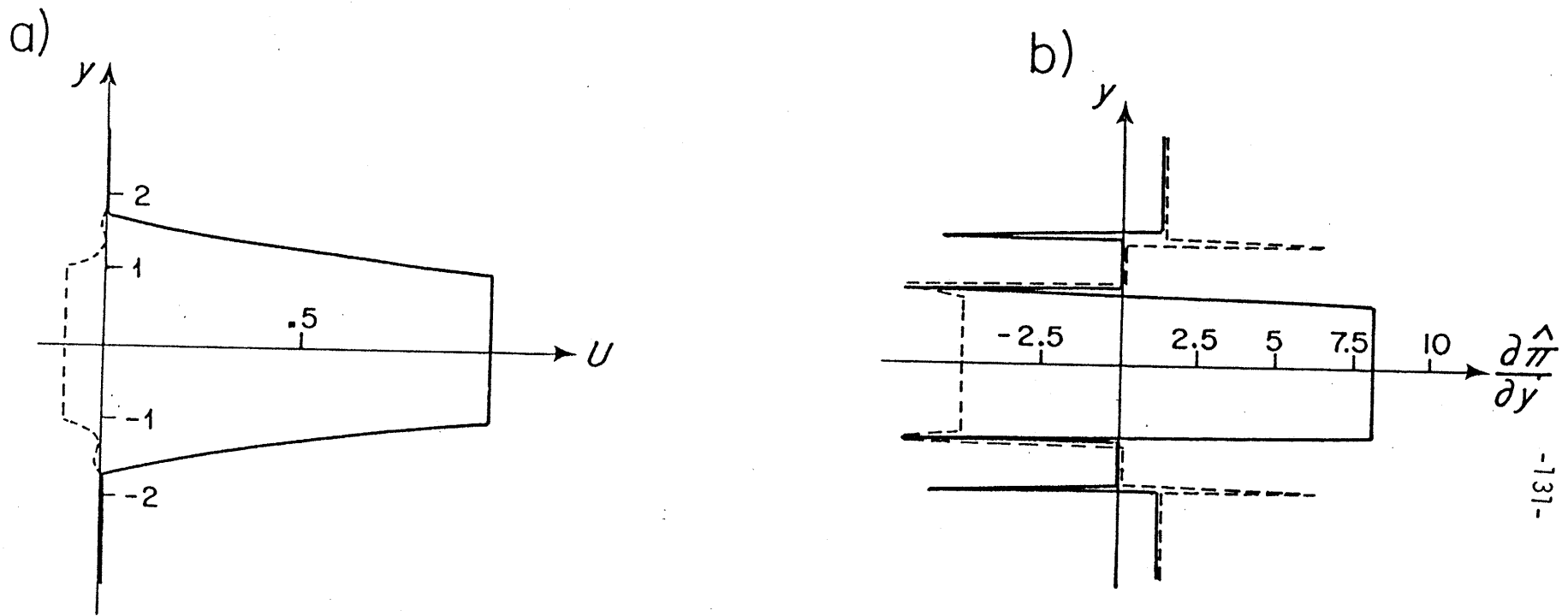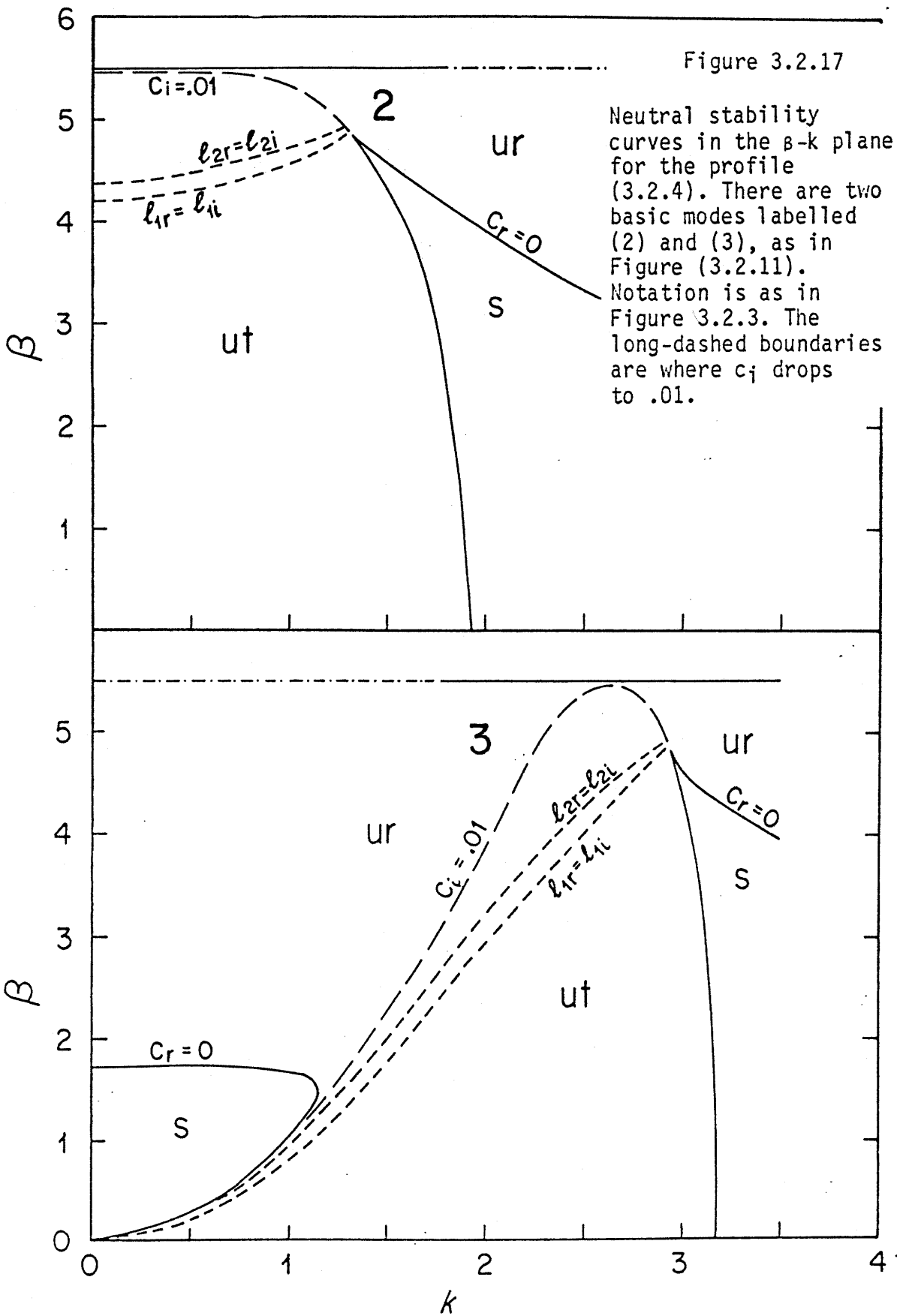
a)

b)

Figure 3.2.16

(a) U(y) as given by (3.2.4) and (b) $\partial\pi/\partial y$, the effective potential vorticity gradient (3.1.8).

Only cases with $\beta > 0$ are considered here. Because of the slightly increased vertical shear in the central jet, we might expect baroclinic instability to be slightly more important than in profile (3.2.2). The shift in importance of baroclinic and barotropic instability is reflected in the decreased β_c for the horizontal shear mode and increased β_c for the vertical shear mode. Also, the phase speed of the central jet vertical shear modes should be a little reduced since the vertically-averaged velocity in the central jet is lower.

Radiation may be possible if unstable modes have negative phase speeds. As β increases to the appropriate β_c for each mode, the phase speed decreases to the minimum speed of its associated part of the flow profile. Each unstable mode is associated with a particular part of the profile: the vertical shear modes with the central jet flow, which has a range of -.1 to 1, and the horizontal shear modes with the upper layer horizontal shear, which has a range of 0 to 1 and with the lower layer horizontal shear which has a range of -.1 to 0. Thus for this profile, we would expect the vertical shear modes of the central jet and the lower layer horizontal shear mode to be much more likely to radiate than the upper layer horizontal shear mode.

The stability diagram is shown in Figure 3.2.17. First some explanation of the notation used in Figure 3.2.17 is in order. As before, "ut" and "ur" indicate trapped and radiating instabilities. The solid curves are the loci $c_i = 0$. There are three dashed curves in each diagram: one is where $c_i = .01$, which is used to informally indicate a boundary between fundamental modes of the jet and destabilized Rossby waves; the other two are the curves $\mathrm{Re}(\ell_1) = \mathrm{Im}(\ell_1)$ and $\mathrm{Re}(\ell_2) = \mathrm{Im}(\ell_2)$. These curves

Figure 3.2.17

Neutral stability curves in the β-k plane for the profile (3.2.4). There are two basic modes labelled (2) and (3), as in Figure (3.2.11). Notation is as in Figure 3.2.3. The long-dashed boundaries are where c_i drops to .01.

indicate, also informally, a transition from trapped behavior to wavelike behavior for each of the two Rossby waves in the far field.

The stability diagram, Figure 3.2.17, is nearly the same as the diagram in the preceding section (Figure 3.2.11). There are still two modes of instability, called Modes 2 and 3, just as in Figure 3.2.12. Both modes are stabilized by $\beta_c = 5.5$: mode 2 is a central jet vertical sehar mode. Mode 3 is also predominantly a central jet vertical shear mode but still incorporates the horizontal shear mode, which affects its longwave behavior. There is one important difference from the preceding jet (Figure 3.2.11): both Modes 2 and 3 have associated radiating instabilities. In the stability diagram, some of the neutral stability curves ($c_i = 0$) are now dashed to indicate where ($c_i = .01$): the modes along the neutral stability curve of Figure 3.2.11 are now slightly unstable. These formerly stable modes have negative phase speeds, satisfy the phase speed condition and are now radiating. The unstable waves between the ($\mathrm{Re}(\ell) = \mathrm{Im}(\ell)$) curves and the ($c_i = .01$) curve correspond with the trapped instabilities of the previous profile: they now satisfy the phase speed condition, because of the slight change in the flow profile, and are now radiating.

It is surprising and interesting that where there was formerly a neutral curve, there is now a small growth-rate curve at high β, for both modes. (The neutral curve for these modes now lies at $\beta = \beta_{c_i}$). Although the growth rate drops precipitously at this "boundary", it does not become zero. Let us discuss Modes 2 and 3 and their associated radiating instabilities separately. Mode 2 satisfies the phase speed condition

only at high β. There are radiating instabilities on both sides of the curve c_i = .01. To the left, they are basically the usual jet modes, which now radiate. To the right, they are destabilized Rossby waves, exactly as found for the westward jets of the two preceding profiles. The destabilized Rossby waves have their own associated neutral curves: one is the boundary β = 5.5 as dictated by the necessary conditions for instability, the second is the curve marked "c_r = 0" and the third, which is not shown, is at $k\sim5$ (where the Rossby wave y-wavenumbers $Im(\ell)$ go to zero).

Dispersion relations are shown in Figure 3.2.18 at β = 5. In contrast to the growth rate of the destabilized Rossby waves for the westward jets, the growth rates of these destabilized Rossby waves are very small. It appears from consideration of various profiles that the growth rate of the destabilized Rossby mode depends strongly on the "window" allowed for satisfaction of the the phase speed condition. For instance, the velocity of the westward jets ranged from -1 to 0 so its destabilized Rossby waves can have any phase speed between -1 and 0. On the other hand, the velocity of the eastward jet with a westward undercurrent ranges from -.1 to 1 with a far field velocity of 0. Destabilized Rossby waves for this flow can have phase speeds only in the range -.1 to 0, a considerably smaller range than for the westward jets. The consequence is that their growth rates are much smaller.

The energy transfers at β = 5 are shown in Figure 3.2.19. This β is considerably in excess of the β_c associated with the upper layer horizontal shear instabilities, so the flow is far from being barotropically unstable. Indeed, the energy transfer <u>to</u> the perturbations is entirely dom-

Figure 3.2.18

For the flow in Figure 3.2.16 at ß = 5: (a) $c_r(k)$ and (b) $c_i(k)$.
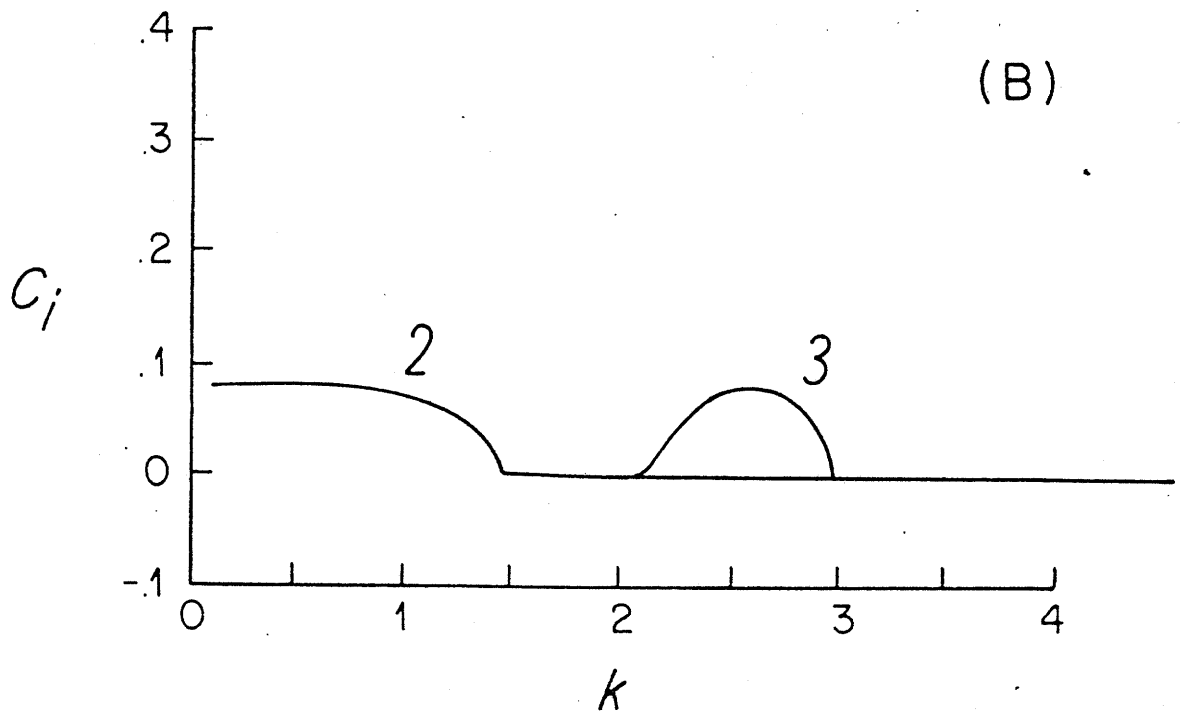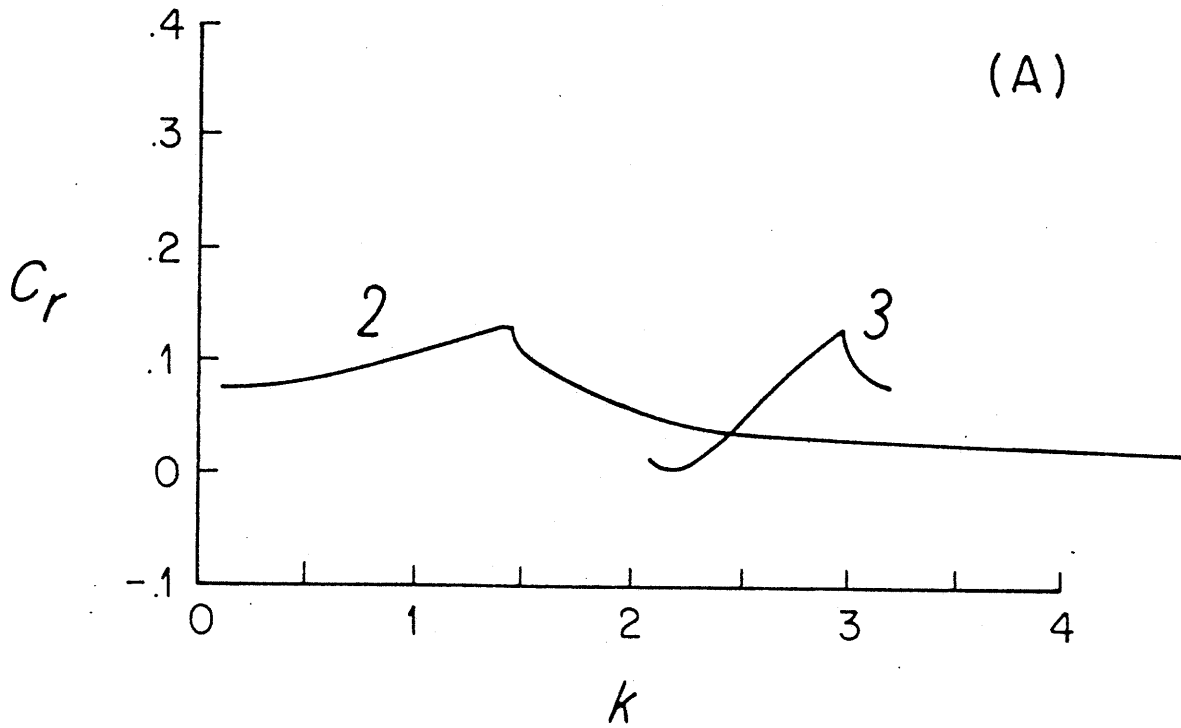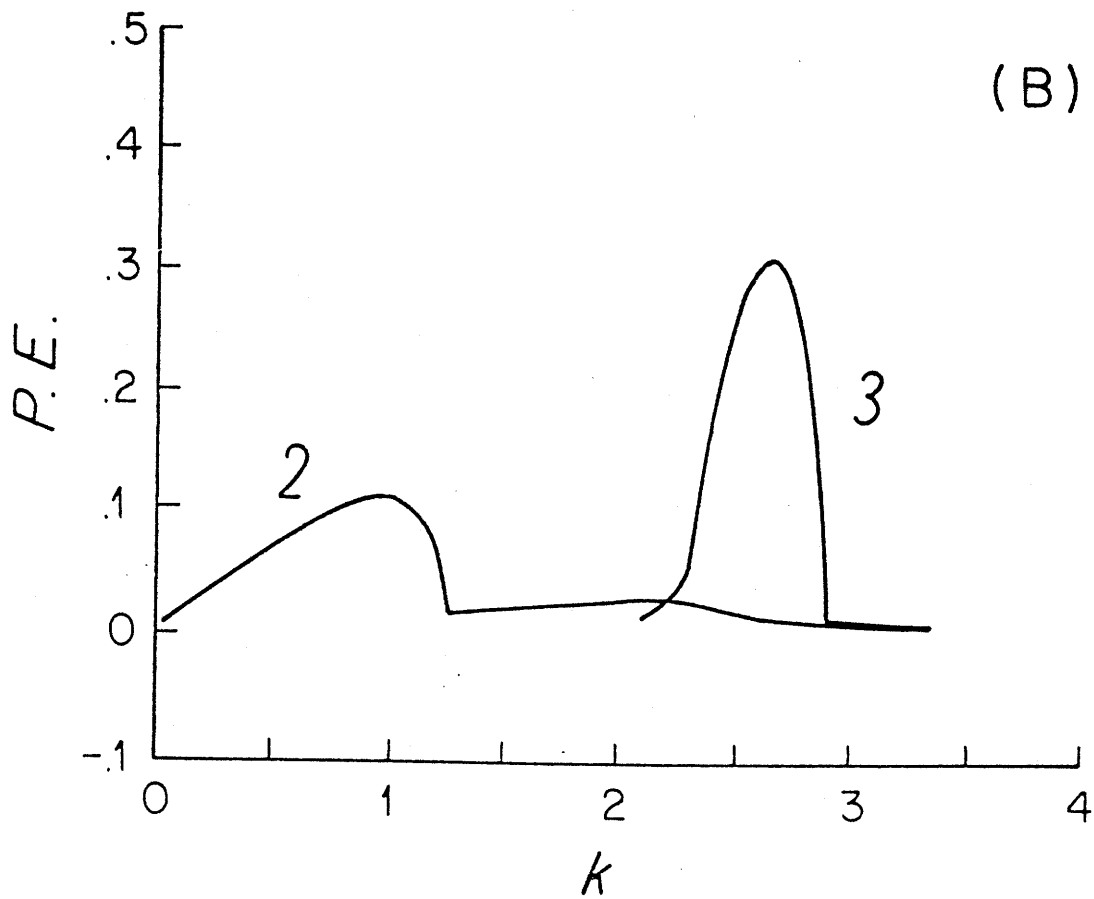
Figure 3.2.19

For the flow in Figure 3.2.16 at ß = 5:
(a) kinetic energy transfer and (b) potential
energy transfer to the perturbations. The
upper layer kinetic energy transfer is
negative and the lower layer transfer is
negligible.
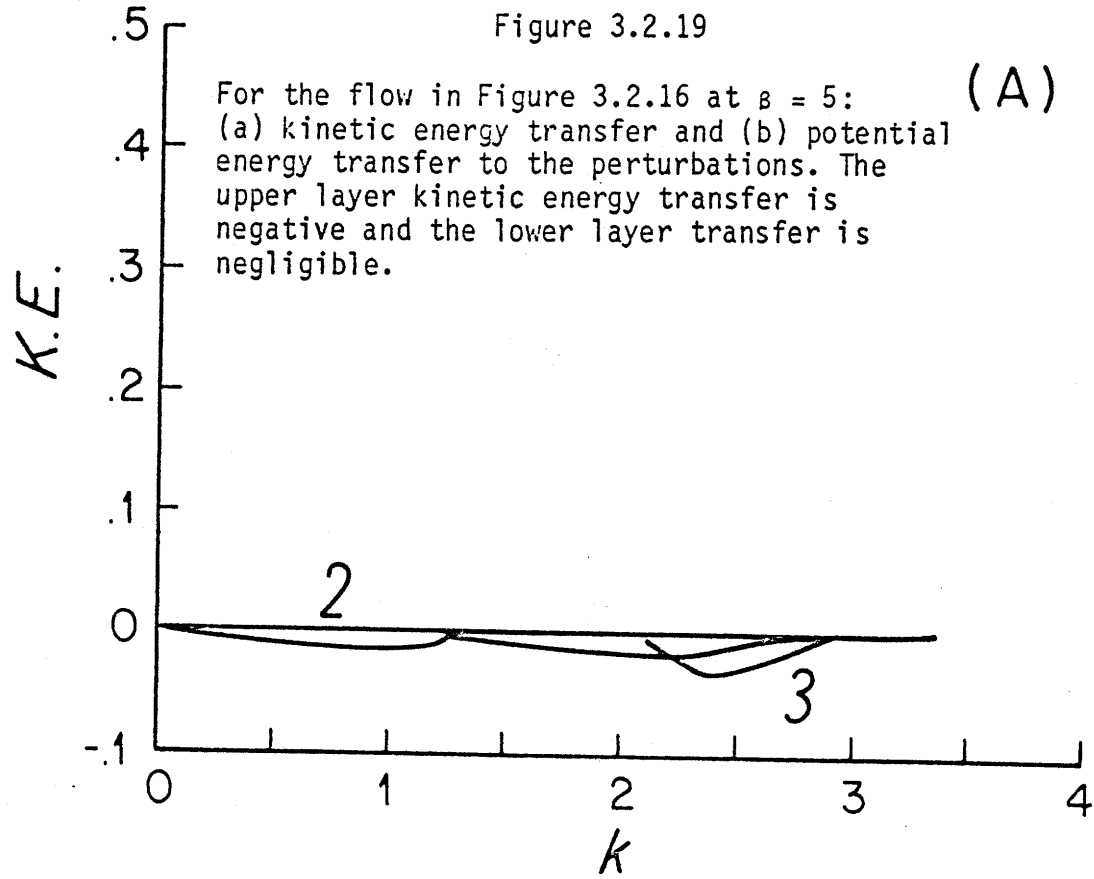
inated by baroclinic instability while the flow is actually <u>losing</u> kinetic energy to the mean flow.

Let us turn now to Mode 3. Returning to the stability diagram, Figure 3.2.17, we see that Mode 3 appears to radiate all along its old, longwave, neutral stability boundary (see Figure 3.2.11) and also on the shortwave side at high β. These short radiating waves are virtually identical with those of Mode 2 and will not be discussed further here. At low β and k there is a stable region, bounded by a neutral curve on which $c_r = 0$. This neutral stability curve seems to be due to the implicit presence of Mode 1 as part of Mode 3: it has been seen before that Mode 1 strongly affects the longwave behavior of Mode 3. As argued above, Mode 1, the horizontal shear mode, will probably not radiate because the minimum velocity of the flow it depends on for energy (the upper layer flow) is 0. The neutral curve along which $c_r = 0$ is probably due to Mode 1: while the phase speeds of the contiguous instabilities are negative, and the instabilities appear to be radiating, the stringent requirement that c_i/ℓ_r remain constant along the neutral curve is not met. The phase speed, c_r, along the neutral curve is consistent with Tung's (1980) prediction that the phase speeds of neutral modes of barotropic instability must be in the range of the flow speed here, the upper layer flow speed has a range of 0 to 1 at higher β and low k. Mode 3 is predominantly a vertical shear mode and has associated destabilized, long, Rossby waves.

We have seen that vertical shear instabilities are present and that the upper layer horizontal shear mode affects the longwaves of Mode 3. A

lower layer horizontal shear mode was not found although the necessary conditions do not rule it out. It may be coalesced with the vertical shear modes and may in fact be responsible for the longwave behavior of Mode 3 at high β.

Dispersion relations at $\beta = 1$ are shown in Figure 3.2.20. The phase speed of Mode 3 at its longwave cutoff is 0. This is the edge of the stable region at low β and k in Figure 3.2.17. However, the phase speed of Mode 3 just inside the neutral curve is negative, as can be seen in Figure 3.2.20. With negative phase speeds, there is a possibility that these instabilities latch onto Rossby waves in the far field although this mode does not strictly radiate, as above. The energy transfers at $\beta = 1$ are shown in Figure 3.2.21. At $\beta = 1$, the necessary conditions for instability say that barotropic instability is possible in the upper layer. While both Modes 2 and 3 are dominated by baroclinic instability, there is a positive contribution from barotropic instability especially on the longwave side of Mode 3, resulting from the horizontal shear mode which is part of Mode 3.

The eigenfunctions for the trapped, high growth-rate modes are similar to those of the previous profiles (Figure 3.2.6) since they depend mainly on the vertical shear in the jet center for their energy and have phase speeds which are too eastward to allow radiation. They are not replotted here. A radiating mode at $\beta=5$ is shown in Figure 3.2.22. It is curious-looking: the amplitude alternates between surface and bottom intensification. This happens because there are two waves outside the jet for the unstable waves to excite, a barotropic and a baro-

For the flow in Figure 3.2.16 at $\beta = 1$: (a) $c_r(k)$ and (b) $c_i(k)$.
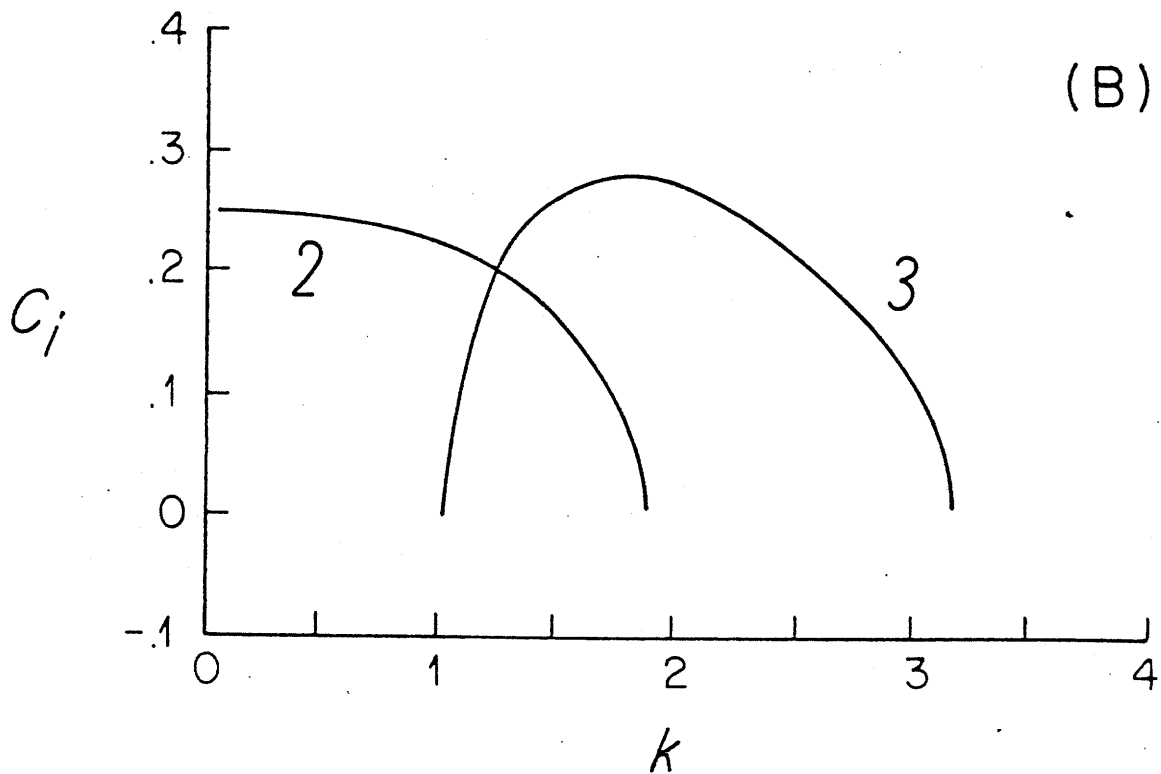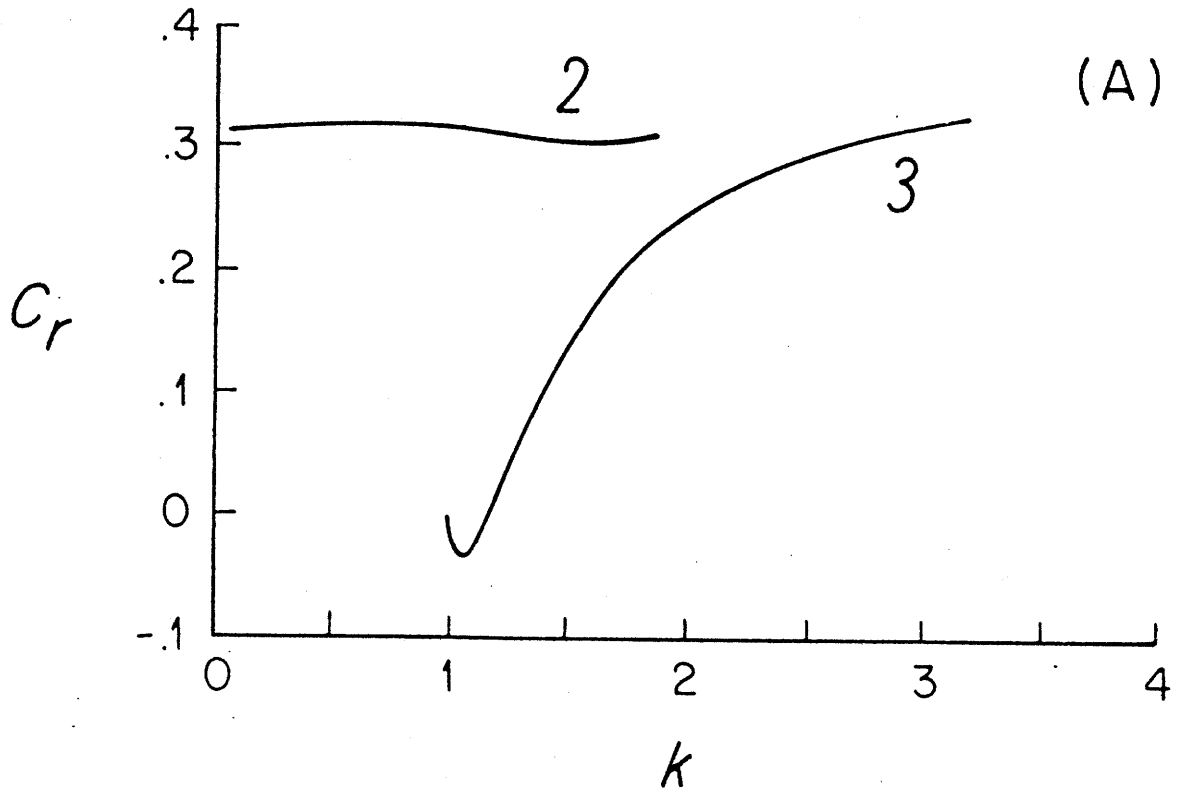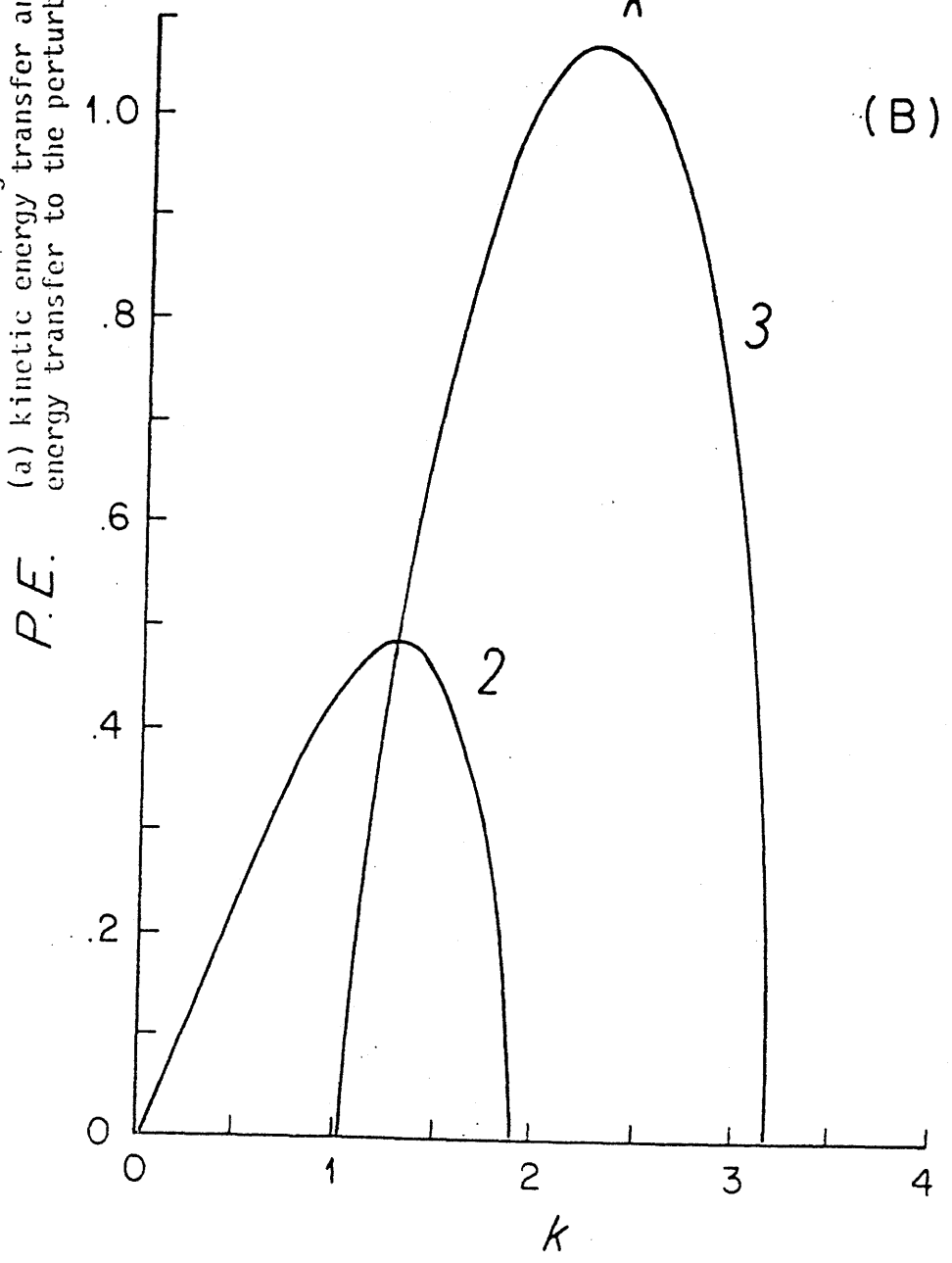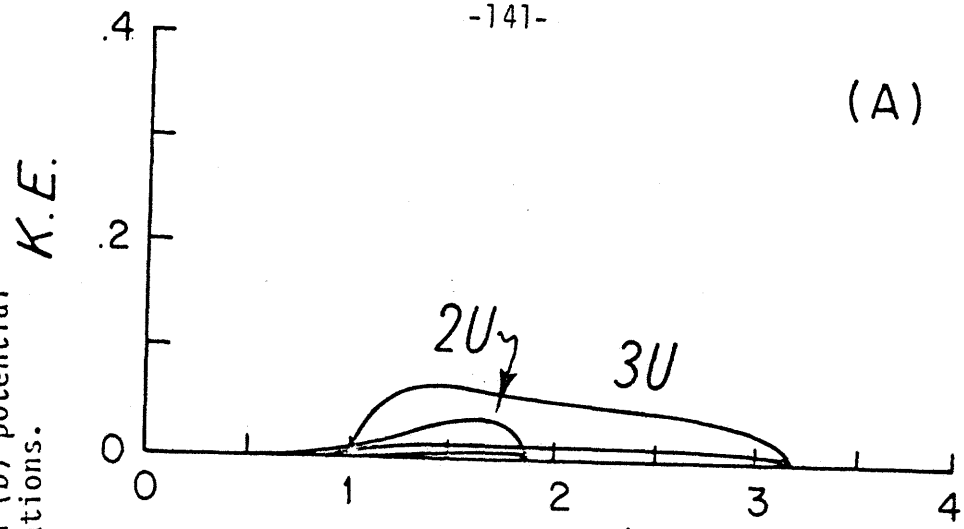
Figure 3.2.21

For the flow in Figure 3.2.16 at B = 1:
(a) kinetic energy transfer and (b) potential
energy transfer to the perturbations.

BETA

5.0
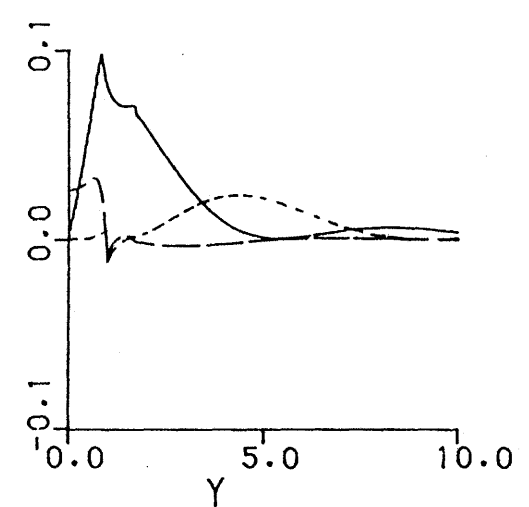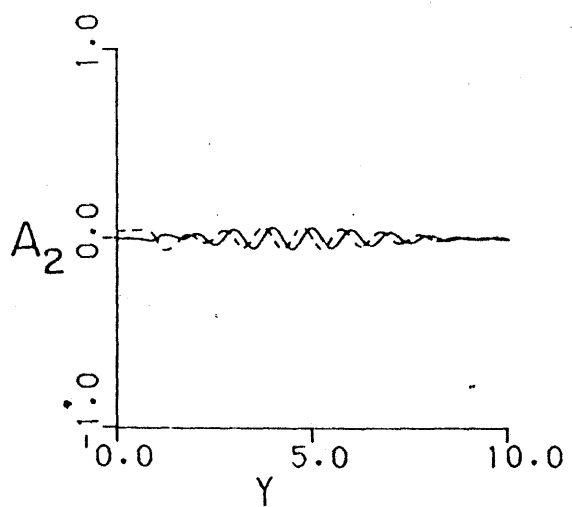
K.C

2.30

-0.103

Figure 3.2.22   0.004

The eigenfunction for a radiating,
horizontal shear mode for the flow in
Figure 3.2.16: the trapped modes are
very similar to the modes shown in
Figure 3.2.6 and are not pictured
here.
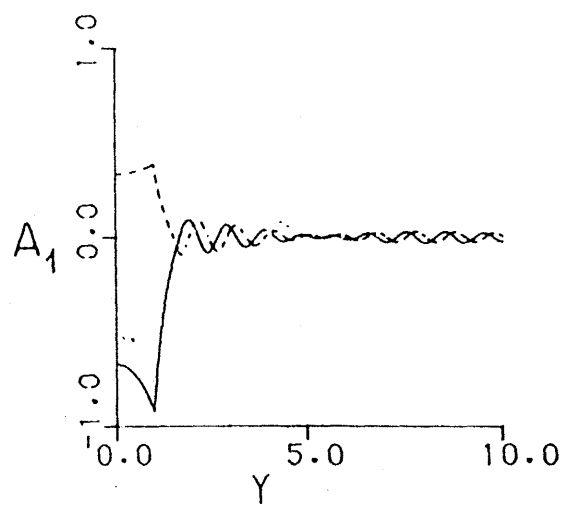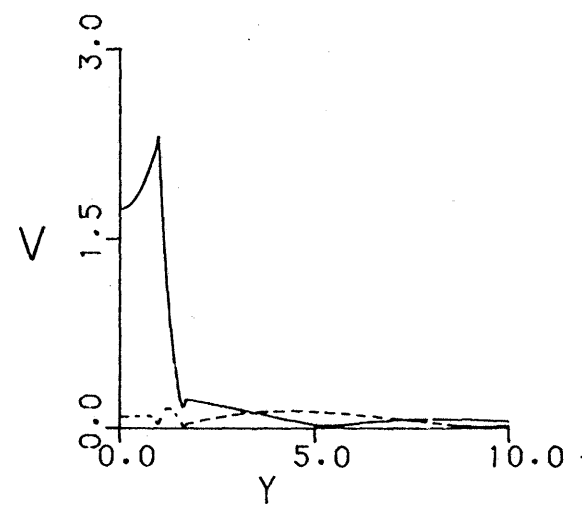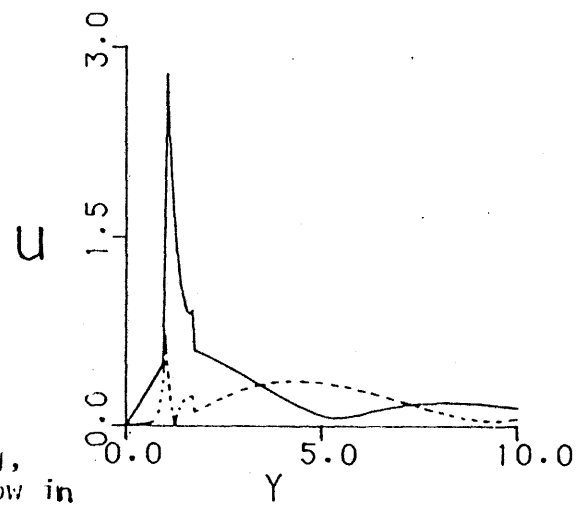
clinic Rossby wave. The dispersion relation for the Rossby waves at $\beta = 5$ is shown in Figure 3.2.23. Superimposed on the diagram are the phase speeds of the unstable waves at $\beta = -5$, but rescaled by $U = -1$. Both Rossby waves have phase speeds which asymptote to 0 at large $K^2 = (k^2 + \ell^2)$. The phase speed ranges overlap considerably. No Rossby waves, and hence no radiating modes, occur when the point defined by c and k falls to the right of the $\ell = 0$ curve. Thus, say, an instability with small, negative phase speed and a specified x-wavenumber within a wide range of k's forces both of these waves, but with different y-wavenumbers, ℓ. The barotropic and baroclinic Rossby waves then add constructively to give the vertical and meridional structure seen in Figure 3.2.22.

Despite the fact that the radiating modes are felt at great distances from the jet, all energy transfer to the perturbations must occur in the jet itself since there is no source of energy outside the jet. The radiating modes themselves can affect the mean flow outside the jet through their Reynolds stress and heat flux which are also shown in Figure 3.2.22.

To summarize, the solutions for the eastward jet with a small westward undercurrent are similar to those of the eastward jet with a quiet lower layer, but with the important difference that radiating modes are excited. In this respect, this jet is more like the westward jets. There are two types of radiating instability: (1) unstable modes of the non-radiating jet which now, thanks to the alteration in configuration, satisfy the phase speed condition and radiate and (2) a whole new class of unstable solutions with small growth rates: these are interpreted as destabilized Rossby waves.

Figure 3.2.23

Rossby wave dispersion relation for a fluid with two layers of equal
depth and vertical shear $(U_1-U_2) = 0.0$ at $\lambda = 0$ and $\lambda = 100$.
The barotropic wave is marked BT and the baroclinic is marked BC.
The dashed curves are the phase speeds of the unstable waves at
$\beta=-5$, rescaled with $U=-1$.

The radiating modes of type (1) were expected on the basis of preceding stability analyses (chapter 2 and non-radiating baroclinic jets): in all cases, as $\beta > \beta_c$, the phase speed of the unstable waves approaches the minimum velocity of the part of the profile responsible for the instability. Thus, if the minimum velocity for, say, the vertical shear instability, is reduced to be more westward than the exterior flow, negative phase speeds can be expected, at least at high β. Such modes might radiate and in fact, they do. The destabilized Rossby waves were not expected, although in retrospect, they are the counterparts of the long, radiating waves of the shear layers and westward jets. The phase speed c_r of the destabilized Rossby waves for a given wavenumber k is determined by the jet instabilities. The y-dependence, ℓ, is then determined by c_r and k. Since the barotropic and baroclinic Rossby waves have similar phase speeds when there is no vertical shear in the exterior region, they can both be forced. The meridional structure of the radiating instabilities, which are combined from these two waves with different y-wavenumbers, alternates between surface and bottom intensification.

(d) Eastward Jet With Small Positive Vertical Shear Outside the Jet

It is anticipated that jets with vertical shear in the exterior Region III will have radiating solutions if the instabilities have phase speeds less than the flow speed in at least one layer in Region III. The free waves of the outer flow will be Rossby waves where the potential vorticity gradient is replaced by $\beta + F(U_1-U_2)$ and $\beta - F(U_1-U_2)$ in the upper and lower layers, respectively. We note that where β is small enough,

small vertical shear in this outer region allows baroclinic instability. For simplicity, the waves which do not extract energy from the vertical shear (interface displacement) in Region III will be referred to as "Rossby waves" and the growing waves which feed on the local available potential energy will be called "baroclinic instabilities". Note that Rossby waves can exist even when $\beta = 0$ since there is an ambient potential vorticity gradient due to the vertical shear.

The dispersion relation for waves in the outer flow is the familiar two-layer relation (3.2.1), listed at the beginning of section 3.2(a). It has neutral solutions in addition to the complex ones which are the focus of discussions of baroclinic instability. The phase speed $c(k)$ (equation 3.2.1) is plotted in Figure 3.2.24 as a function of K, the total wavenumber, for vertical shear $U_S = .15$, $F = 5$ and $\beta = .1$ and 1. For these parameters, the flow may be baroclinically unstable if $\beta < \beta_c = .75$. There is a range of unstable K when $\beta = .1$, but all phase speeds are real when $\beta = 1$, since baroclinic instability for these parameters requires that $\beta < .75$.

When β is non-zero, the limit of (3.2.1) as $K^2 \to 0$ is

$$c = \begin{cases} \dfrac{U_1 + U_2}{2} - \dfrac{\beta}{2F} \\[2ex] -\dfrac{\beta}{K^2} \end{cases} \quad \text{or} \quad c = \begin{cases} 0.75 - \dfrac{\beta}{10} \\[2ex] -\infty \end{cases} \tag{3.2.5}$$

The limit when $K^2 \to \infty$ is $c = U_1$, U_2 or $c = .15$, 0. The phase speeds of the neutral modes thus fall in one of the two ranges $[.075 - \beta/2F, .15]$ and $[-\infty, 0]$. (When there is no vertical shear, the first range corre-
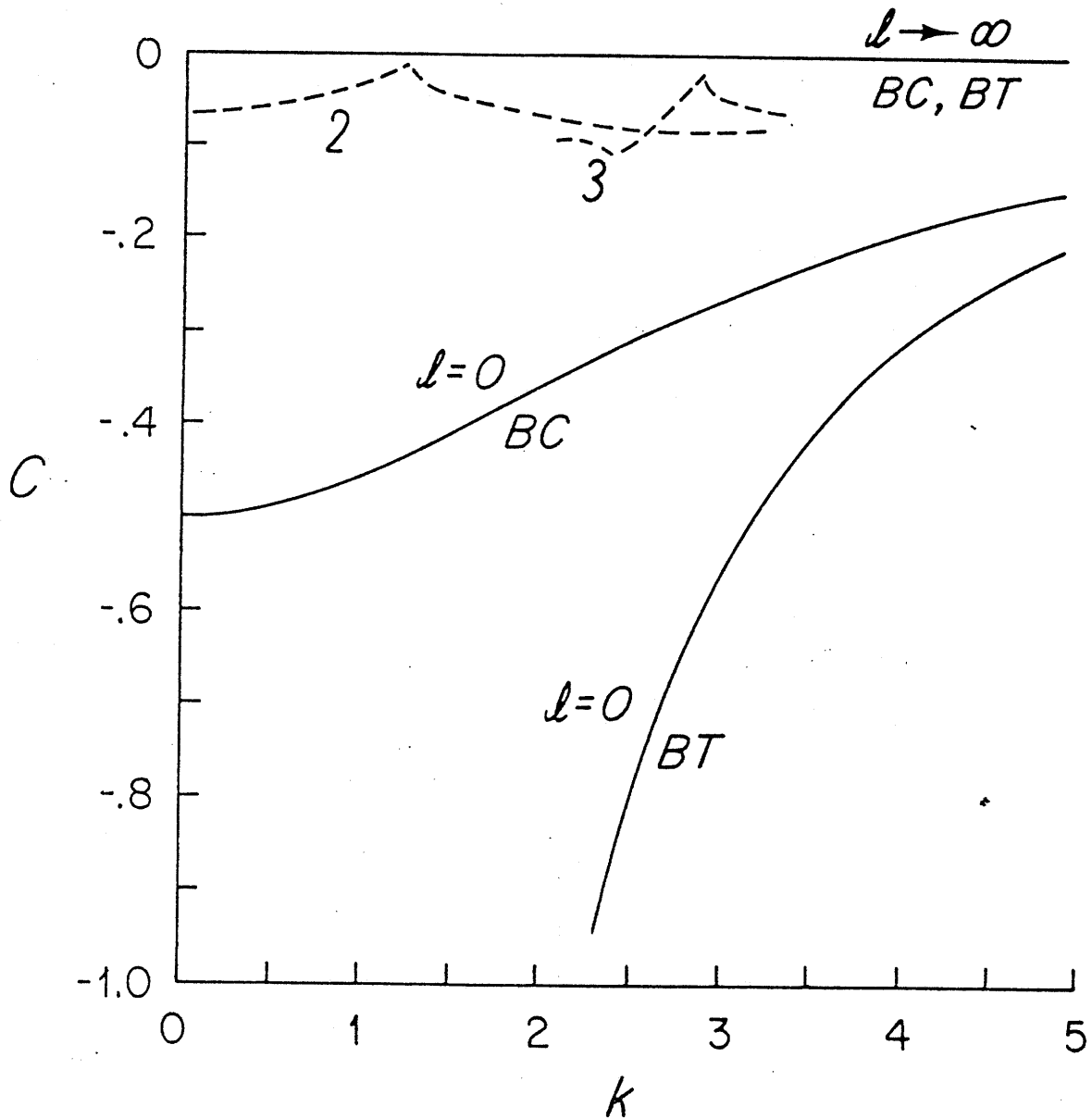
Figure 3.2.24

Rossby wave dispersion relation for a fluid with two layers of equal depth and vertical shear $(U_1-U_2) = .15$. The phase speed is shown as a function of k at $l = 0$ for (a) $\beta = .1$ and (b) $\beta = 1$. Notice that the phase speed is complex for $\beta = .1$. The solid curves are the real part and the dashed curves the imaginary part of c.
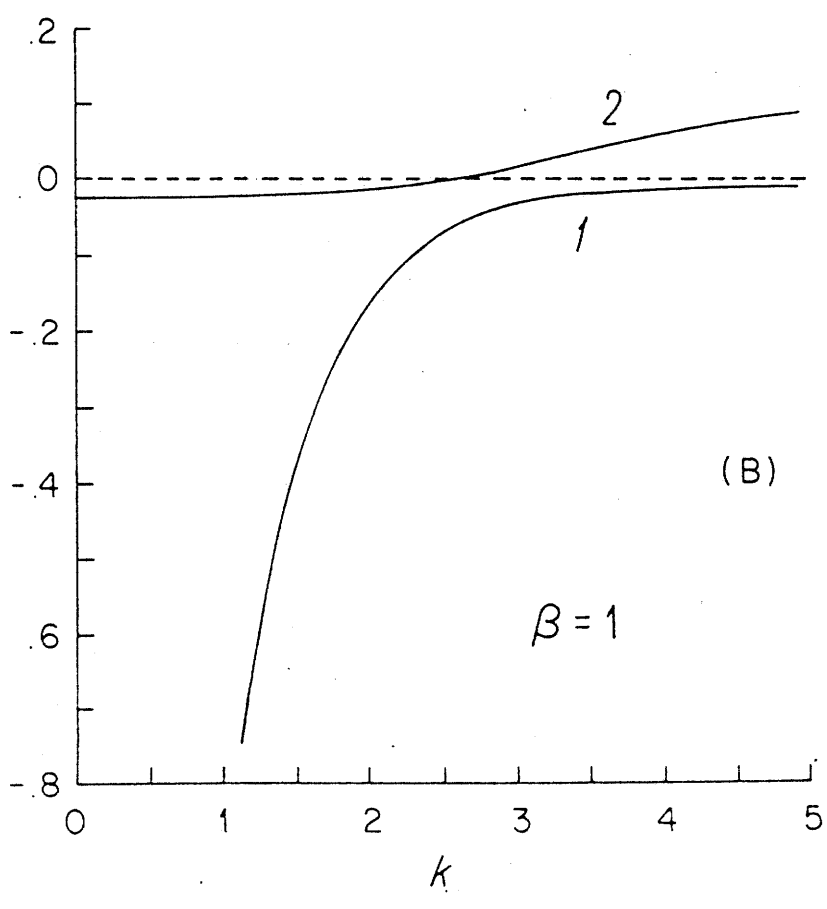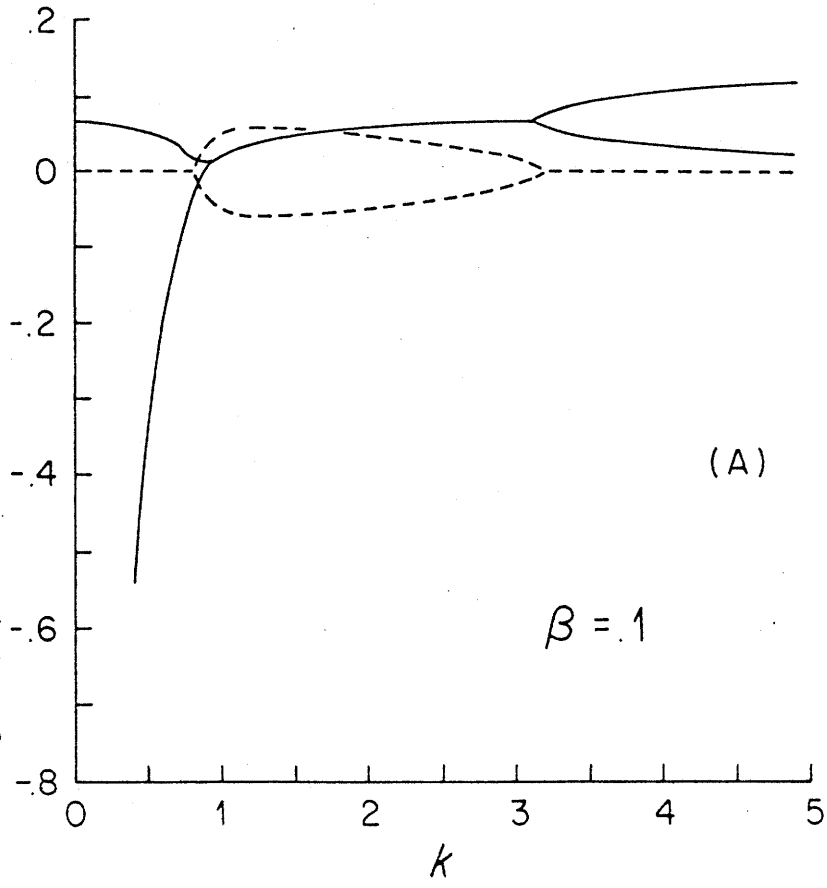
sponds to the baroclinic Rossby waves and the second to the barotropic Rossby waves.) For moderate-sized K, the phase speeds of the two modes do not overlap. Because the phase speeds of eastward jet instabilities are generally positive ($c_r > 0$), it is likely that the second type of Rossby wave will not be excited so that only the first type will be seen. (The first type is surface-intensified.) This is in contrast to the previously examined profile (3.2.4), where both the barotropic and baroclinic Rossby waves in the outer region were excited.

There is a small problem with using an infinite, north-south plane when there is vertical shear outside the jet: the boundary condition at $y = \pm \infty$ is difficult to define if the flow in the far field is baroclinically unstable. The following calculations were therefore initially made in a bounded channel. When β is small, solutions which are baroclinically unstable in the outer region are found - their energy source is clearly the potential energy of the local mean flow. However, it turns out that these baroclinically unstable modes are not matched by jet instabilities and that only neutral Rossby waves radiate energy from the jet. When it was ascertained that only neutral Rossby waves are involved in jet radiation, the hunt for the baroclinically unstable waves in Region III was discontinued and the northern and southern boundaries were removed. This aids the search for radiating solutions since growth rates of destabilized waves are significantly enhanced by removal of the boundaries. A later section deals with this effect of widely spaced northern and southern boundaries on radiating solutions.

The jet considered in this subsection is

$$U_{I1} = 1$$

$$U_{I2} = 0$$

$$U_{01} = .15$$

$$U_{02} = 0$$

$$D = 1.7$$

$$F = 5$$

$$H \rightarrow \infty$$

(3.2.6)

The vertical shear $(U_{01} - U_{02}) = .15$ was chosen rather arbitrarily to be large enough to allow the radiating solutions to be found easily (the growth rates of the radiating modes go to zero as the vertical shear is reduced, i.e., as the opportunity for radiation is eliminated). Using the scaling developed in Chapter 4, this vertical shear corresponds to about 6 cm/sec, which is a trifle high for the ocean interior. The profile and effective potential vorticity gradient are shown in Figure 3.2.25, for $\beta = 1$. Only eastward jets, i.e. $\beta > 0$, are considered.

The necessary conditions for instability are again figured in terms of each possible source of instability. At $F = 5$, there can be (1) horizontal shear instability in the upper layer for $\beta < 2.05$, (2) no horizontal shear instability in the lower layer due to $-U_{yy}$, (3) vertical shear instability of the central jet for $\beta > 5$, (4) vertical shear instability in Region III for $\beta < .75$, and (5) no mixed instability in the lower layer because of the second necessary condition which requires that $U \frac{\partial \pi}{\partial y} > 0$ somewhere for instability.

Radiation is likely to occur where the instability phase speeds fall beneath $U_{01} = .15$ since there are free waves in Region III with these phase speeds. Since instability phase speeds are small at high β, we can predict which modes are likely to radiate: the vertical shear mode, with phase speeds from 0 to 1, may radiate while the up-

a)
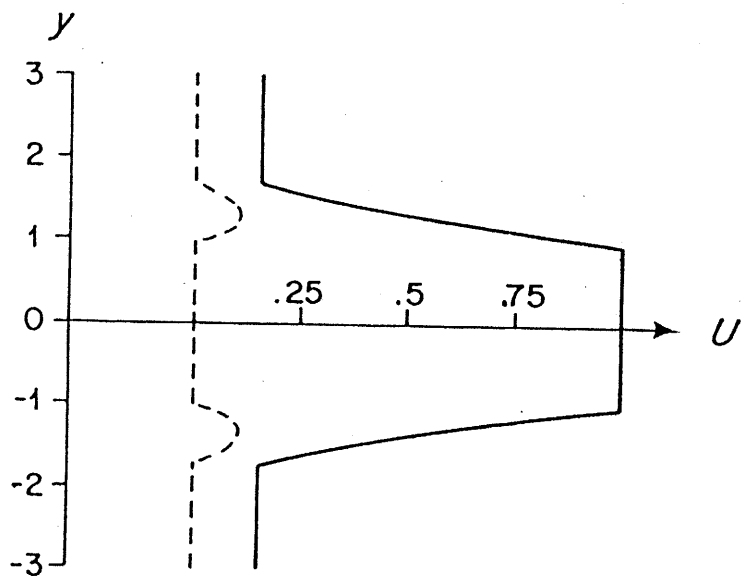
b)
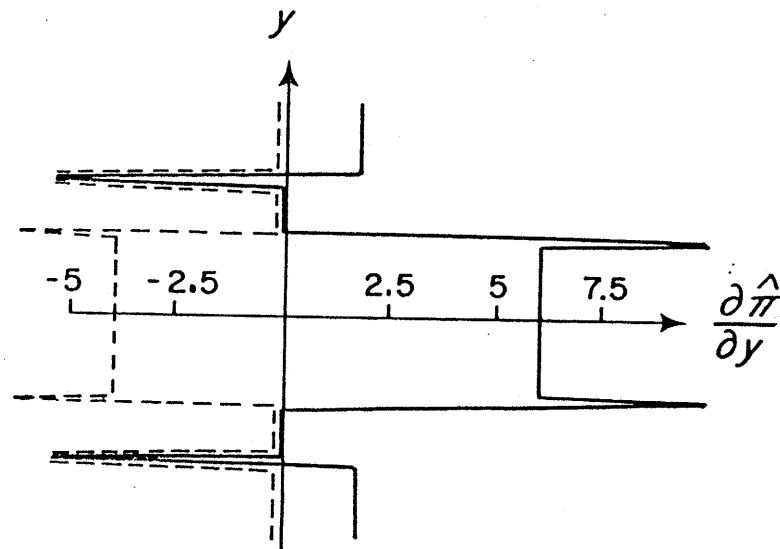
Figure 3.2.25

(a) U(y) as given by (3.2.7) and (b) $\partial\hat{\pi}/\partial y$, the effective potential
vorticity gradient (3.1.8).

per layer horizontal shear mode, with phase speeds from .15 to 1, is not likely to radiate.

Figure 3.2.26 is the stability diagram in the β-k plane, with the two modes plotted separately to reduce confusion. The two familar modes of the non-radiating jet [profile (3.2.3) and Figure 3.2.11] are present and are basically unaltered. These are basically trapped modes associated with the vertical shear of the central jet, with fast eastward phase speeds. In addition, there are many radiating modes, just as for the eastward jet with westward undercurrent (3.2.4). At high β for each mode and along the longwave side of Mode 3, there is no longer a neutral curve (just as in the previous profile with westward undercurrent): instead the neutral waves are slightly destabilized. In the stability diagram, the curve $c_i = .01$ is plotted. Again, there are two types of radiating mode: the basic instabilities associated with the jet, which are present as trapped instabilities even when the conditions for radiation are not, and destabilized Rossby waves, which are only present when conditions are ripe for radiation.

Dispersion relations at $\beta = 4$ (Figure 3.2.27) show how quickly the growth rate falls off near this curve. The imaginary phase speed c_i is of order 10^{-3} or 10^{-4} for the radiating modes. (A "truly" zero c_i registered as order 10^{-12} to 10^{-17} in the numerical scheme used.) The y-dependences, ℓ_1 and ℓ_2, are plotted in Figure 3.2.28: only one Rossby wave is excited in the far field, designated by ℓ_1. (This is the baroclinic mode when the vertical shear is zero and is a surface-intensified mode here.) The energy transfer at $\beta = 4$ looks nearly like that of the previous profile at

Neutral stability curves in the β-k plane for the profile (3.2.7). The notation is as in Figure 3.2.17. The radiating shortwaves become stable at 5 < k < 6. The high β cutoffs of modes 1 and 4 were not determined.
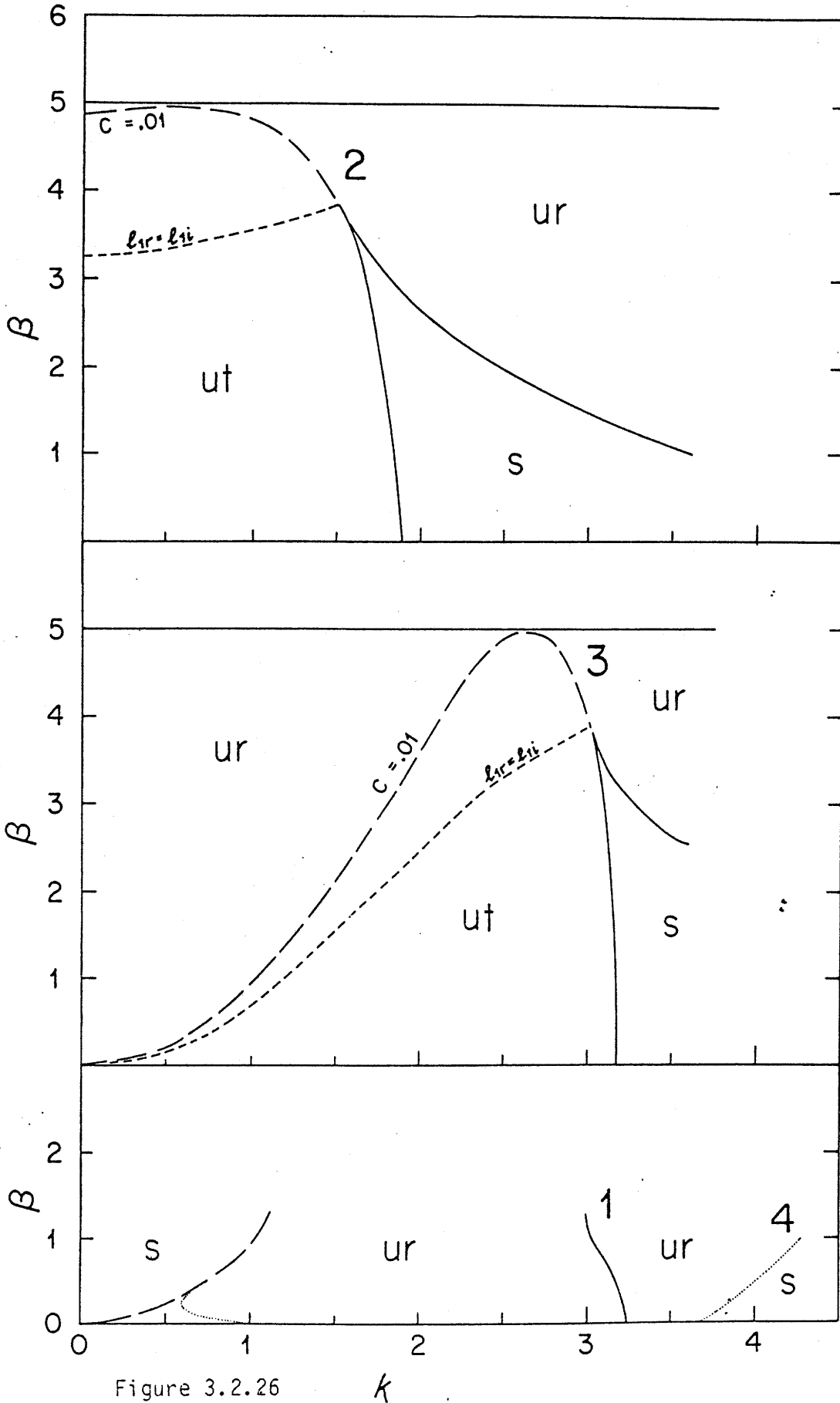
Figure 3.2.26
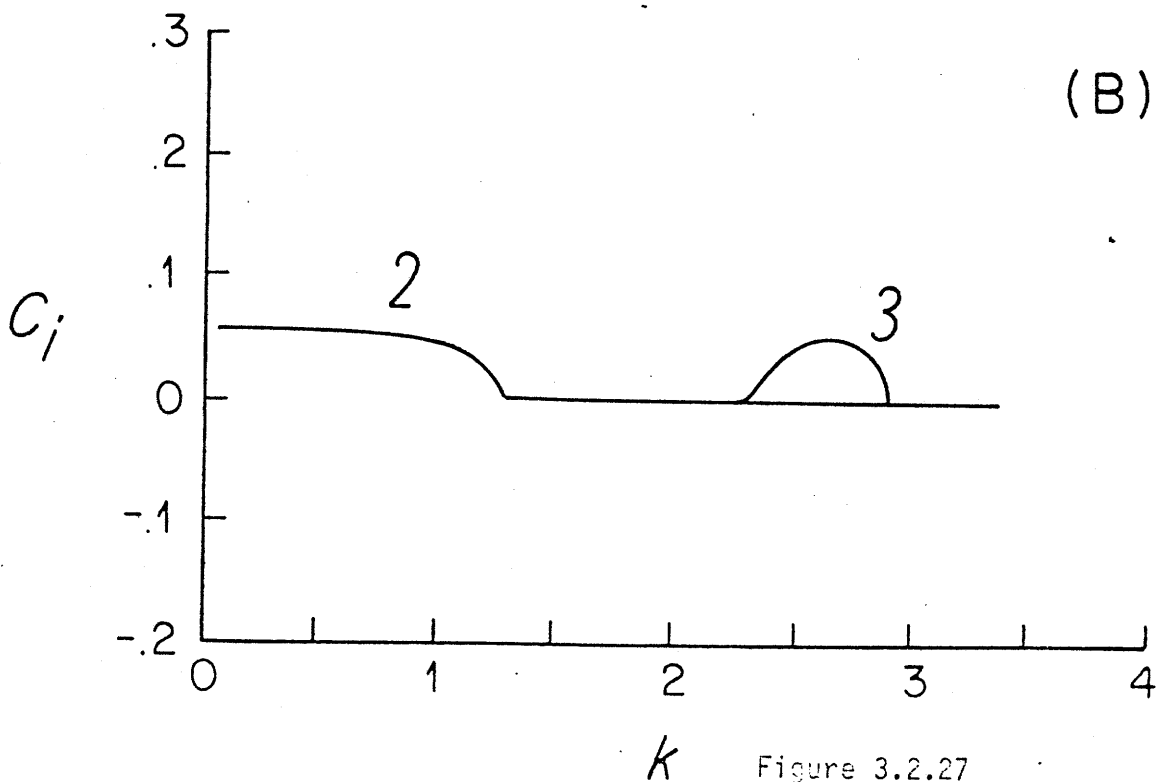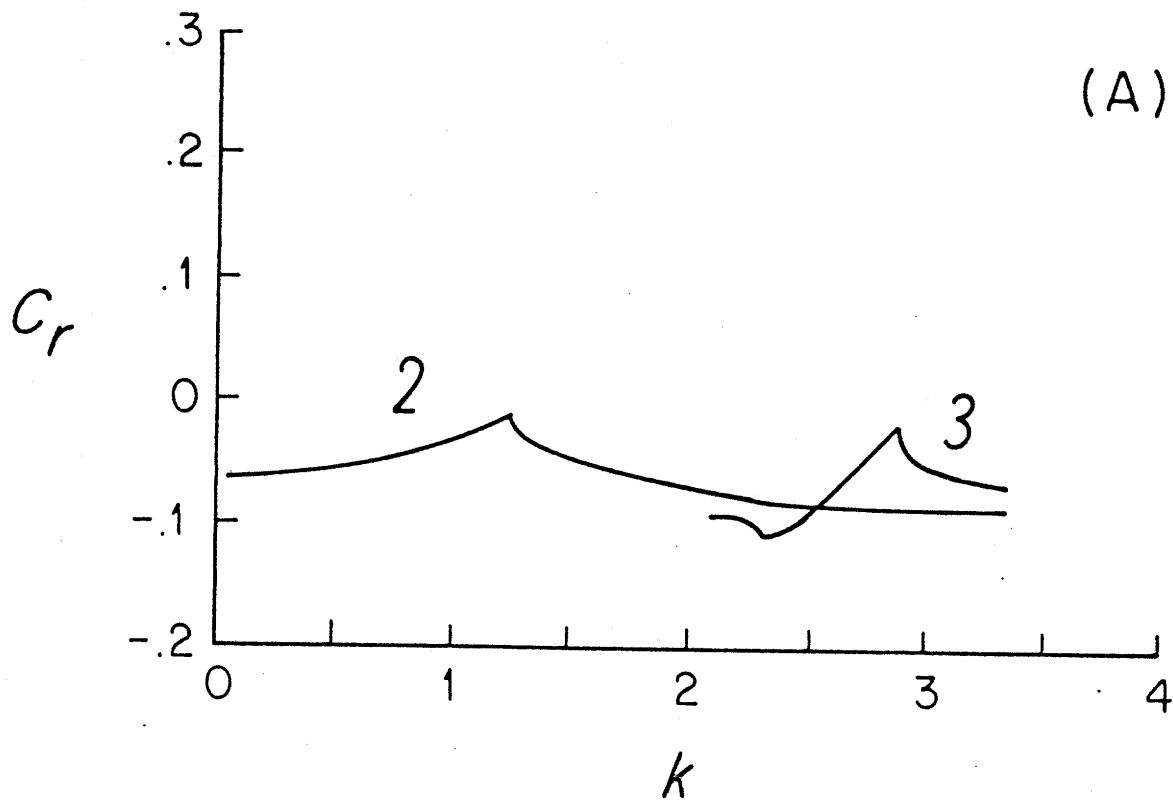
Figure 3.2.27

For the flow of Figure 3.2.25 at $\beta = 4$: (a) $c_r(k)$, (b) $c_i(k)$.

Figure 3.2.28

For the flow of Figure 3.2.25 at $\beta = 4$: (a) $\ell_1(k)$ and (b) $\ell_2(k)$. The solid curves are the real part and the dashed curves the imaginery part ℓ.
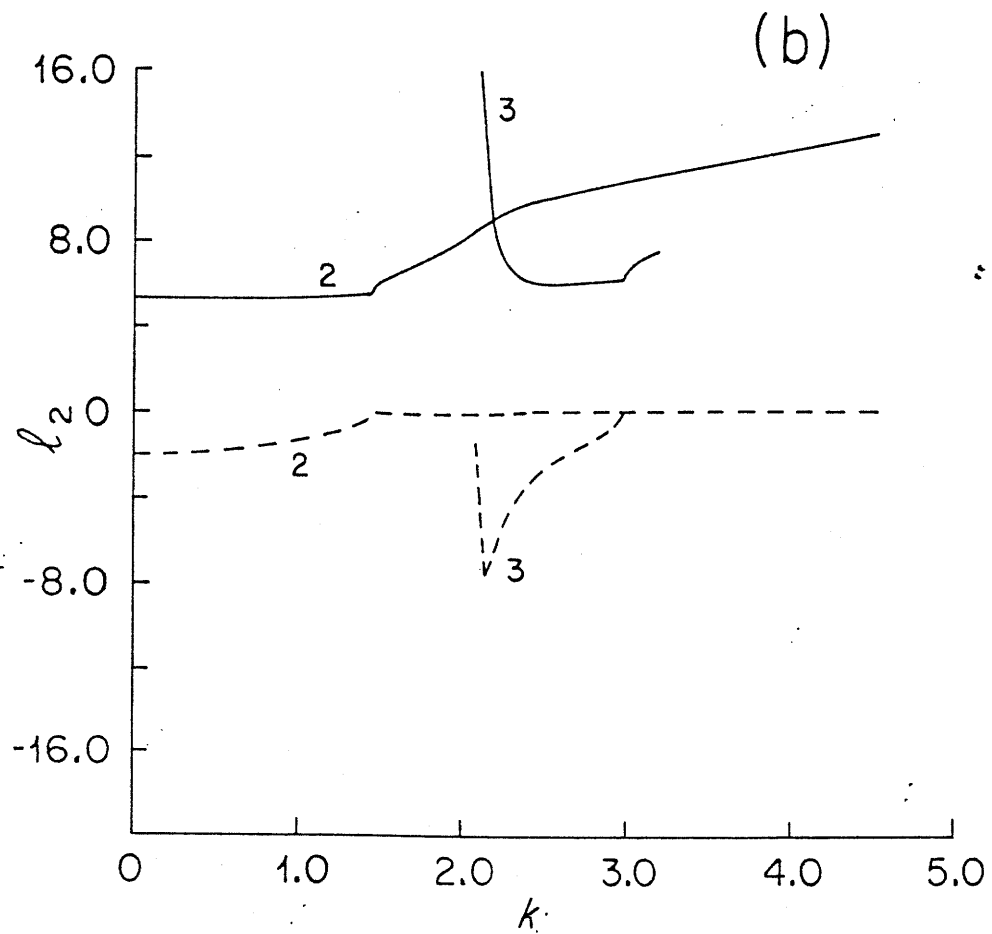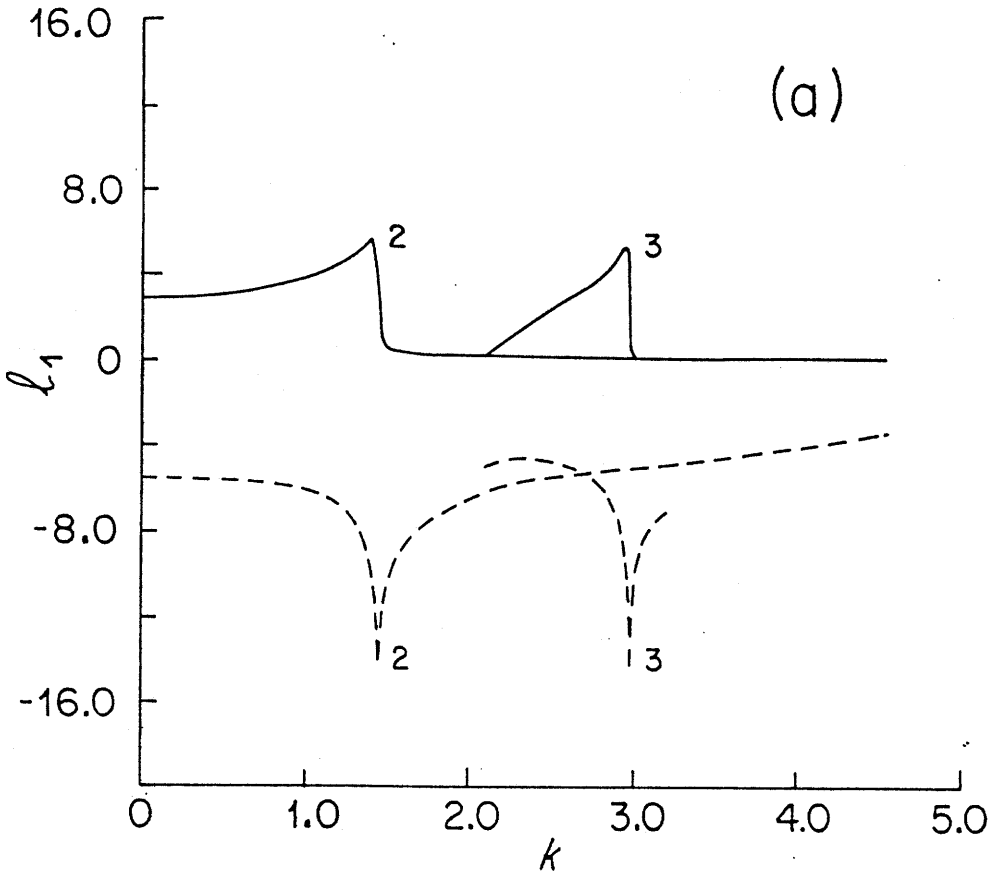
$\beta = 4$ and is not plotted: energy is transferred to the perturbations by baroclinic instability while the perturbations actually lose a little kinetic energy to the mean flow.

In addition to the two main modes, which are closely related to the vertical shear of the jet, there are two modes which may be associated with the horizontal shear. These are labelled Modes 1 and 4. Both modes have phase speeds smaller than .15 and radiate. Because the far field has a non-zero potential vorticity gradient at $\beta = 0$, there can still be radiating waves at $\beta = 0$. The solid boundaries at high k are well-defined stability boundaries. The dashed curve at low k for Mode 1 is nearly a neutral curve: the imaginary phase speed has a minimum here. Both Modes 1 and 4 appear to be unstable up to at least $\beta \sim 1.5$. They are possibly related to the upper layer horizontal shear (which can be unstable for $0 < \beta < 2.05$).

The eigenfunction of a radiating mode at $\beta = 4$ is shown in Figure 3.2.29. Its most important aspect, in addition to its slow meridional decay, is surface-intensification. Characteristically, the Reynolds stress extremum in the dominant layer (the surface layer) is farther away from the jet than the Reynolds stress extremum in the weaker layer (the bottom layer).

To summarize the results for the eastward jet with positive vertical shear in the exterior region, there are the two basic modes present in both non-radiating and radiating jets. Both modes have large growth-rates and strongly trapped solutions which appear to depend mostly on the vertical shear of the central jet for their energy. With positive verti-

BETA

0.0

K.C

2.55

0.096

0.008

Figure 3.2.29

A radiating eigenfunction for the profile (3.2.7): the trapped modes are very similar to the modes shown in Figure 3.2.6 and are not pictured here.
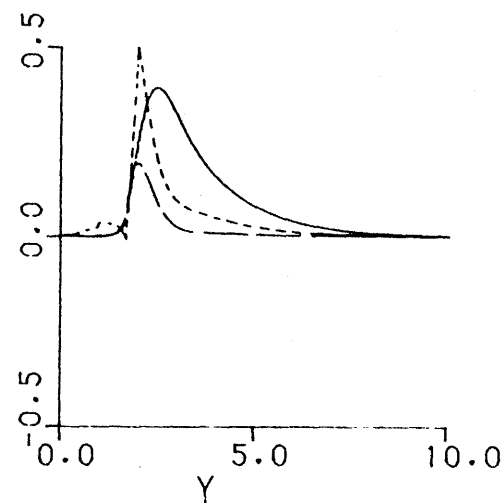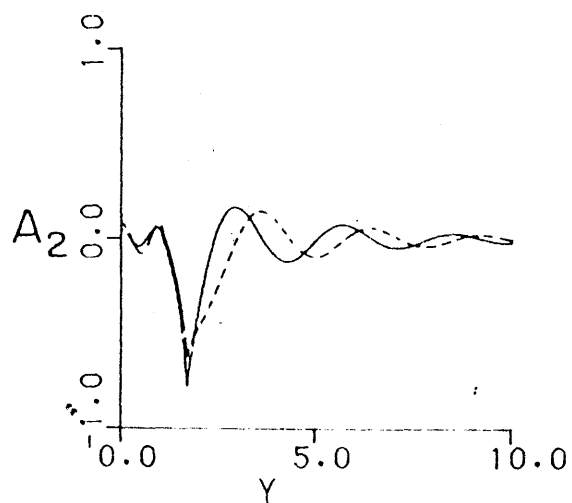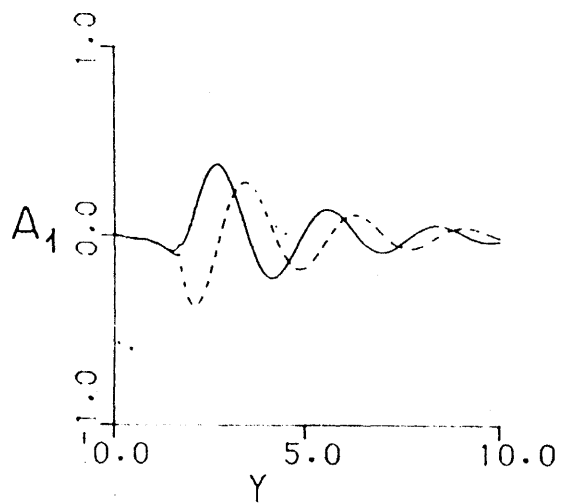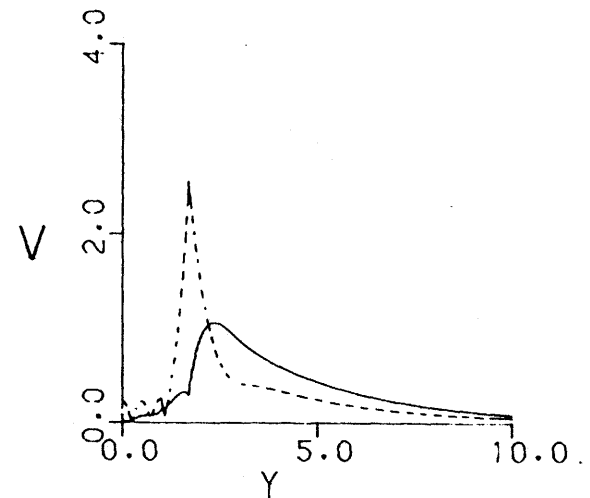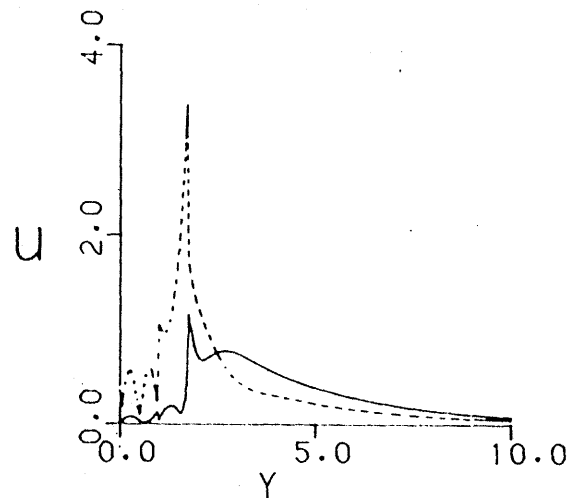
cal shear in Region III, some of these modes (those with $c_r < .15 = U_{01}$ and which are near the neutral curve) radiate. Modes with $c_r < .15$ and which fall on the neutral curve for the non-radiating jet are no longer stable but have small growth rates and connect to a whole range of destabilized Rossby waves. Although there is baroclinic instability in Region III when $\beta < .75$, the locally baroclinically unstable modes are not important for radiation of the central jet. Destabilized Rossby waves exist wherever Rossby waves exist in the β-k plane (and where the necessary conditions for instability are satisfied) for phase speeds, c_r, which are are determined by the jet. In other words, even though there <u>are</u> Rossby waves for <u>all</u> wavenumbers k, the jet does not select the phase speeds of the Rossby waves at high zonal wavenumber for destabilization. Thus there is a distinct shortwave cutoff for the destabilized modes. The mechanism whereby a particular phase speed is selected for destabilization is unclear.

(e) Eastward Jet with Small Negative Vertical Shear Outside the Jet

It was seen in the previous two sections that when conditions allow radiation, (i.e., allowing the instability phase speed to overlap the phase speed range of free Rossby waves) previously trapped modes may radiate if they satisfy the phase speed condition and that a host of Rossby waves is destabilized. This subsection completes the exploration of radiating jets by allowing <u>negative</u> vertical shear outside the jet.

The Rossby wave dispersion relation in Region III is again (3.2.1). The dispersion relation is plotted in Figure 3.2.30 as a function of k for

Figure 3.2.30

Rossby wave dispersion relations for a fluid with two layers of equal depth and vertical shear $(U_1 - U_2) = -.15$. The phase speed is shown as a function of k for $\ell = 0$ for (a) $\beta = .1$ and (b) $\beta = 1$. The solid curves are the real part and the dashed curves the imaginary part of ℓ.
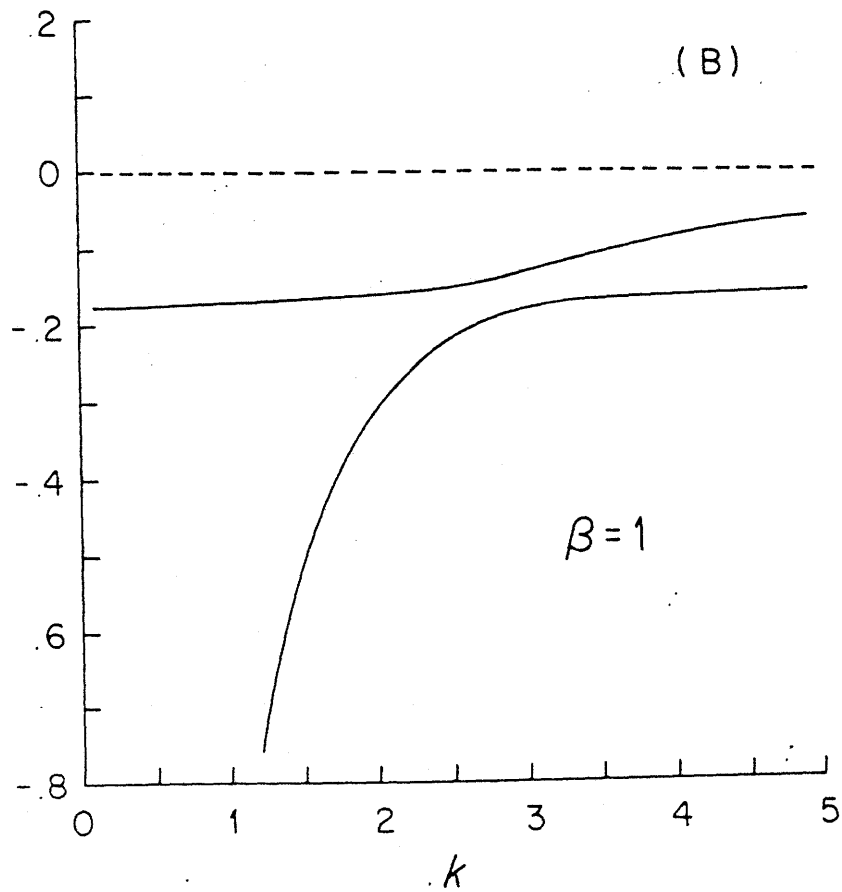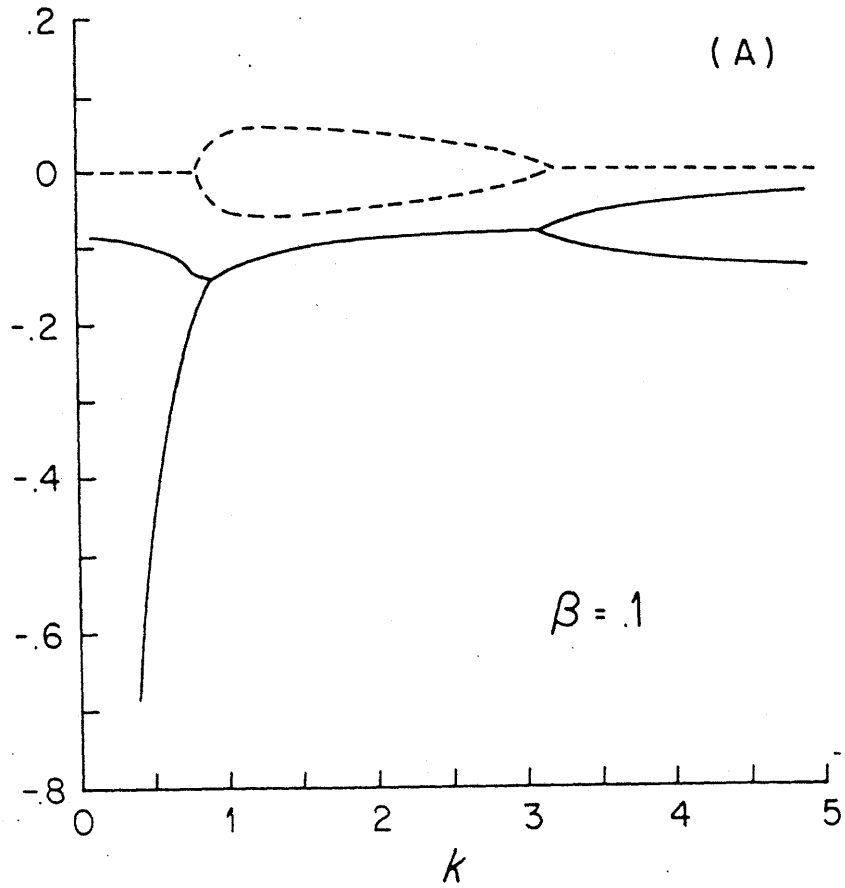
$\ell = 0$ (or equivalently, for the total wavenumber, K) with F = 5, U_1 -.15, U_2 = 0 and for β = .1 and 1.0. The flow is baroclinically unstable when β < .75. The phase speed limits from (3.2.1) for the two modes are [-.075 - $\beta/2F$, 0] and [-∞ , -.15]. The first range corresponds to the ⊕ sign in (3.2.1) and was the baroclinic Rossby wave when there was no vertical shear. The ⊕ mode is strongly bottom-intensified when its phase speed falls between 0 and -.15 (in this range, the phase speed is only westward with respect to the flow in the bottom layer).

The profile used is shown in Figure 3.2.31 with its effective potential vorticity gradient. The profile is

$$
\begin{aligned}
U_{I1} &= 1 & F &= 5 \\
U_{I2} &= 0 & D &= 1.7 \\
U_{01} &= .15 & H &\to \infty \\
U_{02} &= 0
\end{aligned}
\qquad (3.2.7)
$$

The necessary conditions at F = 5 for the various possible sources of instability are: 1) horizontal shear instability in the upper layer for β < 4.04, (2) horizontal shear instability in the lower layer for .655 < β < .75, (3) vertical shear instability in the central jet for β < 5, (4) vertical shear instability outside the jet for β < .75 and (5) no mixed instability in the lower layer because of the second necessary condition which requires that $U \frac{\partial \hat{\pi}}{\partial y} > 0$ somewhere for instability.

Radiation might occur if the instability phase speeds are negative as we can see from Figure (3.2.30) since the phase speeds of all Rossby waves outside the jet are negative. Since the instability phase speeds

a)

b)
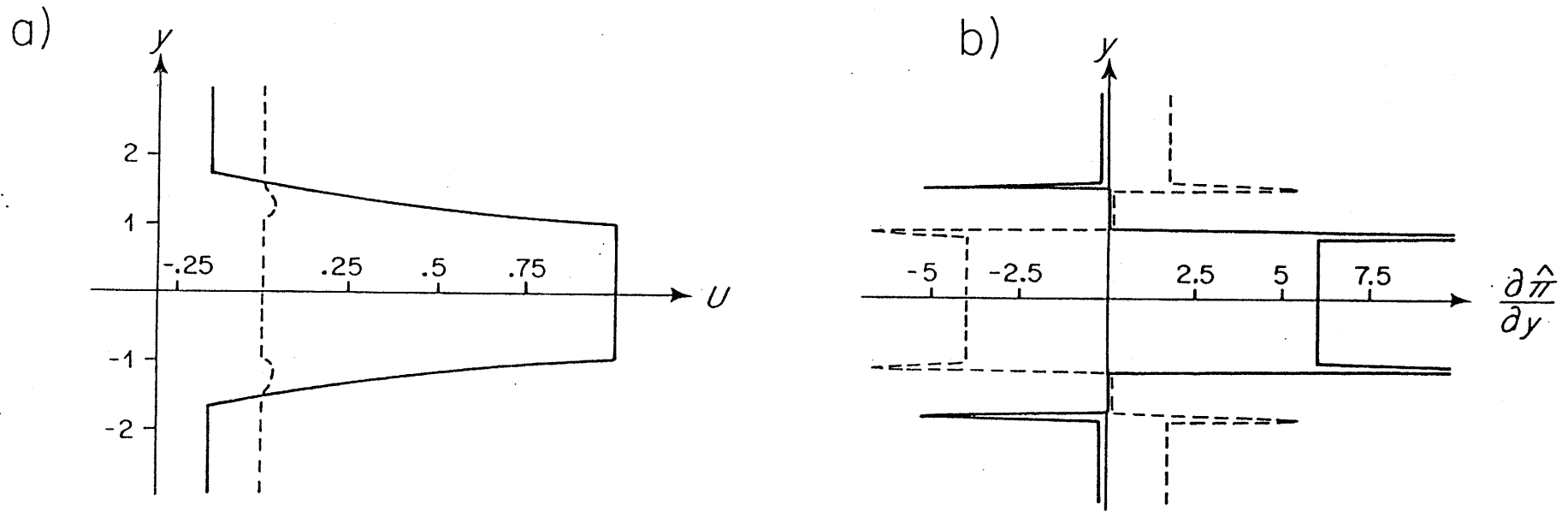
Figure 3.2.31

(a) U(y) as given by (3.2.8) and (b) $\partial\hat{\pi}/\partial y$, the effective potential vorticity gradient (3.1.8).

tend to the minimum flow speed as $\beta \to \beta_c$, there may be radiating modes for the upper layer instabilities at large β. The vertical shear modes are less likely to radiate because their velocity range is 0 to 1.

The stability diagram for this profile is shown in Figure 3.2.32. This is by far the most complicated stability diagram in this chapter. It is divided into three parts, showing the two familiar vertical shear modes and an additional mode. Modes 2 and 3 still become stable at the β_c decreed by the necessary conditions for instability for the vertical shear of the central jet. The additional mode, labelled "4", is an upper layer horizontal shear mode based on the range of β for which it is unstable: it is stabilized by a β of about 4, which is β_c for the horizontal shear in the upper layer.

One informal test for a radiating mode has been the relative size of $\text{Re}(\ell_1)$ and $\text{Im}(\ell_2)$. This criterion does not work for this profile. Instead, we must use the stricter criterion involving c_i/ℓ_r discussed in Chapter 2. This criterion shows that the only portions of Modes 2 and 3 which radiate is $.9 < k < 1.8$ in Mode 3. This is true even though c_r is negative for <u>both</u> modes at <u>high</u> β in the small areas between the $\ell_i = \ell_r$ curves and the neutral stability curves. However, $c_r \to 0$ <u>on</u> the neutral curve at high β and $c_i/\ell_r \to 0$ all along the neutral curve so these modes are not radiating. This confirms the original expectation that the vertical shear mode does not radiate for this profile. At low β, the longwave portion of Mode 3 is dominated by the horizontal shear mode: as noted above, this mode radiates (only the horizontal shear mode was expected to radiate for this profile).

Neutral stability curves in the β-k plane for the profile (3.2.8). The boundaries are as in Figure 3.2.17. (a) Longwave, vertical shear mode (2), (b) combined shortwave vertical shear mode and horizontal shear mode (3), and (c) horizontal shear mode (4). Notation is as in Figure 3.2.17. The dotted curve in (b) and (c) indicates that modes 3 and 4 are connected there.
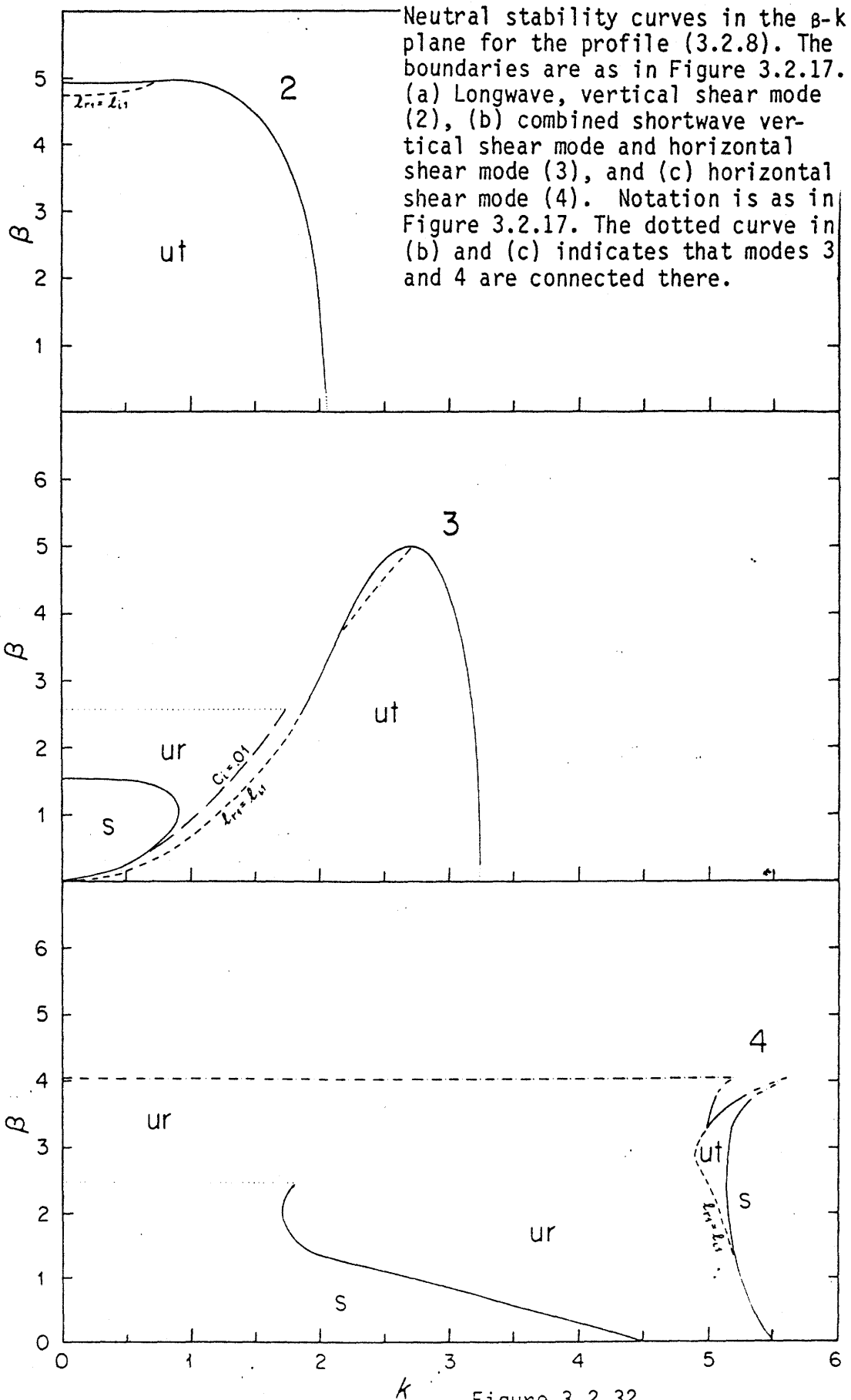
Figure 3.2.32

The new mode (4) which was not present for the other jets is a rad-iating, upper layer mode. At high k, Mode 4 has its highest growth rate and is basically trapped. However, Mode 4 radiates on the longwave side and is associated with destabilized Rossby waves. Because the potential vorticity gradient is non-zero when β is zero because of the vertical shear, this mode can radiate (and does) at $\beta = 0$. The neutral bounda-ries for this mode are (1)$\beta_c = 4.04$, where $c_r \to -.15$ and $c_i \to 0$, (2) the locus $c_r = 0$ and (3) a small section at high k where $\ell_i = 0$.

A pervading problem in finding neutral stability curves and assign-ing each mode to a given instability mechanism is the readiness of the modes to coalesce. In this jet, Modes 3 and 1 partially coalesce, making their stability diagrams quite messy around $\beta = 2.3$. The longwave, radi-ating modes for $\beta < 2.3$ are associated with Mode 3 while the longwave radiating modes for $\beta > 2.3$ are associated with Mode 4. The dotted boun-dary on each diagram gives an indication of this switch: note that the boundary could have been assigned to a constant k, rather than to a con-stant β. The trade is best illustrated with sketches of the imaginary phase speed at β's below and above the transition. At, say, $\beta = 2$, c_i for Modes 3 and 4 looks roughly like
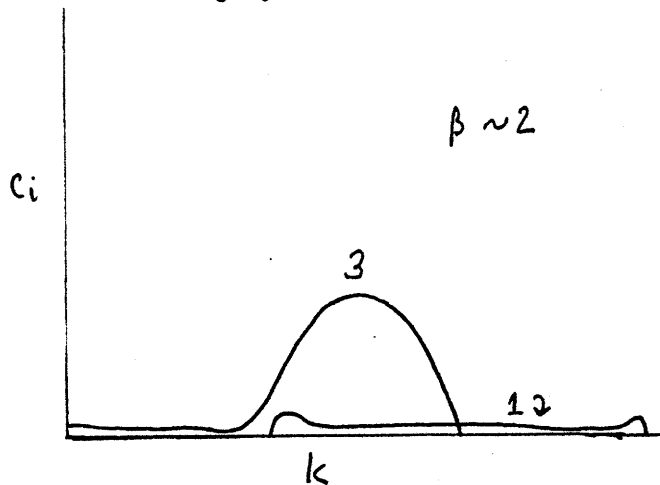
At $\beta = 3$, c_i looks roughly like
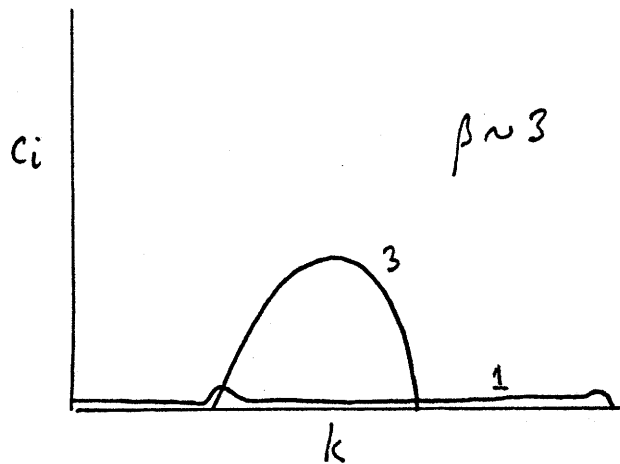
This trade of the radiating long waves is really only a complication of the problem and should not be dwelt upon, except insofar as it clarifies the difficult stability diagrams.

Dispersion relations for the different modes are shown in Figure 3.2.33 at $\beta = 1$. The y-dependences, ℓ_1 and ℓ_2 are shown in Figure 3.2.34. Once again, it is the ℓ_1 wave which is important for radiation. This was the baroclinic mode when the vertical shear was zero. This wave is much more likely to have phase speed between -.15 and 0 than the other Rossby wave (see Figure 3.2.30 and text). This ℓ_1 wave is bottom-intensified when its phase speed lies between 0 and -.15 since such a wave propagates much more successfully in a layer in which its phase speed is westward with respect to the flow speed. For this profile, this is the bottom layer. An example of a radiating mode is shown in Figure 3.2.35 where the bottom intensification is quite clear. This eigenfunction is interesting because it derives its energy from the horizontal shear of the upper layer but propagates meridionally in the lower layer. Hence its amplitude in the jet is large in the shear zone of the upper layer and

Figure 3.2.33

For the flow of Figure 3.2.31 at $\beta = 1$: (a) $c_r(k)$, (b) $c_i(k)$.
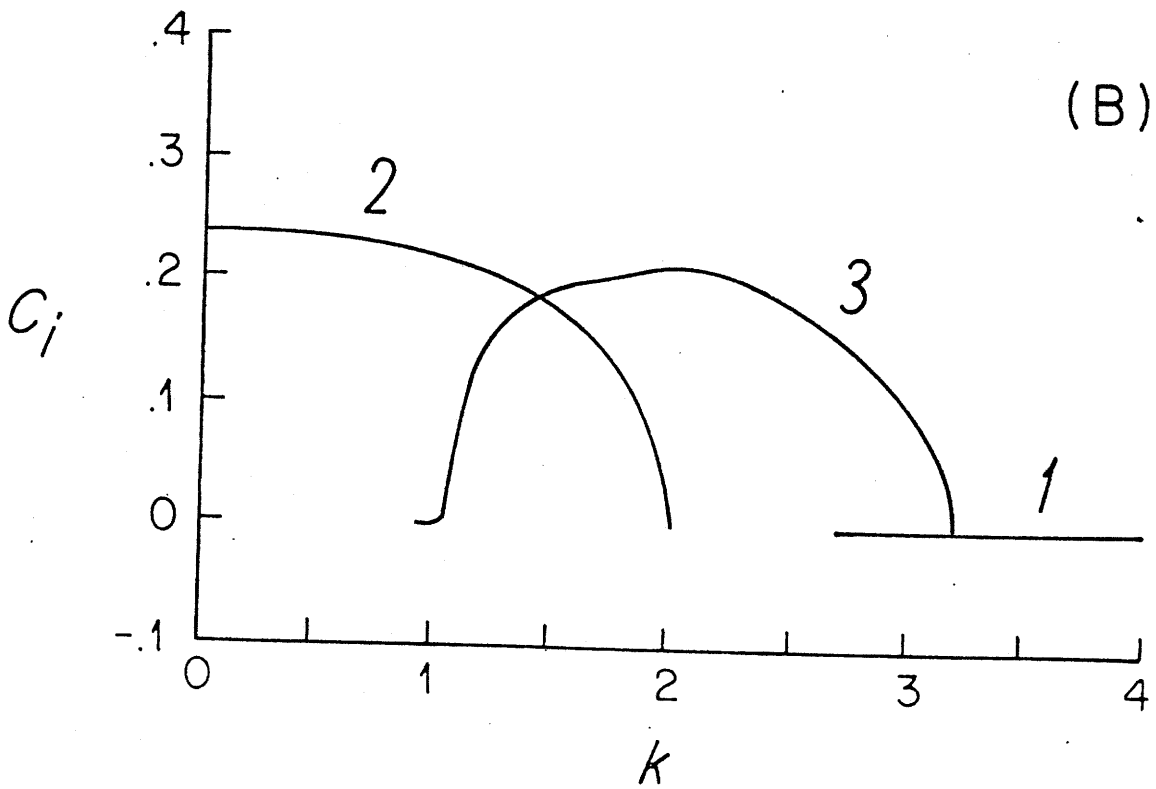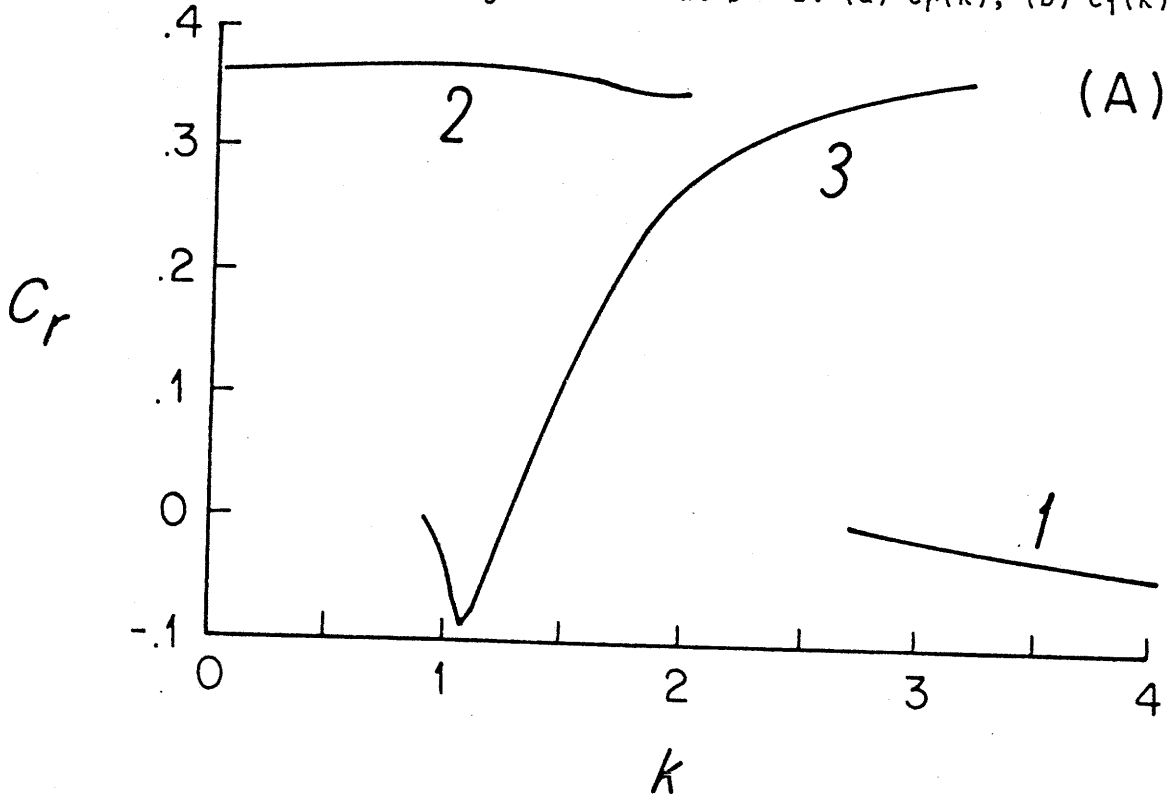
Figure 3.2.34

For the flow of Figure 3.2.31 at B = 1: (a) $\ell_1(k)$ and (b) $\ell_2(k)$.
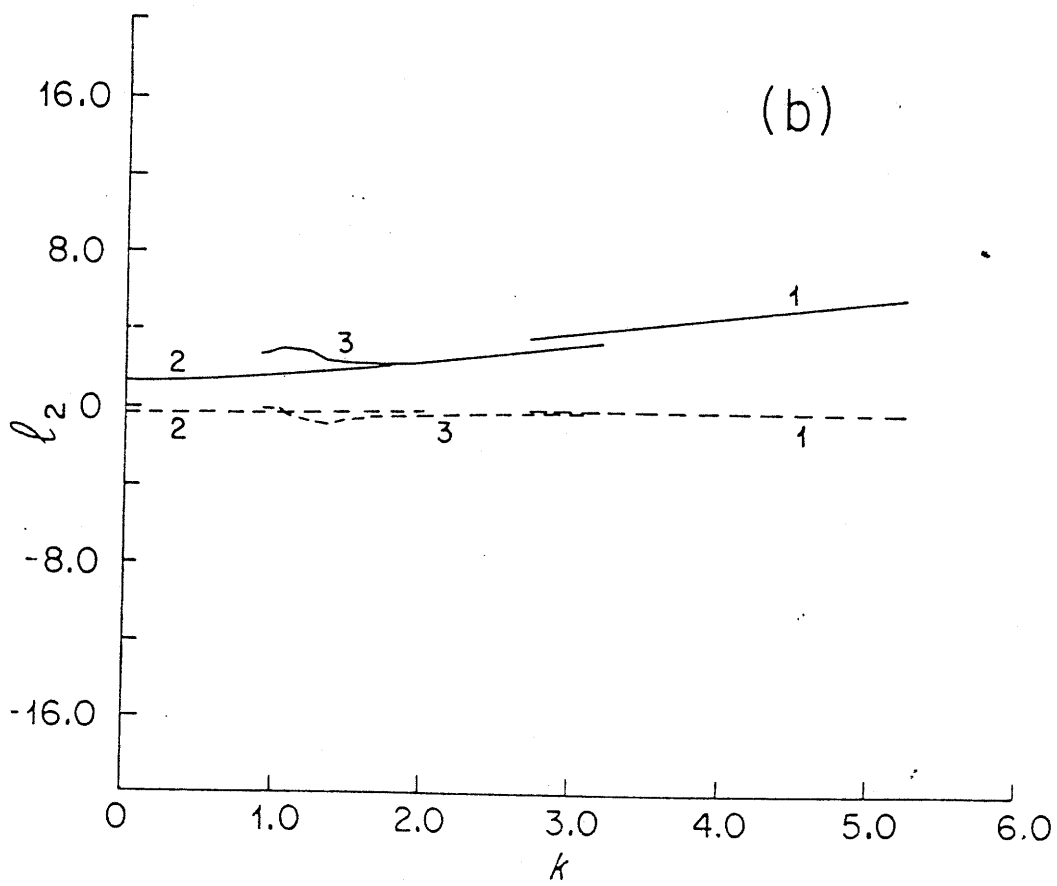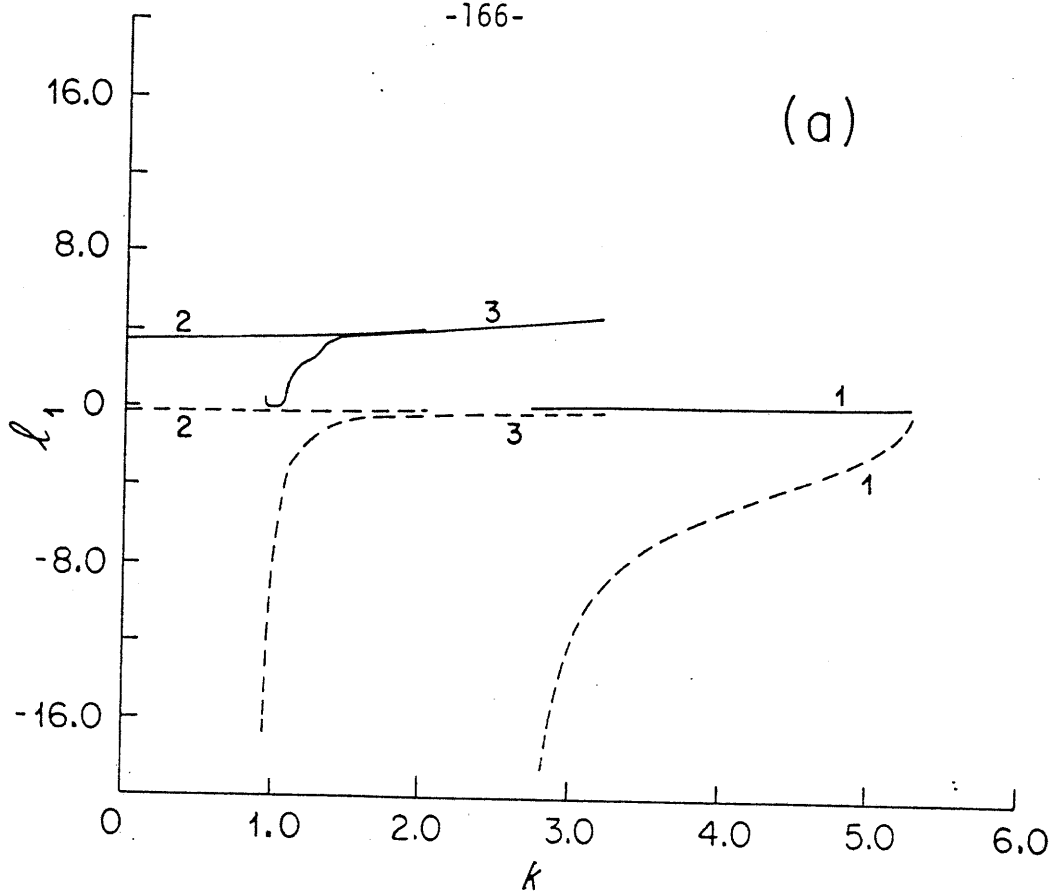
BETA
1.0

K.C
4.50
-0.046
0.004
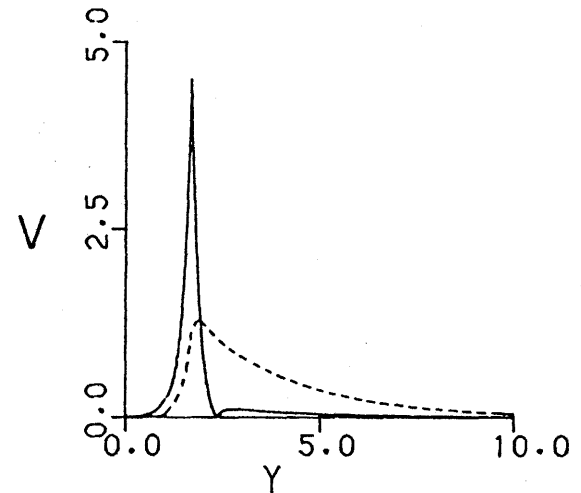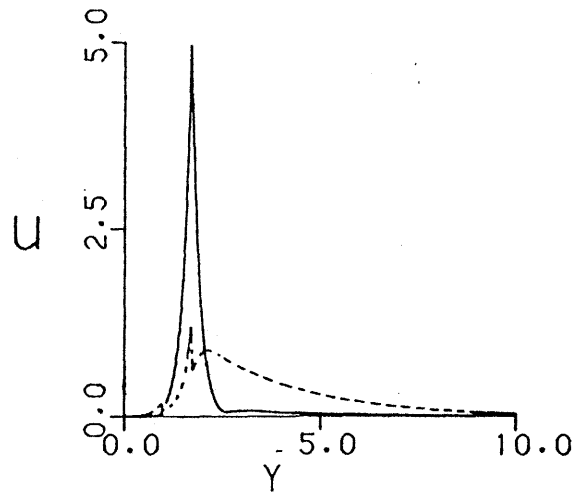
Figure 3.2.35

A radiating eigenfunction at β = 1 for the flow of Figure 3.2.31.
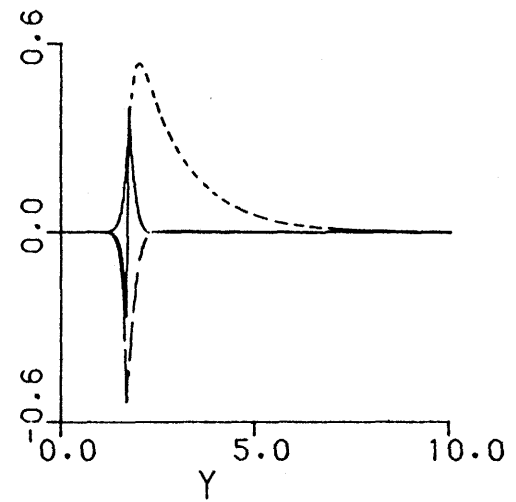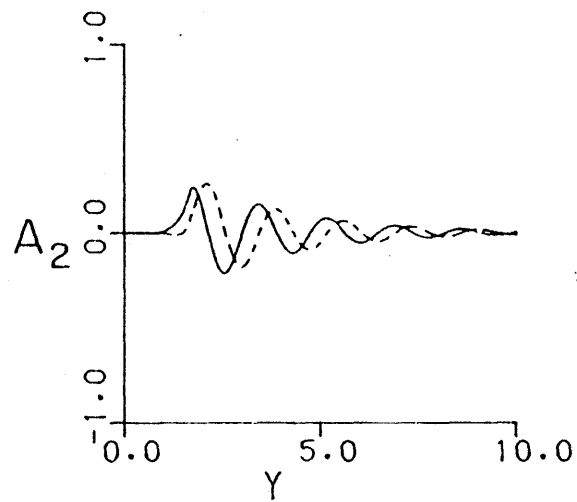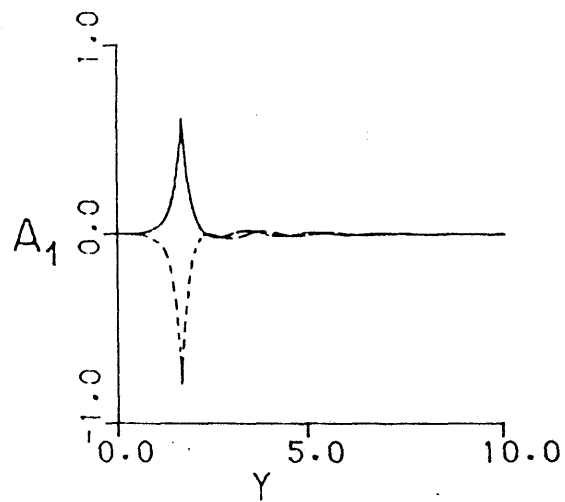
negligible elsewhere, while its amplitude outside the jet is large only in the bottom layer.

3.3   The Effect of Selected Parameter Changes on the Behavior of Non-Radiating Jets

Remarks are made here about the effects of changing the shear zone width (D-1), the stratification parameter F and the width of the total channel H on the instabilities. A limited examination of changes in lower layer velocity in the central jet, U_{I2}, was also made. No study was made of the effect of a range of vertical shears in Region III, $(U_{01} - U_{02})$. The effects of changes in some parameters were quite straightforward, while others were more subtle.

(a) Effect of Changes in Shear Zone Width, (D-1)

It was seen in Chapter 2 that a smaller shear zone width (relative to the central jet width) destabilizes the horizontal shear modes, as is only reasonable since the horizontal shear is increased when D is decreased. Not only are the growth rates higher and the maximum β_c for instability higher, but there are additional destabilized regions of the β-k plane. Only one horizontal shear mode occurs for the barotropic jet with shear zone width (D-1) = .7. (This width has been used for all baroclinic jet calculations so far in Chapter 3.) When the barotropic jet's shear-zone width is reduced to (D-1) = .5, there are additional β-destabilized modes. It is reasonable to expect this to happen for the two-layer jet also.

Two non-radiating jets with shear zones of width 0.5 were examined.

The results are compared with the results for the jets (3.2.2) and (3.2.3). The first profile considered is

$$U_{I1} = 1$$

$$D = 1.5$$

$$U_{I2} = .5$$

$$F = 5$$

$$U_{01} = 0$$

$$H \rightarrow \infty$$

$$U_{02} = 0$$

(3.3.1)

This flow is just the same as (3.2.2) and Figure 3.2.2 with a smaller shear zone. The necessary conditions are broken down just as for the jets of Section 3.2. For $\beta > 0$, there can be (1) horizontal shear instability in the upper layer when $\beta < 7.4$, (2) horizontal shear instability in the lower layer when $\beta < 4.7$, (3) vertical shear instability in the central jet when $\beta < 2.5$, (4) no vertical shear instability outside the jet and (5) no mixed instability in the lower layer.

The neutral stability diagram in the β-k plane is shown in Figure 3.3.1. The diagram is again split into two parts: (a) both vertical shear modes and (b) modes associated with the upper layer horizontal shear. The vertical shear modes are virtually unchanged by the widened shear zones. The main horizontal shear mode, indicated by "1", is unstable to much higher β than before because β_c predicted by the necessary conditions for instability is higher. There are two additional (β-destabilized) modes, associated with the horizontal shear in the upper layer. A separate horizontal shear mode for the lower layer was not found. As in the barotropic jet, the horizontal shear modes at high β are probably higher, cross-jet, symmetric modes of the barotropic instability.

Neutral stability diagram in the β-k plane for the profile (3.3.1). (a) Both vertical shear modes (2) and (3) and (b) upper layer horizontal shear modes (1). Because of the reduced shear zone width, there is more than one horizontal shear mode

Figure 3.3.1
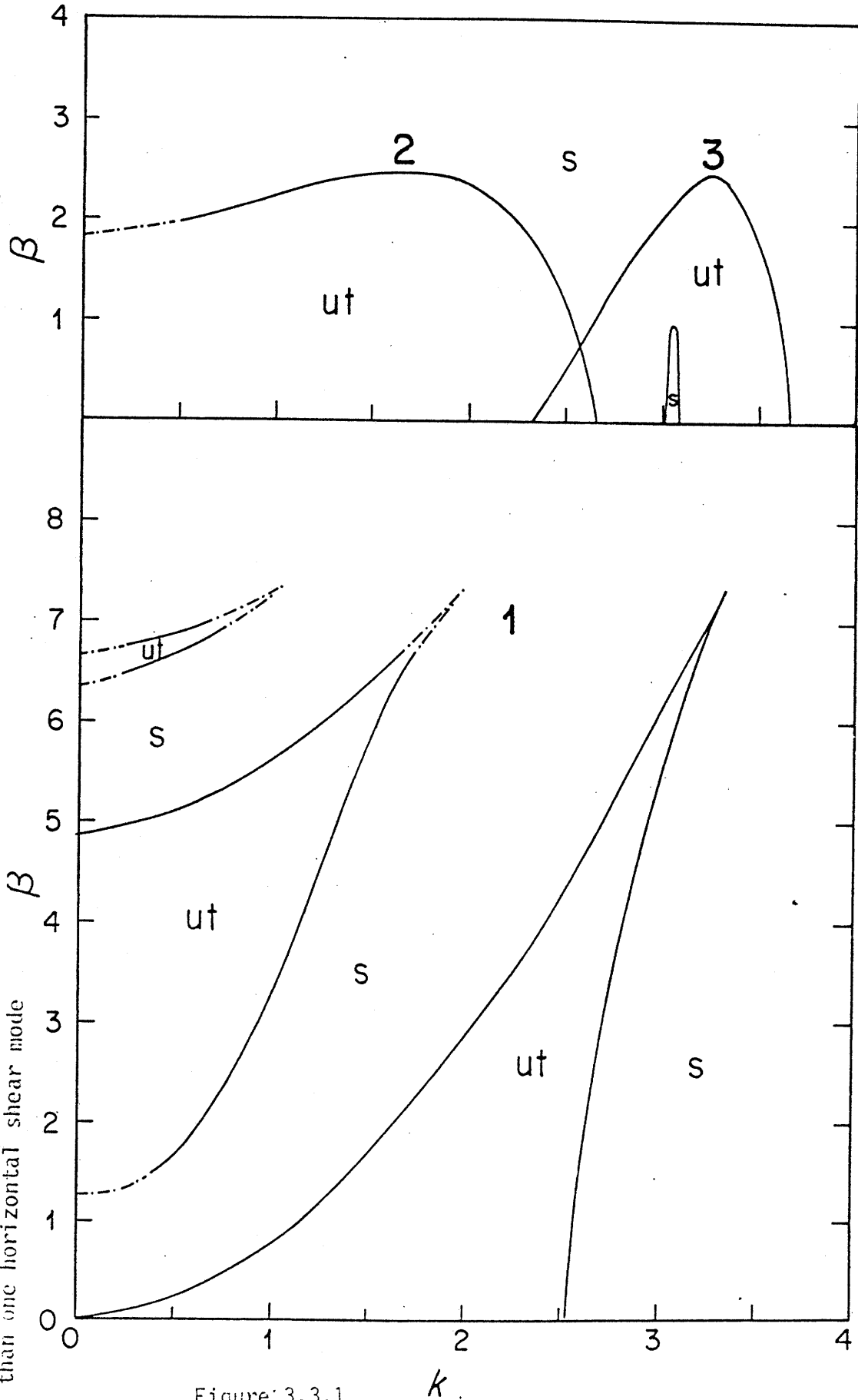
When the horizontal shear in the lower layer is removed, the profile, which is the counterpart of (3.2.3) is

$$U_{I1} = 1$$
$$D = 1.5$$
$$U_{I2} = 0$$
$$F = 5 \qquad\qquad (3.3.2)$$
$$U_{01} = 0$$
$$H \to \infty$$
$$U_{02} = 0$$

The types of instability which might occur, based on the necessary conditions for instability for $\beta > 0$ are (1) horizontal shear instability in the upper layer when $\beta < 6.75$, (2) no horizontal shear instability in the lower layer, (3) vertical shear instability in the central jet when $\beta < 5$, (4) no vertical shear instability outside the jet and (5) no mixed instability in the lower layer.

There are only two separate modes and both are shown in the stability diagram, Figure 3.3.2. The effect of the narrowed shear zone is again to raise the β_c associated with the horizontal shear zone in the upper layer. The horizontal and vertical shear modes have coalesced, as they do when $D = 1.7$, but the horizontal shear mode can be seen clearly at $\beta > 5$, in the peculiar shapes of the neutral curves for both modes. The horizontal shear mode "1" of Figure 3.3.1 has coalesced with Mode 3 and pops out at $\beta > 5$. The first β-destabilized mode of Figure 3.3.1 has coalesced with Mode 2 and accounts for all the instability for $\beta > 5$.

Changing D clearly changes the relative importance of horizontal and vertical shear instabilities. This trade-off between the instabili-
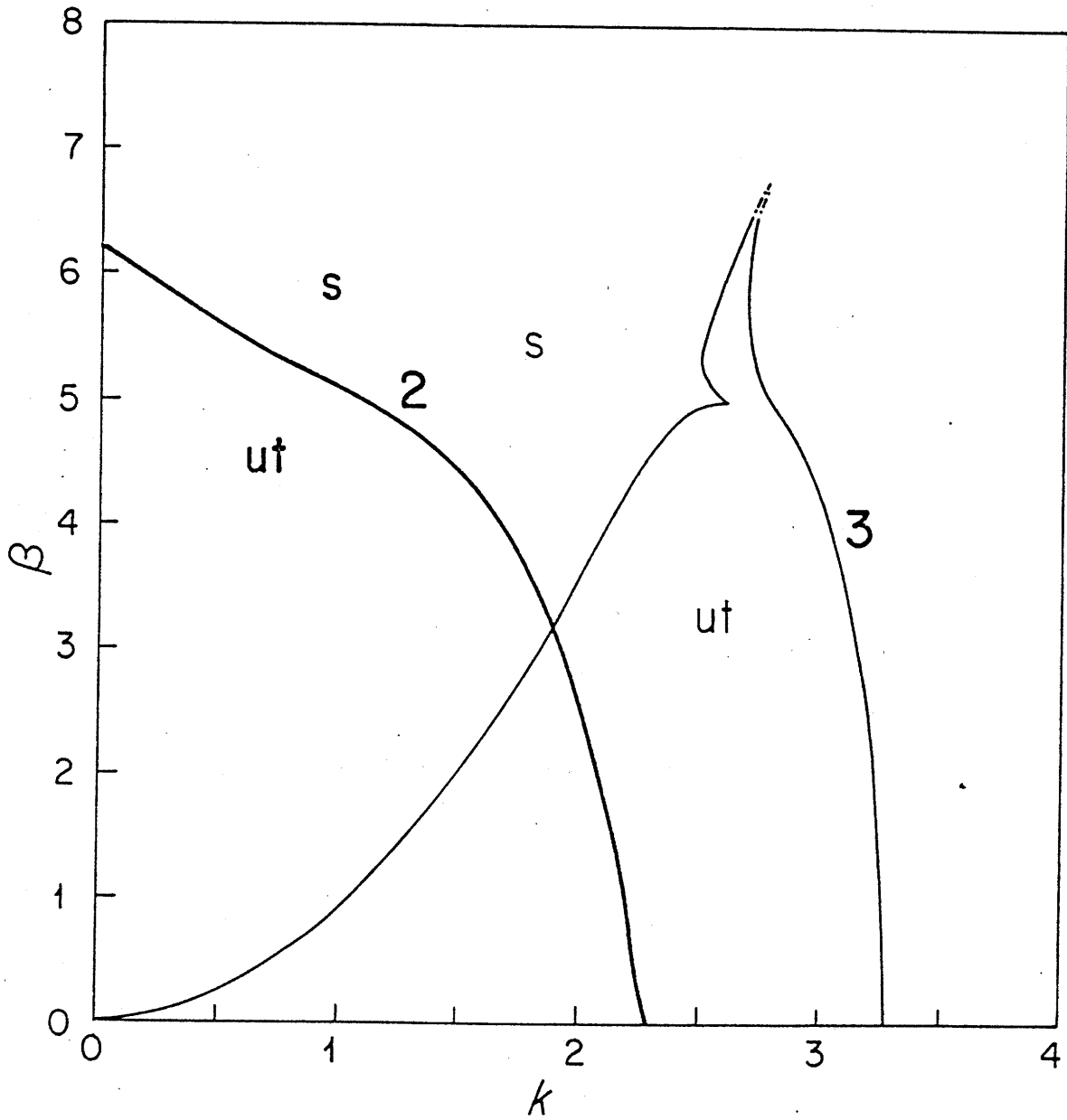
Figure 3.3.2

Neutral stability diagram in the β-k plane for the profile (3.3.2).
The horizontal shear modes of Figure 3.3.1b are coa- lesced with the
vertical shear modes.

ties dominant in a wide jet (baroclinic instabilities) and the instabilities dominant in a narrow jet (barotropic instabilities) is well-known.

(b) Effect of Changes in F

The effect of changes in F on baroclinic instability is also well known. F is the squared ratio of the length scale to the internal deformation radius. As the stratification is weakened, the deformation radius shrinks and F increases. As F increases, the flow becomes more unstable (there are more baroclinically unstable modes in a channel and the growth rates increase), because the interface between the two layers becomes increasingly pliant.

For instance, the dispersion relation (3.2.5) at $\beta = 0$ says that $F > K^2/2$ for the perturbation to grow. If the flow is confined to a channel of half-width L, the total wavenumber is $K^2 = k^2 + (n+1/2)^2(\pi/L)^2$ which is always non-zero if L is finite. Table 3.3.1 lists the minimum value of F required for the first ($n = 0$) and second ($n = 1$) modes to be unstable for three channel half-widths, L:

<div align="center">

Table 3.3.1

L	F_c ($n = 0$)	F_c ($n = 1$)
1.0	1.23	11.10
1.5	.55	4.93
1.7	.43	3.80

</div>

The disturbances will see the jet as a waveguide with "walls" somewhere beyond L = 1. If the "walls" appear to be at $y \geq D$, there is a good chance that there will be two vertical shear modes when $D \geq 1.5$ and $F = 5$.

A stability diagram in which F and k are varied (at $\beta = 0$) and where the flow profile is otherwise given by (3.2.3) is shown in Figure 3.3.3. This figure complements Figure 3.2.11 in which β and k are varied at F = 5. The diagram may not be complete: only Modes 2 and 3 of Figure 3.2.11 were examined. Figure 3.3.3 shows the regions of the F-k plane which are unstable, at $\beta = 0$. Mode 2, identified as the (n = 1) baroclinic instability mode, is stable when F < 1.0. Mode 3, which is a combination of the lowest baroclinic instability mode and the horizontal shear mode, is unstable at all F's: the instability at F = 0 is undoubtedly due to barotropic instability, since there cannot be baroclinic instability when F = 0. Such a result was found by Hart (1974), who examined the effects of changing F and the relative layer depths on the relative amounts of barotropic and baroclinic energy transfer to the most unstable wave for a two-layer flow with a jet confined to the upper layer, just as in the present case.

(c) Effect of Northern and Southern Boundaries

Imposing northern and southern boundaries at a distance that is large compared with the jet width has no effect at all on the trapped modes, which do not influence the flow much beyond the jet. However, boundaries do change the behavior of the radiating modes quite strongly. The net effect is to allow standing modes and to lower their growth rates.

Figure 3.3.4a and b shows the effect of the walls on the growth rate of the radiating modes associated with Mode 3 of the jet (3.2.3). Boundaries are placed at (a) ∞ and (b) H = ±100. When there are walls, there are well-defined c_i minima, each minimum corresponding to a separate standing
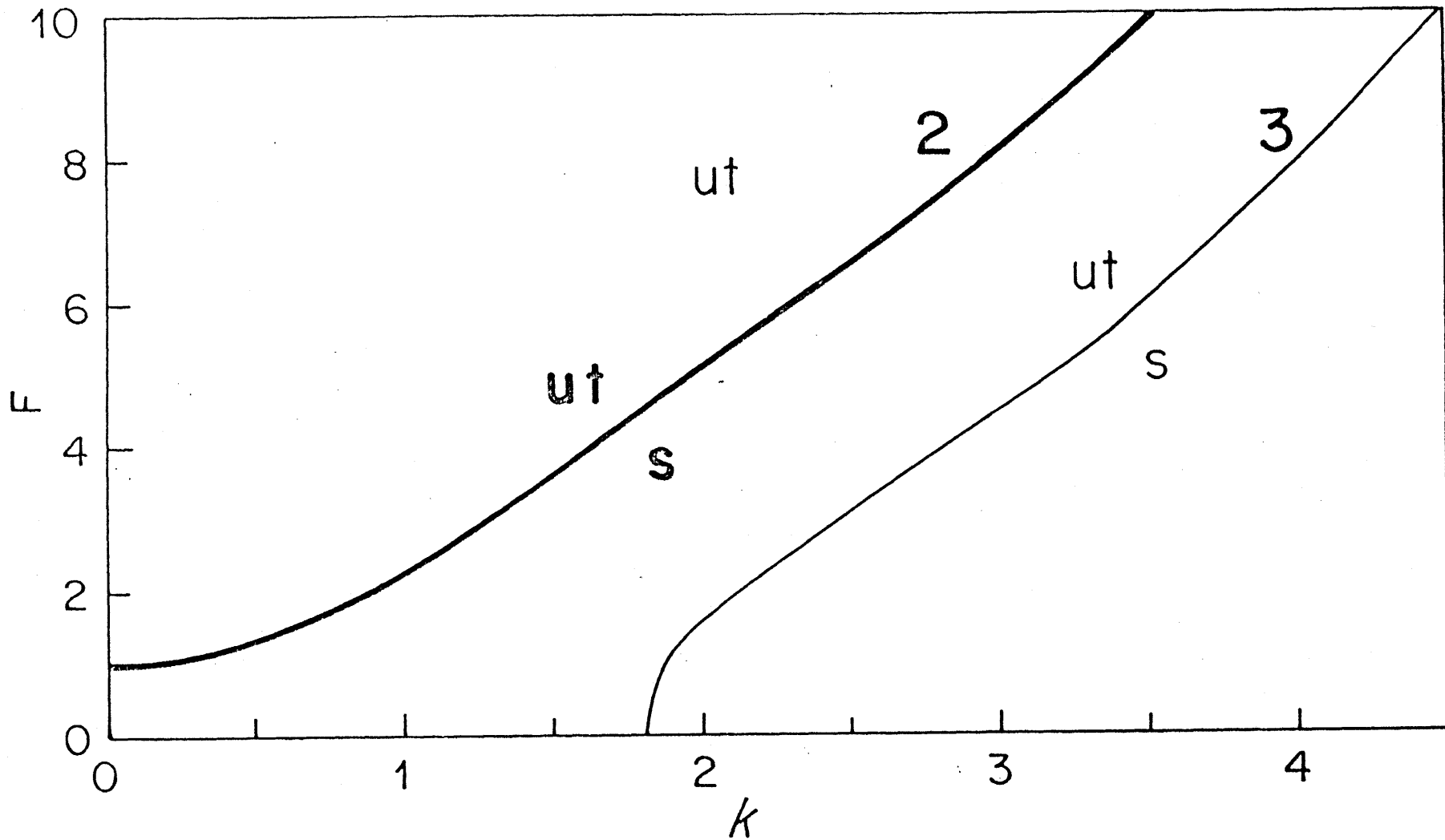
Figure 3.3.3

Neutral stability diagram in the F-k plane for the profile (3.2.3), at $\beta = 0$. There are two unstable modes (see Figure 3.2.9 for the complementary diagram in the β-k plane).

Figure 3.3.4

The effect of channel walls which are distant from the jet relative
to the internal deformation radius: the imaginary phase speed c_i
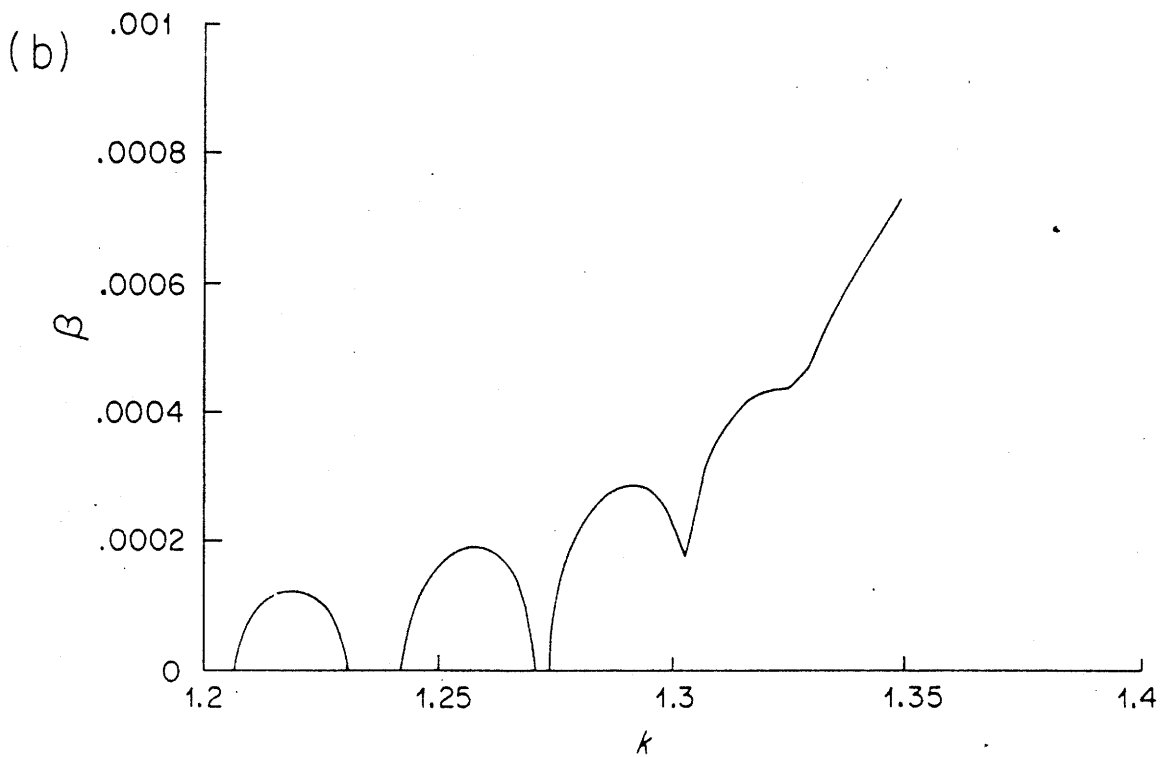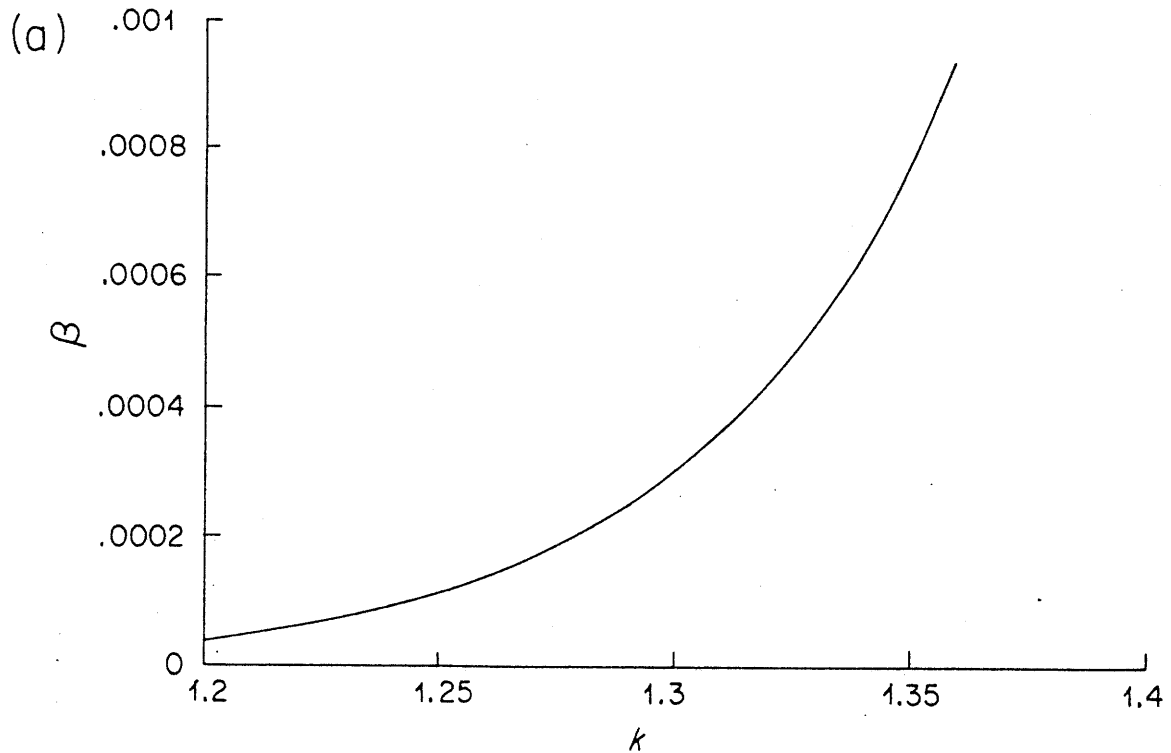
of the long wave, radiating part of the mode shown in Figure
3.2.19b, at $s = 2$, for (a) a channel without walls and (b) a channel
with walls at $H = \pm 100$.

wave of the entire channel. Independent calculations of the channel modes is difficult because of the thin, intense jet in the middle. (The y-wavelengths of the instabilities here are of the order of the jet width, so the waves may be shifted significantly). One might guess that the c_i minima correspond to the standing modes: since standing waves are reflected from the wall, they decay very little in the y-direction, which is one property of waves with minimum c_i.

A similar observation of the effect of boundaries on radiated waves was made by Lindzen (1974), who looked at Kelvin-Helmholtz instability in a fluid which supports internal waves. Radiating instabilities of the shear layer were found and their dispersion relations were somewhat disturbed by the presence of top and bottom boundaries.

(d) The Effect of Variable Vertical Shear in the Central Jet.

Changes in the vertical shear in the central jet should shift the relative importance of baroclinic and barotropic instability. This is seen in the results for jets (3.2.2) and (3.2.3). In the first jet, $U_{I2} = .5$, and in the second jet, $U_{I2} = 0$, but otherwise they were identical. The increase in shear from $(U_1 - U_2) = .5$ to $(U_1 - U_2) = 1.0$ results in an obvious increase in importance of the vertical shear mode in the jet center. It is also accompanied by a coalescence of the main horizontal shear mode with the shortwave vertical shear mode. (When there are the high-β, destabilized horizontal shear modes, they coalesce with the longwave vertical shear mode.) Thus, even when the horizontal shear of the upper layer is unchanged, but the lower layer shear is removed, the overall horizontal shear sensed by the instabilities is reduced.

Holland and Haidvogel (1980) looked at the properties of the most unstable wave of a two-layer jet. They found a decrease in the importance of baroclinic instability as the jet became more barotropic. There were also two distinct modes: one dominated when the jet was more baroclinic and the other when the jet was more barotropic.

3.4 Summary of results and general discussion of the instability of thin baroclinic jets

The linear stability of several thin, baroclinic jets was discussed. This was preceded by a description of the instabilities due to horizontal shear alone (Chapter 2) and vertical shear alone. The parameter dependence of the results was discussed briefly. In this section, specific results (how many modes are there, what do they look like, what is their energy source and can they affect the mean flow) for all jets are brought together, followed by a general discussion of instabilities and radiation.

(a) Summary of results

The instabilities of the five basic jets have many features in common. All jets have two vertical shear modes and one or two horizontal shear modes. The horizontal shear modes are separate (when U_{I2} = .5) or combined with the vertical shear modes (when U_{I2} = 0). The number of vertical shear modes is dictated by the width of the jet and the value of F, both of which were the same for the five jets so it is not surprising that all five have similar vertical shear modes. Based on the results for two layer flow in a channel, the two vertical shear modes are the

lowest cross-jet mode (this was called "Mode 3") and the next lowest cross-jet mode (called "Mode 2" and occurring at lower zonal wavenumber than Mode 3). These, of course, are symmetric modes by initial assumption. The growth rates, kc_i, of Mode 3 are higher than for Mode 2 mainly because its wavenumbers are higher. The phase speeds of Mode 3 are a little lower than those of Mode 2: this is consistent with the phase speeds of the first two baroclinic modes in a channel, where the total wavenumber, $K^2 = k^2 + (n + 1/2)^2 (\pi/L)^2$, of the $(n = 1)$ mode is higher than the $(n = 0)$ mode. The vertical shear modes are not as easily identified by their meridional structure because of the interference of the profile breaks at $|y| = 1$. Generally, Mode 2 has a pronounced, relatively narrow maximum in amplitude at $y = 0$, and a secondary maximum at $y = 1$. Mode 3 often has a slight amplitude minimum in the upper layer at $y = 0$, but otherwise it's mid-jet maximum is broader than that of Mode 2. This weak sign in the eigenfunction identifies Mode 3 as the $(n = 0)$ mode and Mode 2 as the $(n = 1)$ mode. The energy source for both modes is unequivocally dominated by potential energy transfer from the mean flow.

The horizontal shear modes are separate from the vertical shear modes when $U_{I2} = .5$ and combined with Mode 3 when $U_{I2} = 0$. The presence of Mode 1 is pronounced on the long wave side of Mode 3 when they are combined. The horizontal shear mode is called such because of the necessary condition for instability which it is associated with and its distinctive dispersion relation, but its energy source for these jets is often dominated by the potential energy rather than the kinetic energy of the mean flow. However, there is a larger proportion of positive kinetic

energy transfer when this mode is present, compared with Modes 2 and 3. The meridional structure of the horizontal shear mode closely resembles the structure of the unstable modes of the barotropic jet: it has an amplitude minimum at $y = 0$ and a maximum at $y = 1$, and is surface-intensified in the jet when $U_{12} = 0$ (when there is no horizontal shear in the lower layer).

Radiating modes exist whenever the phase speed condition is satisfied: when the jets are westward ($\beta < 0$), when there is westward flow in the lower layer in the jet and when there is vertical shear outside the jet. The radiating modes can be identified with either the horizontal or the vertical shear modes. The horizontal structure of the radiating modes depends strongly on the energy source. If the vertical shear in the central jet provides the energy, the modes have maximum amplitude in the center of the jet. If the upper layer horizontal shear provides the energy, the maximum amplitude occurs in the upper layer in the shear zone (c.f. Figure 3.2.35). The amplitude of the radiated wave near the jet is very often comparable to its amplitude in the jet, although there are cases where it is smaller. The vertical structure of the radiated waves outside the jet depends entirely on the flow configuration which allows the mode to radiate in the first place. That is, the structure depends on how the phase speed conditions is satisfied. There are two "free" waves in the outer region for each k and c, because of the two-layer appoximation. Thus

(1)   the radiating modes of the westward jets excite only the barotropic Rossby wave in an ocean interior with no vertical shear. There are

two radiating modes, one associated with the vertical shear mode and one with the horizontal shear mode.

(2)   The radiating modes of eastward jets with westward undercurrents (with no vertical shear in the ocean interior) excite both Rossby waves. Although the two waves have the same k and c, they have different meridional wavenumbers ℓ. When both Rossby waves are added together, the resulting eigenfunction alternates between surface and bottom intensification in the meridional direction. There is one radiating mode, associated with the trapped vertical shear mode: the upper layer horizontal shear modes do not satisfy the phase speed condition.

(3)   The radiating modes of the jet with eastward vertical shear in the ocean interior ($U_{0s} > 0$) are surface intensified because they force only the Rossby wave which is surface intensified. There are two radiating modes, associated with the two trapped vertical shear modes. The upper layer horizontal shear modes do not satisfy the phase speed condition and do not radiate.

(4)   The radiating mode of the jet with westward vertical shear in the ocean interior ($U_{0s} < 0$) is bottom intensified for the same reason. This radiating mode is associated with the upper layer horizontal shear. The vertical shear modes do not satisfy the phase speed condition.

The energy transfers for the radiating modes of these specific examples are dominated by potential energy transfer, just as the trapped modes are.

In summary, the unstable modes of their baroclinic jets are be cat-
egorized as vertical shear and horizontal shear modes. There are trapped,
high growth rate modes and radiating, low growth rate modes. There are
two types of "radiating" instabilities: (1) horizontal and vertical shear
modes which satisfy the phase speed condition and (2) destabilized Rossby
waves which are contiguous to the type (1) radiating instabilities.

(b) General properties of the instabilities

(1) The necessary conditions for instability for different sources
of energy in the flow (that is, the vertical shear and the horizontal
shear in different regions) were derived. It was found that they were
sufficient for the profiles considered here. There were identifiable
horizontal shear and vertical shear modes, each satisfying its own neces-
sary condition.

(2) Hence, modes can be identifed not only on the basis of their
energy source, but also, and preferably, on the basis of the necessary
condition which they satisfy.

(3) In the parameter range selected for most of the examples in
3.2, baroclinic instability was the dominant source of energy. This is
not to say that horizontal shear modes were not present; on the contrary,
their effect was noted for each profile. However, most of their energy
was derived from the mean flow potential energy in these examples. While
the vertical shear modes obtained almost all of their energy from the po-
tential energy, the horizontal shear modes also obtained kinetic energy
from the mean flow. When the necessary condition for barotropic insta-

bility was satisfied for one of the layers, the kinetic energy transfer, however small, was usually positive. Conversely, when this necessary condition was not satisfied, the perturbations lost kinetic energy to the mean flow.

(4) The relative importance of barotropic instability is increased when the lower layer has significant horizontal shear, when the jet as a whole is narrowed (both as in Holland and Haidvogel, 1980) and when F is decreased (as in Hart, 1974).

(5) As β increases, it exerts a retarding effect on the phase speed and a stabilizing effect on the instabilities. As β approaches β_c, the maximum β for a given type of unstable mode, the instability phase speed approaches the minimum velocity of the part of the flow which produced the instability.

(6) Knowing the necessary conditions for instability (which predict the types of instabilities which might exist), knowing the Rossby wave dispersion relation in the ocean interior and using result (5), it is possible to successfully predict which modes can have radiating solutions.

(7) If the phase speed and zonal wavenumber of a neutral mode with contiguous unstable solutions satisfy the phase speed condition,

(i) that neutral mode is destabilized and looks like a modified Rossby wave in the ocean interior,

(ii) the contiguous unstable modes also radiate in the sense that $c_i/\ell_r > 0$ as the neutral mode is approached (and also in the sense that ℓ_i/ℓ_r becomes large and ℓ_r itself becomes quite small, with the desired effect of producing a large meridional decay scale),

(iii) the contiguous <u>stable</u> modes are <u>destabilized</u> (and are

referred to here as destabilized Rossby waves).

Growth rates of radiating modes (ii) and destabilized Rossby waves (iii)

are lower than growth rates of trapped waves (McIntyre and Weissman,

1978). Growth rates depend strongly on the range of phase speeds which

can radiate. Hence the radiating modes of a westward jet have growth

rates which are comparable to those of the trapped modes, while the

radiating modes of an eastward jet, which radiates because of a weak

westward flow somewhere in the system, have very low growth rates.

CHAPTER IV: COMPARISON OF MODEL RESULTS WITH DATA

FROM THE WESTERN NORTH ATLANTIC

4.1 Introduction

In this chapter we see to what extent the eddy field south of the

Gulf Stream can be attributed solely to the instabilities studied in the

previous chapter. The observed, highly energetic, eddy field in the Gulf

Stream and its broad decay to the south can only be due to the presence

of the Gulf Stream and its recirculation. Direct atmospheric forcing is

not a viable mechanism for producing the eddy field because it does not

have sufficient strength and spatial inhomogeneity. It is assumed here

that the disturbances observed in the western North Atlantic are due to

instabilities of the Gulf Stream system, which includes the Gulf Stream,

possibly an undercurrent and possible flow outside the Gulf Stream. Two

complementary manifestations of instabilities are the finite amplitude

extension of the instabilities studied in this thesis and Gulf Stream

rings (Flierl, 1977). The formation and initial vertical structure of

Gulf Stream rings may be strongly influenced by the instabilities dis-

cussed in the previous chapter. In addition, the region in which rings

propagate may be affected by radiating Gulf Stream instabilities, which

may interact with the rings.

Comparing linearly unstable modes with data is tricky since the

proper basic flow and the finite-amplitude behavior of the instabilities

are unknown. The fully-developed field may not resemble the initially

growing waves if the fastest-growing waves modify the flow quickly (by forcing westward lobes north and south of the eastward jet, say) so that the slowly-growing waves see an environment which is quite different from the initial basic state. The problem of choosing a basic state is handled here by looking at the unstable modes of three radiating, eastward jets and the westward jet of the previous chapter and deciding which, if any, set of results best fits the observations.

There are two types of unstable modes for the basic jets explored in the previous chapter: (1) strongly unstable, trapped modes which do not vary from model to model and (2) weakly unstable, "radiating" modes with large meridional decay scales whose structure and phase speeds depend strongly on the detailed structure of the flow. Good agreement of the model and observations means that the model predicts reasonable frequencies, wavenumbers, and meridional and vertical structure of energy, Reynolds stress and heat flux.

Haidvogel and Holland (1978) examined the linear stability of instantaneous and mean velocity profiles taken from meridional sections of Holland's (1978) general circulation models. They found good agreement between the properties (wavenumber, phase speed and growth rate) of the linearly unstable waves and the actual waves which predominated in the (fully non-linear) numerical models. The higher order quantities (Reynolds stress and heat flux) were not predicted as well by the linear stability analysis. They also found that proper simulation of the barotropic instability process requires a velocity profile which is closer to the instantaneous velocity than to the time-averaged flow: the sharpness

of the Gulf Stream is lost in averaging because of its meandering. Their results indicate that linear stability analysis of observed velocity profiles can yield meaningful predictions of the actual finite-amplitude waves.

The model results are compared primarily with observations made along 55°W in the POLYMODE experiment and at the MODE site. Schmitz (1978, 1980, 1981) has analyzed the current meter data from these moorings and has published the meridional distributions of mean flow, kinetic energy and Reynolds stress. He has also calculated the kinetic energy spectra in the thermocline and the abyss at a mid-field POLYMODE mooring and at the MODE site (1978). Schmitz and Holland (1982) have made a very useful comparison of POLYMODE data and eddy-resolving numerical model results. Hogg (personal communication) calculated the meridional heat flux and also the velocities and temperature perturbations associated with the first empirical orthogonal function for the POLYMODE data. Mention is also made of the LDE results. Bryden (1982) computed the energy transfers between mean and eddy kinetic and potential energy for the LDE (coordinates). Owens, Luyten and Bryden (1982) discuss the ocean variability in the LDE, including kinetic energy spectra which they fruitfully compare with the POLYMODE and MODE spectra.

4.2 Scaling of Model Results

The first step in comparing model and observed results is redimensionalization of the model. We wish to know the physical wavelengths,

phase speeds, growth rates and meridional decay scales of both the trap-
ped and radiating instabilities. The second step is to choose the model
whose instabilities best match the observed fluctuations. The third step
is to decide if the best match is acceptable, with the possibility that
an unexplored basic state may actually be more appropriate.

In scaling the model to the observed Gulf Stream, the total trans-
port of the Gulf Stream is preserved. The observed horizontal shear is
also preserved. Choosing a vertical shear for the two-layer model is
more difficult since the vertical shear varies continuously in the hor-
izontal in the ocean, while it has the same value throughout the jet
center in the model. As long as the vertical shear in the model is a
reasonable average of the net vertical shear in the Gulf Stream, the
scaled model is assumed to be applicable.

The maximum net transport of the Gulf Stream is about 150×10^6 m^3/sec
(Worthington, 1976). This maximum transport is achieved in a rather hor-
izontally constricted area, but for our purposes, it will be assumed to
be the transport of an infinite, eastward, zonal current. The transport
is distributed over 4.5 km in depth. Assuming that all of the transport
in the two-layer model is in the upper layer, of depth 2.25 km, we obtain

$$\int_{-\infty}^{\infty} U \, dy = 5.8 \times 10^3 \, km^2/day \tag{4.2.1}$$

The modelled velocity profile, equation 3.1.5, is written in terms of D,
the position of the edge of the shear zone. Define $\delta = D - 1$ as the width
of the shear zone. Then the nondimensional cross-stream integral of
velocity in the top-layer from 3.1.5 is

$$\int U_1 \, dy = U_0 \left(2 + \frac{\delta}{2}\right) + \beta\delta \left(-\frac{\delta^2}{6} + \delta + 2\right) + \frac{U_0}{\sqrt{2F}} \left[\frac{-1 + \cosh\sqrt{2F}\,\delta}{\sinh\sqrt{2F}\,\delta}\right] \quad (4.2.2)$$

In dimensional form, where asterisks denote dimensional variables:

$$\int U_1^* \, dy^* = U_0^* \left(2L^* + \frac{\delta^*}{2}\right) + \beta_0\delta^* \left(-\frac{\delta^{*2}}{6} + L^*\delta^* + 2L^{*2}\right) + \frac{U_0^* L_R}{\sqrt{2}} \left[\frac{-1 + \cosh\sqrt{2F}\,\delta}{\sinh\sqrt{2F}\,\delta}\right]$$

where L_R is the internal deformation radius. The net horizontal shear of the observed Gulf Stream is about 100 km/day in 100 km. In the model, this shear occurs over the distance δ^*, so

$$U_0^* = \delta^* / \text{day}$$

Because most models in Chapter 3 had $\delta = .7L$ and $F = L^2/L_R^2 = 5$, these relations are assumed here also. The model's integrated velocity becomes

$$\int U^* dy^* = \frac{\delta^{*2}}{\text{day}} (3.36) + \beta_0 \, \delta^{*3} (5.34) + \frac{\delta^* L_R}{\sqrt{2}\,(\text{day})} \left[\frac{-1 + \cosh\sqrt{2F}\,\delta}{\sinh\sqrt{2F}\,\delta}\right] \quad (4.2.3)$$

For reasonable values of δ^* and L_R, the first term of 4.2.3 dominates. The other two terms are the corrections to the shear profile in the wings which make the potential vorticity gradient vanish in the presence of β_0 and vertical shear. Ignoring these two terms and combining (4.2.1) and (4.2.3), we obtain

$$\delta^* = D^* - L^* \simeq 42 \text{ km}$$

$$L^* \simeq 60 \text{ km}$$

$$U_0^* \simeq 42 \text{ km/day} \quad (4.2.4)$$

$$L_R \simeq 27 \text{ km}$$

$$T = L*/U_0* \simeq 1.43 \text{ days}$$

$$\beta = \beta_0 L*^2/U_0* \simeq .1$$

The deformation radius is obtained from $L*$ and the assumed value of 5 for $F = (L*/L_R)^2$.

These scales are reasonable. By definition they give the correct Gulf Stream transport and observed horizontal shear. They give a total Gulf Stream width of 204 km, which may be a little wide, although it includes all of the wings. The vertical shear is also reasonable: the maximum observed vertical shear in the center of the jet is about 100 km/day, but the baroclinic instability may depend more on the average vertical shear. The internal deformation radius is also of the right order: Flierl (1975) calculates internal deformation radii of 26 km in the Gulf Stream and 47 km in the MODE region.

The biggest source of error is probably the choice of horizontal shear, particularly since the actual basic state for the Gulf Stream may be rather different from the observations. If the horizontal shear were doubled, the Gulf Stream width would shrink to 142 km and the internal deformation radius to 19 km, while the time scale would be .72 days. If the horizontal shear were halved, the Gulf Stream width would be 286 km, the internal deformation radius 38 km and the time scale 2.8 days.

Another source of error could be the arbitrarily assumed values of D and F, both of which affect the modelled width of the Gulf Stream and hence the number of cross-stream, baroclinically unstable modes. The choices of $F = 5$ and $D = 1.7L$ yield two cross-stream modes. Increasing

D or F increases the number of cross-stream modes. Because the higher modes are less unstable (Pedlosky, 1979), it does not seem vitally essential to include them. Barotropic instability is unaffected by the choice of F. When D is increased and β (thus L) is held constant, the flow is less barotropically unstable because the horizontal shear is effectively diminished.

4.3 Observations in the Subtropical Gyre

This section is subdivided into many small sections to separate the different types of observations from one another. The first three sections discuss the eddy energy distribution in the subtropical North Atlantic. The next two sections discuss the mean flow, mean potential vorticity gradient and the fluctuations associated with the first empirical orthogonal function for the POLYMODE data. The Reynolds stress, heat flux and energy transfers between the mean and fluctuating flows are discussed in the sixth, seventh and eighth sections. The results of all subsections are summarized in the ninth subsection. Most of the results listed here are published in the cited references.

(i) Horizontal energy distribution

The horizontal distribution of mean and eddy kinetic energy at the surface of the North Atlantic (and world's oceans) was plotted by Wyrtki, Magaard and Hager (1976), using ship-drift observations. At the core of the Gulf Stream, the eddy kinetic energy is in excess of 1500 cm^2/sec^2. The meridional e-folding scale of the kinetic energy at 65°W is about

700 km; at 55°W it is about 600 km: both are calculated roughly from the published maps. The scales are comparable in the Pacific south of the Kuroshio.

Richardson (1981) also plotted the surface kinetic energy in the subtropical North Atlantic based on all available surface drifter data. He estimated a surface eddy kinetic energy of 1630 cm^2/sec^2 at 55°W. The decay scale of the energy was about 500 km south of the Gulf Stream and was nearly independent of longitude. The energy values of Wyrtki et. al. were lower because they could not sample short time-scales very well with ship-drift observations.

Dantzler (1977) plotted the eddy potential energy density for the subtropical Atlantic, using the mean-squared displacement of the 15° isotherm to calculate the eddy potential energy. He obtained values in excess of 1600 cm^2/sec^2 in the Gulf Stream. From his map, an e-folding scale of 300 km south of the Gulf Stream can be estimated.

All three horizontal maps plainly show the intensification of eddy energy in the Gulf Stream (and Kuroshio). In addition, the distribution of eddy energy perpendicular to the Gulf Stream is nearly independent of distance along the Gulf Stream from about 75°W to 50°W. (Wyrtki, et. al. show a weakening of energy along the Gulf Stream but no real change in meridional decay scale.)

(ii) Vertical cross-sections of kinetic energy

The kinetic energy along 55°W at four different depths was discussed by Schmitz (1978). South of the Gulf Stream there were moorings up into the thermocline. In and north of the Gulf Stream, there were moorings

only at 4000 m. Schmitz reports an increase of energy from the interior
ocean to the Gulf Stream by a factor of over 100 below the thermocline
and by a factor of 30 in the thermocline. E-folding scales estimated
from his data are 290 km in the thermocline and 220 km at 4000 m. The
thermocline kinetic energy can be extrapolated into the Gulf Stream using
this e-folding scale, yielding a kinetic energy of about 525 cm^2/sec^2.
This is sensitive to the kinetic energy values at the moorings and to the
position of the moorings relative to the Gulf Stream axis, and is some-
what higher than SOFAR float results in the Gulf Stream at 55°W (Owens,
personal communication; Schmitz et. al., 1981).

(iii) Kinetic energy distribution for different frequencies

Schmitz (1978) calculated the kinetic energy distribution as a
function of frequency at two moorings. One was the POLYMODE mooring
at (37°30'N, 55°W), 200 to 250 km from the mean Gulf Stream. The second
was the MODE mooring at (28°N, 70°W), about 700 to 900 km from the Gulf
Stream. Schmitz focused his attention on "mesoscale" (50 to 100 days)
and "secular" scale (100 to 1000 days) disturbances. The mesoscale fluc-
tuations were weakly surface-intensified at both moorings. They decayed
rapidly to the south, but maintained their relative vertical structure.
The secular scale disturbances decayed more slowly to the south than the
mesoscale disturbances. They were weakly surface-intensified at 37°30'N,
becoming strongly surface-intensified at the MODE site.

Schmitz's energy values for the two frequency ranges at the two
moorings are listed in Table 4.3.1.

| Table 4.3.1 | | | | | |
| PM08 (37.5°N, 55°W) | | MODE (28°N, 70°W) | | K_E = $Ae^{-\ell y}$ | |
Depth	K_E	Depth	K_E	A	$1/\ell$ (km)
Secular Scale	600 m	75	500 m	37	110	640
(> 100 Days)	4000 m	34	4000 m	2.2	155	165
Mesoscale	600 m	222	500 m	15.6	970	170
(50-100 Days)	4000 m	80	4000 m	6.6	320	180

If we assume that the meridional fall-off of energy in each frequency range is a simple exponential $[E(y) = Ae^{-\ell y}]$, we can compute the decay scale $(1/\ell)$ away from and amplitude (A) in the Gulf Stream. The POLYMODE mooring is assumed to be 250 km and the MODE mooring 700 km from the Gulf Stream. The decay scale and amplitude are listed in the right column. The mesoscale disturbance decays much more rapidly than the secular scale disturbance and is much more energetic in the Gulf Stream. The errors in this simple calculation are undoubtedly large: if MODE is farther than 700 km from the Gulf Stream, the decay scales are larger and the amplitudes smaller. (According to this simple extrapolation, the secular scale energy in the Gulf Stream is bottom-intensified: if MODE is really farther than 700 km from the Gulf Stream, the extrapolated secular scale energy would be surface-intensified in the Gulf Stream.)

(iv) Mean flow velocity and potential vorticity gradient

The mean flow at many depths along 55°W was plotted by Schmitz (1978) and discussed in greater detail by Schmitz (1980). The mean flow is shown in Figure 4.3.1. There were no moorings directly in the Gulf Stream but it
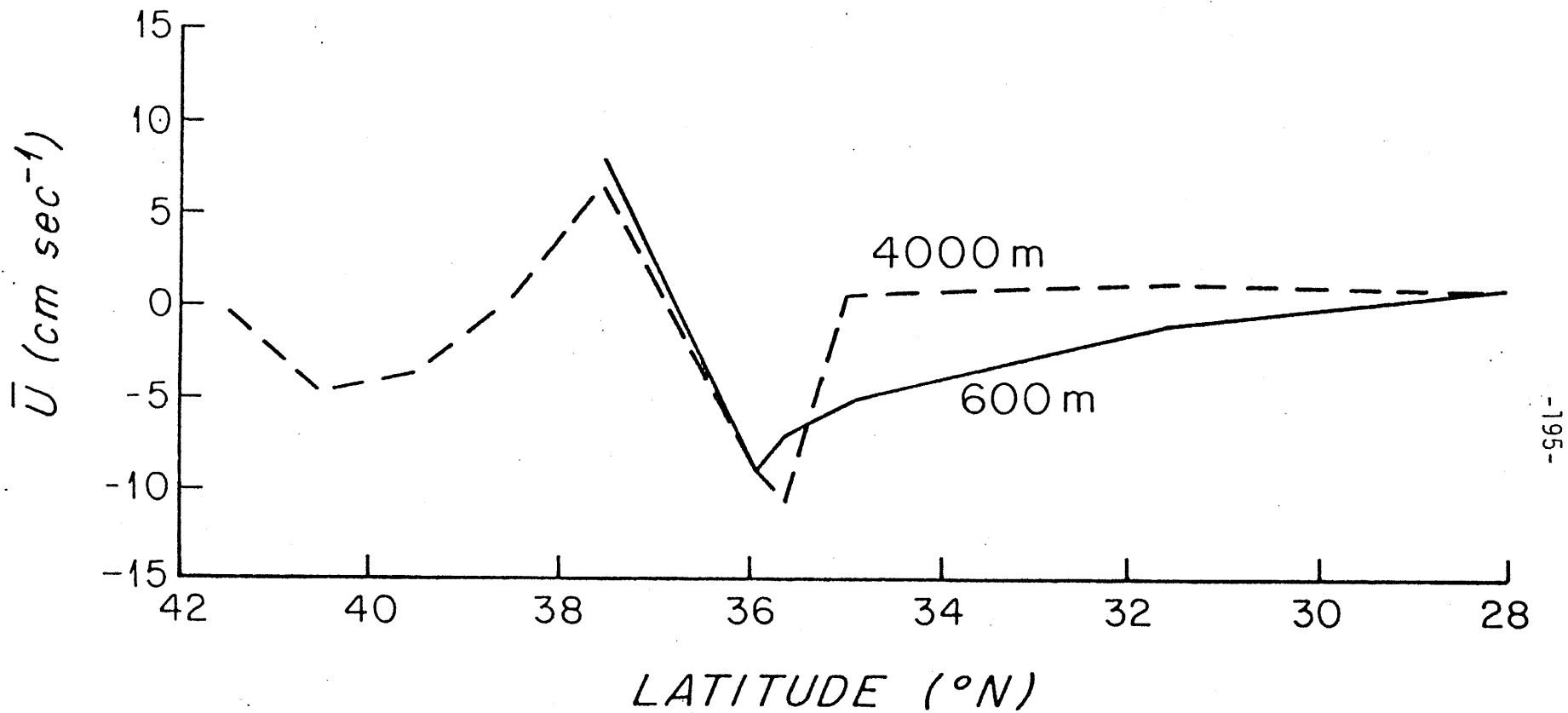
Figure 4.3.1

Mean eastward flow, $\bar{U}$, along 55°W at 600 m and 4000 m using all
three settings of the POLYMODE array. See Schmitz (1978,1980).

is assumed that the Gulf Stream is eastward and centered at about 40°N. The main features of the observations are (1) a westward current of 5 to 7 cm/sec directly under the Gulf Stream's historical axis, (2) a nearly barotropic eastward flow of 7 to 10 cm/sec, centered at 37°30'N, (3) a nearly barotropic westward jet of 10 to 15 cm/sec centered at 36°N and (4) quiet flow of 1 to 2 cm/sec south of 35°N with vertical shear of ambiguous sign, depending on the averaging period used.

In modelling the Gulf Stream, one might include a westward undercurrent since the observations suggest that there is a reversal of flow at depth. However, such a basic state may be incorrect since the mean westward under-current may be under the mean Gulf Stream only at this longitude or the in-stantaneous westward flow may never be under the instantaneous Gulf Stream. The westward undercurrent could have at least two different sources: it could be the abyssal part of a westward recirculation on the northern side of the Gulf Stream, driven by Gulf Stream instabilities or it may be an abyssal flow driven by thermohaline processes and dynamically uncoupled from the Gulf Stream.

The eastward flow centered at 37°30'N can be considered to be a separate eastward filament of the Gulf Stream (Schmitz, 1980). It could also be caused by sporadic Gulf Stream incursions at this latitude.

The nearly barotropic, narrow, westward flow at 36°N (Schmitz, 1978 and 1980) may be the westward part of a highly inertial circulation (c.f. Veronis, 1966), or it may be eddy-induced by the Gulf Stream or it may be partially induced by the thermohaline process of 18° Water formation (Stommel and Veronis, 1980). In the first case, the westward flow should

have been included as part of the model basic state. Apropos of the second case, numerical models with unstable eastward currents produce westward-flowing side lobes (Holland, 1978). The instabilities of the eastward jet should be examined to see if they have appropriate Reynolds stresses to generate such a flow. In the third case, the intensity of the westward current may be seasonal.

The mean potential vorticity gradient along 55°W can be estimated very roughly. It is calculated and shown in Figure 4.3.2 as if for a two-layer system with uniform layer depths, using the 600 m and 4000 m measurements for the top and bottom layers. The potential vorticity gradient in each layer is given by (3.1.2). Because there were no moorings in the Gulf Stream at 600 m, velocities of 50 cm/sec at 40°N and 35 cm/sec at 39°N were assumed. Using Schmitz's mean flow values for both POLYMODE deployments, the eastward velocity profile was fit by a parabola for each group of three adjacent moorings, giving the curvature U_{yy}. The resulting interpolated velocity profile was realistic except in the lower layer at 31.6°N, so this point is not included in the Figure. The stretching terms were evaluated by assuming that the flow could be approximated by two layers of equal depth, with the velocities at 600 and 4000 m assigned to each of the layers. The layer depth was taken to be 2000 m and the reduced gravity to be 1 cm sec^{-2}. The broad pattern in Figure 4.3.2 shows a possibility for baroclinic instability in the Gulf Stream, between 38° and 40°N, (because of the difference in sign of $\partial\pi/\partial y$ in the two layers) and barotropic instability in the upper layer. Details in the westward flow at 36°N are smeared out by the station spacing. It must be emphasized that this calculation is very rough.
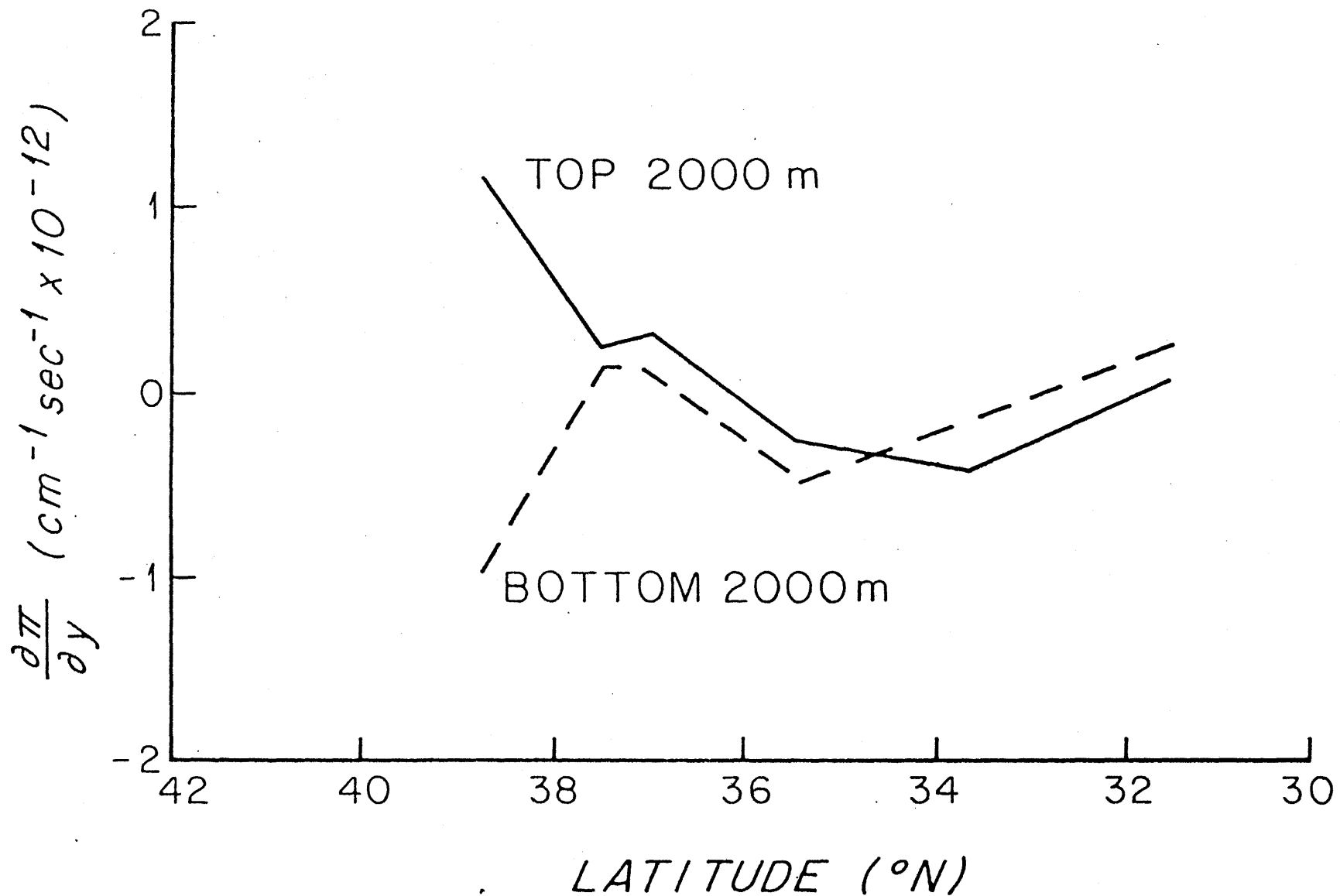
Figure 4.3.2

Approximate mean potential vorticity gradient at 55°W, using the mean flows of Figure 4.3.1, assuming an eastward flow of 50 cm/sec at 600 m at 40°N.

(v) Fluctuation velocities and temperatures

Hogg (personal communication) calculated the first empirical orthogonal function for three frequency ranges, centered at 120 days, 60 days and 40 days, using the meridional POLYMODE array along 55°W and a zonal array along 36°N. The method of empirical orthogonal functions (Wallace and Dickinson, 1972) is used to expose the best-correlated parts of several time series, which in this case are the north and east velocities and temperature at several depths and many sites. The velocity and temperature perturbations of the first empirical orthogonal functions were surface-intensified in the near (37.5°N) and far field (31.5°N) and slightly bottom-intensified at the intermediate moorings (36°N).

(vi) Momentum flux (Reynolds stress)

The momentum flux, $\overline{u'v'}$, along 55°W was described by Schmitz (1981) and used by Schmitz, Niiler, Bernstein and Holland (1982) in a comparison of observations and numerical results. The momentum flux is shown in Figure 4.3.3. North of the Gulf Stream, the only data was at 4000 m and the momentum flux was negative. South of the Gulf Stream, the momentum flux was positive at all depths with a maximum whose latitude depended on depth: at 600 m it reached a maximum at 35°N while at 4000 m, it reached a maximum at 37.5°N. The momentum flux at 4000 m was thus antisymmetric with respect to the Gulf Stream, consistent with the Gulf Stream being a localized source of eddy energy. This was also the case in the Pacific at shallower depths (Schmitz, Niiler, Bernstein and Holland, 1982).

From Hogg's first empirical orthogonal function, the north and east velocities at 55°W were nearly in phase with each other except at 36°N,

Figure 4.3.3

LATITUDE (°N)

Mean momentum flux, $\overline{u'v'}$, along 55°W at 600 m and 4000 m using all three settings of the POLYMODE array. See Schmitz and Holland (1981).

where they were $\pi/2$ out of phase. The momentum flux $\overline{u'v'}$ was therefore positive except at 36°N where it was nearly zero. Bryden (1982) calculated the momentum flux in the LDE area (30°30'N to 31°30'N and 69°W to 71°W) and found that the momentum flux was positive there.

The vertically-averaged momentum flux external to a localized source of energy, such as an infinite zonal current concentrated at one latitude, will increase to the north if the background potential vorticity gradient is positive (Held, 1977). If the momentum flux goes to zero far from the current, its only possible configuration is positive far to the south and negative north of the current (if the potential vorticity gradient far from the current is β). This is the configuration which is observed in all unstable modes examined in the previous chapter, in eddy-resolving general circulation models and along 55°W (Schmitz et. al., 1982).

The Reynolds stress has a direct effect on the mean flow since

$$\frac{\partial U}{\partial t} = - \frac{\partial}{\partial y} \overline{u'v'} + \bar{v}_1 \qquad (4.3.1)$$

is the x-averaged, non-dimensional momentum equation (Pedlosky's (1979) equation 7.2.13). U, u' and v' are the zero order mean and perturbation velocities (geostrophic) and v_1 is the ageostrophic correction to the northward velocity. The observed, antisymmetric momentum flux decelerates the flow north of the momentum flux minimum (on the north side of the Gulf Stream) and south of the momentum flux maximum (on the south side of the Gulf Stream): its effect on the the eastward Gulf Stream is unknown since details of the momentum flux distribution in the Gulf Stream are unknown. (The details of the distribution in the Gulf Stream depend on whether the

barotropic instability mechanism is operating and which way the kinetic energy flows between the mean flow and perturbations.) Because the latitude of the momentum flux maximum depends on depth, the mean flow south of 35°N at 600 m and south of 37.5°N at 4000 m is forced westward. The direct effect of the momentum flux, i.e., $-\frac{\partial}{\partial y}(\overline{u'v'})$, is to weaken the observed, nearly barotropic, westward flow at 600 m and strengthen it at 4000 m. However, the total effect of the momentum flux is more complicated than this since the term v_1 depends on the momentum flux.

(vii) Heat flux

The heat flux for all fluctuations along 55°W at 600 and 4000 m is shown in Figure 4.3.4: there was tremendous southward heat flux between the Gulf Stream and 36°N in the thermocline. South of 36°N, the thermocline heat flux and its meridional gradient were much reduced and the heat flux was slightly positive. Bryden (1982) found southward heat flux in the thermocline in the LDE, which corresponds with latitudes 32°-35°N at 55°W. The heat fluxes associated with the first empirical orthogonal functions for the POLYMODE data (Hogg, personal communication) were also southward since the northward velocity and temperature perturbations were more than $\pi/2$ out of phase.

(viii) Energy transfer

The time-averaged transfers between mean and eddy energy, assuming a meaningful separation between mean flow and fluctuations, are given by Bryden (1982). If, additionally, the transfer equations are averaged over the volume of the flow, assuming that the flow is inviscid and that the mean flow U(y,z) is independent of x and has no northward component, the energy equations for the mean and fluctuating flows are:
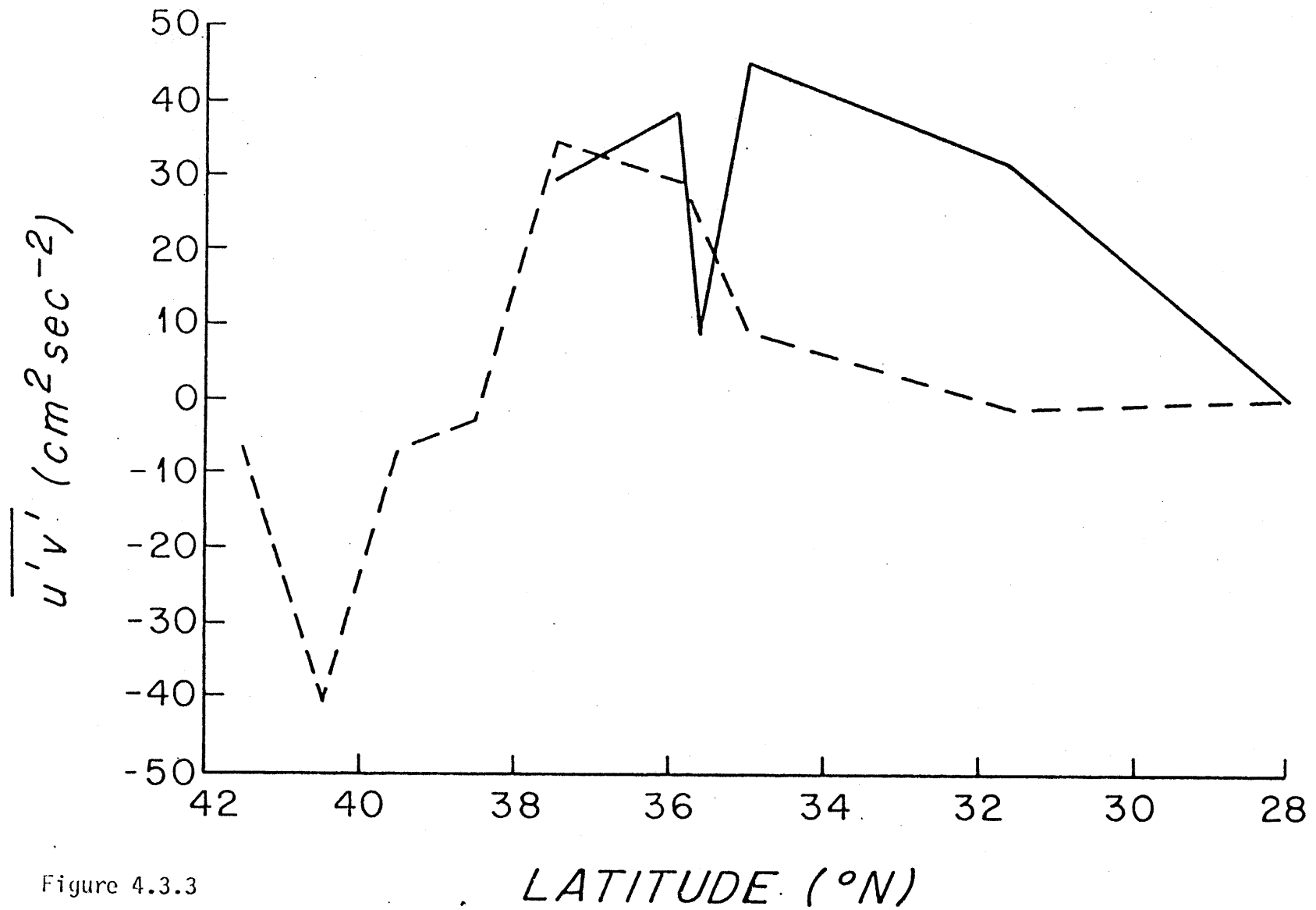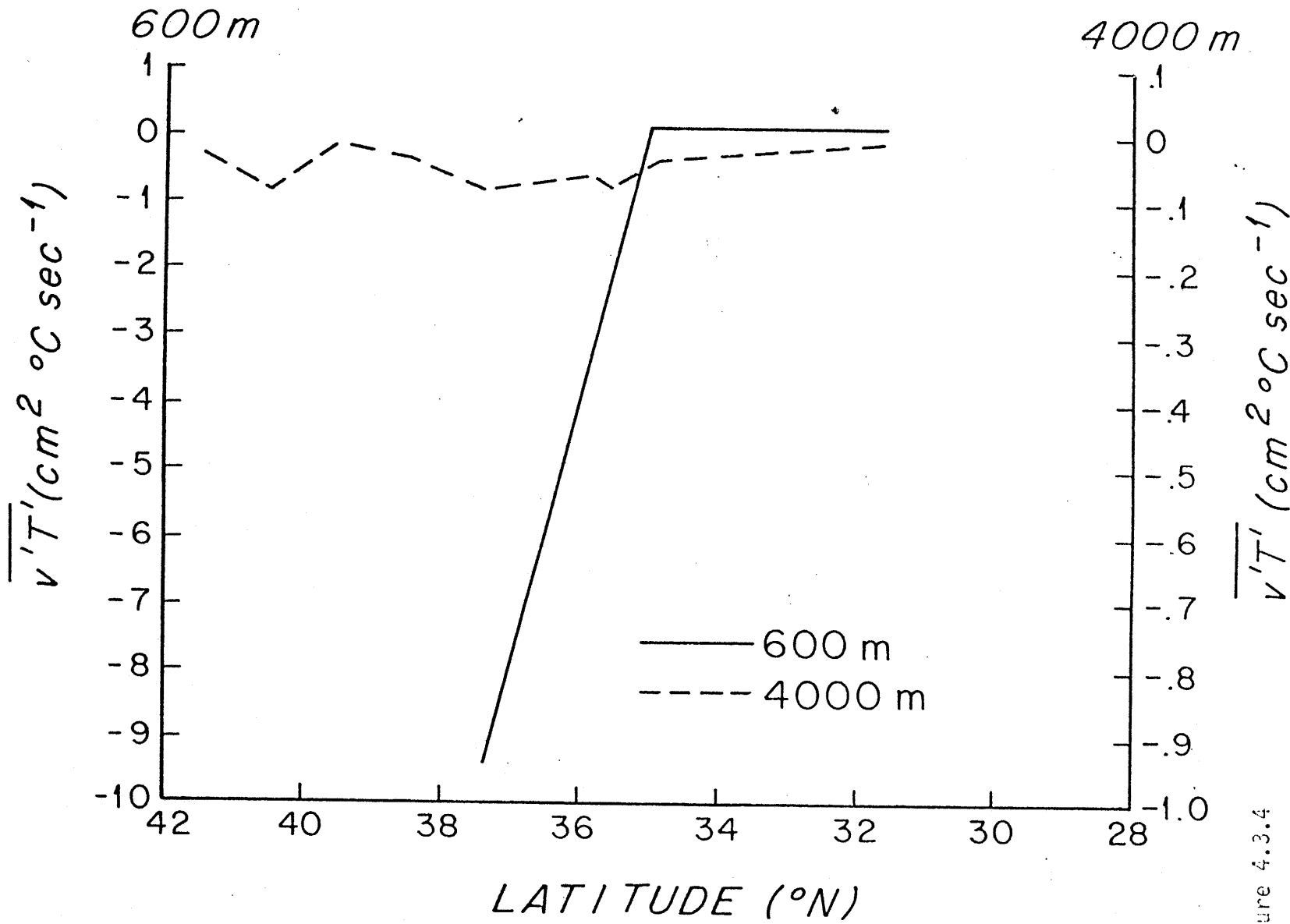
Figure 4.3.4

Mean heat flux, $\overline{v'T'}$, along 55°W at 600 m and 4000 m using all three settings of the POLYMODE array.

$$\frac{\partial E(\phi)}{\partial t} = \int\!\!\int dy\ dz\ \left[- \overline{u'v'}\ \frac{\partial U}{\partial y} + \frac{\overline{\theta'v'}}{S}\ \frac{\partial U}{\partial z}\right]$$

(4.3.2a,b)

$$\frac{\partial \overline{E}}{\partial t} = \int\!\!\int dy\ dz\ \left[- U\ \frac{\partial}{\partial y}\ \overline{u'v'} - \frac{H}{S}\ \frac{\partial}{\partial y}\ \overline{\theta'v'}\right]$$

where $E(\phi)$ is the energy of the perturbations and $\overline{E}$ is the mean flow energy. The notation of Pedlosky (1979) is used. In equation 4.3.2a, the eddy energy is changed by potential and kinetic energy transfers from the mean flow. In equation 4.3.2b, the mean energy is changed by potential and kinetic energy transfer from the eddies. (When these equations are not integrated in y and z, there are additional energy flux terms in both equations. They are not important in the global energy balance, but may be quite important locally.

The energy transfers are difficult to evaluate from observations along 55°W because (1) the meridional spacing of the moorings is wide, (2) the record length is finite and a time average may not remove the longest period fluctuations and the zonal dependence from the full local energy equations, (3) the actual flow is not exactly x-independent, although a comparison of POLYMODE, LDE and MODE data shows that the assumption of x-independence is not bad (zonal derivatives were also unimportant in energy transfers in Holland and Lin's model of the subtropical gyre). The first problem leads to errors in evaluating meridional derivatives. The other two problems mean that the basic assumptions leading to equation 4.3.2 could be faulty when applied to data in the western Atlantic.

A thorough energy analysis was made by Bryden (1982) for the LDE site, which is about 480 km from the Gulf Stream and 300 km from MODE.

While the spacing of the moorings was close enough to evaluate spatial derivatives, the record length was not long enough to yield meaningful mean northward flows (Owens, Luyten and Bryden, 1982). This mainly caused problems in the kinetic energy transfers. The potential energy transfer to the eddies was almost entirely due to vertical shear along the direction of the mean flow, parallel to the Gulf Stream (there was little rotation of the velocity vector with depth so that the mean flow and vertical shear were almost aligned). However, the kinetic energy transfers were dominated by zonal derivatives, particularly of the northward flow, because of substantial curvature in the "mean" flow. This was true even when the axes were realigned with the overall "mean" flow. An increase in averaging period reduced the zonal derivatives and increased the importance of the meridional derivatives, leading one to believe that a much longer record would yield a mean flow nearly independent of distance parallel to the Gulf Stream. Thus the record length can make a substantial difference in computed "mean" quantities, such as energy transfers between eddies and mean flow. It is probably safe to use equations 4.3.2 to compute energy transfers without including zonal derivatives if the record is long enough.

With these warnings, the energy transfer terms of 4.3.2 are computed for the POLYMODE data along 55°W. It is assumed that the array is nearly perpendicular to the Gulf Stream [this is supported by Worthington's (1976) circulation scheme]. The POLYMODE records average 700 days in length, as opposed to the 225-day averages used for the LDE. The kinetic energy transfers from the mean-to-eddies and eddies-to-mean at 600 and 4000 m and the

potential energy transfer from the mean-to-eddies in the thermocline are shown in Figure 4.3.5. A systematic error analysis has not been done. Bryden (1982) optimistically calculated an error of about 1×10^{-5} cm^2 sec^{-3} for the energy transfers. Using this as a guide, only the transfers in the area of the westward recirculation (centered at 36°N) are meaningful. In the thermocline: the mean flow gains kinetic energy in the recirculation and loses it at 35°N; the eddies lose kinetic energy near 37°N and gain energy on the south side of the recirculation (35.5°N); the eddies gain potential energy in the recirculation. Between 32° and 35°N, the latitudes which correspond with the LDE site, the potential energy transfer is still positive but smaller than at the LDE (where it was 3.2×10^{-5} cm^2 sec^{-3}), and may not be significant. At 4000 m, eddies lose energy on the northern side and lose kinetic energy on the southern side of the recirculation; the mean flow gains energy right in the recirculation.

The westward recirculation is a fertile region for baroclinic instability. In contrast, it is also a place where the mean flow gains kinetic energy from the eddies. Eddies gain kinetic energy on the south side and lose it on the north side of the recirculation.

[A possible problem in computing energy transfers arises from the low Reynolds stress in the thermocline at 35°N - see Figure 4.3.3. The low Reynolds stress may be due to the seamount underlying the mooring: the seamount demonstrably affects the mean flow here (Hogg, personal communication). If this point is removed from the calculation, the kinetic energy transfer to the mean flow is substantially reduced and the kinetic energy transfer to the eddies is greatly increased at this latitude.]

Figure 4.3.5

(A)

$600\,m$

(a) Transfer of kinetic energy at 600 m from the mean to the eddies, $-(\overline{u'v'})\partial\overline{U}/\partial y$; kinetic energy at 600 m from the eddies to the mean, $-\overline{U}(\partial\overline{u'v'}/\partial y)$; potential energy at 800 m from the mean to the eddies, $-(f/\overline{T}_z)\overline{v'T'}(\partial\overline{U}/\partial z)$. (b) Transfer of kinetic energy at 4000 m from the mean to the eddies, $-(\overline{u'v'})\partial\overline{U}/\partial y$; kinetic energy at 4000 m from the eddies to the mean, $-\overline{U}(\partial\overline{u'v'}/\partial y)$.

$\dfrac{f}{\overline{\theta}_z}\overline{v'T'}\dfrac{\partial\overline{U}}{\partial z}(800\,m)$

$(-\overline{U}\dfrac{\partial}{\partial y}\overline{u'v'})$

$(-\overline{u'v'}\dfrac{\partial\overline{U}}{\partial y})$

(B)

$4000\,m$

$(-\overline{u'v'}\dfrac{\partial\overline{v}}{\partial y})$

$(-\overline{U}\dfrac{\partial}{\partial y}\overline{u'v'})$

$\dfrac{f}{\overline{\theta}_z}\overline{v'T'}\dfrac{\partial\overline{U}}{\partial z}(2750\,m)$

$10^5\,cm^2/sec^3$

LATITUDE (°N)

In general, mean-to-eddy energy transfer is not locally balanced
by eddy-to-mean energy transfer, although they must balance globally.
The biggest sources of energy for the eddies are of course the vertical
and horizontal shear of the Gulf Stream and cannot be assessed with this
data set.

If the jet model of the previous chapter is qualitatively correct,
conversion of mean-to-eddy energy outside the Gulf Stream should be unim-
portant, while the effect of the eddies on the mean flow outside the Gulf
Stream could be important. In fact, the westward recirculation, which may
be such a product of the fastest-growing instabilities, is quite impor-
tant in the overall structure of observed energy transfers, allowing sub-
stantial potential energy transfer to the eddies to occur south of the
Gulf Stream.

(ix) Summary of observations

(1) The surface eddy kinetic and thermocline potential energies are
     maximum in the Gulf Stream with values in excess of 1000 cm^2/sec^2.
     Their meridional decay scales are about 600 and 300 km respectively.

(2) The total eddy kinetic energy along 55°W is surface-intensified and
     has a meridional decay scale of 290 km in the thermocline and 220 km
     at 4000 m.

(3) Mesoscale disturbances (50 to 100 days) at 55°W are surface-intensi-
     fied and have decay scales of about 170 km. Secular scale disturb-
     ances (100 to 1000 days) decay much more slowly, with a scale of
     about 600 km in the thermocline, becoming strongly surface-intensi-
     fied away from the Gulf Stream.

(4) The mean flow at 55°W includes an eastward Gulf Stream and a west-ward undercurrent at 40°N, nearly barotropic eastward flow at 37°50'N, nearly barotropic westward flow at 36°N and weak flow of nearly indeterminate sign south of 35°N. The mean potential vorticity gradient is large in the Gulf Stream and close to zero south of the recirculation. The Gulf Stream itself is baroclin-ically supercritical. Reversals in sign of the potential vortic-ity gradient also occur laterally in the thermocline and at 4000 m, allowing the possibility of barotropic instability.

(5) The perturbation velocities and temperatures of the empirical orthog-onal function (Hogg, personal communication) are surface-intensified at 37°30'N, bottom-intensified at 36°N and surface-intensified at 31°30'N. This apparently contradicts the observation in (3) because only two stations were used for the statements made in (3): one at 37°30'N and one in the MODE region where the observations closely resembled the observations at 31°30'N. The source of bottom-intensification at 36°N may not be the Gulf Stream instabilities: other possible sources are mentioned in the next section.

(6) The momentum flux along 55°W is antisymmetric with respect to the Gulf Stream and is positive to the south of the Gulf Stream. This is consistent with the export of energy from the unstable Gulf Stream (Held, 1977). The momentum flux maximum occurs farther to the south in the thermocline than in the deep water.

(7) The heat flux is large and southward in the westward recirculation.

(8) Energy transfers along 55°W show that the westward recirculation is an active site of baroclinic instability. Kinetic energy transfer is into the mean flow in the recirculation. Meaningful transfers probably cannot be calculated south of the recirculation. In the LDE, centered at 69.5°W, 31°N (roughly equivalent to 33°N at 55°W), Bryden found the mean-to-eddy potential energy conversion was positive while the mean-to-eddy kinetic energy was negative and the eddy-to-mean kinetic energy conversion was negligible.

4.4 Model-Data Comparison

A proper comparison of data and the model depends on the proper choice of a basic flow for the model. However, the observed mean flow has already been influenced by instabilities so it may not be correct to use the observed mean flow as a basic state. In particular, the basic flow in the gyre interior and the observed westward recirculation at 36°N are strongly affected by instabilities. Instead of choosing a basic state first, the structure of the observed fluctuations is used to define the possible basic flows. Remaining ambiguities in the basic flow after this choice may be resolved using other knowledge about how the circulation arises.

In comparing the observations with the models, the first step is to see which jet model can produce surface-intensified disturbances (perhaps with bottom-intensification at an intermediate latitude) where the longer period waves decay much more slowly than the short period waves. The second step is to see if the Reynolds stress, heat flux and energy transfers

of the model perturbations chosen in step one resemble the observed Reynolds stress and heat flux. The third step is to decide if the model basic state which is chosen in steps one and two is "realistic" (on the basis of the observed mean flow and various general circulation theories) and whether there is any correspondence between the observed and modelled mean potential vorticity gradients. Of course the last test is somewhat dubious because the observed mean flow is already altered by the instabilities.

The radiating modes of three eastward jet models have wildly varying structures, while the trapped modes (more unstable and higher frequency) are basically the same. The jet with eastward vertical shear in the outer region has surface-intensified modes. The jet with westward vertical shear in the outer region has bottom-intensified modes. The jet with a westward undercurrent excites both the barotropic and baroclinic modes outside the jet; these waves interfere with each other, setting up an alternating pattern of surface- and bottom-intensified modes.

All three models have positive momentum flux south of the jet with surface- and bottom-intensification according to the model. The momentum flux maximum in the upper layer was well to the south of the momentum flux maximum in the lower layer for the jet with eastward vertical shear outside. The momentum flux maximum in the bottom layer of the bottom-intensified modes was to the south of the upper layer momentum flux maximum. The heat flux in all models was negligible outside the jet and was slightly negative.

A fourth jet which can radiate is a westward jet (section 3.2). It is possible that the westward flow south of the Gulf Stream is set up quickly by fast-growing instabilities of the Gulf Stream and may itself be unstable to other perturbations. (This is observed in eddy-resolving general circulation models (Holland, Haidvogel, personal communication). The ideal model for comparison at this point would have both a Gulf Stream and westward side lobes. Since such a model has not been explored, we can only look at the results for eastward and westward jets separately. The radiating modes of westward jets have penetration scales of 300 to 400 km, which is quite sufficient for the Sargasso Sea. The most important feature of the structure of these radiating modes is that they are <u>barotropic</u> in the far field. The maximum momentum flux occurs farther to the north (closer to the westward jet) in the upper layer. The energy transfer is dominated by potential energy transfer to the instabilities, particularly at the low β's which best represent the ocean flow.

Figures 4.4.1 and 4.4.2 show the dimensional frequency and growth rate as a function of wavenumber and Figure 4.4.3 shows the frequency as a function of meridional decay scale for the three eastward jets and the westward jet. Scales were selected in Section 4.2. β was chosen to be .1 for the eastward jets and -.1 to give a westward jet. The eastward jets are supposed to model the Gulf Stream while the westward jet is to model the westward flow south of the Gulf Stream. All jets have two basic, trapped modes which are associated with the vertical and horizontal shear. The most unstable waves of the two modes have (x-wavelengths, periods and e-folding times) of (175 km, 10 days, 15 days) and

(Dimensional) frequency vs. wavenumber of the unstable modes for four jets: (a) eastward jet with a westward undercurrent and no vertical shear in the ocean interior; (b) eastward jet in the upper layer with small eastward vertical shear in the ocean interior;
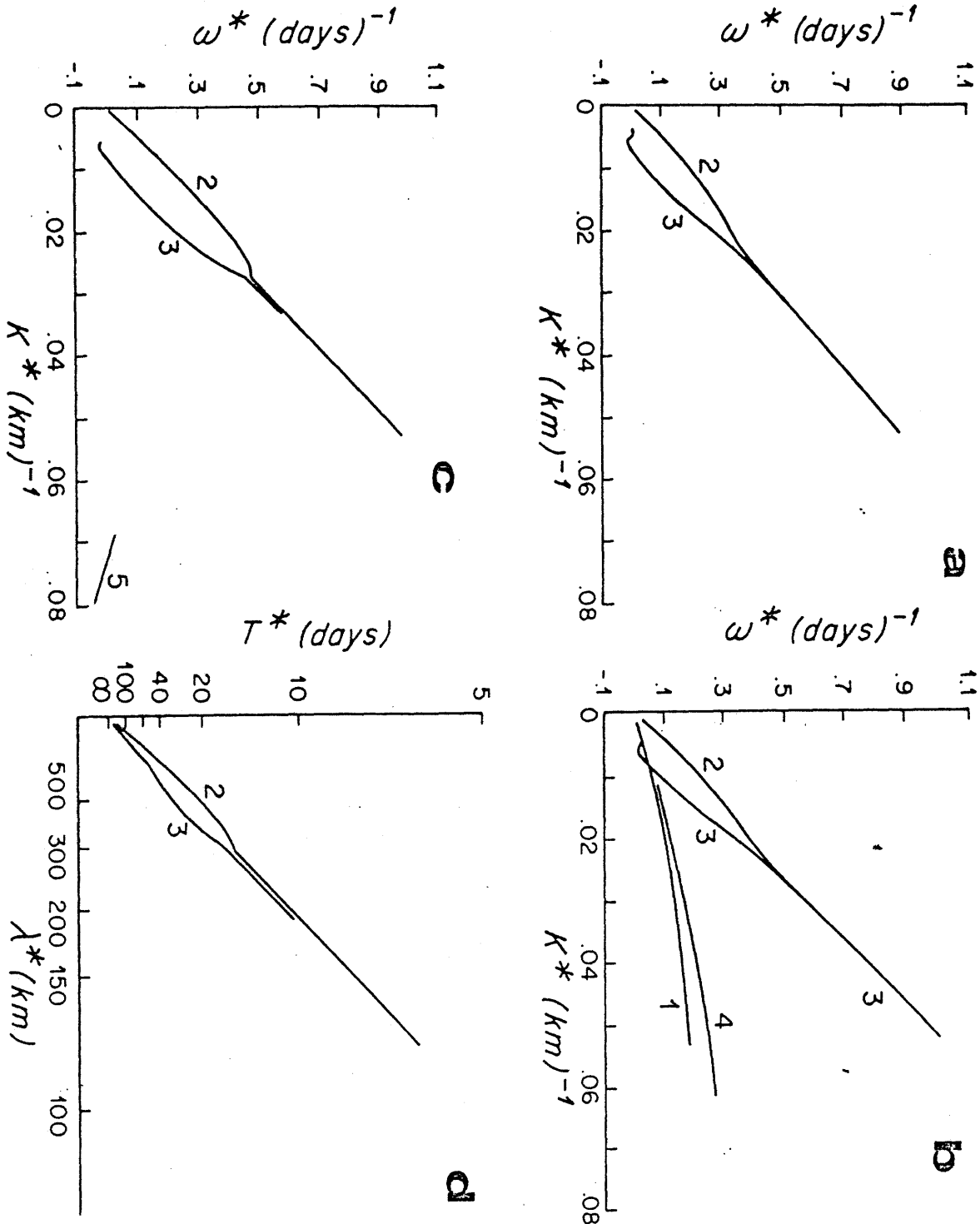
(c) eastward jet in the upper layer with small, westward vertical shear in the ocean interior; (d) westward jet in the upper layer, no vertical shear in the interior. All jets have non-dimensional values of .1 for β. [The scales for (d) show the wavelength in kilometers and period in days.]

Figure 4:4.1
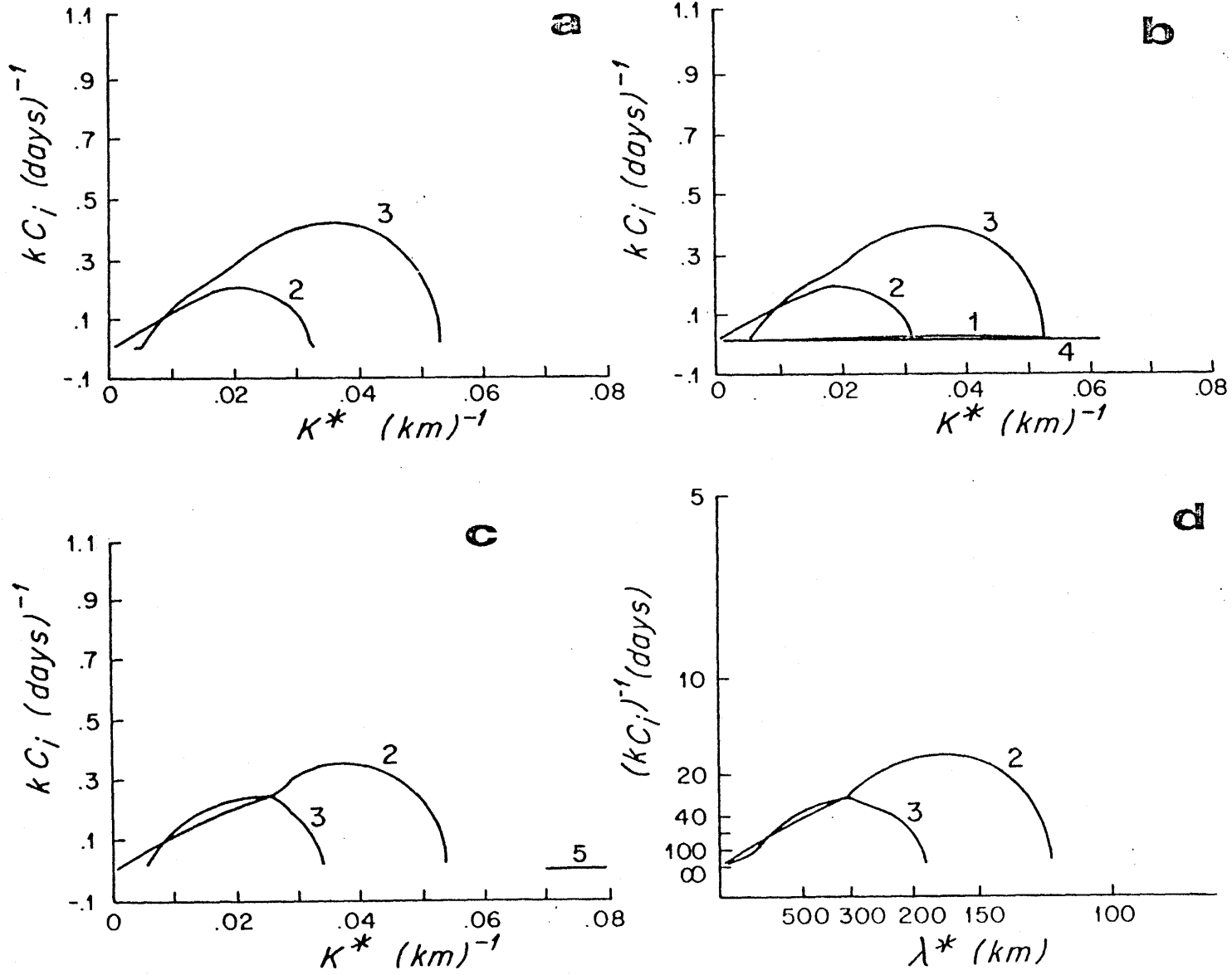
(Dimensional) growth rate, kc_i, vs. wavenumber for the same cases as Figure 4.4.1. Wavelength and period scales are shown in (d).

Figure 4.4.2
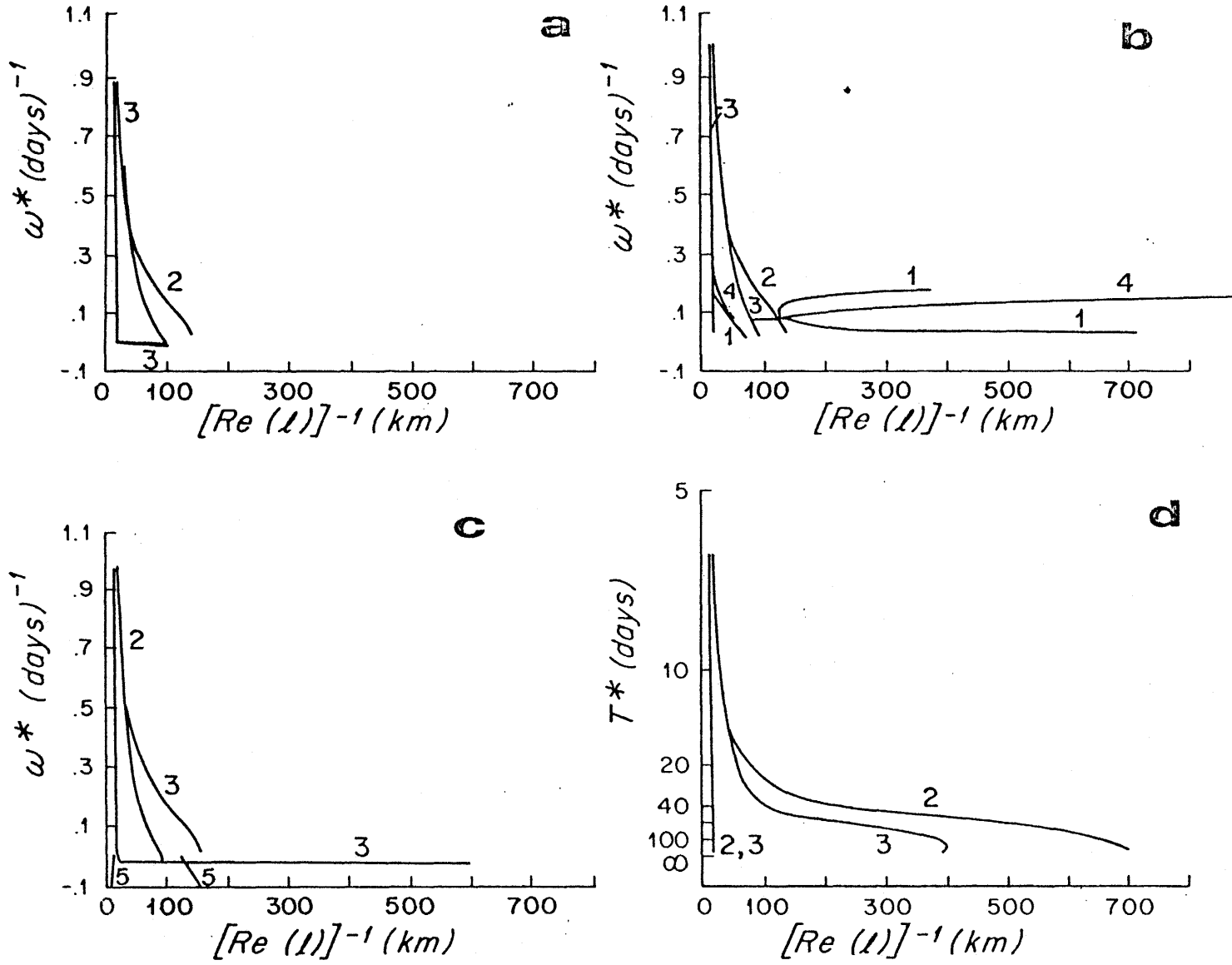
(Dimensional) frequency vs. meridional decay scale for the same cases as Figure 4.4.1. A period scale is also shown in (d).

Figure 4.4.3

(315 km, 20 days, 35 days) respectively. The low frequency, long waves are radiating for all jets. There are additional radiating modes for the two jets with vertical shear to the south. From Figure 4.4.3, it can be seen that the waves with longest meridional decay scales generally have low frequencies (periods greater than about 30 days).

The decay scales of the trapped instabilities are seen from Figure 4.4.3 to be less than 100 km (at β = .1) while the radiating modes can have decay scales of 100 to 1000 km. In the western North Atlantic, we are looking for disturbances with decay scales of 500 or 600 km south of the Gulf Stream, or 300 km or so south of the westward recirculation. These must be radiating modes since the trapped unstable modes are more tightly bound to the Gulf Stream. The eastward jets with vertical shear to the south have radiating modes with very large decay scales. The westward jet at β = .1 has modes with decay scales of 100 to 700 km. The eastward jet with a westward undercurrent has radiating modes with large decay scales at large β but does not radiate efficiently at β = .1. Thus, unstable modes exist which can produce the observed, slowly decaying, eddy energy.

The first observation to be matched to the model is the surface-intensification of eddy energy and the difference in decay scales and vertical structure of the secular and mesoscale disturbances. The long period ("secular scale") waves decayed very slowly and became more surface-intensified in the gyre interior; the medium period ("meso-scale") waves decayed more quickly and were surface-intensified, but not as strongly as the secular scale waves. The momentum flux for the

whole spectrum of fluctuations was positive to the south of the Gulf Stream but had marked vertical dependence: the momentum flux maximum in the upper water (600 m) was well to the south of the maximum in the lower water (4000 m) and decayed more slowly. These observations can be explained by the model with eastward vertical shear outside the jet: the secular scale disturbances are identified with radiating modes and the mesoscale with the trapped modes.

Hogg's (personal communication) empirical orthogonal functions and heat fluxes from the POLYMODE array complicate the comparison. While the first empirical orthogonal functions were surface-intensified at 37°30'N and 31°30'N, they were bottom-intensified at 36°N. There are at least three different possibilities: (1) The topography at 36°N excited bottom-intensified waves (suggestion of Nelson Hogg) so the proper model is still the jet with eastward vertical shear to the south. This can be tested by looking at results of numerical models without topography to see if bottom-intensified modes occur in the westward recirculation. (2) There were radiating, unstable modes arising from a Gulf Stream with a westward under-current and propagating in a region with no vertical shear: these modes are alternately surface- and bottom-intensified. (3) The westward recirculation at 36°N, which had some vertical shear (more westward at the surface) was transmitting the Gulf Stream instabilities more efficiently in the lower water column, thus making them bottom-intensified in the westward flow. Because the mean flow and Reynolds stress seem to be strongly affected by the topography at 36°N (Hogg, personal communication), the first alternative is the most probable.

The observed meridional heat flux at 600 and 1000 m is large and southward in the westward recirculation. The heat flux due to radiating modes south of the modelled, eastward jets is negative but very small so the westward flow itself is probably responsible for the large, southward heat flux, as a result of baroclinic instability. The heat flux due to the radiating modes south of the modelled, westward jet is also very small which agrees with the observation of greatly reduced heat flux in the ocean interior.

The energy transfers between mean and eddy potential and kinetic energy are the next quantities to be compared. In the thermocline (upper layer) the transfers can only be compared up to the southern flank of the Gulf Stream. In the models, transfers to the eddies are dominated by baroclinic instability in the jet center. Kinetic energy transfer occurs only in the shear zones: it is positive in the upper layer and positive but small in the lower layer. Transfers to the mean kinetic energy are surprising: in general, for all unstable modes, the mean flow gains kinetic energy in the shear zones, along with the eddies. [This must be true since $\partial U/\partial y$ and $\partial(\overline{u'v'})/\partial y$ have the same sign in the shear zones.] For many unstable modes, the mean flow gains and loses energy in an alternating pattern of gain in the center of the jet, loss farther out and gain in the shear zones. A small amount of energy is lost just outside the shear zone if there is non-zero flow there to begin with. This pattern tends to produce a banded mean flow.

Because there is little real difference in the energy transfer pattern from model to model, comparison with data can only tell us if the ob-

served energy transfers are consistent with current instabilities. In a general way, the data (Figure 4.4.3) and models are consistent: energy transfer falls off greatly south of the westward recirculation and Gulf Stream. Kinetic energy transfers are much reduced at depth where the horizontal shear is less. The observed transfer of energy to the eddies in the thermocline in the westward recirculation (large potential energy transfer in the center of the flow and positive kinetic energy transfer) shows that the westward flow centered at 36°N is itself unstable. The negative transfer of kinetic energy to the eddies north of 36°N is not predicted by any of the modelled instabilities and may result from the presence of both eastward and westward jets.

The abyssal energy transfers are not as easily compared: three of the four models essentially had no velocity in the lower layer so that kinetic energy transfers were negligible. Kinetic energy transfer in the lower layer of the jet with a westward undercurrent was also small since the lower layer was barotropically stable. The observations also have small, but non-zero, kinetic energy transfers at 4000 m. The pattern of transfers may be important: the abyssal flow gains energy in both the westward recirculation and the adjacent eastward flow to the north, while the undercurrent at 40°N loses energy.

The energy transfers leave the strong impression that the westward recirculation should be included as part of the basic unstable flow. Since no models with adjacent eastward and westward jets were run, the next best thing is to consider the results for the westward jet model. Radiating eigenfunctions for the westward jet model were barotropic in

the ocean interior: this was the case only because no vertical shear was included in the interior. With eastward vertical shear, there could be surface-intensified modes and with westward vertical shear, there could be bottom-intensified modes in the interior, just as for the eastward jets.

It would be most instructive to perform the same exercise with the recent Pacific data set which extends all the way across the Kuroshio in the thermocline (Schmitz, Niiler, Bernstein and Holland, 1982) to see what the energy transfers in the main eastward jet are.

In summary, the model which compares most favorably with the observations has eastward vertical shear in the ocean interior. This model and the data both have: increasing surface-intensification away from the Gulf Stream, increasing redness of the spectrum away from the Gulf Stream (and hence difference in meridional decay scales for different frequencies) and the Reynolds stress pattern. In addition, the energy transfers highlight the importance of the westward recirculation for the instabilities. The ideal model of the Gulf Stream system would have a strong eastward Gulf Stream, weaker westward side lobes and weak eastward vertical shear in the ocean interior. Is such a basic state consistent with general circulation theories and numerical model results?

The frictional, barotropic, wind-driven circulation models of Stommel (1948) and Munk (1950) are symmetric in the north-south direction. They have no intense Gulf Stream along the northern side. The inertial circulation of Fofonoff (1954) has westward flow throughout the interior with zonal eastward flow only in a narrow, interior northern boundary cur-

rent.   Circulation with both inertia and friction (Veronis, 1966) has a

Gulf Stream which overshoots the western boundary, follows the northern

boundary for a while to the east and then loops back to the west and then

to the east.   A north-to-south section in mid-gyre would have a strong,

narrow, eastward current (the Gulf Stream), weaker, broader westward flow

(the recirculation), gentle, broad, eastward flow (the interior of the

northern part of the gyre) and gentle westward flow (the interior of the

southern part of the gyre). If the frictional-inertial flow were the flow

in the upper layer of an ocean with a quiescent bottom layer, we would

have just the basic state suggested in the previous paragraph.   The mean

flow in the upper layer of eddy-resolving models of the circulation (Hol-

land and Lin, 1975) basically resembles Veronis' circulation.   However,

eddy-resolving models also have mean flow in the lower layer which is

strictly eddy-driven.   If this eddy-driven mean flow is included in the

basic state (a questionable proposition), the eastward vertical shear

in the ocean interior is no longer present and the proposed basic state

model is not viable.

In spin-up of the Gulf Stream system in numerical models, before Gulf

Stream rings develop, the instabilities discussed in this thesis are the

only source of variability.   One important result of Chapters 2 and 3 was

that the instabilities of eastward jets are usually more trapped than those

of westward jets.   (Even when basically eastward jets are set up with ad-

ditional geometry to allow radiation, the growth rates of the radiating

modes are much lower than those of westward jets.)   Holland (personal

communication) finds that in the spin-up of basin-scale layer models,

the initial instabilities of the eastward Gulf Stream are trapped until a westward recirculating jet is induced. This westward flow is itself unstable and its instabilities radiate readily into the ocean interior. This suggests that an eastward jet with westward sidelobes is the next reasonable model of the basic state which should be explored.

The question of whether to include eddy-driven flows in the basic state is difficult. If only the most unstable waves are important and all other instabilities ineffective in the fully-developed flow, then of course the basic state cannot include eddy-driven flow. If, however, instabilities with low growth rates are important in the final state, they may see a basic state which includes the effect of the fastest-growing instabilities. In this case, mean flow driven by the fastest-growing instabilities should be included in the basic state if the existence and structure of slowly-growing, radiating modes is being examined. My prejudice is to first examine the fastest-growing instabilities of an eastward jet to see what their effect on the mean flow is. In general, their Reynolds stress is such as to aid in setting up or reinforcing the westward recirculation. The westward recirculation should then be included in a new model of the basic state in which the radiating modes are of prim- ary interest. The radiating modes may not see the initial basic state, but could exist in some fashion in the flow altered by the most unstable waves.

Let us list the points at which the model and the Western Atlantic data agree and disagree:

(1) The observed surface intensification in the gyre interior can be explained by radiating modes of jets with eastward vertical shear in the interior.

(2)   The low frequency disturbances decay more slowly than the higher frequency disturbances in the data and the models.

(3)   The momentum flux is positive south of the Gulf Stream with a maximum farther south in the upper layer, which agrees with models with eastward vertical shear in the interior.

(4)   The structure of the westward recirculation may be affected by the Reynolds stress exerted by Gulf Stream instabilities.

(5)   Large negative heat flux in the westward recirculation suggests that the recirculation be included in the basic model.

(6)   The alternation of surface and bottom-intensified perturbations could possibly be radiating modes of an eastward jet with a westward undercurrent, but this model does not radiate well in the parameter range of the Gulf Stream. Bottom-intensification at 36°N is more likely to be due to topography.

APPENDIX

The dispersion relation for the two layer, baroclinic jet (Figure 3.1.1) is obtained from the matching and boundary conditions imposed on the solutions (3.1.18). The channel is assumed to have walls at $y = \pm H$. The boundary conditions there are that $\Phi_n = 0$. This simplifies (3.1.18) to

I.
$$\Phi_1 = a_1 \left(e^{-2\ell_1 H + \ell_1 y} + e^{-\ell_1 y} \right) + a_3 \left(-e^{-2\ell_2 H + \ell_2 y} + e^{-\ell_2 y} \right)$$

$$\Phi_2 = f_1 a_1 \left(e^{-2\ell_1 H + \ell_1 y} + e^{-\ell_1 y} \right) + f_2 a_3 \left(-e^{-2\ell_2 H + \ell_2 y} + e^{-\ell_2 y} \right)$$

II.
$$\Phi_1 = b_1 e^{ky} + b_2 e^{-ky} + b_3 e^{\ell y} + b_4 e^{-\ell y}$$

$$\Phi_2 = b_1 e^{ky} + b_2 e^{-ky} - b_3 e^{\ell y} - b_4 e^{-\ell y}$$

III.
$$\Phi_1 = c_1 \left(e^{m_1 y} + e^{-m_1 y} \right) + c_2 \left(e^{m_2 y} + e^{-m_2 y} \right)$$

$$\Phi_2 = d_1 c_1 \left(e^{m_1 y} + e^{-m_1 y} \right) + d_2 c_2 \left(e^{m_2 y} + e^{-m_2 y} \right)$$

The dispersion relation obtained from the matching conditions is written below as two coupled equations in the unknowns c_3 [one of the coefficients in (A.1)] and the complex phase speed c. The equations are solved to eliminate c_3, resulting in a transcendental, but algebraic, equation, for c. This is solved numerically using the root-finding secant method with complex arithmetic. The dispersion relation is listed on the next two pages.

In the following dispersion relation,

$$\delta \equiv D$$

$$\text{den} \equiv (1-d_1)(1+d_2) - (1+d_1)(1-d_2)$$

$$A \equiv U_{I1}-c$$

$$B \equiv U_{I2}-c$$

$$D \equiv U_{01}-c$$

$$E \equiv U_{02}-c$$

$$U_{11} \equiv \frac{dU_{I1}}{dy} \quad y = 1$$

$$U_{1\delta} \equiv \frac{dU_{I2}}{dy} \quad y = 1$$

$$U_{21} \equiv \frac{dU_{01}}{dy} \quad y = D$$

$$U_{2\delta} = \frac{dU_{02}}{dy} \quad y = D$$

$$e^{-l_1 H} \sinh l_1 (\delta - H) \left\{ -(1+f_1)(kB - U_{2_1}) e^{k(1-\delta)} - (1-f_1)(-lB + U_{2_1}) e^{l(1-\delta)} \right.$$

$$- \frac{2B}{den} e^{k(1-\delta)} \left[d_1 m_1 \tanh m_1 (1-d_2) - d_2 m_2 \tanh m_1 (1-d_1) \right] (1+f_1) - \frac{2B}{den} e^{l(1-\delta)} (1-f_1) \left[-d_1 m_1 \tanh m_1 (1+d_2) \right.$$

$$\left. \left. + d_2 m_2 \tanh m_2 (1+d_1) \right] \right\}$$

$$+ \frac{e^{-l_1 H}}{k} \left\{ l_1 (1+f_1) \cosh l_1 (\delta - H) - \left[k(1+f_1) - \frac{U_{1\delta}}{D} - f_1 \frac{U_{2\delta}}{E} \right] \sinh l_1 (\delta - H) \right\} \cdot$$

$$\left\{ -kB \cosh k(1-\delta) + U_{2_1} \sinh k(1-\delta) - \frac{2B}{den} \sinh k(1-\delta) \left[d_1 (1-d_2) m_1 \tanh m_1 - d_2 (1-d_1) m_2 \tanh m_2 \right] \right\}$$

$$+ \frac{e^{-l_1 H}}{l} \left\{ l_1 (1-f_1) \cosh l_1 (\delta - H) - \left[l(1-f_1) - \frac{U_{1\delta}}{D} + f_1 \frac{U_{2\delta}}{E} \right] \sinh l_1 (\delta - H) \right\} \cdot$$

$$\left\{ lB \cosh l(1-\delta) - U_{2_1} \sinh l(1-\delta) + \frac{2B}{den} \sinh l(1-\delta) \left[d_1 (1+d_2) m_1 \tanh m_1 - d_2 (1+d_1) m_2 \tanh m_2 \right] \right\}$$

-226-

$$+ a_2 \left\{ e^{-l_2 H} \sinh l_2 (\delta - H) \left\{ -(1+f_2)(kB - U_{2_1}) e^{k(1-\delta)} - (1-f_2)(-lB + U_{2_1}) e^{l(1-\delta)} \right. \right.$$

$$\left. - \frac{2B}{den} e^{k(1-\delta)} (1+f_2) \left[d_1 (1-d_2) m_1 \tanh m_1 - d_2 (1-d_1) m_2 \tanh m_2 \right] - \frac{2B}{den} e^{l(1-\delta)} [1-f_2] \left[-d_1 (1+d_2) m_1 \tanh m_1 \right. \right.$$

$$\left. \left. + d_2 (1+d_1) m_2 \tanh m_2 \right] \right\}$$

$$+ \frac{e^{-l_2 H}}{k} \left\{ l_2 (1+f_2) \cosh l_2 (\delta - H) - \sinh l_2 (\delta - H) \left[k(1+f_2) - \frac{U_{1\delta}}{D} - f_2 \frac{U_{2\delta}}{E} \right] \right\} \cdot$$

$$\left\{ -kB \cosh k(1-\delta) + U_{2_1} \sinh k(1-\delta) - \frac{2B}{den} \sinh k(1-\delta) \left[d_1 (1-d_2) m_1 \tanh m_1 - d_2 (1-d_1) m_2 \tanh m_2 \right] \right\}$$

$$+ \frac{e^{-l_2 H}}{l} \left\{ l_2 (1-f_2) \cosh l_2 (\delta - H) - \sinh l_2 (\delta - H) \left[l(1-f_2) - \frac{U_{1\delta}}{D} + f_2 \frac{U_{2\delta}}{E} \right] \right\} \left\{ lB \cosh l(1-\delta) - U_{2_1} \sinh l(1-\delta) + \frac{2B}{den} \sinh l(1-\delta) \cdot \right.$$

$$\left. \left. \left[d_1 (1+d_2) m_2 \tanh m_2 - d_2 (1+d_1) m_2 \tanh m_2 \right] \right\} \right\} = 0$$

$$e^{-\ell_1 H} \sinh \ell_1 (\delta - H) \left\{ -(1+f_1)(kA - U_{11}) e^{k(1-\delta)} - (1-f_1)(\ell A - U_{11}) e^{\ell(1-\delta)} - \frac{2A}{den} e^{k(1-\delta)} (1+f_1) \cdot \right.$$

$$\left[m_1(\tanh m_1)(1-d_2) - m_2(\tanh m_2)(1-d_1) \right] - \frac{2A}{den} e^{\ell(1-\delta)} (1-f_1) \left[-m_1(\tanh m_1)(1+d_2) + (1+d_1) m_2 \tanh m_2 \right] \Big\}$$

$$+ \frac{e^{-\ell_1 H}}{k} \left\{ \ell_1 (1+f_1) \cosh \ell_1 (\delta - H) - \sinh \ell_1 (\delta - H) \left[k(1+f_1) - \frac{U_{1\delta}}{D} - f_1 \frac{U_{2\delta}}{E} \right] \right\} \cdot$$

$$\left\{ -kA \cosh k(1-\delta) + U_{11} \sinh k(1-\delta) - \frac{2A}{den} \sinh k(1-\delta) \left[m_1 \tanh m_1 (1-d_2) - (1-d_1) m_2 \tanh m_2 \right] \right\}$$

$$+ \frac{e^{-\ell_1 H}}{\ell} \left\{ \ell_1 (1-f_1) \cosh \ell_1 (\delta - H) - \sinh \ell_1 (\delta - H) \left[\ell(1-f_1) - \frac{U_{1\delta}}{D} + f_1 \frac{U_{2\delta}}{E} \right] \right\} \cdot$$

$$\left\{ -\ell A \cosh \ell(1-\delta) + U_{11} \sinh \ell(1-\delta) + \frac{2A}{den} \sinh \ell(1-\delta) \left[(1+d_2) m_1 \tanh m_1 - (1+d_1) m_2 \tanh m_2 \right] \right\}$$

$$+ a_2 \left\{ e^{-\ell_2 H} \sinh \ell_2 (\delta - H) \left\{ -(1+f_2)(kA - U_{11}) e^{k(1-\delta)} - (1-f_2)(\ell A - U_{11}) e^{\ell(1-\delta)} \right. \right.$$

$$\left. - \frac{2A}{den} e^{k(1-\delta)} \left[(1-d_2) m_1 \tanh m_1 - (1-d_1) m_2 \tanh m_2 \right] - \frac{2A}{den} e^{\ell(1-\delta)} \left[-(1+d_2) m_1 \tanh m_1 + (1+d_1) m_2 \tanh m_2 \right] \right\}$$

$$+ \frac{e^{-\ell_2 H}}{k} \left[\ell_2 (1+f_2) \cosh \ell_2 (\delta - H) - \sinh \ell_2 (\delta - H) \left\{ k(1+f_2) - \frac{U_{1\delta}}{D} - f_2 \frac{U_{2\delta}}{E} \right\} \right] \cdot$$

$$\left\{ -kA \cosh k(1-\delta) + U_{11} \sinh k(1-\delta) - \frac{2A}{den} \sinh k(1-\delta) \left[(1-d_2) m_1 \tanh m_1 - (1-d_1) m_2 \tanh m_2 \right] \right\}$$

$$+ \frac{e^{-\ell_2 H}}{\ell} \left\{ \ell_2 (1-f_2) \cosh \ell_2 (\delta - H) - \sinh \ell_2 (\delta - H) \left[\ell(1-f_2) - \frac{U_{1\delta}}{D} + f_2 \frac{U_{2\delta}}{E} \right] \right\} \cdot$$

$$\left. \left\{ -\ell A \cosh \ell(1-\delta) + U_{11} \sinh \ell(1-\delta) + \frac{2A}{den} \sinh \ell(1-\delta) \left[m_1 \tanh m_1 (1+d_2) - (1+d_1) m_2 \tanh m_2 \right] \right\} \right\} = 0$$

References

Bernstein, R. L. and W. B. White (1977) Zonal variability in the distribution of eddy energy in the mid-latitude North Pacific Ocean. J. Phys. Oceanog. 7, 123-126.

Betchov, R. and W. O. Criminale (1967) Stability of Parallel Flows, Academic Press, 330 pp.

Bryden, H. L. (1981) Sources of eddy energy in the Gulf Stream recirculation regions. Submitted to J. Mar. Res.

Charney, J. G. (1947) The dynamics of long waves in a baroclinic westerly current. J. Meteor. 4, 135-163.

Charney, J. G. and M. Stern (1962) On the stability of internal baroclinic jet in a rotating atmosphere. J. Atmos. Sci. 19, 159-172.

Dantzler, H. L. (1977) Potential energy maxima in the tropical and subtropical North Atlantic. J. Phys. Oceanog. 7, 512-519.

Dickinson, R. E. and F. L. Clare (1973) Number of unstable modes of a hyperbolic-tangent barotropic shear flow. J. Atmos. Sci. 30, 1035-1049.

Drazin, P. G. and L. N. Howard (1962) The instability to long waves of unbounded parallel inviscid flow. J. Fluid Mech. 14, 257-283.

Eady, E. T. (1949) Long waves and cyclone waves. Tellus 1, 33-52.

Flierl, G. R. (1977) The application of linear quasigeostrophic dynamics to Gulf Stream rings. J. Phys. Oceanog. 7, 365-379.

Flierl, G. R. (1975) Gulf Stream meandering, ring formation and ring propagation. Ph.D. Thesis, Harvard University, 270 pp.

Flierl, G. R., V. D. Larichev, J. C. McWilliams and G. M. Reznik (1980) The dynamics of baroclinic and barotropic solitary eddies. _Dyn. of Atmos. and Oceans_ _5_, 1-41.

Fjørtoft, R. (1950) Application of integral theorems in deriving criteria of stability for laminar flow and for the baroclinic circular vortex. _Geof. Publ._ _17_(6), 52 pp.

Fofonoff, N. P. (1954) Steady flow in a frictionless homogeneous ocean. _J. Mar. Res._ _13_, 254-262.

Frankignoul, C. and P. Muller (1979) On the generation of geostrophic eddies by surface buoyancy flux anomalies. _J. Phys. Oceanog._ _9_, 1207-1213.

Garcia, R. V. and R. Norscini (1970) A contribution to the baroclinic instability problem. _Tellus_ _22_,   .

Gent, P. R. (1974) Baroclinic instability of a slowly varying zonal flow. _J. Atmos. Sci._ _31_, 1983-1994.

Gent, P. R. (1975) Baroclinic instability of a slowly varying zonal flow. Part 2. _J. Atmos. Sci._ _32_, 2094-2102.

Gill, A. F., J.S.A. Green and A. J. Simmons (1974) Energy partition in the large-scale ocean circulation and the production of mid-ocean eddies. _Deep-Sea Res._ _21_, 499-528.

Haidvogel, D. B. and W. R. Holland (1978) The stability of ocean currents in eddy-resolving general circulation models. _J. Phys. Oceanog._ _8_, 393-413.

Hart, J. E. (1974) On the mixed stability problem for quasi-geostrophic ocean currents. _J. Phys. Oceanog._ _4_, 349-356.

Held, I. M. (1975) Momentum transport by quasi-geostrophic eddies. J. Atmos. Sci. 32, 1494-1497.

Helmholtz, H. V. (1868) On discontinuous movements of fluids. Phil. Mag. 4(36), 337-346.

Holland, W. R. and L. B. Lin (1975) On the generation of mesoscale eddies and their contribution to the oceanic general circulation. I. A preliminary experiment. J. Phys. Oceanog. 5, 642-657.

Holland, W. R. (1978) The role of mesoscale eddies in the general circulation of the ocean. Numerical experiments using a wind-driven quasi-geostrophic model. J. Phys. Oceanog. 8, 363-392.

Holland, W. R. and Haidvogel, D. B. (1980) A parameter study of the mixed instability of idealized ocean currents. Dynamics of Atmos. and Oceans 4, 185-215.

Howard, L. N. (1961) Note on a paper of John Miles. J. Fluid Mech. 10, 509-512.

Howard, L. N. (1964) The number of unstable modes in hydrodynamic stability problems. Journal de Mecanique 3, 433-443.

Howard, L. N. and P. G. Drazin (1964) On instability of parallel flow of inviscid fluid in a rotating system with variable Coriolis parameter. J. Math. and Phys. 43, 83-99.

Kuo, H. L. (1949) Dynamic instability of two-dimensional nondivergent flow in a barotropic atmosphere. J. Meteor. 6, 105-122.

Kuo, H. L. (1973) Dynamics of quasi-geostrophic flows and instability theory. In: Advances in Applied Mechanics 13, 247-330.

Lindzen, R. S. (1974) Stability of a Helmholtz velocity profile in a continuously stratified, infinite Boussinesq Fluid - applications to clear air turbulence. J. Atmos. Sci. 31, 1507-1514.

Loesch, A. Z. (1974) Resonant interactions between unstable and neutral baroclinic waves: Part I. J. Atmos. Sci. 31, 1177-1201.

McIntyre, M. E. and M. A. Weissman (1978) On radiating instabilities and resonant over-refection. J. Atmos. Sci. 35, 1190-1196.

Muller, P. and C. Frankignoul (1981) Direct atmospheric forcing of geo-strophic eddies. J. Phys. Oceanog. 11, 287-308.

Munk, W. H. (1950) On the wind-driven ocean circulation. J. Meteor. 7, 79-93.

Orlanski, I. (1969) The influence of bottom topography on the stability of jets in a baroclinic fluid. J. Atmos. Sci. 26, 1216-1232.

Pedlosky, J. (1964a) The stability of currents in the atmosphere and the oceans. Part I. J. Atmos. Sci. 27, 201-219.

Pedlosky, J. (1964b) The stability of currents in the atmosphere and the oceans. Part II. J. Atmos. Sci. 21, 342-353.

Pedlosky, J. (1970) Finite amplitude baroclinic waves. J. Atmos. Sci. 20, 448-464.

Pedlosky, J. (1975) The amplitude of baroclinic wave triads and mesoscale motion in the ocean. J. Phys. Oceanog. 5, 608-614.

Pedlosky, J. (1976) On the radiation of meso-scale energy in the mid-ocean. Deep-Sea Res. 24, 591-600.

Pedlosky, J. (1979) Geophysical Fluid Dynamics, Springer-Verlag, Inc. New York, 624 pp.

Pedlosky, J. (1980) The destabilization of shear flow by topography.

J. Phys. Oceanog. 10, 1877-1880.

Pedlosky, J. (1981) The nonlinear dynamics of baroclinic wave ensembles.

J. Fluid Mech. 102, 169-209.

Philander, S.G.H. (1978) Forced oceanic waves. Rev. Geophysics and

Space Physics 16, 15-46.

Phillips, N. A. (1954) Energy transformations and meridional circula-

tions associated with simple baroclinic waves in a two-level, quasi-

geostrophic model. Tellus, 6, 273-286.

Rayleigh, Lord (1879) On the instability of jets. Scientific Papers 1,

361-371, Dover, New York (1964).

Rayleigh, Lord (1880) On the stability, or instability, of certain fluid

motions. Scientific Papers 1, 474-487, Dover, New York (1964).

Rayleigh, Lord (1887) On the stability or instability of certain fluid

motions, II. Scientific Papers 3, 17-23, Dover, New York (1964).

Richardson, P. L. (1982) North Atlantic current variability from drifting

buoys. In preparation.

Schmitz, W. J. (1978) Observations of the vertical distribution of low

frequency energy in the western North Atlantic. J. Mar. Res. 36,

295-310.

Schmitz, W. J. (1980) Weakly depth-dependent segments of the North At-

lantic circulation. J. Mar. Res. 38, 111-133.

Schmitz, W. J. (1981) A comparison of the mid-latitude eddy fields in the

western North Atlantic and North Pacific Oceans. J. Phys. Oceanog.

62, 208-210.

Schmitz, W. J. and W. R. Holland (1981) A preliminary comparison of selected numerical eddy-resolving general circulation experiments with observations. J. Mar. Res., In press.

Schmitz, W. J., P. P. Niiler, R. L. Bernstein, W. R. Holland (1982) Recent long-term moored instrument observations in western North Pacific. Submitted to J. Geophys. Res.

Schmitz, W. J., J. F. Price, P. L. Richardson, W. B. Owens, D. C. Webb, R. E. Cheney and H. T. Rossby (1981) A preliminary exploration of the Gulf Stream system with SOFAR floats. J. Phys. Oceanog. 11, 1194-1204.

Stommel, H. (1948) The westward intensification of wind-driven ocean currents. Trans. Amer. Geophys. Union 99, 202-206.

Stommel, H. and G. Veronis (1980) Barotropic response to cooling. J. Geophys. Res. 85, 6661-6666.

Tung, K. K. (1981) Barotropic instability of zonal flows. J. Atmos. Sci. 38, 308-321.

Veronis, G. (1966) Wind-driven ocean circulation - Part 2. Numerical solutions of the non-linear problem. Deep-Sea Res. 13, 31-55.

Wallace, J. M. and R. E. Dickinson (1972) Empirical orthogonal representations of time series in the frequency domain. Part I: Theoretical considerations. J. App. Meteor. 11, 887-892.

Worthington, L. V. (1976) On the North Atlantic Circulation. The Johns Hopkins University Press, Baltimore and London, 110 pp.

Wyrtki, K., L. Magaard and J. Hager (1976) Eddy energy in the oceans. J. Geophys. Res. 81, 2641-2646.